# Multiwavelet-based hp-adaptation for discontinuous Galerkin methods

Javier Garcia Bautista

▶ **To cite this version:**

Javier Garcia Bautista. Multiwavelet-based hp-adaptation for discontinuous Galerkin methods. Fluids mechanics [physics.class-ph]. École centrale de Nantes, 2022. English. NNT : 2022ECDN0046 . tel-03952019

**HAL Id: tel-03952019**
**https://theses.hal.science/tel-03952019**

Submitted on 23 Jan 2023

**HAL** is a multi-disciplinary open access archive for the deposit and dissemination of scientific research documents, whether they are published or not. The documents may come from teaching and research institutions in France or abroad, or from public or private research centers.

L'archive ouverte pluridisciplinaire **HAL**, est destinée au dépôt et à la diffusion de documents scientifiques de niveau recherche, publiés ou non, émanant des établissements d'enseignement et de recherche français ou étrangers, des laboratoires publics ou privés.

# THÈSE DE DOCTORAT DE

L'ÉCOLE CENTRALE DE NANTES

ÉCOLE DOCTORALE N° 602
*Sciences pour l'Ingénieur*
Spécialité : *Mécanique des Milieux Fluides*

Par

**Javier GARCÍA BAUTISTA**

# Multiwavelet-based *hp*-adaptation for discontinuous Galerkin methods

Thèse présentée et soutenue à ONERA Châtillon, le 7 novembre 2022
Unité de recherche : *UMR 6598, Laboratoire de Recherche en Hydrodynamique, Energétique et Environnement Atmosphérique (LHEEA)*

**Rapporteurs avant soutenance :**

| | |
|---|---|
| Siegfried MÜLLER | Professor, Rheinisch-Westfälische Technische Hochschule Aachen, Allemagne |
| Esteban FERRER | Professor, Universidad Politécnica de Madrid, Espagne |

**Composition du Jury :**

| | | |
|---|---|---|
| Présidente : | Paola CINNELLA | Professeure des universités, Sorbonne Université |
| Examinateurs | Georg MAY | Associate professor, Von Karman Institute for Fluid Dynamics, Belgique |
| | Frédéric ALAUZET | Directeur de Recherche, INRIA Saclay, Palaiseau |
| Dir. de thèse : | Michel VISONNEAU | Directeur de Recherche, École Centrale de Nantes |
| Co-dir. de thèse : | Kai SCHNEIDER | Professeur des Universités, Aix-Marseille Université |
| Co-encadrante : | Marta DE LA LLAVE PLATA | Ingénieure de recherche, ONERA, Toulouse |

# MULTIWAVELET-BASED HP-ADAPTATION FOR DISCONTINUOUS GALERKIN METHODS

JAVIER GARCÍA BAUTISTA


This project has received funding from the European Union's Horizon 2020 research and innovation program under the Marie Skłodowska-Curie grant agreement No. 675008 for the years 2018 to 2019 and from ONERA for 2020 onwards.

Javier García Bautista: *Multiwavelet-based hp-adaptation for discontinuous Galerkin methods*, © September 2022

# RÉSUMÉ

L'objectif principal de cette thèse est de développer une approche adaptative à la *hp*-méthode efficace en termes de calcul pour les schémas Galerkin discontinus des équations de Navier-Stokes, en combinant la flexibilité de l'adaptation a posteriori et la précision de l'adaptation multi-résolution. Les performances de l'algorithme de la *hp*-méthode sont illustrées par plusieurs flux stables en une et deux dimensions.

La nouveauté de l'étude réside dans l'utilisation des multi-ondelettes et la façon dont leurs propriétés remarquables peuvent apporter un éclairage nouveau sur la conduite du processus d'adaptation. Ceci est motivé par le fait que les multi-ondelettes décomposent n'importe quelle entrée en une hiérarchie de données de basse résolution et ensuite de détails plus fins. Notre méthodologie utilise les propriétés des multi-ondelettes tout en étant locale à l'élément, en gardant ainsi l'efficacité parallèle du shéma de DG.

La première direction de recherche emploie une nouvelle méthodologie basée sur les multi-ondelettes pour estimer l'erreur de discrétisation de la solution numérique dans le contexte des simulations adaptives à la *h*-méthode. Cette nouvelle méthodologie est ensuite comparée à des estimateurs d'erreur bien établis dans la littérature afin d'évaluer leur efficacité globale. Les résultats démontrent clairement la viabilité de la *h*-méthode pour atteindre un gain de calcul significatif par rapport aux maillages uniformément raffinés. La méthodologie basée sur les multi-ondelettes est nettement plus performante que les estimateurs de la littérature, en particulier pour les simulations d'ordre inférieur. Plus particulièrement, la fiabilité et la précision de la méthodologie proposée augmentent avec les ordres de simulation plus élevés grâce à la plus grande quantité d'informations récupérées avec succès par les multi-ondelettes.

La deuxième ligne d'investigation aborde l'analyse et le développement d'une nouvelle stratégie adaptative à la *hp*-méthode basée sur la décroissance du spectre des multi-ondelettes pour diriger les simulations adaptatives à la *hp*-méthode. Cette stratégie permet de discriminer avec succès les régions caractérisées par une grande régularité et des phénomènes discontinus, ainsi que leur proximité. Nous nous concentrons sur l'étude de la distribution optimale de la *hp*-méthode et de ses performances globales par rapport à l'adaptation pure par la *h*- ou *p*-méthode. Les analyses globales et locales menées de cette manière indiquent une réduction significative du coût de calcul de la simulation lorsque la *hp*-méthode est sélectionnée par rapport à la *h*- ou *p*-méthode. De manière remarquable, l'algorithme d'adaptation à la *hp*-méthode développé est capable d'atteindre la haute précision caractéristique des solutions numériques d'ordre élevé tout en évitant les oscillations indésirables en adoptant des approximations d'ordre réduit à proximité des singularités.

# ABSTRACT

The main objective of the present thesis is to devise, construct and validate computationally efficient *hp*-adaptive discontinuous Galerkin schemes of the Navier-Stokes equations by bringing together the *flexibility* of *a posteriori* error driven adaptation and the *accuracy* of multiresolution-based adaptation. The performance of the *hp*-algorithm is illustrated by several steady flows in one and two dimensions.

The novelty of the study resides in the use of multiwavelets and how their remarkable properties may shed new light on driving the adaptation process. This is motivated by the fact that multiwavelets break any input apart into a hierarchy of low-resolution data and subsequently finer details. Our methodology makes use of multiwavelets' properties while being local to the element, thereby maintaining the parallel efficiency of the solver.

The first research direction employs a new multiwavelet-based methodology to estimate the discretization error of the numerical solution in the context of *h*-adaptive simulations. This novel methodology is then compared against well-established error estimators from the literature to evaluate their overall performance. The results certainly demonstrate the viability of *h*-refinement to reach a significant computational gain with respect to uniformly refined grids. The multiwavelet-based methodology performs substantially better than the literature estimators, and in particular for low-order simulations. Most notably, the reliability and accuracy of the proposed methodology increases with higher simulation orders thanks to the higher amount of information successfully retrieved by the multiwavelets.

The second line of investigation addresses the analysis and development of a new *hp*-adaptive strategy based on the decay of the multiwavelet spectrum to drive *hp*-adaptive simulations. The strategy successfully discriminates between regions characterized by high regularity and discontinuous phenomena and their vicinity. We focus our attention on studying the optimal *hp*-distribution and its overall performance with respect to single *h*- or *p*-adaptation. Both global and local analyses conducted in this manner report a significant reduction in the computational cost of the simulation when *hp* is selected over either *h* or *p*. Remarkably, the developed *hp*-adaptation algorithm is able to achieve the high accuracy characteristic of high-order numerical solutions while avoiding unwanted oscillations by adopting low-order approximations in the proximity of singularities.

# ACKNOWLEDGEMENTS

A PhD thesis is daunting odyssey, a form of rite of passage for the ingenuous researcher. Upon concluding this doctoral research, I would like to express my gratitude to the people that have been part of this journey and that have helped me to grow both personally and as a researcher.

I would like to start by thanking my supervisors at ONERA, Marta de la Llave Plata and Vincent Couaillier, for their constant support and guidance from start to finish. Despite moving out of Paris, Marta has always gone the extra mile to follow the technical progress of my thesis and to offer insightful comments and suggestions. In addition to academic guidance, Vincent has helped me in countless occasions navigating through the administration at ONERA, for which I am very thankful. I would also like to express my sincere appreciation to the directors of this thesis, the professors Michel Visonneau and Kai Schneider, for their time and effort spent in supervising this thesis remotely. Although located in Nantes and Marseille respectively, they were always available for long and enriching video-calls, especially at the end of my thesis.

This research was made possible by the SSeMID project, which has been funded by the European Commission. This project has promoted an extraordinary environment of international cooperation and research exchange; in my opinion, it demonstrates the potential of the European Union.

I also would like to send a huge thanks to my friends at the NFLU unit and at ONERA. Pratik, Emma, Fabio, Francesca, Federico, Jorge, and Matthias. Thank you for the cherished time spent together; we have had a lot of fun, both in the office and going out in Paris. I would also like to extend my thanks to my friends in the SSeMID project. Francesco, Souvik, Andrés, Luigi, Catherine, Thibaut, and Iván. We had met for the first time in Montestigliano (except you, Francesco!) and since then shared many trips together all around Europe. And of course, a big shot-out to my friend Jan in Berlin for his warm support, and to my old friends back in Málaga: the Marios, Ayu, Pedro, Sergio, and Ernesto; who I always met during my holidays in Spain and support me over the years regardless of the distance.

Finally, words cannot express my gratitude to my family and to my partner. To my parents Begoña and Antonio and my sister Sofi, for their infinite support, caring, patience, and belief in me; and to Nina, for your love, trust and understanding. You are my North Star! I love you and am proud of you.

# CONTENTS

# LIST OF FIGURES

# LIST OF TABLES

# Chapter 1

# INTRODUCTION

## 1.1 BACKGROUND AND MOTIVATION

In this day and age computational fluid dynamics (CFD) has become an invaluable vehicle to understand the complex behavior of fluid flow. The set of conservation laws that governs the motion of fluids are represented as a system of partial differential equations (PDEs), for which, in the general case, no analytical solution is available besides some very specific conditions in the laminar regime. As an alternative, a great number of techniques to numerically approximate the solution to these equations has been historically put forward and developed. Among the most illustrative techniques we identify the finite-volume methods (FVMs) (LeVeque, 2002; Ferziger et al., 2020) and the finite-element methods (FEMs) (Donéa and Huerta, 2003; Reddy and Gartling, 2010). These methods are based on the discretization of the physical domain into a computational grid consisting of a collection of elements where the numerical solution is defined.

Since their first use in the 1960s, finite-volume methods have been extensively studied and advanced by the CFD community (Godlewski and Raviart, 1996; Eymard et al., 2000). Their numerical solution is represented by an averaged value of the solution in a control volume obtained by flux balance across the volume interfaces. The *physical* fluxes at the interfaces are replaced by numerical fluxes solving the problem of discontinuity between left and right elements (Riemann solver for the convective term) (Toro, 2009). Conventional FVMs are second order accurate and offer a simple and robust formulation suitable for both structured and unstructured grids. However, FVMs with higher orders of accuracy involve wider stencils, which considerably reduce their flexibility.

Finite-element methods were introduced to CFD in the late 1970s and have also proved to be very successful in fluid dynamics (Babuvška, 1973; Pironneau, 1989). Unlike FVMs, their numerical solution is locally defined by a linear combination of polynomials assumed to be continuous across element interfaces. Originally, FEMs were designed with polynomials of low degree (Boyd, 2001). The extension to higher degrees receives the name of spectral elements methods (SEMs) (Patera, 1984), which inherit the properties of high-order accuracy and low-dispersion errors of spectral methods (Karniadakis and Sherwin, 2005). However, these methods rely on polynomials with continuous global support, which introduces potential stability problems when dealing with hyperbolic configurations (Hesthaven and Warburton, 2008).

A compact combination of the spectral-element and the finite-volume methods, which seems to offer many of the required characteristics, consists in using high-order polynomials with spectral accuracy that mirror the spectral element method while retaining the conservativity of the finite volume method. This selective combination plus the introduction of a highly local stencil catalyzes into the discontinuous Galerkin method (DGM).

Discontinuous Galerkin methods have the benefit of attaining high parallel efficiency on distributed memory machines thanks to their local nature, their large on-processor operation count, and a small communication footprint (Giraldo and Restelli, 2008). These factors make the DGMs especially well-adapted for high-performance computing (HPC).

Solutions of the conservation laws governing fluid dynamics are often characterized by heterogeneous flow features with different length scales. As such, in some regions the solution is smooth, whereas in other regions non-regular structures such as strong gradients, shear layers, or shocks occur. For a fixed target accuracy, the smallest scale of these events determines the resolution of the spatial discretization. An uniform resolution approach, such as refining uniformly the grid, extends this resolution throughout the computational domain. Conversely, adaptive resolution approaches, such as *remeshing* (Mavriplis, 1990) or *h/p adaptation* (Wackers et al., 2012; Rueda-Ramírez et al., 2019a), allow for the optimization of the spatial discretization by selectively adjusting its resolution to the localization of the event. In this way, resources are distributed more efficiently and the computational cost is significantly reduced without compromising the overall accuracy.

In particular, DGMs are especially well-suited to efficiently adapt the spatial resolution of the numerical solution by either modifying the local mesh size ($h$-adaptation), the local polynomial degree ($p$-adaptation), or both simultaneously ($hp$-adaptation). By this line of thought, smooth regions are better tailored to $p$-adaptation, which helps to improve the accuracy of the numerical solution; whereas regions featuring non-regular behavior (e.g. shocks and boundary layers) are better captured using $h$-adaptation, so that the production of numerical fluctuations and errors is minimized. Overall, the process should maintain to a feasible extent the same accuracy than the uniformly refined grid (for the same minimum effective mesh size), yet for a lower number of degrees of freedom (DOFs).

To guide any of the aforementioned adaptation approaches we must firstly come up with some mechanism to estimate the error distribution in the numerical solution. There are multiple *a posteriori* methodologies accessible to secure these estimates (Ainsworth and Oden, 1997). Examples range from feature-based estimators, which originate from the study of certain physical features of the flow (Kasmai et al., 2011), to goal-oriented estimators, which measures the error of a specific target quantity by solving an adjoint problem (Kast, 2017), to local error-based estimators, which assess the local error of the numerical solution. In the context of DGMs, the latter technique is of particular significance. In this category, we can highlight two methods based on the estimation of the discretization error. Either by extrapolating

selected Legendre expansion coefficients (Mavriplis, 1994), or by evaluating the higher-order modes of the numerical solution (Naddei et al., 2018).

Another methodology of special interest is the so-called *multiresolution-based grid adaptation* (Gottschlich-Müller and Müller, 1999). This approach is designed with unsteady problems in mind and does not depend on *a posteriori* estimation, but relies on the concept of *multiresolution analysis* (MRA) (Müller, 2003). This theory refers to the possibility of representing the numerical solution as a hierarchy of increasingly fine details built on *wavelets* (Mallat, 2008) plus a coarse-scale component which offers an overall picture of the solution. The decay of these details provides information on the local regularity of the solution which, in turn, allows for the local truncation error to be measured (Schneider and Vasilyev, 2010). By applying an appropriate thresholding to the wavelet details one can perform error control and guide grid adaptation. The fundamental idea of the MRA-based grid adaptation is to perform a multiresolution analysis of the reference solution and evolve only meaningful local information in time.

The idea behind multiresolution analysis emerges from the work of Harten (1996) who, in the context of finite-volume methods, designed a cost-effective flux evaluation based on MRA. Despite reducing the number of flux evaluations, Harten's original concept did not consider grid adaptation and was only applied to uniform grids.

A fully adaptive FVM-MRA approach based on MRA was later developed by Müller (2003, 2009) by explicitly using biorthogonal wavelets to represent the numerical solution. In his work, Müller applies data compression based on the values of the wavelet coefficients, which in turn defines a locally refined grid. Roussel et al. (2003), Domingues et al. (2009) and Deiterding et al. (2009, 2016) independently developed another fully adaptive FVM-MRA method which relies on the recursive use of projection and prediction operators to define the coarse and fine levels of the cell-averaged values of the solution.

A later extension to the DGM framework by Hovhannisyan et al. (2014), Gerhard et al. (2015a,b), and Gerhard and Müller (2016) involve the use of *multiwavelets* (MWs), which are commonly described as the vector variant of wavelets (Strela, 1996). Multiwavelets can be easily combined with the DGM thanks to their flexibility in matching the high-order of the approximation while keeping compact support (Gerhard, 2017). A similar DGM-MRA which includes the numerical solution along with the derivative operators from the partial differential equation in a MRA representation was also developed independently by Shelton (2008) and Archibald et al. (2011). On a different line of research, the works of Vuik and Ryan (2014, 2016) and Vuik (2017) combine the DGM and MWs for the detection of shocks in 2-D configurations.

The concept of MRA-based grid adaptation, while soundly based on wavelet theory and accurate (Hovhannisyan et al., 2014), also faces some limitations. In principle, a solution on a uniform sufficiently fine *reference* grid should

be initially foreknown. This is required so that the multi-scale structure is defined at the initial time and the relevant information correctly captured for subsequent time steps.

In the context of unsteady problems, Gerhard (2017) avoids the application of the fine reference grid to initialize the grid by using a MRA version of the reference grid (approximation) as initialization instead. In order to reduce the computational complexity of the reference grid, they apply an algorithm on the initial solution $\boldsymbol{u}_0$ that proceeds level-wise from coarse to fine scale. However, this strategy may overlook significant information on higher scales and thus it must be applied prudently.

In the framework of steady problems, Bramkamp et al. (2004) and Müller and Stiriba (2009) have demonstrated that the MRA strategy can be efficiently applied when combined with a multilevel strategy. In this manner, the authors effectively circumvent the use of the costly reference grid. In particular, they employ the *Full Approximation Storage* algorithm (FAS, see Brandt (1977)), which is suitable for an adaptive multigrid approach, together with MRA using biorthogonal wavelets in the context of FVMs. However, this approach requires two different grids associated with the multigrid scheme: at level $L$ (fine grid) and at level $L - 1$ (coarse grid).

A second constraint resides in the fact that only grids which support uniform dyadic subdivisions of the elements are allowed, which mean that the elements are split into sub-elements of equal size and shape. This methodology can also be applied on triangles as presented by Yu et al. (1999). An alternative approach is the *wavelet-free* method developed by Gerhard (2017), which extends the MRA to non-uniform grid hierarchies. Finally, another limitation of the MRA-based grid adaptation is that, due to the pyramidal structure of the MRA technique, parallelization might prove challenging.

## 1.2 SCOPE OF THE THESIS

The main goal of this work is to develop computationally efficient *hp*-adaptive DG schemes of the Navier-Stokes equations by drawing together the *flexibility* of *a posteriori* driven adaptation and the *accuracy* of multiresolution-based adaptation. The validation of the methodology is performed for several steady flows in one and two dimensions.

In a first research direction, we focus exclusively on *h*-adaptation. The idea is to examine the constraints of traditional multiresolution-based adaptation and come up with an alternative multiwavelet-based methodology compatible with *a posteriori* local error estimation. In a second line of investigation, we look further from the *h*-adaptivity of the original MRA-based approach and investigate novel ways of providing the new multiwavelet-based methodology with *hp*-capabilities.

In order to address the shortcomings of MRA-based grid adaptation, the new multiwavelet expansion of the numerical solution is performed locally

within each element. By being local to the element, adaptation can be applied by starting from a coarse mesh. In this manner, we avoid the need to operate a costly reference grid. Besides, more general grids may also be used (not limited by the strict translation and dilation properties of multiwavelets) and the compacity and thus parallel efficiency of the original DG method is conserved.

This new methodology requires that the original DG element-wise solution undergoes a post-processing treatment, so that the new local multiwavelet expansion may extract significant information. This is done by employing a reconstruction process involving the current element and its immediate neighbors. The multiwavelet decomposition is then locally performed on the new reconstructed DG solution. The resulting details then constitute the backbone of the multiwavelet-based error estimation.

We give prominence to configurations that exhibit physical and/or geometrical singularities, which would significantly benefit from *h*-adaptation. For the *h*-adaptive simulations, we compare our multiwavelet-based estimation against pertinent error estimators from the literature and measure their overall performance.

The extension to *hp*-adaptation is based on an evaluation of the local smoothness of the solution. Following on the footsteps of the previous multiwavelet-based error estimator, we give evidence of a consistent association between local solution regularity and the decay of the multiwavelet spectrum. This measurement constitutes an estimation of the error and, together with an appropriate *hp*-decision strategy, determines whether to perform mesh size or polynomial degree adaptation.

To validate the proposed *hp*-strategy, we perform a series of *hp*-adaptive simulations on flow configurations characterized by both, regions of smooth and non-regular solution behavior. We then focus our attention on studying the optimal *hp*-distribution and on its overall performance with respect to single *h*- or *p*-adaptation.

## 1.3 FRAMEWORK OF THE THESIS

The present work is performed in the context of the development of the CFD solver *Aghora* at ONERA. The *Aghora* solver is built on a high-order discontinuous Galerkin discretization based on either modal or nodal formulations for the simulation of compressible flows on unstructured non-conforming grids. The solver is written in `Fortran90` and benefits from distributed memory and CPU-based parallelization using MPI. Different publications have corroborated the capabilities of the solver. These studies range from turbulence modeling in DNS (Chapelier et al., 2012, 2014), RANS (Renac et al., 2015), and LES (De la Llave Plata et al., 2018; Lorteau et al., 2018); to simulations of two-phase flows (Rai et al., 2021). More recently added *h/p*-capabilities allow the solver to benefit from local degree adaptation (Naddei et al., 2018, 2019) and local mesh refinement (Naddei, 2019). This PhD

thesis builds on the solver's *h*-adaptive capability and paves the way to full *hp*-adaptation.

This PhD thesis is part of the Marie Skłodowska-Curie Innovative Training Network (ITN) *Stability and Sensitivity Methods for Industrial Design* (SSeMID) funded by the European Union's Horizon 2020 research and innovation programme.

## 1.4 OUTLINE OF THE THESIS

Besides the current chapter serving as the introduction to the thesis, the remaining chapters are organized into three major parts as follows:

Part I presents an overview of the physical models spanning this work and the discretization methodology to numerically approximate their solution. Additionally, multiresolution analysis based on multiwavelets is introduced as a mathematical tool to better understand the features of the numerical solution.

Chapter 2 briefly describes the two-dimensional Navier-Stokes equations and the one-dimensional Burgers equation used for the validation of the methodology. We spend most of the chapter covering the discontinuous Galerkin method and the details of the spatial and temporal discretizations used throughout this work.
Chapter 3 starts by providing a brief historical context to multiresolution analysis. We then discuss the basics of wavelet theory and conclude the chapter by focusing our attention on multiwavelets and their associated multiresolution analysis.

Part II details the roadmap to our *hp*-adaptive scheme. We start by tailoring the DG solution to fit a multiwavelet expansion. We then measure the solution error and regularity of the solution, based on such expansion, and clearly lay out the ingredients required by the *hp*-adaptation algorithm.

Chapter 4 begins by finding common ground between the multiwavelet expansion and the DG formulation. We aim to improve previous approaches in the literature by proposing a new local expansion applied to a reconstructed enriched version of the original DG solution.
Chapter 5 provides a comprehensive literature review of error estimator techniques, adaptation approaches, and *hp*-adaptive strategies. After that, we describe our novel multiwavelet-based error estimator and regularity indicator, the latter of which originates from a thorough interpretation of the multiwavelet spectrum. These two ingredients plus additional marking and *hp*-decision criteria constitute the structure of the *hp*-algorithm.

Part III presents the numerical results from *h*- and *hp*-adaptive simulations of three different steady configurations. The considered configurations allow for the analysis of the performance of our adaptive algorithm under various parameters of interest.

Chapter 6 provides a comparison of our multiwavelet-based estimator against selected estimators from the literature in the context of *h*-adaptive simulations. We evaluate their overall performance by analyzing relevant quantities of interest. We focus our attention on the 1-D viscous Burgers equation in the presence of a shock, and the 2-D laminar flow over a backward-facing step.

Chapter 7 offers an evaluation of the performance of our multiwavelet-based *hp*-strategy in driving *hp*-adaptation. To assess the performance of our strategy we compare the optimal *hp*-distribution to equivalent purely *h*- and *p*-adaptive simulations. The 2-D laminar backward-facing step and square cylinder configurations are considered in these studies.

Finally, Chapter 8 wraps up the thesis with the main conclusions and perspectives for future work.

# Part I

# BACKGROUND

# Chapter 2

# PHYSICAL MODEL AND NUMERICAL METHODS

In this chapter we establish the physical models adopted throughout the present work and the theoretical bedrock to numerically calculate their solution.

Section 2.1 presents the general expression that underpins these physical models. The subsequent Section 2.1.1 introduces the two-dimensional compressible Navier-Stokes equations as the principal physical model of this work. Section 2.1.2 discusses the one-dimensional viscous Burgers equation as a simplification of the Navier-Stokes equations and its role as an early litmus test.

Section 2.2 introduces the discontinuous Galerkin method applied to the aforementioned physical models. After a short account of the historical evolution of the method, we describe how the domain is accommodated to the discretization in Section 2.2.1. The accompanying DG solution and its features are covered in Sections 2.2.2 and 2.2.3. The formulation of the DG method is explained in Section 2.2.4. We describe first the spatial discretization of the convective and viscous terms in Sections 2.2.5 and 2.2.6; and follow with the temporal discretization in Section 2.2.7. Finally, Section 2.2.8 closes the chapter by addressing the numerical computation of volume and surface integrals.

## 2.1 PHYSICAL MODEL

In this work we make use of the two-dimensional compressible Navier-Stokes equations and the one-dimensional viscous Burgers equation. Let $\Omega \subset \mathbb{R}^d$ be a bounded domain, where $d$ is the spatial dimension. Given appropriate boundary conditions on $\partial\Omega$ and in the absence of source terms, these equations can be written under the general expression

$$\frac{\partial \boldsymbol{u}}{\partial t} + \nabla \cdot \left[ \boldsymbol{\mathcal{F}}_c(\boldsymbol{u}) - \boldsymbol{\mathcal{F}}_v(\boldsymbol{u}, \nabla \boldsymbol{u}) \right] = 0\,, \quad \forall \boldsymbol{x} \in \Omega\,, t > 0\,, \tag{2.1}$$

$$\boldsymbol{u}(\boldsymbol{x}, t) = \boldsymbol{u}_0(\boldsymbol{x}), \quad \forall \boldsymbol{x} \in \Omega\,, \text{ at } t = 0\,, \tag{2.2}$$

where $\boldsymbol{u}$ is the state vector of conservative variables. The vectors $\boldsymbol{\mathcal{F}}_c$, and $\boldsymbol{\mathcal{F}}_v$ are the convective and viscous fluxes, respectively.

### 2.1.1 *Navier-Stokes equations*

We define the domain $\Omega \subset \mathbb{R}^2$. The state vector and the fluxes of Eqs. (2.1, 2.2) are given, respectively, by

$$\boldsymbol{u} = \begin{bmatrix} \rho \\ \rho\boldsymbol{v} \\ \rho E \end{bmatrix}, \quad \boldsymbol{\mathscr{F}}_c = \begin{bmatrix} \rho\boldsymbol{v}^T \\ \rho\boldsymbol{v} \otimes \boldsymbol{v} + p\boldsymbol{I} \\ (\rho E + p)\boldsymbol{v}^T \end{bmatrix}, \quad \text{and} \quad \boldsymbol{\mathscr{F}}_v = \begin{bmatrix} 0 \\ \boldsymbol{\tau} \\ \boldsymbol{\tau} \cdot \boldsymbol{v} - \boldsymbol{q}^T \end{bmatrix}; \tag{2.3}$$

with $\rho$ representing the density. The velocity vector, $\boldsymbol{v}$, and the specific total energy, $E$, are defined, respectively, by

$$\boldsymbol{v} = \begin{bmatrix} u \\ v \end{bmatrix}, \quad \text{and} \quad E = \frac{p}{(\gamma - 1)\rho} + \frac{1}{2}(\boldsymbol{v} \cdot \boldsymbol{v}); \tag{2.4}$$

where $\gamma = \frac{C_p}{C_v} > 1$ is the ratio of specific-heat coefficients, and $p$ is the static pressure, as defined by the perfect-gas law

$$p = \rho R T, \tag{2.5}$$

with $R$ the specific gas constant and $T$ the temperature. The static pressure represents the normal component of the stress tensor, whereas the shear-stress component is described by

$$\boldsymbol{\tau} = 2\mu \left( \boldsymbol{D} - \tfrac{1}{3} \operatorname{tr}(\boldsymbol{D}) \boldsymbol{I} \right); \tag{2.6}$$

$$\boldsymbol{D} = \tfrac{1}{2}\left(\nabla \boldsymbol{v} + (\nabla \boldsymbol{v})^T\right), \quad \operatorname{tr}(\boldsymbol{D}) = \nabla \cdot \boldsymbol{v}; \tag{2.7}$$

where $\boldsymbol{D}$ and $\operatorname{tr}(\boldsymbol{D})$ are the instantaneous strain-rate tensor and its trace, respectively. The dynamic viscosity, $\mu$, is defined by Sutherland's law (Schlichting et al., 2017). Finally, the heat-flux vector, $\boldsymbol{q}$, follows Fourier's law:

$$\boldsymbol{q} = -k \nabla T, \tag{2.8}$$

with $k$ being the thermal conductivity given by

$$k = \frac{\mu}{Pr} C_p, \quad C_p = \frac{\gamma}{\gamma - 1} R, \tag{2.9}$$

where $Pr$ denotes the Prandtl number, that is assumed to have a constant value of 0.72.

We measure the contribution of the different terms in Eqs. (2.1–2.3) by establishing two dimensionless parameters based on characteristic quantities of the phenomenon considered. The Reynolds number, $Re$, represents the ratio of convective to viscous effects:

$$Re = \frac{\rho_{\text{ref}}\, v_{\text{ref}}\, L_{\text{ref}}}{\mu_{\text{ref}}}, \tag{2.10}$$

and the Mach number, $Ma$, denotes the ratio of the characteristic flow veloc-

ity to the sound speed:

$$Ma = \frac{v_{\text{ref}}}{\sqrt{\gamma R T_{\text{ref}}}} \tag{2.11}$$

### 2.1.2 *Burgers equation*

The Burgers equation can be understood as a simplified version of the Navier-Stokes equations (Burgers, 1995), for which exact solutions are known. In later chapters, we justify the use of this equation as an early benchmark problem for our adaptation approach.

To obtain the Burgers equation we assume that the flow is incompressible. Therefore, we can integrate the continuity equation to the momentum equation and drop the state and energy equations. Additionally, we also neglect the effect of the pressure. With these considerations, the state vector and fluxes of Eq. (2.3) can be simplified to

$$\boldsymbol{u} = \boldsymbol{v}, \quad \boldsymbol{\mathcal{F}}_c = \boldsymbol{v} \otimes \boldsymbol{v}, \quad \text{and} \quad \boldsymbol{\mathcal{F}}_v = 2\nu \boldsymbol{D}; \tag{2.12}$$

where $\nu = \mu/\rho$ represents the kinematic viscosity. Unlike the Navier-Stokes equations, the Burgers equation can be studied in one-spatial dimension. In this particular case $\Omega \subset \mathbb{R}$ and Eq. (2.12) simply becomes

$$\boldsymbol{u} = u, \quad \boldsymbol{\mathcal{F}}_c = \tfrac{1}{2}u^2, \quad \text{and} \quad \boldsymbol{\mathcal{F}}_v = \nu \frac{\partial u}{\partial x}, \tag{2.13}$$

in which $\nu$ is considered to be constant.

## 2.2 THE DISCONTINUOUS GALERKIN METHOD

The origins of the discontinuous Galerkin method (DGM) can be traced back to the pioneering work of Reed and Hill (1973) on approximating the hyperbolic neutron transport equation. The discretization was later brought to hyperbolic problems in fluid dynamics by Cockburn and Shu (2001). Soon after, generalizations to parabolic and elliptic problems were also developed (Cockburn and Shu, 1998; Baumann and Oden, 1999; Arnold et al., 2002). These led to the first DGM discretization of the compressible Navier-Stokes equations by Bassi and Rebay (1997). Since its conception, the DGM has experienced a constant growth in many areas of computational physics and engineering, such as aerodynamics (Van der Vegt and van der Ven, 2002) and in particular turbulent flows (Chapelier et al., 2012; Wurst et al., 2015).

### 2.2.1 *Domain discretization*

The underlying notion of the DGM is to transfer the continuous problem in Eqs. (2.1–2.2) into a discrete counterpart from which an approximate solution can be reached. We start by partitioning the domain $\Omega$ into a shape-regular

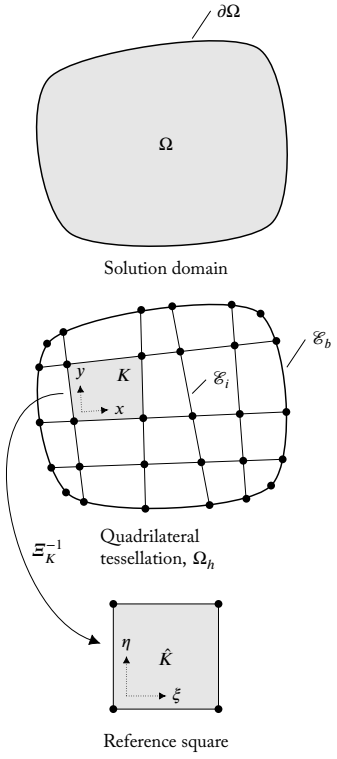


*Figure 2.1:* The solution domain $\Omega$ is decomposed into a series of non-overlapping quadrilaterals, $K$, which are then mapped to the reference square $\hat{K}$ to perform the relevant operations.

grid, $\Omega_h$, formed by $N_K$ non-overlapping and non-empty elements $K$ of characteristic size $h_K$. Interior and boundary faces in $\Omega_h$ are defined by $\mathscr{E}_i$ and $\mathscr{E}_b$, respectively, such that $\mathscr{E}_h = \mathscr{E}_i \cup \mathscr{E}_b$. This process is illustrated in Figure 2.1. In our study, we are concerned with quadrilaterals, therefore we will be using the designations *element/quadrilateral* interchangeably.

Additionally, we introduce the reference (square) element $\hat{K} = \{-1, 1\}^d$, where $d$ refers to the dimension of the present problem. We define for every $K \in \Omega_h$ the bijective transformation $\boldsymbol{\Xi}_K$, such that $K = \boldsymbol{\Xi}_K(\hat{K})$, which relates the coordinates of the reference element, $\boldsymbol{\xi} = (\xi, \eta) \in \hat{K}$, to their counterparts in the physical element, $\boldsymbol{x} = (x, y) \in K$. This is equivalent to the notation $\boldsymbol{x} = \boldsymbol{\Xi}_K(\boldsymbol{\xi})$, also called *parametric mapping* (Karniadakis and Sherwin, 2005). Finally, the Jacobian associated with the transformation is represented by $\boldsymbol{\mathcal{J}}_K = \nabla \boldsymbol{\Xi}_K$, with determinant $\mathcal{J}_K = \det(\boldsymbol{\mathcal{J}}_K)$.

### 2.2.2 *Solution approximation*

We now proceed to approximate the solution of Eqs. (2.1–2.2) on the new discretized domain $\Omega_h$. Therefore, we approximate $\boldsymbol{u}$ by a polynomial expansion $\boldsymbol{u}_h$ such that $\boldsymbol{u}_h \in \mathscr{V}_h^p$, where $\mathscr{V}_h^p$ is the approximation space defined as

$$\mathscr{V}_h^p = \left\{ \Phi_h \in L^2(\Omega_h) \,:\, \Phi_{h|K} = \phi\left(\boldsymbol{\Xi}_K^{-1}(\boldsymbol{x})\right), \forall K \in \Omega_h \right\}, \tag{2.14}$$

where $\phi \in \mathscr{P}^p(\hat{K})$ is a function of the subspace of continuous polynomials with degree at most $p$ defined on the reference element $\hat{K}$, and $\Phi_{h|K} = \phi\left(\boldsymbol{\Xi}_K^{-1}(\boldsymbol{x})\right)$ is its representation on a physical element $K$. If we let $\phi = \left\{\phi^\ell\right\}_{\ell=1}^{N_p}$, with $N_p = (p+1)^d$, be a set of linearly independent basis functions of $\mathscr{P}^p(\hat{K})$, we have

$$\mathscr{P}^p(\hat{K}) = \operatorname*{span}_{\ell=1,\dots,N_p} \left\{ \phi^\ell(\boldsymbol{\xi}), \boldsymbol{\xi} \in \hat{K} \right\}. \tag{2.15}$$

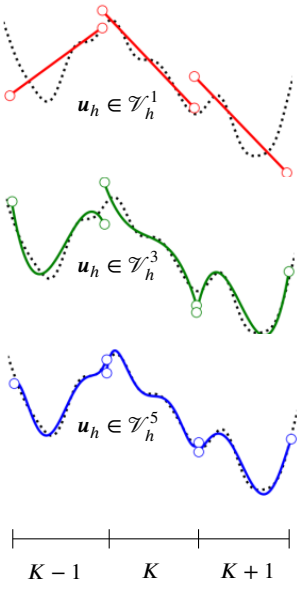


*Figure 2.2:* DGM piecewise solution on a 1-D discretized domain for different degrees of the approximation space $\mathscr{V}_h^p$.

Similarly, by means of the bijective transformation we get

$$\mathscr{V}_h^p = \operatorname*{span}_{\ell=1,\dots,N_p} \left\{ \phi^\ell\left(\boldsymbol{\Xi}_K^{-1}(\boldsymbol{x})\right), \boldsymbol{x} \in K, \forall K \in \Omega_h \right\}, \tag{2.16}$$

and the polynomial expansion $\boldsymbol{u}_h$ can be then expressed as

$$\boldsymbol{u}_h(\boldsymbol{x}, t) = \sum_K \sum_{\ell=1}^{N_p} \boldsymbol{U}_K^\ell(t)\, \phi^\ell\left(\boldsymbol{\Xi}_K^{-1}(\boldsymbol{x})\right), \quad \boldsymbol{x} \in K, \forall K \in \Omega_h, \forall t > 0\,, \tag{2.17}$$

where the coefficients $(\boldsymbol{U}_K^\ell)_{1 \le \ell \le N_p}$ are the degrees of freedom (DOFs) representing the approximate solution on element $K$. Examples of approximate solutions of varying degree are illustrated in Figure 2.2.

The idea of prescribing the coefficients or *modes* of the local expansion in Eq. (2.17) as the unknowns to solve is called modal representation. In contrast, a nodal representation would portray the local expansion through an interpolating polynomial, with given quadrature points (e.g., Gauss or Gauss-

Lobatto points) as the unknowns to evaluate. The two representations are mathematically equivalent but computationally different (Hesthaven and Warburton, 2008). In this work, the use of a modal representation is justified by the use of the multiresolution analysis (MRA), as will become apparent in Chapter 3.

### 2.2.3 *Expansion basis*

We now describe the expansion basis employed in Eqs. (2.15–2.16). Similarly to the question of modal versus nodal, the choice of the expansion basis determines the numerical efficiency and accuracy of the DGM (Boyd, 2001). Following the path of other studies that combine a form of DGM and MRA (e.g., Vuik and Ryan (2014, 2016)), we select the Legendre polynomials as our expansion basis. They represent the optimal selection when paired with Alpert's multiwavelets (Alpert et al., 2002).

The definition of a tensor-product basis within the reference element $\hat{K}$ allows us to build the basis functions as follows:

$$\phi^{\ell}(\boldsymbol{\xi}) = h^i(\xi)h^j(\eta), \quad \ell = 1, ..., N_p, \tag{2.18}$$

where $\left\{h^i\right\}_{i=1}^{p+1}$ is a basis for $\mathscr{P}^p([-1,1])$. In particular, we choose the scaled Legendre polynomials

$$h^i(\xi) = \sqrt{i - \tfrac{1}{2}}P^i(\xi), \tag{2.19}$$

so that we insure orthonormality in the $L^2$-norm $\left\|h^i(\xi)\right\|_{L^2} = 1$. Moreover, the basis is hierarchical, meaning that $h^i \subset h^{i+1}$. Both properties of orthonormality and being hierarchical are inherited by the basis $\phi^{\ell}(\boldsymbol{\xi})$.

### 2.2.4 *Discontinuous Galerkin formulation*

The discrete variational form of Eq. (2.1) is obtained by multiplying the system of equations by a test function $\Phi_h \in \mathscr{V}_h^p$ and integrating over the tessellation $\Omega_h$. It yields

$$\frac{\partial}{\partial t}\int_{\Omega_h} \boldsymbol{u}_h\Phi_h \,\mathrm{d}V + \int_{\Omega_h} \nabla \cdot \left[\boldsymbol{\mathscr{F}}\left(\boldsymbol{u}_h, \nabla\boldsymbol{u}_h\right)\right]\Phi_h \,\mathrm{d}V = 0, \tag{2.20}$$

where

$$\boldsymbol{\mathscr{F}}\left(\boldsymbol{u}_h, \nabla\boldsymbol{u}_h\right) = \boldsymbol{\mathscr{F}}_c\left(\boldsymbol{u}_h\right) - \boldsymbol{\mathscr{F}}_v\left(\boldsymbol{u}_h, \nabla\boldsymbol{u}_h\right) \tag{2.21}$$

collects the convective and viscous fluxes in one term. If we apply the divergence theorem to the second term in Eq. (2.20), we get

$$\begin{aligned}\frac{\partial}{\partial t}\int_{\Omega_h} \boldsymbol{u}_h\Phi_h \,\mathrm{d}V - \int_{\Omega_h} \boldsymbol{\mathscr{F}}\left(\boldsymbol{u}_h, \nabla\boldsymbol{u}_h\right) \cdot \nabla\Phi_h \,\mathrm{d}V \\ + \int_{\mathscr{E}_h} \left[\boldsymbol{\mathscr{F}}\left(\boldsymbol{u}_h, \nabla\boldsymbol{u}_h\right) \cdot \boldsymbol{n}\right] \Phi_h \,\mathrm{d}S = 0,\end{aligned} \tag{2.22}$$

where $\boldsymbol{n}$ is the normal unit vector on the boundary $\mathscr{E}_h$. To allow information to propagate between elements, the last term of Eq. (2.22) must be evaluated at the interfaces between adjacent elements. However, the flux $\boldsymbol{\mathscr{F}}$ is not uniquely defined at the interfaces due to $\boldsymbol{u}_h$ and $\Phi_h$ being discontinuous. Therefore, we replace $\boldsymbol{\mathscr{F}}$ by a numerical flux $\boldsymbol{\mathscr{F}}^*$, which is a function of both interface states. Additionally, by restricting our analysis to the physical element $K \in \Omega_h$, the vectors $\boldsymbol{u}_h$ and $\Phi_h$ become $\boldsymbol{u}_{h|K}$ and $\phi = \Phi_{h|K}$, respectively; and we can express Eq. (2.22) in the following elemental form

$$\begin{aligned}\frac{\partial}{\partial t}\int_K \boldsymbol{u}_{h|K}\phi \,\mathrm{d}V - \int_K \boldsymbol{\mathscr{F}}\left(\boldsymbol{u}_{h|K}, \nabla \boldsymbol{u}_{h|K}\right)\cdot\nabla\phi \,\mathrm{d}V \\ + \int_{\partial_i K} \boldsymbol{\mathscr{F}}^*\left(\boldsymbol{u}^{\pm}_{h|\partial_i K}, \nabla \boldsymbol{u}^{\pm}_{h|\partial_i K}; \boldsymbol{n}\right)[\![\phi]\!]\,\mathrm{d}S \\ + \int_{\partial_b K}\left[\boldsymbol{\mathscr{F}}\left(\boldsymbol{u}_b, \nabla \boldsymbol{u}_b\right)\cdot\boldsymbol{n}\right]\phi^+ \mathrm{d}S = 0,\end{aligned} \tag{2.23}$$

where the elemental boundary $\partial K$ has been broken down into internal faces, $\partial_i K = \partial K \cap \mathscr{E}_i$, and boundary faces, $\partial_b K = \partial K \cap \mathscr{E}_b$. The boundary values $\boldsymbol{u}_b = \boldsymbol{u}_b\left(\boldsymbol{u}^+_{h|\partial_b K}, \boldsymbol{u}_{\text{ext}}; \boldsymbol{n}\right)$, with $\boldsymbol{u}_{\text{ext}}$ a reference external state, are computed so that the boundary conditions are satisfied on $\mathscr{E}_b$. The presence of interface integrals requires the definition of interface states. For a given internal face $e \in \partial_i K$, the interior state is denoted by $\boldsymbol{u}^+_{h|e}$ and the neighboring state by $\boldsymbol{u}^-_{h|e}$. This nomenclature originates from applying the limit of the elemental approximation $\boldsymbol{u}_{h|K^\pm}$ as it approaches the interface $e$, i.e:

$$\boldsymbol{u}^{\pm}_{h|e}(\boldsymbol{x}_e) = \lim_{\boldsymbol{x}\to\boldsymbol{x}_e, \boldsymbol{x}\in K^\pm} \boldsymbol{u}_{h|K^\pm}(\boldsymbol{x}), \quad \forall \boldsymbol{x}_e \in e, \tag{2.24}$$

where $K^+$ denotes the current element and $K^-$ the neighboring element, and $\boldsymbol{n}$ represents the outward unit vector normal to $K^+$. This is illustrated in Figure 2.3. In addition, we define the average $\{\!\{\cdot\}\!\}$ and jump $[\![\cdot]\!]$ operators as follows:

$$\begin{aligned}\{\!\{\phi\}\!\} &= \tfrac{1}{2}\left(\phi^+ + \phi^-\right), & [\![\phi]\!] &= \phi^+ - \phi^-, \\ \{\!\{\boldsymbol{u}_{h|K^\pm}\}\!\} &= \tfrac{1}{2}\left(\boldsymbol{u}^+_{h|e} + \boldsymbol{u}^-_{h|e}\right), & [\![\boldsymbol{u}_{h|K^\pm}]\!] &= \left(\boldsymbol{u}^+_{h|e} - \boldsymbol{u}^-_{h|e}\right)\otimes\boldsymbol{n}.\end{aligned} \tag{2.25}$$

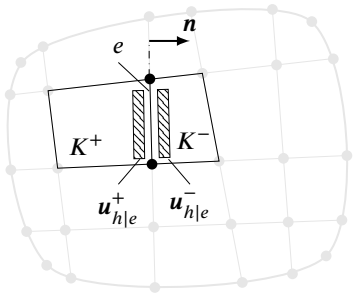


*Figure 2.3:* Definition of interface states $\boldsymbol{u}^{\pm}_{h|e}$ approaching from current $K^+$ and neighboring $K^-$.

Finally, if we replace Eq. (2.21) into Eq. (2.23) and adopt appropriate numerical fluxes, we reach the compact elemental expression

$$\frac{\partial}{\partial t}\int_K \boldsymbol{u}_{h|K}\phi \,\mathrm{d}V + \mathscr{L}_c\left(\boldsymbol{u}_{h|K}, \phi\right) + \mathscr{L}_v\left(\boldsymbol{u}_{h|K}, \phi\right) = 0\,. \tag{2.26}$$

where $\mathscr{L}_c$ and $\mathscr{L}_v$ represent the discrete variational projection of the convective and the viscous terms onto $\mathscr{V}^p_h$. They will be described in the following sections for the Navier-Stokes equations and the Burgers equation.

### 2.2.5 *Discretization of convective terms*

*Navier-Stokes equations* The discrete variational form of the convective terms in Eq. (2.26) reads

$$\begin{aligned}\mathscr{L}_c(\boldsymbol{u}_{h|K}, \phi) = &- \int_K \boldsymbol{\mathcal{F}}_c(\boldsymbol{u}_{h|K}) \cdot \nabla\phi \, \mathrm{d}V \\ &+ \int_{\partial_i K} \boldsymbol{\mathcal{F}}_c^*(\boldsymbol{u}^{\pm}_{h|\partial_i K}; \boldsymbol{n}) \, [\![\phi]\!] \, \mathrm{d}S \\ &+ \int_{\partial_b K} \left[\boldsymbol{\mathcal{F}}(\boldsymbol{u}_b) \cdot \boldsymbol{n}\right] \phi^+ \mathrm{d}S \,, \end{aligned} \tag{2.27}$$

The convective numerical flux $\boldsymbol{\mathcal{F}}_c^*$ must satisfy the conditions of consistency and conservativity (Cockburn, 1998). There are several numerical flux functions satisfying the above criteria such as the Lax–Friedrichs, Roe, or Godunov (Bassi and Rebay, 1997); which are also used in finite-volume methods (Toro, 2009). In this work we use the local Lax-Friedrichs flux (LLF) (Cockburn, 1998):

$$\boldsymbol{\mathcal{F}}_c^*(\boldsymbol{u}^{\pm}_{h|\partial_i K}; \boldsymbol{n}) = \left\{\!\!\left\{ \boldsymbol{\mathcal{F}}_c(\boldsymbol{u}_{h|K^{\pm}}) \right\}\!\!\right\} \cdot \boldsymbol{n} + \tfrac{1}{2}\alpha^{\mathrm{LLF}} [\![\boldsymbol{u}_{h|K^{\pm}}]\!] \,, \tag{2.28}$$

with

$$\alpha^{\mathrm{LLF}} = \max\left\{ \rho_s\left(\boldsymbol{\mathcal{J}}(\boldsymbol{u})\right) \,:\, \boldsymbol{u} = \boldsymbol{u}^{\pm}_{h|\partial_i K} \right\}, \tag{2.29}$$

where $\boldsymbol{\mathcal{J}}(\boldsymbol{u}) = \nabla_{\boldsymbol{u}} \left(\boldsymbol{\mathcal{F}}_c(\boldsymbol{u}) \cdot \boldsymbol{n}\right)$ denotes the Jacobian matrix of the convective fluxes in the direction of $\boldsymbol{n}$, and $\rho_s$ is its spectral radius.

*Burgers equation* The discrete variational projection of the convective terms in Eq. (2.26) yields

$$\begin{aligned}\mathscr{L}_c(u_{h|K}, \phi) = &- \int_K \mathcal{F}_c(u_{h|K}) \frac{\mathrm{d}\phi}{\mathrm{d}x} \, \mathrm{d}x \\ &+ \sum_{e \in \partial_i K} \mathcal{F}_c^*(u^{\pm}_{h|e}) [\![\phi]\!] + \mathcal{F}_c(u_b) \, \phi^+ \,, \end{aligned} \tag{2.30}$$

with $\mathcal{F}_c(u) = \frac{1}{2}u^2$. The structure follows the arrangement presented by Alhawwary and Wang (2018). The approximation of the numerical convective flux $\mathcal{F}_c^*$ on the internal faces is fully defined by the local Lax-Friedrichs flux, similarly to Eqs. (2.28–2.29).

### 2.2.6 *Discretization of viscous terms*

*Navier-Stokes equations* For the discrete variational form of the viscous terms, we employ the *Bassi-Rebay-2* scheme (BR2) presented by Bassi and Rebay (2000), in which the authors consider the gradient of the state vector $\nabla\boldsymbol{u} = \boldsymbol{\sigma}$ as an auxiliary variable. This new variable is then accommodated in a discrete variational formulation, which in turn introduces several new terms. These

new terms are bundled up under the so called global lifting operator $\boldsymbol{L}_h$ such that

$$\boldsymbol{\sigma}_h = \nabla \boldsymbol{u}_h + \boldsymbol{L}_h. \tag{2.31}$$

At this point, the resulting scheme is known as the *Bassi-Rebay-1* scheme (BR1) (Bassi and Rebay, 1997). This scheme is not compact as the computation of $\boldsymbol{L}_{h|K}$ at the interior faces of the current element $K$ extends the stencil farther than just its neighbours (Bassi et al., 2005). Conversely, the BR2 scheme replaces $\boldsymbol{L}_{h|K}$ by the so called local lifting operator $\boldsymbol{l}_h^e$, which satisfies:

$$\int_{K^+ \cup K^-} \phi\, \boldsymbol{l}_h^e \,\mathrm{d}V = -\int_e [\![\phi]\!] [\![\boldsymbol{u}_{h|K^\pm}]\!] \,\mathrm{d}S\,, \qquad e \in \partial_i K\,. \tag{2.32}$$

The use of the local lifting operator makes the BR2 scheme compact, as only the interface integrals at $e \in \partial_i K$ need to be evaluated. An analogous equation consistent with the boundary conditions can be obtained for the boundary faces $\partial_b K$. The global lifting operator $\boldsymbol{L}_{h|K}$ can be then reconstructed as the sum of the local lifting operators, that is

$$\boldsymbol{L}_{h|K} = \sum_{e \in \partial_i K} \boldsymbol{l}_h^e\,. \tag{2.33}$$

The discrete variational form of the viscous terms in Eq. (2.26) therefore reads

$$\begin{aligned} \mathscr{L}_v(\boldsymbol{u}_{h|K}, \phi) = &\int_K \boldsymbol{\mathscr{F}}_v(\boldsymbol{u}_{h|K}, \boldsymbol{\sigma}_{h|K}) \cdot \nabla\phi \,\mathrm{d}V \\ &- \int_{\partial_i K} \boldsymbol{\mathscr{F}}_v^*(\boldsymbol{u}^\pm_{h|\partial_i K}, \boldsymbol{\sigma}^\pm_{h|\partial_i K}; \boldsymbol{n})\, [\![\phi]\!] \,\mathrm{d}S \\ &- \int_{\partial_b K} \left[\boldsymbol{\mathscr{F}}_v\left(\boldsymbol{u}_b, \boldsymbol{\sigma}_b\right) \cdot \boldsymbol{n}\right] \phi^+ \mathrm{d}S\,. \end{aligned} \tag{2.34}$$

From applying Eq. (2.31) we have

$$\boldsymbol{\sigma}_{h|K} = \nabla \boldsymbol{u}_{h|K} + \boldsymbol{L}_{h|K}, \tag{2.35}$$

$$\boldsymbol{\sigma}^\pm_{h|\partial_i K} = \nabla \boldsymbol{u}^\pm_{h|\partial_i K} + \eta_{\mathrm{BR2}} \boldsymbol{l}_h^e; \qquad e \in \partial_i K, \tag{2.36}$$

$$\boldsymbol{\sigma}_b = \nabla \boldsymbol{u}_b + \eta_{\mathrm{BR2}} \boldsymbol{l}_h^f; \qquad f \in \partial_b K, \tag{2.37}$$

The boundary values $\boldsymbol{u}_b, \nabla \boldsymbol{u}_b$ are consistent with the boundary conditions imposed on $\mathscr{E}_b$, and $\eta_{\mathrm{BR2}}$ is a user-defined parameter necessary for the stabilization of the method. Lastly, the numerical flux function $\boldsymbol{\mathscr{F}}_v^*$ in Eq. (2.34) is given by

$$\boldsymbol{\mathscr{F}}_v^*(\boldsymbol{u}^\pm_{h|\partial_i K}, \boldsymbol{\sigma}^\pm_{h|\partial_i K}; \boldsymbol{n}) = \left\{\!\!\left\{ \boldsymbol{\mathscr{F}}_c\left(\boldsymbol{u}_{h|K^\pm}, \boldsymbol{\sigma}_{h|K^\pm}\right) \right\}\!\!\right\} \cdot \boldsymbol{n} \tag{2.38}$$

*Burgers equation* The discrete variational projection of the viscous terms in Eq. (2.26) yields

$$\begin{aligned}\mathscr{L}_v(u_{h|K},\phi) = &\int_K \mathscr{F}_v\Big(\tfrac{\mathrm{d}}{\mathrm{d}x}u_{h|K}\Big)\frac{\mathrm{d}\phi}{\mathrm{d}x}\,\mathrm{d}x \\ &- \sum_{e\in\partial_i K}\Theta_v\Big(u^{\pm}_{h|e},\tfrac{\mathrm{d}}{\mathrm{d}x}u^{\pm}_{h|e}\Big)[\![\phi]\!] - \Theta_v\Big(u_b,\tfrac{\mathrm{d}}{\mathrm{d}x}u_b\Big)\,\phi^+ \\ &- \sum_{e\in\partial_i K} h_v\big(u^{\pm}_{h|e}\big)\left[\!\!\left[\frac{\mathrm{d}\phi}{\mathrm{d}x}\right]\!\!\right] - h_v(u_b)\,\frac{\mathrm{d}\phi^+}{\mathrm{d}x}\,, \end{aligned} \tag{2.39}$$

with $\mathscr{F}_v = \nu\frac{\partial u}{\partial x}$. The numerical viscous fluxes $h_v$ and $\Theta_v$ are approximated by the symmetric interior penalty method (SIP) described by Arnold et al. (2002). They read

$$h_v\big(u^{\pm}_{h|e}\big) = \tfrac{1}{2}[\![u_{h|K^{\pm}}]\!]\,, \tag{2.40}$$

$$\Theta_v\Big(u^{\pm}_{h|e},\tfrac{\mathrm{d}}{\mathrm{d}x}u^{\pm}_{h|e}\Big) = \Big\{\!\!\Big\{\mathscr{F}_v\Big(\tfrac{\mathrm{d}}{\mathrm{d}x}u_{h|K^{\pm}}\Big)\Big\}\!\!\Big\} - \alpha^{\mathrm{SIP}}[\![u_{h|K^{\pm}}]\!]\,. \tag{2.41}$$

The penalty parameter, $\alpha^{\mathrm{SIP}}$, depends on the size of the element and the polynomial degree $p$ (Alhawwary and Wang, 2018).

### 2.2.7 *Time integration*

*Navier-Stokes equations* Once every term has been defined, Eq. (2.26) results in a non-linear system of ordinary differential equations. By using Eq. (2.17), this system of equations can be written as

$$\boldsymbol{M}_K^{\ell r}\frac{\partial \boldsymbol{U}_K^{\ell}}{\partial t} + \boldsymbol{R}\big(\boldsymbol{U}_K^{\ell}\big) = 0, \qquad \ell, r = 1, ..., N_p\,, \tag{2.42}$$

where the degrees of freedom, $\boldsymbol{U}_K^{\ell}(t)$, are the unknowns to be determined; $\boldsymbol{R}$ is the local residual vector, which includes the convective and viscous terms $\mathscr{L}_c$ and $\mathscr{L}_v$; and $\boldsymbol{M}_K$ is the diagonal mass matrix of element $K$, defined as

$$\boldsymbol{M}_K^{\ell r} = \int_K \phi^{\ell}\phi^{r}\,\mathrm{d}V\,. \tag{2.43}$$

By considering the contribution of all elements $K \in \Omega_h$, Eq. (2.42) becomes

$$\boldsymbol{M}\frac{\partial \boldsymbol{U}}{\partial t} + \boldsymbol{R}(\boldsymbol{U}) = 0\,, \tag{2.44}$$

where $\boldsymbol{M}$, $\boldsymbol{U}$ and $\boldsymbol{R}$ denote the block diagonal mass matrix, the global vector of degrees of freedom, and the residual vector, respectively. The system in Eq. (2.44) can be linearized by Newton's method and its solution advanced in time by means of the implicit Euler scheme, which can be written as

$$\frac{\boldsymbol{M}}{\Delta t}\big(\boldsymbol{U}^{n+1} - \boldsymbol{U}^{n}\big) + \boldsymbol{R}(\boldsymbol{U}^{n}) + \frac{\partial \boldsymbol{R}(\boldsymbol{U}^{n})}{\partial \boldsymbol{U}}\big(\boldsymbol{U}^{n+1} - \boldsymbol{U}^{n}\big) = 0 \tag{2.45}$$

As mentioned earlier, we focus on steady problems. Therefore, we start the temporal discretization scheme in Eq. (2.45) from the initial condition $\boldsymbol{u}_h(\boldsymbol{x}, 0)$

and advance the solution in time until the steady-state solution is reached.

Every temporal step in Eq. (2.45) requires the solution of a linear system of equations. If we describe the system as $\boldsymbol{A}\boldsymbol{x} + \boldsymbol{b} = 0$, the term $\boldsymbol{A}$ represents a $N_K \times N_K$ block sparse matrix, with $N_K$ denoting the total number of elements. In turn, each block can be regarded as a $(N_{\text{eq}} N_p) \times (N_{\text{eq}} N_p)$ matrix, with $N_{\text{eq}}$ being the number of fields of the state vector $\boldsymbol{u}$ and $N_p$ the number of degrees of freedom per element $K$. Finally, the linear system $\boldsymbol{A}\boldsymbol{x} + \boldsymbol{b} = 0$ is solved by means of the GMRES iterative method with an incomplete $LU$ preconditioning (Bassi et al., 2005; Renac et al., 2015).

In general, simulations are started with a low CFL (CFL $\approx 1$) and then it is progressively increased up to CFL $\approx 1\times10^3$ or even CFL $\approx 1\times10^6$, depending on the configuration, polynomial degree and mesh analysed. The choice of uniform or local step size depends on the overall convergence behavior. The time evolution is stopped once the time residual of the conservative variables is dropped below $1 \times 10^{-10}$.

*Burgers equation* Unlike the Navier-Stokes equations, in which an implicit scheme has been used to evolve the solution in time, for the Burgers equation we use an explicit scheme instead. In particular, the solution in Eq. (2.44) is advanced in time by means of the explicit strong stability preserving (SSP) 3rd-order 4-stage Runge-Kutta method. We refer the reader to the work of Carpenter and Kennedy (1994) for further details on this scheme.

The time restriction in the explicit scheme is controlled by insuring that for the entire simulation the imposed time step $dt$ is always smaller than the the internal time step $dt_{\text{CFL}}$ calculated for every element. In turn, the internal time step is selected as the minimum value of the convective and viscous contributions. The time evolution is stopped once the time residual is dropped below $1 \times 10^{-12}$.

### 2.2.8 *Quadrature rules*

*Volume integrals* Regarding the computation of the volume integrals in Eq. (2.26) we employ Gaussian quadrature. In particular, the coordinates of the physical element $K$ are mapped to their counterparts in the reference element $\hat{K}$ and the integrals are evaluated numerically by Gauss-Legendre quadrature with $Q = p+1$ quadrature points along the $\xi$ and $\eta$ directions (see Figure 2.1). For a smooth integrand $f(\boldsymbol{x})$, we have

$$\begin{aligned}\int_K f(\boldsymbol{x})\,\mathrm{d}\boldsymbol{x} &= \int_{\hat{K}} f\big(\Xi_K(\boldsymbol{\xi})\big)\mathcal{J}_K(\boldsymbol{\xi})\,\mathrm{d}\boldsymbol{\xi} \\ &= \sum_{i,j=1}^{Q} \omega_i\omega_j f\big(\Xi_K(\xi_i,\eta_j)\big)\mathcal{J}_K(\xi_i,\eta_j)\,, \end{aligned} \tag{2.46}$$

where $\xi_i, \eta_j$ are the quadrature points at which the integrand $f(\boldsymbol{\xi})$ is evaluated, $\omega_i, \omega_j$ are the weights, and $\mathcal{J}_K$ is the determinant of the Jacobian of the

transformation, defined as

$$\mathcal{J}_K = \begin{vmatrix} \frac{\partial x}{\partial \xi} & \frac{\partial x}{\partial \eta} \\ \frac{\partial y}{\partial \xi} & \frac{\partial y}{\partial \eta} \end{vmatrix} = \frac{\partial x}{\partial \xi}\frac{\partial y}{\partial \eta} - \frac{\partial x}{\partial \eta}\frac{\partial y}{\partial \xi}\,. \tag{2.47}$$

The points of the Gauss-Legendre quadrature are interior to the interval $-1 < \xi_i, \eta_j < 1$ for $i, j = 1, ..., Q$ (Karniadakis and Sherwin, 2005). By using Eq. (2.46) we can integrate exactly a polynomial of degree lower than or equal to $2Q - 1$.

*Surface integrals* The surface integrals in Eq. (2.26) can be evaluated as a series of integrals over the different faces of the element. For example, by choosing $e \in \partial_i K^+$ from Figure 2.3, we have the following line integral

$$\begin{aligned} \int_e f(\boldsymbol{x})\,\mathrm{d}S &= \int_{-1}^{1} f\big(\boldsymbol{\Xi}_K(1,\eta)\big)\mathcal{J}_e(1,\eta)\,\mathrm{d}\eta \\ &= \sum_{j=1}^{Q} \omega_j f\big(\boldsymbol{\Xi}_K(1,\eta_j)\big)\mathcal{J}_e(1,\eta_j)\,, \end{aligned} \tag{2.48}$$

where $\mathrm{d}S$ is the differential length, and $\mathcal{J}_e$ is the evaluation of the surface Jacobian. We can relate the differential change in physical coordinates $\boldsymbol{x}$ in terms of the differential change in reference coordinates $\boldsymbol{\xi}$ using the chain rule (Karniadakis and Sherwin, 2005):

$$\mathrm{d}x = \frac{\partial x}{\partial \xi}\mathrm{d}\xi + \frac{\partial x}{\partial \eta}\mathrm{d}\eta\,, \tag{2.49}$$

$$\mathrm{d}y = \frac{\partial y}{\partial \xi}\mathrm{d}\xi + \frac{\partial y}{\partial \eta}\mathrm{d}\eta\,. \tag{2.50}$$

It is worth noting that the selected face $e$ is fully characterized in reference space by the coordinate $\eta$ (see Figure 2.1), as the other coordinate remains a constant of value $\xi = 1$. Therefore, by considering Eqs. (2.49 and 2.50), the differential length $\mathrm{d}S$ can be expressed as

$$\begin{aligned} \mathrm{d}S &= \sqrt{(\mathrm{d}x)^2 + (\mathrm{d}y)^2} \\ &= \sqrt{\left(\frac{\partial x}{\partial \eta}\right)^2 + \left(\frac{\partial y}{\partial \eta}\right)^2}\,\mathrm{d}\eta \\ &= \mathcal{J}_e(1,\eta)\,\mathrm{d}\eta\,, \end{aligned} \tag{2.51}$$

involved in the transformation given in Eq. (2.48).

# Chapter 3

# MULTIRESOLUTION ANALYSIS FUNDAMENTALS

In this chapter we introduce the foundations of multiresolution analysis based on multiwaveles as a mathematical tool which deconstructs any given signal and allows us to better interpret its component parts.

Section 3.1 provides a brief historical context to multiresolution analysis. In particular, Sections 3.1.1 and 3.1.2 highlight the contributions from classical Fourier and Windowed Fourier transform. The limitations of these approaches are outlined in Section 3.1.3.

As an alternative to overcome these limitations, Section 3.2 presents the basics of wavelet theory. The more numerically efficient orthonormal wavelets are introduced in Section 3.2.1, together with the concept of multiresolution analysis. Section 3.3 concludes the chapter by describing the one- and two-dimensional multiwavelets and their properties. Multiwavelets become especially relevant in the context of discontinuous Galerkin schemes, as we will demonstrate in Chapter 4.

## 3.1 CLASSICAL SIGNAL ANALYSIS

The history of wavelets is closely linked to the history of Fourier analysis (Hubbard, 1998). Thus it seems natural to start by giving a brief introduction to Fourier's contribution. In its essence, Fourier analysis states that certain signals or functions can be represented as a sum of sines and cosines. This process is called *Fourier series* for periodic functions, and *Fourier transform* when dealing with nonperiodic functions. Next we will describe the latter.

### 3.1.1 *Fourier transform*

The Fourier transform disassembles a function into the frequencies that constitute it. We are interested in functions that vary with space, therefore we transform a function $f(x) \in L^2$ into a new function $\widetilde{f}(\lambda) \in L^2$ that depends on the *wave number* $\lambda$, which is inversely proportional to $x$. That is

$$\mathcal{F}\{f(x)\} = \widetilde{f}(\lambda) = \frac{1}{\sqrt{2\pi}} \int_{-\infty}^{\infty} f(x)\, \mathrm{e}^{-ix\lambda}\, \mathrm{d}x\,, \tag{3.1}$$

$$f(x) = \begin{cases} \cos(2\pi x), & -1 < x \leq -\frac{1}{2} \\ \cos(2\pi 2x), & -\frac{1}{2} < x \leq 0 \\ \cos(2\pi 4x), & 0 < x < \frac{1}{2} \\ \cos(2\pi 8x), & \frac{1}{2} < x \leq 1 \end{cases}$$

*(a)* Sample signal.

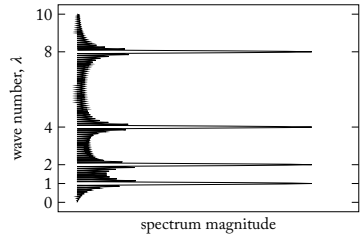


*(b)* Fourier transform.

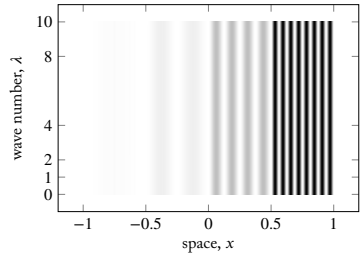


*(c)* Windowed Fourier transform. *Small* window (better spatial resolution).

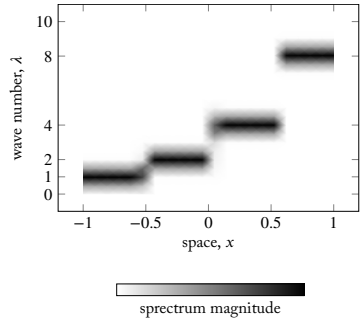


*(d)* Windowed Fourier transform. *Large* window (better wave number resolution).

*Figure* 3.1*:* Examples of classical signal analysis.

with $i = \sqrt{-1}$. An example will help us understand how Eq. (3.1) works. Given the sample signal from Figure 3.1A, the Fourier transform is able to distinctly extract its spatial frequencies, as illustrated by Figure 3.1B.

From the Fourier transform we can reconstruct the original function, meaning that no information is lost during the transformation. However, the Fourier transform hides information about space, in the same manner that the original function is not explicit about the wave number. Moreover, the Fourier analysis is poorly adapted to brief or sudden changes in $f(x)$ (e.g. high frequency bursts). These confined changes would lose its locality and become spread throughout the entire transform (Hubbard, 1998). This phenomenon can be certainly observed in Figure 3.1B, where spurious oscillations between wave numbers are due to the discontinuity of the signal $f(x)$.

### 3.1.2 *Windowed Fourier transform*

The shortcomings of the Fourier analysis led to the development of the windowed Fourier transform, in which space and wave number can be studied simultaneously within certain constraints (Gabor, 1946). The idea is to window the function $f(x)$ so that the space interval remains fixed in size, and then applying the Fourier transform defined in Eq. (3.1). By defining the regularly spaced intervals $x = jx_0$ and $\lambda = m\lambda_0$, with $j, m \in \mathbb{Z}$ and $x_0, \lambda_0 > 0$, we have the *discrete* windowed Fourier transform:

$$\mathcal{F}^{\text{win}}_{(m,j)}\{f(x)\} = \int_{-\infty}^{\infty} f(s)\, g\big(s - jx_0\big)\, e^{-im\lambda_0 s}\, \mathrm{d}s\,. \tag{3.2}$$

with $i = \sqrt{-1}$. Adjusting $j$ amounts to shifting the window by increments of $x_0$ and its multiples along the signal. The window function $g$ is normally well located in both space and wave number, thus providing a description of $f$ in the time-frequency plane (Daubechies, 1992).

Examples of the windowed Fourier transform applied to the sample signal in Figure 3.1A are illustrated in Figures 3.1C and 3.1D. In these examples the window function $g$ is composed by a summation of cosines given by Blackman and Tukey (1958). Figure 3.1C represents a short window, so that higher wave numbers peaks are clearly located, in detriment of lower wave number components. On the other hand, Figure 3.1D employs a large window resulting on a full representation of the spatial frequencies of the signal. However, spatial localization is lost, with no clear distinction where the peaks occur.

The windowed Fourier transform has two major shortcomings. Firstly, different resolutions require different window sizes to be properly localized. In this regard, the fixed resolution of the windowed Fourier analysis imposes a severe compromise. Secondly, the relation between spatial resolution and wave number resolution is guided by the Heisenberg uncertainty principle (Keinert, 2003), which we will briefly discuss next.

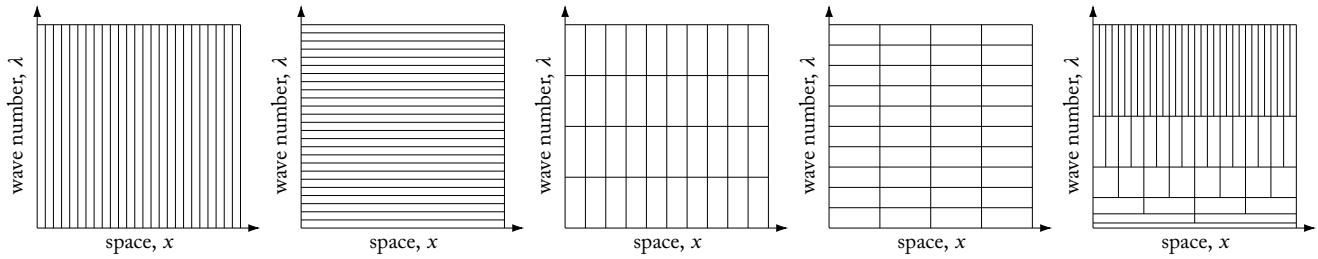


*(a)* Physical space. *(b)* Fourier space. *(c)* Windowed Fourier analysis. Narrow window. *(d)* Windowed Fourier analysis. Wide window. *(e)* Wavelets.

*Figure 3.2:* Different representations of the idealized space-wave number plane (Farge, 1992).

### 3.1.3 *Heisenberg uncertainty principle*

The Heisenberg principle states that a signal cannot be defined simultaneously in space and in wave number (Hubbard, 1998). For a function $f(x) \in L^2$ with $\|f(x)\|_{L^2} = 1$ (where $f$ is a normalized signal), we define the mean and the standard deviation of $x$ as

$$\mu = \int_{-\infty}^{\infty} x|f(x)|\mathrm{d}x, \qquad \sigma = \left(\int_{-\infty}^{\infty} (x-\mu)^2|f(x)|^2\mathrm{d}x\right)^{\frac{1}{2}}, \tag{3.3}$$

and the corresponding $\widetilde{\mu}, \widetilde{\sigma}$ of $\lambda$ in the Fourier space (by application of Eq. (3.1)). The uncertainty principle states that

$$\sigma \cdot \widetilde{\sigma} \geq \tfrac{1}{2}. \tag{3.4}$$

Therefore, the more $f$ is focused in a short spatial window (better $x$-localization), the smaller $\sigma$ will be. In turn, the range of spatial frequencies of $\widetilde{f}$ will be more spread out, resulting in a larger $\widetilde{\sigma}$ (worse $\lambda$-localization).

This compromise can be illustrated with the so-called *space-wave number plane* (Farge, 1992; Hubbard, 1998), in which space is measured horizontally and wave number vertically, as shown by Figure 3.2. This plane is then tiled with rectangles of size $\sigma$ by $\widetilde{\sigma}$ known as *Heisenberg boxes*.

Equation 3.4 requires each box to have a minimum area of 1/2, but depending on the analysis used, they will have different forms and placements. In physical space the boxes become tall, narrow bands spanning multiple wave numbers (Figure 3.2A); whereas in Fourier space the boxes are short, wide bands over a long spatial distance (Figure 3.2B).

With windowed Fourier analysis, the shape of the Heisenberg boxes is provided by the size of the window function $g$. A narrow window gives more precision about space at the cost of worse wave number resolution, as shown in Figure 3.2C. Conversely, Figure 3.2D displays a wide window, which increases wave number resolution at the expense of being vague about space. In both cases, they build a rectangular grid of fixed cell shape, providing the same spatial and wave number resolution everywhere.

However, the windowed Fourier analysis imposes some compromises. By fixating the window size we either miss the large scales (short window), or the small scales (wide window). This brings us to an alternative approach called *wavelet analysis*. They will allow us to study a signal at different scales by stretching or compressing the size of the window, as shown in Figure 3.2E.

## 3.2 WAVELET ANALYSIS

The wavelet transform also decomposes a given signal simultaneously by space and by scale (related to wave number) (Hubbard, 1998). Similarly to Eq. (3.2) we have

$$\mathscr{W}_{(m,j)}\{f(x)\} = a_0^{m/2} \int_{-\infty}^{\infty} f(x)\, \psi_{(m,j)}(x)\, \mathrm{d}x\,, \tag{3.5}$$

where $\psi_{(m,j)}(x)$ is used to create a family of wavelets $\psi\left(a_0^m x - j b_0\right)$ with $j, m \in \mathbb{N}$ and $a_0 > 1$, $b_0 > 0$ fixed. By definition (Daubechies, 1992), $\psi_{(m,j)}(x)$ satisfies

$$\int_{-\infty}^{\infty} \psi_{(m,j)}(x)\, \mathrm{d}x = 0\,. \tag{3.6}$$

The *dilation* parameter $m$ controls the *deformation* of the wavelet (the shape of the wavelet does not change). Higher values of $m$ produce a compressed $\psi$ to better capture brief, high wave number components. On the other hand, lower $m$ values result in a stretched $\psi$, more adequate to record long-lived, low wave number components. Lastly, the *translation* parameter $j$ shifts the spatial localization of the wavelet. The effects of dilation and translations are distinctly displayed in Figure 3.3. This structure paves the way to *multiresolution analysis* (MRA) (Mallat, 1989; Harten, 1996). By this analysis, the function is studied at a coarse scale to obtain a global picture and at ever increasing resolutions to capture gradually finer details.

Without further constraints the inverse of the transformation in Eq. (3.5), that is $\mathscr{W}_{(m,j)}^{-1}$, leads to a redundant recovery of the original signal (Daubechies, 1992). In this case an *orthogonal* transformation may be desired. It provides an accurate reconstruction of the original signal while avoiding redundancy (Hubbard, 1998). Moreover, orthogonality ensures that the energy of the signal is preserved in the transformation.

### 3.2.1 *Orthonormal wavelets and multiresolution*

By setting $a_0 = 2$ (*dyadic* dilation) and $b_0 = 1$, the $\psi_{(m,j)}$ in Eq. (3.5) becomes

$$\psi_{(m,j)}(x) = 2^{m/2} \psi\left(2^m x - j\right), \quad j, m \in \mathbb{N}\,, \tag{3.7}$$

Additionally, we set $\psi_{(m,j)}$ to constitute an orthonormal basis in $L^2(\mathbb{R})$, leading to the definition of the wavelet subspace $W_m = \left\{\psi_{(m,j)}\right\}_{j,m\in\mathbb{N}}$. This means that any $L^2$-function $f$ can be represented by a linear combination of the $\psi_{(m,j)}$ (Daubechies, 1992).

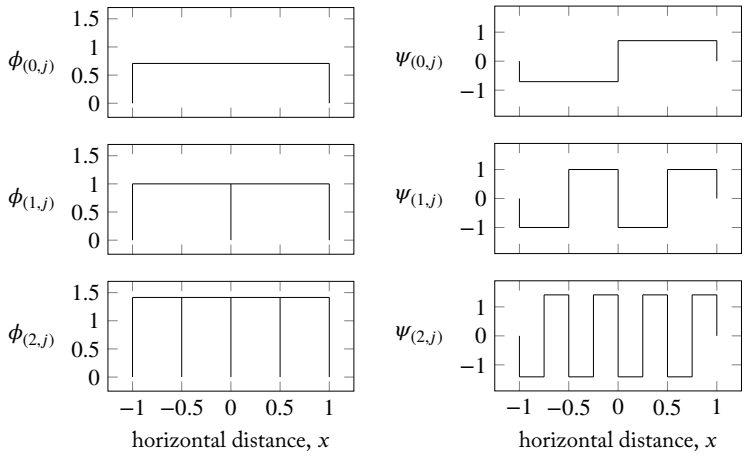


*(a)* Haar scaling function. *(b)* Haar wavelet.

*Figure 3.3:* Example of an orthonormal family of wavelets. Different values of the dilation parameter $m$ and the resulting subspaces $W_m$ and $V_m$. The number of functions increases by a factor of $2^m$, with the translation parameter $j$ controlling their placement along $x$.

Next we introduce a cascade of subspaces $\{V_m\}_{m\in\mathbb{N}}$ representing the successive resolution levels. A given level would contain all the information of coarser resolutions. That is

$$V_m \subset V_{m+1}, \quad \forall m \in \mathbb{N}\,. \tag{3.8}$$

Multiresolution analysis is achieved by further requiring that all the subspaces $V_m$ in Eq. (3.8) are scaled variations of the initial space $V_0$. That is

$$f(x) \in V_0 \iff f(2^m x) \in V_m, \qquad m \in \mathbb{N}\,, \tag{3.9}$$

which assigns the name *scaling subspace* to $V_m$. The next attribute that the MRA demands is the invariance of $V_m$ under integer translations, which means

$$f(2^m x) \in V_m \iff f(2^m x - j) \in V_m, \qquad m, j \in \mathbb{N}\,. \tag{3.10}$$

Finally, we close the multiresolution requirements with the properties

$$\bigcap_{m\in\mathbb{N}} V_m = \{0\}, \qquad \bigcup_{m\in\mathbb{N}} V_m = L^2(\mathbb{R})\,. \tag{3.11}$$

The latter property ensures that any function can be approximated with arbitrary precision. Namely

$$\lim_{m\to\infty} P_m f(x) = f(x)\,, \quad \forall f(x) \in L^2(\mathbb{R})\,, \tag{3.12}$$

where $P_m$ is the orthogonal projection operator onto $V_m$. To compute this orthogonal projection there exists a unique function named *scaling function*

$$\phi_{(m,j)}(x) = 2^{m/2}\phi\big(2^m x - j\big)\,, \quad j, m \in \mathbb{N}\,, \tag{3.13}$$

which is an orthonormal basis of the scaling subspace $V_m$. Consequently:

$$\begin{aligned} P_m f &= \sum_{j\in\mathbb{N}} \Big\langle f, \phi_{(m,j)} \Big\rangle \phi_{(m,j)} \\ &= \sum_{j\in\mathbb{N}} s_{(m,j)} \phi_{(m,j)}\,, \end{aligned} \tag{3.14}$$

with $s_{(m,j)}$ representing the so-called *scaling function coefficients*, and $\langle\ \rangle$ referring to the inner product in $L^2$, such that

$$s_{(m,j)} = \left\langle f, \phi_{(m,j)} \right\rangle = \int f\, \phi_{(m,j)}\, \mathrm{d}x\,. \tag{3.15}$$

The relation between Eq. (3.7) and Eq. (3.13) is given by the fact that $W_m$ is the orthogonal complement of $V_m$ in $V_{m+1}$ (Daubechies, 1992). Namely

$$V_{m+1} = V_m \oplus W_m; \quad W_m \perp V_m\,, \tag{3.16}$$

which implies that the difference between the two levels of resolution $m+1$ and $m$ is given by

$$\begin{aligned} Q_m f &= P_{m+1} f - P_m f \\ &= \sum_{j\in\mathbb{N}} \left\langle f, \psi_{(m,j)} \right\rangle \psi_{(m,j)} \\ &= \sum_{j\in\mathbb{N}} d_{(m,j)} \psi_{(m,j)}\,, \end{aligned} \tag{3.17}$$

where $Q_m$ is the orthogonal projection operator onto $W_m$, and $d_{(m,j)}$ are the commonly named *orthogonal wavelet coefficients*. By successive application of Eq. (3.16), a hierarchy of wavelet subspaces can be derived:

$$V_m = V_0 \oplus W_0 \oplus W_1 \oplus \ldots \oplus W_{m-1}\,. \tag{3.18}$$

By considering Eq. (3.14) and Eq. (3.17), Eq. (3.18) becomes

$$\begin{aligned} P_m f &= P_0 f + \sum_{i=0}^{m-1} Q_i f \\ &= s_{(0,0)} \phi_{(0,0)} + \sum_{i=0}^{m-1} \sum_{j\in\mathbb{N}} d_{(i,j)} \psi_{(i,j)}\,, \end{aligned} \tag{3.19}$$

which is commonly known as the *multiscale decomposition* of the signal $f$ (Mallat, 1989). In summary, multiresolution analysis requires the conditions from Eq. (3.8) to Eq. (3.11) to be met. Then, the signal can be represented by a series of approximations which differ from each other by a factor of two, as shown by Eq. (3.14). These successive estimations approximate the signal with higher and higher precision, approaching the original. This hierarchy is rendered by Eq. (3.19). The difference of information from one resolution to the next is encoded by the wavelet coefficients, as described in Eq. (3.17) (Hubbard, 1998).

The hierarchical nature of the development in Eq. (3.19) can be observed in Figure 3.4, where a multiresolution analysis has been performed by using the Haar basis (Haar, 1910). The Haar basis is the simplest wavelet generating

an orthonormal family of wavelets. It is built from

$$\psi(x) = \begin{cases} -1, & -1 < x < 0 \\ 1, & 0 \le x < 1 \\ 0, & \text{elsewhere} \end{cases}, \quad \text{and} \quad \phi(x) = \begin{cases} 1, & -1 < x < 1 \\ 0, & \text{elsewhere} \end{cases} \tag{3.20}$$

The pair of Haar functions $\phi, \psi$ are illustrated in Figure 3.3A and Figure 3.3B, respectively.

The Haar basis is compactly supported and discontinuous, which makes them a very good fit to the discontinuous Galerkin framework presented in Chapter 2. However, they are not very efficient at approximating signals with higher-order terms (high frequency) due to their low-order nature. To remedy this, the work of Daubechies (1992) developed higher-order orthogonal wavelets with compact support. However, they are computed as the limit of an iterative process. Consequently, the commonly named *Daubechies wavelets* can not be created from analytical formulas.

The target is to find higher order wavelets with compact support that are analytically defined, so that they can be easily connected to the discontinuous Galerkin method presented in Chapter 2. These conditions can be fulfilled by using multiple scaling functions and wavelets, the so-called *multi-scaling functions* and *multiwavelets*, respectively (Alpert, 1993; Plonka and Strela, 1998).

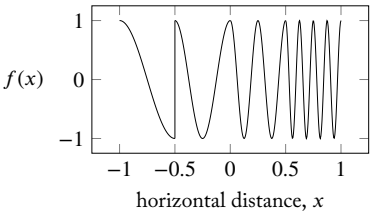


*(a)* Signal from Figure 3.1A.

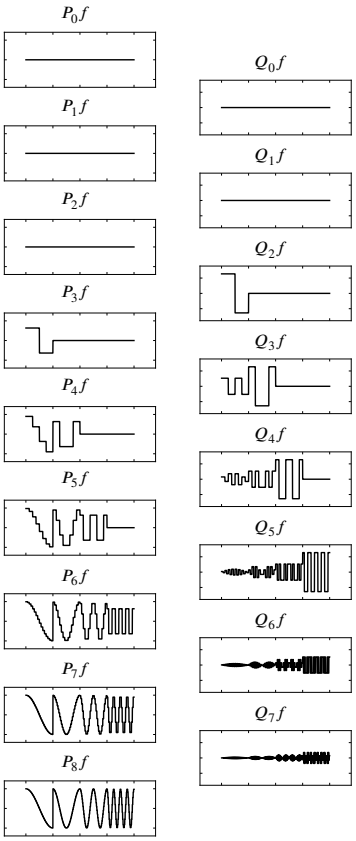


*(b)* The wavelet transform of the signal, over eight scales, varying by a factor of two. From the coarser resolutions at the top to the finest scales at the bottom.

*Figure 3.4:* Example of wavelet analysis.

## 3.3 MULTIWAVELETS

As described in the previous section, multiresolution analysis allows us to decompose a given signal into a hierarchy of approximations of that signal at different levels of resolution. The changes between successive resolutions are captured by the wavelets. Multiwavelets (MWs) constitute a generalization of this approach, by allowing several wavelet functions to be used simultaneously. For this purpose, we will be employing the so-called *Alpert multiwavelet* (Alpert, 1993; Alpert et al., 2002), which is a compactly supported, orthonormal, piecewise polynomial multiwavelet. For a detailed introduction to the theory behind multiwavelets, we refer to the work of Strela (1996). Additionally, concerning the construction of other types of multiwavelets, the interested reader can refer to Donovan et al. (1996) and Keinert (2003).

### 3.3.1 *One-dimensional multiwavelets*

Firstly, the concepts will be described in a one-dimensional framework. We will then move to higher spatial dimensions. Therefore, we define the multi-scaling functions and multiwavelets of *multiplicity* $r$ as

$$\phi^{\ell}_{(m,j)} \quad \text{and} \quad \psi^{\ell}_{(m,j)}, \qquad \ell = 1, \dots, r. \tag{3.21}$$

where $r = p + 1$ in the current 1-D context, with $p$ being the polynomial degree. Similarly to Section 3.2, the resolution level will be denoted by $m$, with the finest resolution given by $m = \mathscr{M}$. How much detail is captured by a particular resolution level depends on how many subdivisions or elements, $N_K$, this level owns. Each element $K_{(m,j)}$ in a given level $m$ is identified by the index $j$. Knowing that the relation between level and number of subdivisions is dyadic (i.e. given a power of two, $N_K = 2^m$) and that we work in $L^2([-1,1])$, then the support of the elements is determined by

$$K_{(m,j)} = \left[-1 + 2^{-m+1}j, -1 + 2^{-m+1}(j+1)\right], \tag{3.22}$$

with $m = 0, ..., \mathscr{M}$ and $j = 0, ..., N_K - 1$. In the same way than Section 3.2, the functions described in Eq. (3.21) become the orthonormal basis of the two subspaces $V_m^p, W_m^p$ associated with each $K_{(m,j)}$. Namely

$$V_m^p = \operatorname{span}\{\phi_{(m,j)}^\ell\}, \quad W_m^p = \operatorname{span}\{\psi_{(m,j)}^\ell\}, \qquad \ell = 1, ..., r. \tag{3.23}$$

Moreover, the conditions Eq. (3.8) to Eq. (3.11) that enable multiresolution analysis in the case of wavelets also apply for the more general case of multi-wavelets with multiplicity $r$. For a more detailed description of the MRA in the context of multiwavelets, the interested reader may refer to Strela (1996).

Similarly, the orthogonal projection operators defined in Eq. (3.14) and Eq. (3.17) become, respectively:

$$P_m^p f = \sum_{j=0}^{N_K-1} \sum_{\ell=1}^{r} s_{(m,j)}^\ell \phi_{(m,j)}^\ell, \tag{3.24}$$

$$Q_m^p f = \sum_{j=0}^{N_K-1} \sum_{\ell=1}^{r} d_{(m,j)}^\ell \psi_{(m,j)}^\ell, \qquad m = 0, ..., \mathscr{M}, \tag{3.25}$$

with $N_K = 2^m$ and $r = p + 1$. These new definitions allow us to generalize the multiscale decomposition given by Eq. (3.19) to the new MRA framework with multiplicity $r$. Namely

$$P_{\mathscr{M}}^p f = \sum_{\ell=1}^{r} s_{(0,0)}^\ell \phi_{(0,0)}^\ell + \sum_{i=0}^{\mathscr{M}-1} \sum_{j=0}^{N_K-1} \sum_{\ell=1}^{r} d_{(i,j)}^\ell \psi_{(i,j)}^\ell, \tag{3.26}$$

where we have chosen $m = \mathscr{M}$ as the highest resolution level to approximate the signal $f$. The multi-scaling function coefficients at $m = 0$, $s_{(0,0)}^\ell$, represent the lowest resolution approximation; while a cascade of multiwavelet coefficients, $d_{(i,j)}^\ell$, carry the information across resolutions up to $\mathscr{M} - 1$.

We move now on to how to build the basis $\phi_{(m,j)}^\ell$ and $\psi_{(m,j)}^\ell$. We start from the coarsest level $m = 0$ and build up from there. In this case the subspace of multi-scaling functions results in $V_0^p$, and its basis are given in the work of

Alpert et al. (2002). Namely:

$$\phi^{\ell}_{(0,0)}(\xi) = \phi^{\ell}(\xi) = \begin{cases} \sqrt{\frac{2(\ell-1)+1}{2}}\, P^{\ell}(\xi), & \xi \in [-1,1] \\ 0, & \text{otherwise} \end{cases} \tag{3.27}$$

where $P^{\ell}(\xi)$ indicates the Legendre polynomial of degree $\ell - 1$. Multi-scaling functions in Eq. (3.27) with degree $p = 1, 2$ are plotted in Fig. 3.5A. On the other hand, multiwavelets undergo a more complex building process. The algorithm starts with a piecewise monomial of degree $\ell - 1$ defined in $[-1, 1]$. A Gram-Schmidt orthonormalisation is followed by an operation to increase the number of vanishing moments of the resulting function. This is enforced by ensuring orthogonality with respect to a higher degree monomial. The complete algorithm can be found in the study of Alpert (1993). The multiwavelets that span the subspace $W_0^p$ are thus formed by these orthonormal functions $f^{(\ell,p)}(x)$ as follows:

$$\psi^{\ell}_{(0,0)}(\xi) = \psi^{\ell}(\xi) = \begin{cases} (-1)^{(\ell-1)+p+1} f^{(\ell,p)}(-\xi), & \xi \in [-1,0] \\ f^{(\ell,p)}(\xi), & \xi \in [0,1] \\ 0, & \text{otherwise} \end{cases} \tag{3.28}$$

Multiwavelets in Eq. (3.28) with $p = 1, 2$ are plotted in Fig. 3.5B and Fig. 3.5C, respectively. At this point, the basis of $V_0^p, W_0^p$ have been defined. To describe the successive subspaces when $m > 0$ we require the mapping $\xi \mapsto \frac{2(x-x_c)}{h_K}$, with $x \in K_{(m,j)}$. Additionally, $x_c$ and $h_K$ represent the center and the size of element $K_{(m,j)}$, respectively. The basis $\phi^{\ell}_{(m,j)}, \psi^{\ell}_{(m,j)} \in V_m^p, W_m^p$ are generated by dilation and translation of $\phi^{\ell}_{(0,0)}, \psi^{\ell}_{(0,0)} \in V_0^p, W_0^p$, namely,

$$\phi^{\ell}_{(m,j)}(x) = \sqrt{\frac{2}{h_K}}\, \phi^{\ell}\left(\frac{2(x-x_c)}{h_K}\right), \quad \ell = 1, ..., r; \quad j = 0, ..., N_K - 1, \tag{3.29}$$

$$\psi^{\ell}_{(m,j)}(x) = \sqrt{\frac{2}{h_K}}\, \psi^{\ell}\left(\frac{2(x-x_c)}{h_K}\right), \quad m = 0, ..., \mathscr{M}. \tag{3.30}$$

Both multi-scaling functions and multiwavelets support extends to the current element defined by $K_{(m,j)}$. That is $\text{supp}(\phi^{\ell}_{(m,j)}) = \text{supp}(\psi^{\ell}_{(m,j)}) = K_{(m,j)}$. Moreover, they are $L^2$-normalised, i.e. $\|\phi^{\ell}_{(m,j)}\|_{L^2} = \|\psi^{\ell}_{(m,j)}\|_{L^2} = 1$, and share the following orthonormality relations (Hovhannisyan et al., 2014):

$$\left\langle \phi^{\ell}_{(m,j)}, \phi^{\ell'}_{(m,j')} \right\rangle_{K_{(m,j)}} = \delta_{\ell,\ell'}\delta_{j,j'}, \tag{3.31a}$$

$$\left\langle \phi^{\ell}_{(m,j)}, \psi^{\ell'}_{(m,j')} \right\rangle_{K_{(m,j)}} = 0, \tag{3.31b}$$

$$\left\langle \psi^{\ell}_{(m,j)}, \psi^{\ell'}_{(m',j')} \right\rangle_{K_{(m,j)}} = \delta_{\ell,\ell'}\, \delta_{j,j'}\, \delta_{m,m'}, \tag{3.31c}$$

with $\langle\ \rangle$ representing the inner product. Additionally, inherited by Alpert's algorithm, multiwavelets have $M = \ell + r - 1$ vanishing moments, which means that the multiwavelets are orthogonal to polynomials of degree $M - 1$.

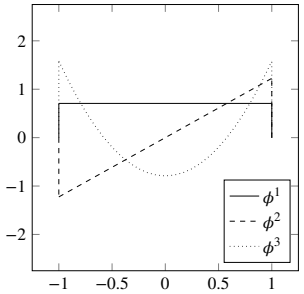


*(a)* Multi-scaling functions, $p = 1, 2$.

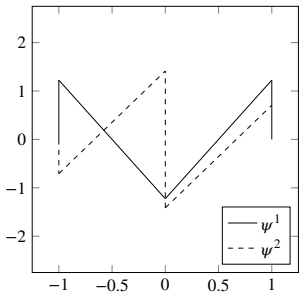


*(b)* Multiwavelets, $p = 1$.

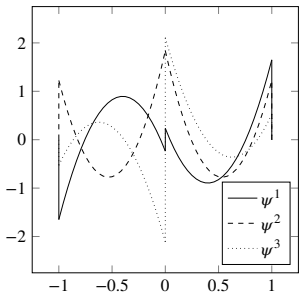


*(c)* Multiwavelets, $p = 2$.

*Figure 3.5:* 1-D Alpert's multi-scaling functions and multiwavelets.

Namely,

$$\left\langle P,\, \psi^{\ell}_{(m,j)} \right\rangle_{K_{(m,j)}} = 0, \quad \forall P \in \mathscr{P}^M\big(K_{(m,j)}\big), \qquad \ell = 1, ..., r\,. \tag{3.32}$$

with $r = p + 1$. This concept will be further explored in Chapter 5.

### 3.3.2 *Two-dimensional multiwavelets*

We construct orthonormal multiwavelet bases for $L^2([-1,1]^2)$ by considering the tensor product of two one-dimensional multiresolution analyses, similarly to the generalization presented in Mallat (1989) and Daubechies (1992). Therefore, we define the initial subspace $\boldsymbol{V}_0^p$ as

$$\boldsymbol{V}_0^p = V_0^p \otimes V_0^p = \operatorname{span}\big\{F(x,y) = f(x)g(y) \mid f, g \in V_0^p\big\}\,, \tag{3.33}$$

and build the multiresolution cascade in $L^2([-1,1]^2)$

$$\boldsymbol{V}_m^p \subset \boldsymbol{V}_{m+1}^p, \quad \forall m \in \mathbb{N}\,, \tag{3.34}$$

which satisfies

$$\bigcap_{m\in\mathbb{N}} \boldsymbol{V}_m^p = \{0\}\,, \tag{3.35a}$$

$$\bigcup_{m\in\mathbb{N}} \boldsymbol{V}_m^p = L^2([-1,1]^2)\,, \tag{3.35b}$$

$$F(x,y) \in \boldsymbol{V}_0^p \iff F(2^m x, 2^m y) \in \boldsymbol{V}_m^p\,, \tag{3.35c}$$

$$F(2^m x, 2^m y) \in \boldsymbol{V}_m^p \iff F\big(2^m x - j_x, 2^m y - j_y\big) \in \boldsymbol{V}_m^p\,, \tag{3.35d}$$

with $m, j_x, j_y \in \mathbb{N}$. The orthonormal basis of the subspace $\boldsymbol{V}_m^p$ is given by

$$\boldsymbol{\Phi}^{\ell}_{(m,j)}(\boldsymbol{x}) = \phi^{\ell_x}_{(m,j_x)}(x)\, \phi^{\ell_y}_{(m,j_y)}(y)\,, \tag{3.36}$$

where $\phi^{\ell}_{(m,j)}$ can be calculated by Eq. (3.29) along each of the $x$- and $y$-directions. Then the involved indices can be summarised by

$$\begin{aligned} &\ell_x, \ell_y = 1, ..., r; && \ell = r(\ell_x - 1) + \ell_y, \\ &j_x, j_y = 0, ..., N_K - 1; && j = N_K j_x + j_y, \end{aligned} \tag{3.37}$$

with multiplicity $r = p+1$. It is worth noting that in the 2-D case the domain is discretised into an equal number of $N_K = 2^m$ elements along each direction, resulting in a total of $N_K^2$ elements per level $m$. Similarly to the 1-D case, we define the subspace $\boldsymbol{W}_m^p$ to be the orthogonal complement of $\boldsymbol{V}_m^p$ in $\boldsymbol{V}_{m+1}^p$.

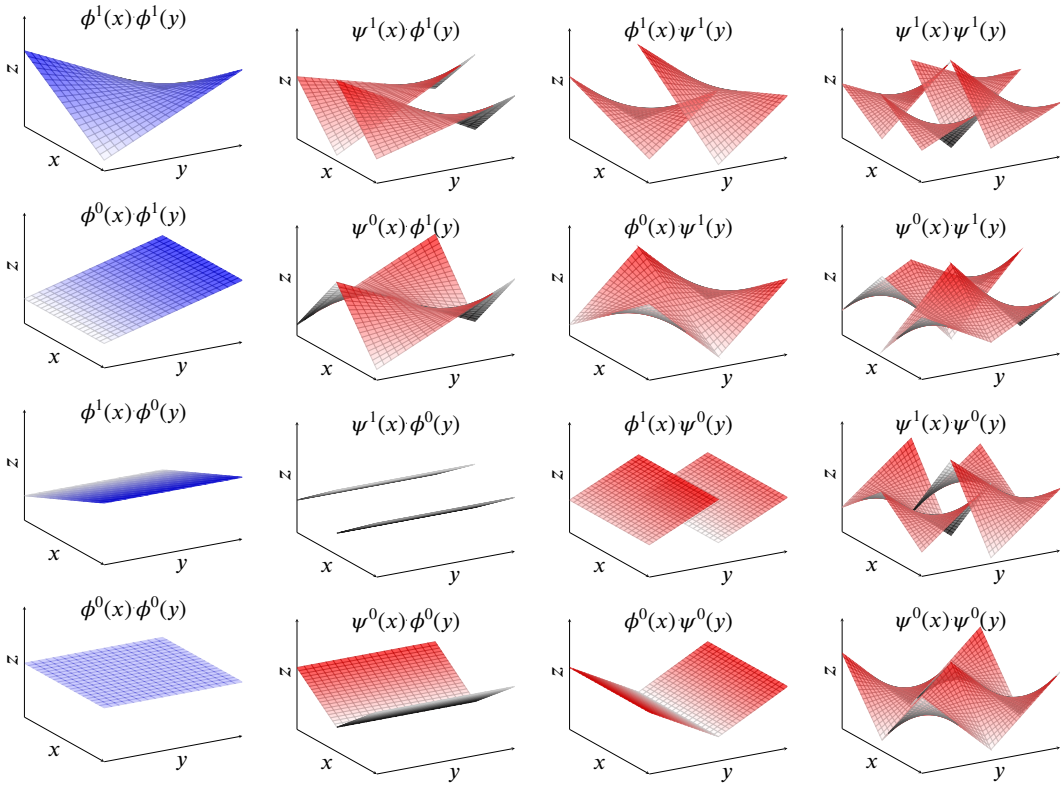


*(a)* Multi-scaling functions. *(b)* Horizontal MWs. *(c)* Vertical MWs. *(d)* Diagonal MWs.

*Figure* 3.6: 2-D Multi-scaling functions and multiwavelets with multiplicity $r = 2$. We use the nomenclature $\phi^{\ell} = \phi^{\ell}_{(0,0)}$ and $\psi^{\ell} = \psi^{\ell}_{(0,0)}$.

Namely,

$$\begin{aligned}
\boldsymbol{V}^p_{m+1} &= V^p_{m+1} \otimes V^p_{m+1} \\
&= \left(V^p_m \oplus W^p_m\right) \otimes \left(V^p_m \oplus W^p_m\right) \\
&= \left(V^p_m \otimes V^p_m\right) \oplus \left[\left(W^p_m \otimes V^p_m\right) \oplus \left(V^p_m \otimes W^p_m\right) \oplus \left(W^p_m \otimes W^p_m\right)\right] \\
&= \boldsymbol{V}^p_m \oplus \boldsymbol{W}^{p,\alpha}_m \oplus \boldsymbol{W}^{p,\beta}_m \oplus \boldsymbol{W}^{p,\gamma}_m \\
&= \boldsymbol{V}^p_m \oplus \boldsymbol{W}^p_m
\end{aligned} \tag{3.38}$$

We observe that the detail space $\boldsymbol{W}^p_m$ is made up of three contributions, denoted by the superscripts $\alpha, \beta$ and $\gamma$. This terminology follows the notation proposed by Vuik (2017). Their respective orthonormal bases are given by

$$\boldsymbol{\Psi}^{\ell,\alpha}_{(m,j)}(\boldsymbol{x}) = \psi^{\ell_x}_{(m,j_x)}(x)\,\phi^{\ell_y}_{(m,j_y)}(y)\,, \tag{3.39a}$$

$$\boldsymbol{\Psi}^{\ell,\beta}_{(m,j)}(\boldsymbol{x}) = \phi^{\ell_x}_{(m,j_x)}(x)\,\psi^{\ell_y}_{(m,j_y)}(y)\,, \tag{3.39b}$$

$$\boldsymbol{\Psi}^{\ell,\gamma}_{(m,j)}(\boldsymbol{x}) = \psi^{\ell_x}_{(m,j_x)}(x)\,\psi^{\ell_y}_{(m,j_y)}(y)\,, \tag{3.39c}$$

where $\phi^{\ell}_{(m,j)}, \psi^{\ell}_{(m,j)}$ can be calculated by Eq. (3.29) and Eq. (3.30), in that order. The superscripts $\alpha, \beta$ and $\gamma$ denote the $x$-, $y$-, and $xy$-directions, respectively. Therefore, they will lean toward details in those directions. Figure 3.6 shows the basis for the different contributions with $p = 1$. Further details can be found in the work of Vuik and Ryan (2014). We can now build the gener-

alization to 2-D of the orthogonal projection operator onto $\boldsymbol{V}_m^p$, Eq. (3.24). Namely

$$\boldsymbol{P}_m^p F = \sum_{j=0}^{N_K^2-1} \sum_{\ell=1}^{r^2} \boldsymbol{s}_{(m,j)}^{\ell} \boldsymbol{\Phi}_{(m,j)}^{\ell}, \qquad m = 0, ..., \mathscr{M}, \tag{3.40}$$

and the orthogonal projection operator onto the detail subspaces $\boldsymbol{W}_m^{p,\alpha}$, $\boldsymbol{W}_m^{p,\beta}$, and $\boldsymbol{W}_m^{p,\gamma}$. That is

$$\boldsymbol{Q}_m^{p,\lambda} F = \sum_{j=0}^{N_K^2-1} \sum_{\ell=1}^{r^2} \boldsymbol{d}_{(m,j)}^{\ell,\lambda} \boldsymbol{\Psi}_{(m,j)}^{\ell,\lambda}, \qquad \lambda = \alpha, \beta \text{ or } \gamma. \tag{3.41}$$

Finally, the multiscale decomposition of a function $F$ can be expressed as

$$\boldsymbol{P}_{\mathscr{M}}^p F = \boldsymbol{P}_0^p F + \sum_{i=0}^{\mathscr{M}-1} \left( \boldsymbol{Q}_i^{p,\alpha} F + \boldsymbol{Q}_i^{p,\beta} F + \boldsymbol{Q}_i^{p,\gamma} F \right), \tag{3.42}$$

with $m = \mathscr{M}$ defined as the finest approximation to $F$.

# Part II

# HP-ADAPTIVE FRAMEWORK

# Chapter 4

# UNITING DGM AND MULTIWAVELETS

We have spent previous chapters outlining the theoretical framework of this research. In this manner, we have presented both the physical models and their numerical discretization by means of the discontinuous Galerkin method (DGM). We have also introduced the multiresolution analysis (MRA) based on multiwavelets as a tool to better interpret a given signal.

The objective of this chapter is to unify the MRA scheme and the DGM formulation. We first review previous attempts in the literature to establish this union and then suggest an alternative approach.

Section 4.1 describes the classical approach of globally combining the MRA and the DGM (see e.g. Gerhard et al. (2015b)). Sections 4.1.1 and 4.1.2 present the union in one- and two-dimensional configurations, respectively.

Section 4.2 offers an overview of how the union of MRA and DGM sets the stage to mesh adaptation. The literature approach is examined in Section 4.2.1, and an outline of the new alternative is unveiled in Section 4.2.2.

The new approach requires a prior post-processing step, which is introduced in Section 4.3. Different one-dimensional post-processing methods are discussed in Sections 4.3.1 to 4.3.3. The extension to two-dimensions is presented in Section 4.3.4. Finally, the new approach come into being in Section 4.4. Both one- and two-dimensional configurations are explored in Sections 4.4.1 and 4.4.2, in that order. Lastly, the main conclusions of this chapter are outlined in Section 4.5.

## 4.1 MULTIRESOLUTION IN THE CONTEXT OF DGM

### 4.1.1 *One-dimensional configuration*

When describing the discontinuous Galerkin method (DGM) in Chapter 2, we characterized its discretized solution, given by Eq. (2.17), as a local polynomial expansion of degree $p$. We also determined that the basis employed in this polynomial expansion are built upon Legendre polynomials, as described by Eq. (2.19). If we now draw a parallel to Chapter 3, and in particular to the multiwavelet formulation from Section 3.3, we observe that the same basis is employed when expressing a signal in the (MRA) framework, Eq. (3.24).

Certainly, the signal is approximated by a summation of multi-scaling functions, which in turn are given by Eq. (3.27), as a scaled version of Legendre polynomials. Based on these observations, a direct relation can be established between the two approaches. Initially, we will establish the relation in 1-D and then move to its generalization to higher dimensions.

We consider a dyadic mesh $\Omega_h$ composed of $N_K = 2^{\mathscr{M}}$ elements and domain $\Omega = [-1, 1]$, so that the multiwavelet formulation from Section 3.3 holds. Each element $K$ is then defined by Eq. (3.22) with $m = \mathscr{M}$. That is

$$K = K_{(\mathscr{M},j)} = \left[-1 + 2^{-\mathscr{M}+1} j, -1 + 2^{-\mathscr{M}+1}(j+1)\right], \tag{4.1}$$

with $j = 0, ..., N_K - 1$. Here, we have combined the nomenclature of DGM and MRA. We remind the reader that the parameter $\mathscr{M}$ refers to the highest resolution level in the MRA of a signal, and the index $j$ identifies each element of that level. Therefore, we have associated the concept of *mesh* in DGM with the notion of *highest resolution level* in MRA. We now define a DG solution $u_h(x,t)$ in $\Omega_h$ as an approximation to a conservative variable $u(x,t)$ defined in $\Omega$. By application of Eq. (2.17) we have:

$$\begin{aligned} u_h(x,t) &= \sum_K \sum_{\ell=1}^{N_p} U_K^\ell(t)\, \phi^\ell\left(\Xi_K^{-1}(x)\right) \\ &= \sum_{j=0}^{N_K-1} \sum_{\ell=1}^{N_p} U_{(\mathscr{M},j)}^\ell(t)\, \phi^\ell\left(\tfrac{2(x-x_c)}{h_K}\right), \quad \forall x \in K_{(\mathscr{M},j)}, K_{(\mathscr{M},j)} \in \Omega_h. \end{aligned} \tag{4.2}$$

with $h_K = 2^{-\mathscr{M}+1}$; and $x_c$ being the size and the center of element $K_{(\mathscr{M},j)}$, respectively. Additionally, by using the multiresolution framework presented in Chapter 3, we can express the conservative variable $u$ in terms of a single-scale decomposition (Vuik and Ryan, 2014; Gerhard et al., 2015b). Certainly, we can approximate $u$ up to the level $m = \mathscr{M}$ by a multi-scaling function expansion as described in Eq. (3.24). Namely,

$$\begin{aligned} P_{\mathscr{M}}^p u(x,t) &= \sum_{j=0}^{N_K-1} \sum_{\ell=1}^{r} s_{(\mathscr{M},j)}^\ell(t)\, \phi_{(\mathscr{M},j)}^\ell(x) \\ &= \sqrt{\tfrac{2}{h_K}} \sum_{j=0}^{N_K-1} \sum_{\ell=1}^{r} s_{(\mathscr{M},j)}^\ell(t)\, \phi^\ell\left(\tfrac{2(x-x_c)}{h_K}\right). \end{aligned} \tag{4.3}$$

where $\phi_{(\mathscr{M},j)}^\ell$ is given by Eq. (3.29), and $r$ is the multiplicity of the multiresolution approach. We observe that the single-scale decomposition differs from the DG representation only by a scaling term. Hence, by comparing Eq. (4.2) to Eq. (4.3) and assuming $r = N_p$, the relation between the DG coefficients and the single-scale coefficients is given by

$$s_{(\mathscr{M},j)}^\ell(t) = 2^{-\mathscr{M}/2} U_{(\mathscr{M},j)}^\ell(t). \tag{4.4}$$

The result above enables us to represent the DG solution in the form of a single-scale decomposition. This is possible due to the fact that the DG basis and the multi-scaling functions both use Legendre polynomials, only set

apart by a scaling term. Moreover, as discussed in Chapter 3, the single-scale decomposition in Eq. (4.3) can be hierarchically divided into a cascade of multiwavelet subspaces plus a baseline multi-scaling function subspace corresponding to the lowest resolution level. Consequently, by putting together Eq. (4.2) with Eq. (4.4), we obtain the multiscale decomposition of the approximate solution $u_h$. Namely:

$$u_h = \sum_{\ell=1}^{r} \left( s^{\ell}_{(0,0)}\, \phi^{\ell}_{(0,0)} + \sum_{i=0}^{\mathscr{M}-1} \sum_{j=0}^{N_K-1} d^{\ell}_{(i,j)}\, \psi^{\ell}_{(i,j)} \right), \quad \text{with } r = N_p\,, \tag{4.5}$$

where

$$s^{\ell}_{(m,j)} = \left\langle u_h,\, \phi^{\ell}_{(m,j)} \right\rangle_{K_{(m,j)}}, \qquad d^{\ell}_{(m,j)} = \left\langle u_h,\, \psi^{\ell}_{(m,j)} \right\rangle_{K_{(m,j)}}, \tag{4.6}$$

are the multi-scaling function and multiwavelet coefficients, respectively. We have already described them in Eq. (3.14) and Eq. (3.17) from Chapter 3. However, it is worth mentioning that we do not need to calculate the inner product $\langle\ \rangle$ to compute every coefficient of the hierarchy. Instead, these coefficients can be computed efficiently using the so-called *quadrature mirror filter* (QMF) coefficients, which in turn are borrowed from filter theory (Smith and Barnwell, 1986). The QMF coefficients associated with Alpert's multiwavelets are described in detail in the work of Geronimo et al. (2017). In this regard, we define the *lowpass* QMF coefficient matrices $H^{(0)}_{\ell k}$ and $H^{(1)}_{\ell k}$ as follows

$$H^{(0)}_{\ell k} = \left\langle \phi^{\ell}_{(m-1,j)},\, \phi^{k}_{(m,2j)} \right\rangle_{K_{(m-1,j)}}, \quad H^{(1)}_{\ell k} = \left\langle \phi^{\ell}_{(m-1,j)},\, \phi^{k}_{(m,2j+1)} \right\rangle_{K_{(m-1,j)}}. \tag{4.7}$$

with $\ell, k = 1, ..., r$. Similarly, the *highpass* QMF coefficient matrices $G^{(0)}_{\ell k}$ and $G^{(1)}_{\ell k}$ take the form

$$G^{(0)}_{\ell k} = \left\langle \psi^{\ell}_{(m-1,j)},\, \phi^{k}_{(m,2j)} \right\rangle_{K_{(m-1,j)}}, \quad G^{(1)}_{\ell k} = \left\langle \psi^{\ell}_{(m-1,j)},\, \phi^{k}_{(m,2j+1)} \right\rangle_{K_{(m-1,j)}}. \tag{4.8}$$

Despite the presence of the pair $(m, j)$, the QMF coefficients do not depend on the resolution level $m$ or element $j$ (Vuik, 2017). Knowing that

$$K_{(m-1,j)} = K_{(m,2j)} \cup K_{(m,2j+1)}\,, \tag{4.9}$$

the coefficients measure $\phi, \psi$ at element $K_{(m-1,j)}$ in terms of $\phi$ at $K_{(m,2j)}$ and $K_{(m,2j+1)}$. Due to the nature of the dilation and translation properties, Eq. (3.9) and Eq. (3.10), this measurement remains constant independently of $m$ and $j$. Therefore, the QMF coefficients only depend on the multiplicity $r$ used. Tabulated values for the QMF coefficients up to $r = 10$ can be found in (Geronimo et al., 2017). With this in mind, the multi-scaling functions and multiwavelets between two consecutive levels can be expressed as

$$\phi^{\ell}_{(m-1,j)} = \sum_{k=1}^{r} \left( H^{(0)}_{\ell k} \phi^{k}_{(m,2j)} + H^{(1)}_{\ell k} \phi^{k}_{(m,2j+1)} \right), \qquad m = 1, ..., \mathscr{M}; \tag{4.10a}$$

$$\psi^{\ell}_{(m-1,j)} = \sum_{k=1}^{r} \left( G^{(0)}_{\ell k} \phi^{k}_{(m,2j)} + G^{(1)}_{\ell k} \phi^{k}_{(m,2j+1)} \right), \qquad j = 0, ..., 2^{(m-1)} - 1\,. \tag{4.10b}$$

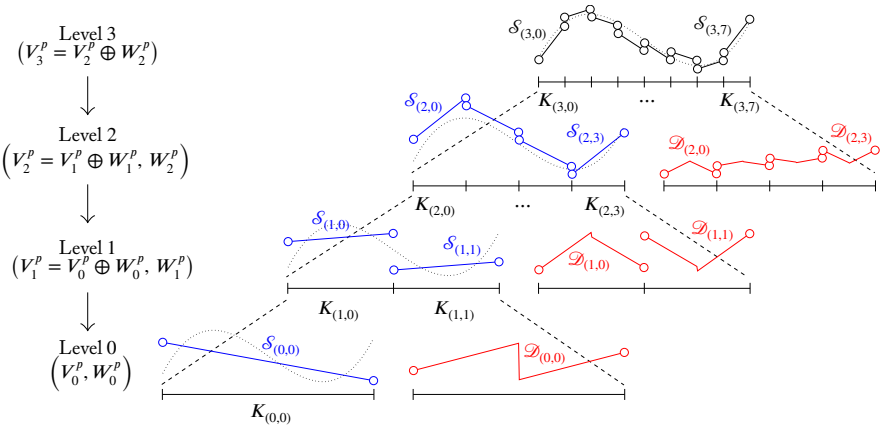


*Figure* 4.1: 1-D four-level multiscale representation by multiwavelets of second order DG solution $u_h$. We use the nomenclature $\mathcal{S}_{(m,j)} = \sum_\ell s^\ell_{(m,j)} \phi^\ell_{(m,j)}$ (single-scale) and $\mathcal{D}_{(m,j)} = \sum_\ell d^\ell_{(m,j)} \psi^\ell_{(m,j)}$ (multiscale). The highest resolution level is $\mathscr{M} = 3$ and $u_h = \sum_j \mathcal{S}_{(\mathscr{M},j)}$.

with $\ell = 1, ..., r$. Similarly, by application of Eq. (4.6) plus the linearity of the inner product, the multi-scaling function and multiwavelet coefficients between two consecutive levels are given by:

$$s^\ell_{(m-1,j)} = \sum_{k=1}^{r} \left( H^{(0)}_{\ell k} s^k_{(m,2j)} + H^{(1)}_{\ell k} s^k_{(m,2j+1)} \right), \tag{4.11a}$$

$$d^\ell_{(m-1,j)} = \sum_{k=1}^{r} \left( G^{(0)}_{\ell k} s^k_{(m,2j)} + G^{(1)}_{\ell k} s^k_{(m,2j+1)} \right). \tag{4.11b}$$

Coarser scales of the solution can be obtained by the successive application of Eq. (4.11a). Furthermore, the multiwavelet coefficients between scales are given by Eq. (4.11b). Figure 4.1 shows the multiscale representation for a second order DG solution. Effectively, the multiscale decomposition divides the single-scale coefficients $s^\ell_{(\mathscr{M},j)}$ into a smaller group of coefficients $s^\ell_{(0,0)}$ and $(\mathscr{M} - 1)$ blocks of multiwavelet or detail coefficients $d^\ell_{(m,j)}$. The former is a coarse approximation of the original solution and the latter carries the information between scales. This multiscale information represent the individual characteristics of the solution in a hierarchy of ascending resolution.

### 4.1.2 *Two-dimensional configuration*

In the 2-D context, the relation between the DG coefficients and the single-scale coefficients is equivalent to Eq. (4.4), and is now given by

$$\boldsymbol{s}^\ell_{(\mathscr{M},j)} = 2^{-\mathscr{M}} \boldsymbol{U}^\ell_{(\mathscr{M},j)}. \tag{4.12}$$

The multiscale decomposition of the DG solution presented in Eq. (4.5) can be generalized to

$$\boldsymbol{u}_h = \sum_{\ell=1}^{r^2} \left( s^\ell_{(0,0)} \boldsymbol{\Phi}^\ell_{(0,0)} + \sum_{i=0}^{\mathscr{M}-1} \sum_{j=0}^{N_K^2-1} \left[ \boldsymbol{d}^{\ell,\alpha}_{(i,j)} \boldsymbol{\Psi}^{\ell,\alpha}_{(i,j)} + \boldsymbol{d}^{\ell,\beta}_{(i,j)} \boldsymbol{\Psi}^{\ell,\beta}_{(i,j)} + \boldsymbol{d}^{\ell,\gamma}_{(i,j)} \boldsymbol{\Psi}^{\ell,\gamma}_{(i,j)} \right] \right), \tag{4.13}$$

where the three multiwavelet contributions $\alpha, \beta$ and $\gamma$ were previously explained in Eq. (3.39). Figure 4.2 features the multiscale representation of a 2-D second order DG solution. The coefficients can be explicitly computed

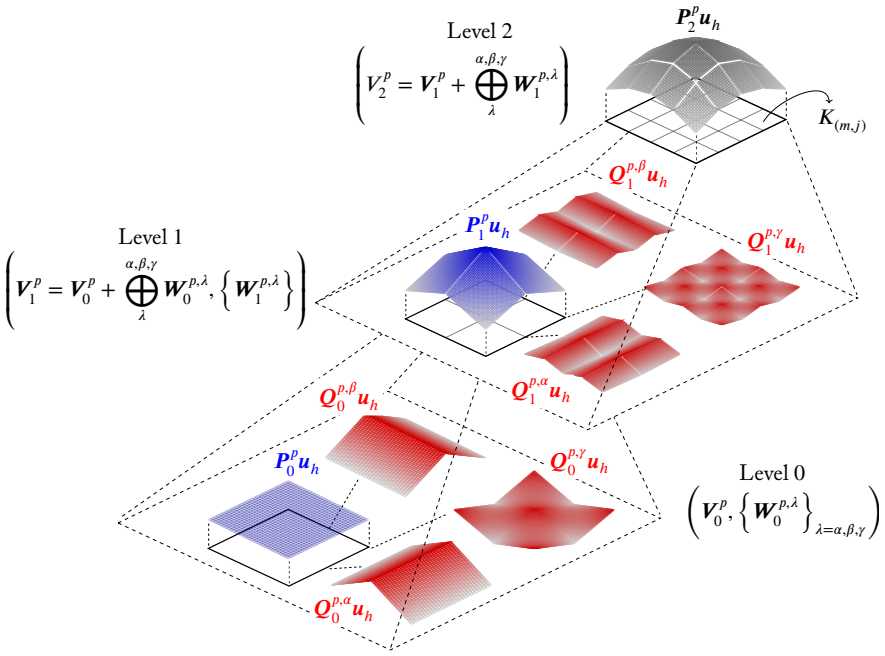


*Figure 4.2:* 2-D three-level multiscale representation by multiwavelets of second order DG solution $\boldsymbol{u}_h$. The terms $\boldsymbol{P}_m^p \boldsymbol{u}_h$ and $\boldsymbol{Q}_m^{p,\lambda} \boldsymbol{u}_h$ refer to the orthogonal projection onto $\boldsymbol{V}_m^p$ and $\boldsymbol{W}_m^{p,\lambda}$, as defined by Eq. (3.40) and Eq. (3.41), respectively. The highest resolution level is $\mathscr{M} = 2$. At that level we have $\boldsymbol{u}_h = \boldsymbol{P}_{\mathscr{M}}^p \boldsymbol{u}_h$.

as follows:

$$\boldsymbol{s}_{(m,j)}^{\ell} = \left\langle \boldsymbol{u}_h, \boldsymbol{\Phi}_{(m,j)}^{\ell} \right\rangle_{K_{(m,j)}}, \qquad \boldsymbol{d}_{(m,j)}^{\ell,\alpha} = \left\langle \boldsymbol{u}_h, \boldsymbol{\Psi}_{(m,j)}^{\ell,\alpha} \right\rangle_{K_{(m,j)}}, \tag{4.14a}$$

$$\boldsymbol{d}_{(m,j)}^{\ell,\beta} = \left\langle \boldsymbol{u}_h, \boldsymbol{\Psi}_{(m,j)}^{\ell,\beta} \right\rangle_{K_{(m,j)}}, \qquad \boldsymbol{d}_{(m,j)}^{\ell,\gamma} = \left\langle \boldsymbol{u}_h, \boldsymbol{\Psi}_{(m,j)}^{\ell,\gamma} \right\rangle_{K_{(m,j)}}. \tag{4.14b}$$

Similarly to the 1-D study, we apply the QMF coefficients presented in the work of Geronimo et al. (2017), and earlier described in Eq. (4.7) to Eq. (4.8). In this case, the relation between elements of two consecutive levels given by Eq. (4.9) becomes

$$K_{(m-1,j)} = \bigcup_{\bar{j}_x,\bar{j}_y=0}^{1} K_{(m,2j+\bar{j})}, \qquad \bar{j} = 2\bar{j}_x + \bar{j}_y, \quad j = N'_K j_x + j_y, \tag{4.15}$$

where $j_x, j_y = 0, ..., N'_K - 1$ with $N'_K = 2^{(m-1)}$. Figure 4.3 shows how the elements of two successive levels are related. Consequently, the lower-lever single-scale coefficients and the multiwavelet coefficients for each component

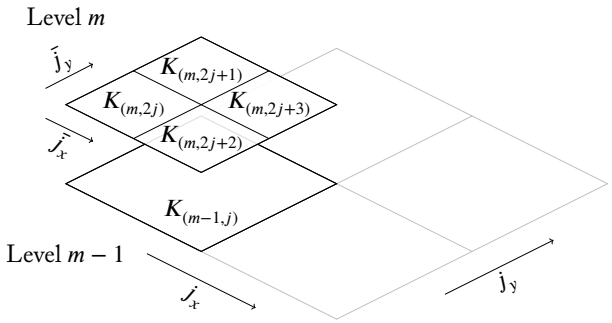


*Figure 4.3:* Relation between the elements of two consecutive multiresolution levels. Four elements at level $m$ contribute to one element at level $m-1$.

$\alpha, \beta$ and $\gamma$ can be calculated efficiently as follows:

$$\boldsymbol{s}^{\ell}_{(m-1,j)} = \sum_{\bar{j}_x,\bar{j}_y=0}^{1} \sum_{k_x,k_y=1}^{r} \left[ H^{(\bar{j}_x)}_{\ell_x,k_x} H^{(\bar{j}_y)}_{\ell_y,k_y} \boldsymbol{s}^{k}_{(m,2j+\bar{j})} \right], \quad m = 1, ..., \mathscr{M}; \tag{4.16a}$$

$$\boldsymbol{d}^{\ell,\alpha}_{(m-1,j)} = \sum_{\bar{j}_x,\bar{j}_y=0}^{1} \sum_{k_x,k_y=1}^{r} \left[ G^{(\bar{j}_x)}_{\ell_x,k_x} H^{(\bar{j}_y)}_{\ell_y,k_y} \boldsymbol{s}^{k}_{(m,2j+\bar{j})} \right], \quad k = r(k_x - 1) + k_y, \tag{4.16b}$$

$$\boldsymbol{d}^{\ell,\beta}_{(m-1,j)} = \sum_{\bar{j}_x,\bar{j}_y=0}^{1} \sum_{k_x,k_y=1}^{r} \left[ H^{(\bar{j}_x)}_{\ell_x,k_x} G^{(\bar{j}_y)}_{\ell_y,k_y} \boldsymbol{s}^{k}_{(m,2j+\bar{j})} \right], \tag{4.16c}$$

$$\boldsymbol{d}^{\ell,\gamma}_{(m-1,j)} = \sum_{\bar{j}_x,\bar{j}_y=0}^{1} \sum_{k_x,k_y=1}^{r} \left[ G^{(\bar{j}_x)}_{\ell_x,k_x} G^{(\bar{j}_y)}_{\ell_y,k_y} \boldsymbol{s}^{k}_{(m,2j+\bar{j})} \right], \tag{4.16d}$$

The index $\bar{j}$ is inherited from Eq. (4.15) and accounts for the fact that one coefficient at level $m-1$ results from the contribution of four coefficients at level $m$.

## 4.2 PROSPECTS OF MULTIRESOLUTION AND DGM

### 4.2.1 *Global coupling and mesh adaptation*

Hovhannisyan et al. (2014) have presented one of the first studies on multiresolution-based grid adaptation formulated on multiwavelets. In that work and in the research that followed by Gerhard et al. (2015a,b) and Gerhard and Müller (2016), the numerical solution is simply represented as data on some coarse level plus multiwavelet coefficients which embody the individual features of the solution (see Section 4.1). Thresholding of these detail coefficients then drives the adaptation process, i.e. each multiwavelet coefficient is related to an element in the MRA cascade and nullifying a coefficient is thus analogous to removing its associated element. Therefore, the more cancelled details, the smaller the number of DOFs in the adapted grid.

In the work presented by Vuik and Ryan (2014, 2016) and Vuik (2017), the same concept of MRA cascading is studied to develop a multiwavelet troubled-cell indicator to identify elements in the vicinity of a shock. However, unlike the work of Hovhannisyan et al. (2014), in which the entirety of the MRA levels are considered, here the authors base their indicator on the multiwavelet contribution from a single level (specifically, the level $\mathscr{M} - 1$, which is the second to finest) of the MRA decomposition.

When applying the MRA-based grid adaptation, the relation between the elements in the physical domain and the intervals in the multiwavelet decomposition is bijective, which means that we have a one-to-one correspondence, as described by Eq. (4.1). This fact makes the adaptive procedure reliant on the nature of the multiwavelets. To be able to use the dilation and translation properties of the multiwavelets, as presented by Eq. (3.29) and Eq. (3.30), a sequence of nested dyadic grids is thus required. Certainly, the work of

Hovhannisyan et al. (2014) in the 1-D context, and the later extension to 2-D by Gerhard and Müller (2016), only employ grids which satisfy this condition. Moreover, their starting grid (MRA approximation of the reference grid) must have enough resolution as to capture the relevant features of the solution. This is equivalent to starting from an accurate reference solution, which may not always be available.

On the other hand, in non-Cartesian grids, dilation and translation are no longer available and multiwavelets must be calculated separately for each level and interval of the decomposition. This represents an important constraint which increases the cost of the computation. To minimize this limitation, Gerhard (2017) developed the *wavelet-free* approach, which extends the MRA to non-uniform grid hierarchies. Additionally, due to the duality physical-domain/multiwavelet-domain decomposition, further difficulties as regards parallelisation may arise.

### 4.2.2 *Local coupling: a new path to adaptation*

As an alternative to the concept of MRA-based grid adaptation, in this work we aim at developing an adaptation algorithm that starts from a coarse solution and proceed with the refinement where required, with no initial reference grid involved. Traditionally, to deal with this problem, *a posteriori* error estimators have been used to drive the adaptation, which are computed from the discrete solution and try to measure the error of the adaptive solution. Examples of these indicators can be found in the work of Mavriplis (1994), Mitchell and McClain (2014), Bey and Oden (1996), and Adjerid et al. (2002). They will be explored in detail later in Chapter 5.

Here we propose a method which locally confines the MRA decomposition to the element. More specifically, an independent multiwavelet decomposition is performed locally for every element of the physical domain. We call our approach *local multiresolution*. This is a departure from the MRA-based grid adaptation approach, which is characterized by a *global multiresolution* covering the entire domain. In contrast with this global approach, local multiresolution may be extended to non-structured stretched Cartesian grids, in which elements of equal refinement level do not necessarily have the same size, which allows for anisotropic refinement. Additionally, dealing with each element independently simplifies its use for local *hp*-adaptation in the context of DGMs. Finally, the excellent parallel properties of DGMs can be perfectly exploited thanks to the local character of the error estimator.

Figure 4.4 outlines the two approaches described above. The global MRA, Figure 4.4A, produces multiple levels of information thanks to the highly detailed approximate solution $u_h^{\text{ref}}$ at level $\mathscr{M}$. On the other hand, the local MRA, Figure 4.4B, does not require such a solution. Instead, our target is to sufficiently resemble its behavior by providing extra information (*enriching*). To achieve this, we manufacture a more accurate approximation for each element $K$ separately. Then a subsequent MRA is applied locally, producing a two-level multiscale representation within the element. In particular, we

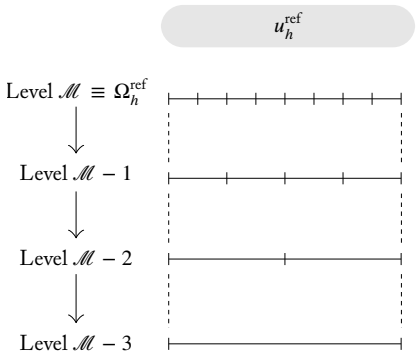


*(a)* Global multiresolution, representative of (Hovhannisyan et al., 2014). It requires $u_h^{\text{ref}}$ to be the initial solution calculated on a MRA approximation of the reference grid, $\Omega_h^{\text{ref}}$. Multiscale decomposition spans the entire domain.

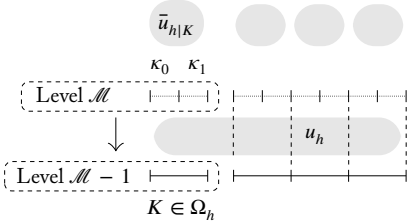


*(b)* Local multiresolution. The initial solution $u_{h|K}$ is enriched locally to $\bar{u}_{h|K}$. Then it is subjected to a two-level multiscale decomposition.

*Figure 4.4:* Different approaches to couple multiresolution analysis and discontinuous Galerkin methods.

are interested in the multiwavelet part of the multiscale representation. Indeed, multiwavelet coefficients can be interpreted as messengers of individual features of the approximation (Hovhannisyan et al., 2014). Thanks to this property multiwavelets represent an excellent candidate to measure the discretization error, which can be used later to drive *hp*-adaptation.

In the following sections we describe in detail each of the aforementioned steps, starting with the procedure to manufacture a new local enriched approximation from the existing DG solution.

## 4.3 LOCAL RECONSTRUCTION OF DG SOLUTION

We intend to reach an analogue to the highly detailed approximate solution $u_h^{\text{ref}}$ from which Hovhannisyan et al. (2014) and Gerhard and Müller (2016) start their global MRA, as illustrated in Figure 4.4A, but at a lower cost. The idea being that we can use that analogue later as a launchpad to start our local MRA, as represented in Figure 4.4B.

To build the analogue we turn to the work of Dolejší and Solin (2016). In their research, the authors assemble a high-order reconstruction of a DG solution. They then measure the new reconstruction against the original solution to guide an *hp*-adaptation process. By observing that the discretization error, $e_h = u - u_h$, and its approximation by the higher-order reconstruction, $\mathscr{E}_h = \tilde{u}_h - u_h$, have similar element-wise distribution, $e_h \approx \mathscr{E}_h$, they verify numerically that the reconstruction approximates better the exact solution than the original. Inspired by this idea, we build a more accurate local approximation $\bar{u}_{h|K}$ by considering the contribution of the current element $K$ and its neighbours. This procedure will be presented first in the 1-D setup. The extension to higher dimensions will be described later.

We define the support of $\bar{u}_{h|K}$ according to the two-level multiscale representation of element $K$, as shown in Figure 4.4B. In this context, we have

$$\operatorname{supp}\left(\bar{u}_{h|K}\right) = \bigcup_{i=0}^{N_{\text{art}}-1} \kappa_i\,, \qquad \text{with } N_{\text{art}} = 2, \tag{4.17}$$

where the *artificial* sub-elements $\kappa_i$ would originate from the twofold isotropic subdivision of element $K$. The new approximation $\bar{u}_{h|K}$ is then described by $N_{\text{art}}$ piecewise polynomial functions. Namely:

$$\bar{u}_{h|K} = \sum_i \bar{u}_{h,i}\,, \qquad \bar{u}_{h,i} \in \mathscr{P}^p(\kappa_i), \qquad i = 0, \dots, N_{\text{art}} - 1. \tag{4.18}$$

Note that the term *artificial* is employed to indicate $\kappa_i$. This is to emphasize the fact that no actual mesh subdivision actually occurs at this stage. In fact, our implementation associates $\bar{u}_{h|K}$ with the element $K$. However we believe that the definition of $\kappa_i$ may help the reader to better understand the procedure.

In order to assemble $\bar{u}_{h|K}$ we propose three different approaches depending on how data from neighboring elements are accounted for:

1. $\kappa$-*reconstruction*: $\bar{u}_{h|K}$ is built from the immediate neighbors of the sub-elements $\kappa_i$.
2. $K$-*reconstruction*: $\bar{u}_{h|K}$ is constructed from the immediate neighbors of the element $K$.
3. $\Gamma$-*reconstruction*: $\bar{u}_{h|K}$ is set up from the solution jumps at the faces of the sub-elements $\kappa_i$.

Figure 4.5 to 4.7 illustrate the three methods. The following sections 4.3.1 to 4.3.3 will describe the different procedures in detail.

### 4.3.1 $\kappa$-*reconstruction*

The construction of $\bar{u}_{h|K}$ is performed by a *least-square function approximation* from the block $\mathscr{A}_i$, defined as follows:

$$\mathscr{A}_i = \kappa_{1-i}^{(K+i-1)} \cup \kappa_i^{(K)} \cup \kappa_{1-i}^{(K+i)}, \qquad i = 0, \dots, N_{\text{art}} - 1, \tag{4.19}$$

where $N_{\text{art}} = 2$ and the superscript indicates from which $K \in \Omega_h$ the artificial sub-element $\kappa$ originates. Then we define the polynomial function $\overline{\mathscr{U}}_{h,i} \in \mathscr{P}^p(\mathscr{A}_i)$ by

$$\overline{\mathscr{U}}_{h,i}(x,t) = \sum_{\ell=1}^{N_p} \overline{X}_{\mathscr{A}_i}^{\ell}(t)\, \phi^{\ell}\big(\Xi_{\mathscr{A}_i}^{-1}(x)\big), \qquad \forall x \in \mathscr{A}_i, \quad N_p = p+1, \tag{4.20}$$

where $\overline{X}_{\mathscr{A}_i}^{\ell}$ are the unknown coefficients, and $\Xi_{\mathscr{A}_i}$ is the bijective transformation which relates the coordinates of the reference element to their counterparts in the physical block $\mathscr{A}_i$. The unknown coefficients are calculated by minimising the error in the least-square sense with respect to the original approximation $u_h$. Namely:

$$\overline{X}_{\mathscr{A}_i}^{\ell} = \arg\min \left\| u_{h|\kappa_i} - \overline{\mathscr{U}}_{h,i} \right\|_{L^2(\mathscr{A}_i)}^2. \tag{4.21}$$

Solving the optimization problem in Eq. (4.37), we obtain the linear algebraic system

$$A_{k,\ell}\, \overline{X}_{\mathscr{A}_i}^{\ell} = b^k, \tag{4.22}$$

where:

$$A_{k,\ell} = \sum_{\kappa \in \mathscr{A}_i} \left\langle \phi^k, \phi^{\ell} \right\rangle_{\kappa}, \quad b^k = \sum_{\kappa \in \mathscr{A}_i} \left\langle \phi^k, u_h \right\rangle_{\kappa}, \qquad k, \ell = 1, \dots, N_p\,. \tag{4.23}$$

Now the polynomial function $\overline{\mathscr{U}}_{h,i}$ is fully characterized within the block $\mathscr{A}_i$. Lastly, we restrict $\overline{\mathscr{U}}_{h,i}$ just to sub-element $\kappa_i^{(K)}$ and arrive to the piecewise polynomial function $\bar{u}_{h,i}$. Namely:

$$\bar{u}_{h,i} = \overline{\mathscr{U}}_{h,i|\kappa_i^{(K)}}, \qquad i = 0, \dots, N_{\text{art}} - 1. \tag{4.24}$$

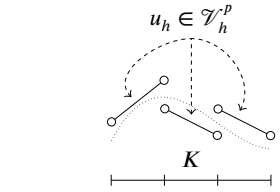


*(a)* Original solution $u_h$.

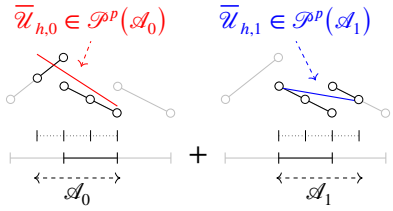


*(b)* Least-square function approximation $\overline{\mathscr{U}}_{h,i}$ from the block $\mathscr{A}_i$.

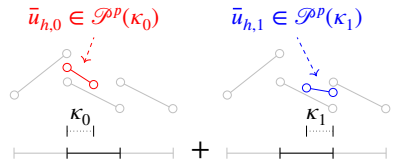


*(c)* Restriction of $\overline{\mathscr{U}}_{h,i}$ to artificial sub-element $\kappa_i$.

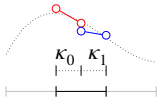


*(d)* Reconstructed piecewise polynomial function $\bar{u}_{h,i}$.

*Figure 4.5:* Chronological steps of the $\kappa$-*reconstruction* procedure for an element $K$.

The complete reconstruction procedure is featured in Figure 4.5.

### 4.3.2 *K-reconstruction*

The first steps in the assembly of $\bar{u}_{h|K}$ follow the same instructions described by Dolejší and Solin (2016). That is, we build a high-order polynomial reconstruction by a *least-square function approximation* from a block $\mathscr{A}_K$ defined as follows:

$$\mathscr{A}_K = K \cup \{K' \in \Omega_h \mid K' \text{ share at least a face with } K\}. \tag{4.25}$$

We then establish the higher-order polynomial $\overline{\mathscr{U}}_h \in \mathscr{P}^{p+1}(\mathscr{A}_K)$ by

$$\overline{\mathscr{U}}_h(x,t) = \sum_{\ell=1}^{N_p'} \overline{X}^{\ell}_{\mathscr{A}_K}(t)\, \phi^{\ell}\big(\Xi^{-1}_{\mathscr{A}_K}(x)\big), \qquad \forall x \in \mathscr{A}_K, \quad N_p' = p+2. \tag{4.26}$$

Their unknown coefficients $\overline{X}^{\ell}_{\mathscr{A}_K}$ are determined by solving the optimization problem presented in Eq. (4.37) and the following linear system on the new block $\mathscr{A}_K$. It is worth mentioning that the optimization problem is solved by using the $L^2$-norm, whereas Dolejší and Solin (2016) employ the $H^1$-norm. We have tested both norms and found very little difference in the final reconstruction. This justifies the use of the simpler and less costly $L^2$-norm in our work. Next we define the higher-order piecewise polynomial $\overline{w}_h \in \mathscr{P}^{p+1}(K)$ as the restriction of $\overline{\mathscr{U}}_h$ on $K$. Namely:

$$\overline{w}_h = \overline{\mathscr{U}}_{h|K}. \tag{4.27}$$

Once the higher-order approximation $\overline{w}_h$ is restricted to $K$, we move to set up $\bar{u}_{h|K}$ by using the information provided by this new approximation. If we recall the definition of $\bar{u}_{h|K}$, that is, Eq. (4.18):

$$\bar{u}_{h|K} = \sum_i \bar{u}_{h,i} = \sum_i \sum_{\ell=1}^{N_p} \overline{U}^{\ell}_{\kappa_i}\, \phi^{\ell}\big(\Xi^{-1}_{\kappa_i}(x)\big), \quad \forall x \in \kappa_i, \quad i = 0, \dots, N_{\text{art}} - 1. \tag{4.28}$$

In order to build $\bar{u}_{h|K}$ we use a $p$-degree *spline interpolation* on the artificial subelements $\kappa_i$. Therefore, we have $N_{\text{art}} N_p$ unknown coefficients $\overline{U}^{\ell}_{\kappa_i}$ to evaluate. The same numbers of conditions are required to evaluate the unknowns. We meet the conditions by projecting $\overline{w}_h$ on a set of $N_p$ *Gauss-Lobatto* integration points for each $\kappa_i$. Thus reaching $N_{\text{art}} N_p$ conditions for the same number of unknowns. This results in a linear system that solves for $\overline{U}^{\ell}_{\kappa_i}$.

Figure 4.6 shows the complete reconstruction procedure by illustrating graphically each of its steps.

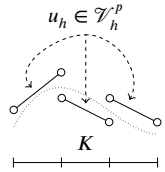


*(a)* Original solution $u_h$.

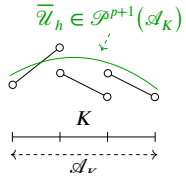


*(b)* High-order approximation $\overline{\mathscr{U}}_h$ from the block $\mathscr{A}_K$.

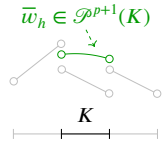


*(c)* Restriction of $\overline{\mathscr{U}}_{h,i}$ to $K$.

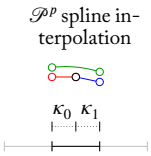


*(d)* Projecting $\overline{w}_h$ on $\kappa_i$.

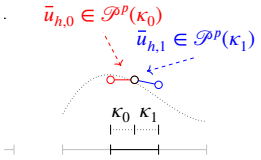


*(e)* Reconstructed piecewise polynomial function $\bar{u}_{h,i}$.

*Figure* 4.6*:* Sequential steps of the *K-reconstruction* method for an element $K$.

### 4.3.3 Γ-*reconstruction*

In the final method, $\bar{u}_{h|K}$ is built from a simpler *least-square function approximation* from the block $\mathscr{Z}_i$. The block is defined as

$$\mathscr{Z}_i = \kappa_i^{(K)} \cup \Gamma_i, \quad \text{where } \Gamma_i = \left\{ \partial\kappa_{1-i}^{(K-1+2i)} \cap \partial\kappa_i^{(K)} \right\}, \tag{4.29}$$

with $i = 0, \dots, N_{\text{art}} - 1$. Equation (4.29) is simply $\kappa_i$ plus the shared face of the nearest neighboring element, denoted by $\Gamma_i$. This means that this method integrates the solution jump between element $K$ and their neighbors $K-1$ and $K+1$ into $\bar{u}_{h|K}$. Similarly to the two earlier methods, we define the polynomial function $\overline{\mathscr{U}}_{h,i} \in \mathscr{P}^p(\mathscr{Z}_i)$ by

$$\overline{\mathscr{U}}_{h,i}(x,t) = \sum_{\ell=1}^{N_p} \overline{X}^{\ell}_{\mathscr{Z}_i}(t)\, \phi^{\ell}\left(\Xi^{-1}_{\mathscr{Z}_i}(x)\right), \qquad \forall x \in \mathscr{Z}_i, \quad N_p = p+1, \tag{4.30}$$

where the coefficients $\overline{X}^{\ell}_{\mathscr{Z}_i}$ are calculated by solving Eq. (4.37) on the new block $\mathscr{Z}_i$. The resulting linear system can be expressed as

$$A_{k,\ell}\, \overline{X}^{\ell}_{\mathscr{Z}_i} = b^k, \tag{4.31}$$

where

$$A_{k,\ell} = \left[\phi^k \phi^{\ell}\right]_{\Gamma_i} + \left\langle \phi^k, \phi^{\ell} \right\rangle_{\kappa_i}, \qquad b^k = \left[\phi^k u_h\right]_{\Gamma_i} + \left\langle \phi^k, u_h \right\rangle_{\kappa_i}, \tag{4.32}$$

with $k, \ell = 1, \dots, N_p$ and the operator $[\cdot]_{\Gamma_i}$ referring to the values at the shared face $\Gamma_i$. Finally, we define $\bar{u}_{h,i}$ by restricting $\overline{\mathscr{U}}_{h,i}$ just to the sub-element $\kappa_i^{(K)}$, in the same way as Eq. (4.24).

A detailed diagram of the reconstruction procedure is displayed in Figure 4.7.

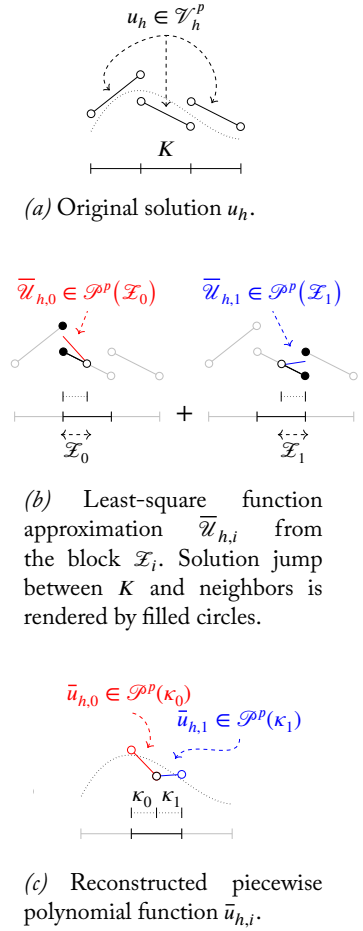


*(a)* Original solution $u_h$.

*(b)* Least-square function approximation $\overline{\mathscr{U}}_{h,i}$ from the block $\mathscr{Z}_i$. Solution jump between $K$ and neighbors is rendered by filled circles.

*(c)* Reconstructed piecewise polynomial function $\bar{u}_{h,i}$.

*Figure 4.7:* Chronological steps of the Γ-*reconstruction* procedure for an element $K$.

### 4.3.4 *Two-dimensional reconstruction*

In the case of a 2-D reconstruction we define the support of the new enriched approximation $\bar{\boldsymbol{u}}_{h|K}$ as follows:

$$\text{supp}\left(\bar{\boldsymbol{u}}_{h|K}\right) = \bigcup_{i=0}^{N_{\text{art}}-1} \kappa_i, \quad \text{with } N_{\text{art}} = 4, \tag{4.33}$$

where $\kappa_i$ represent the artificial sub-elements from the 2-D isotropic subdivision of element $K$. The term *artificial* retains the same meaning as described in the 1-D reconstruction. Similarly, $\bar{\boldsymbol{u}}_{h|K}$ is composed of $N_{\text{art}}$ piecewise polynomial functions. That is:

$$\bar{\boldsymbol{u}}_{h|K} = \sum_i \bar{\boldsymbol{u}}_{h,i}, \quad \text{with } \bar{\boldsymbol{u}}_{h,i} \in \mathscr{P}^p(\kappa_i), \qquad i = 0, \dots, N_{\text{art}} - 1. \tag{4.34}$$

Of the three reconstructions approaches proposed in the previous 1-D setting, only the $\kappa$*−reconstruction* method (see Section 4.3.1) will extended to

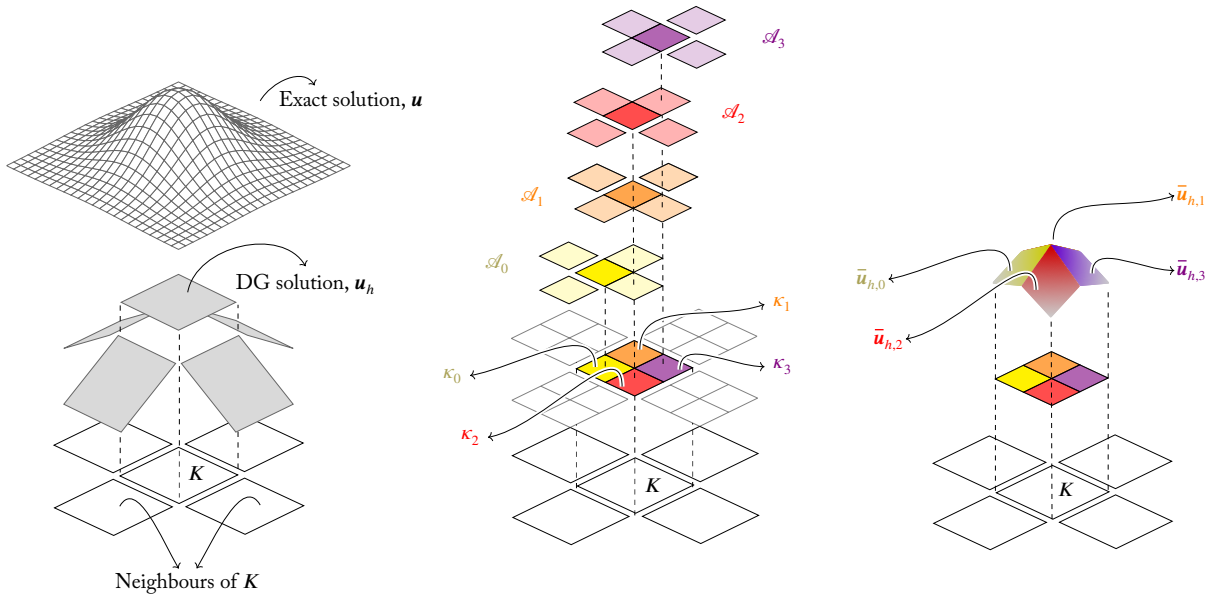


*(a)* Original solution $\boldsymbol{u}_h$.

*(b)* 2-D isotropic subdivision of element $K$ resulting in artificial sub-elements $\kappa_i$. Each of $\kappa_i$ and its immediate neighbors build the block $\mathscr{A}_i$.

*(c)* A least-square approximation is applied to every block $\mathscr{A}_i$ to obtain $\overline{\boldsymbol{\mathcal{U}}}_{h,i}$. The enriched solution $\bar{\boldsymbol{u}}_{h,i}$ results from restricting $\overline{\boldsymbol{\mathcal{U}}}_{h,i}$ to $\kappa_i$.

*Figure* 4.8*:* Chronological steps (left to right) of the 2-D reconstruction procedure for an element $K$.

the 2-D context. If we recall this method, the new approximation $\bar{\boldsymbol{u}}_{h|K}$ is set up by considering the immediate neighbors of sub-elements $\kappa_i$. This is performed by a *least-square function approximation* applied to the block $\mathscr{A}_i$, which is characterized by

$$\mathscr{A}_i = \bigcup_{e \in \partial\kappa_i} \left\{\kappa^+ \cup \kappa^-\right\}^e, \qquad i = 0, \dots, N_{\text{art}} - 1, \tag{4.35}$$

where $e \in \partial\kappa_i$ represent the individual faces of $\kappa_i$. The next step is to define the polynomial function $\overline{\boldsymbol{\mathcal{U}}}_{h,i} \in \mathscr{P}^p(\mathscr{A}_i)$ by

$$\overline{\boldsymbol{\mathcal{U}}}_{h,i}(\boldsymbol{x}, t) = \sum_{\ell=1}^{N_p} \overline{\boldsymbol{X}}^{\ell}_{\mathscr{A}_i}(t)\, \phi^{\ell}\big(\Xi^{-1}_{\mathscr{A}_i}(\boldsymbol{x})\big), \quad \forall \boldsymbol{x} \in \mathscr{A}_i, \quad N_p = (p+1)^2, \tag{4.36}$$

where $\overline{\boldsymbol{X}}^{\ell}_{\mathscr{A}_i}$ are the coefficients to be calculated. Similarly to 1-D, the idea is to find which value of the coefficients minimize the difference between the original $\boldsymbol{u}_h$ and the new approximation $\overline{\boldsymbol{\mathcal{U}}}_{h,i}$. That is:

$$\overline{\boldsymbol{X}}^{\ell}_{\mathscr{A}_i} = \arg\min \left\| \boldsymbol{u}_{h|\kappa_i} - \overline{\boldsymbol{\mathcal{U}}}_{h,i} \right\|^2_{L^2(\mathscr{A}_i)}, \tag{4.37}$$

which leads to the linear system

$$\boldsymbol{A}_{k,\ell}\, \overline{\boldsymbol{X}}^{\ell}_{\mathscr{A}_i} = \boldsymbol{b}^k, \quad \boldsymbol{A}_{k,\ell} = \sum_{\kappa \in \mathscr{A}_i} \left\langle \phi^k, \phi^{\ell} \right\rangle_{\kappa}, \quad \boldsymbol{b}^k = \sum_{\kappa \in \mathscr{A}_i} \left\langle \phi^k, \boldsymbol{u}_h \right\rangle_{\kappa}, \tag{4.38}$$

with $k, \ell = 1, \dots, N_p$. By solving the above system for $\overline{\boldsymbol{X}}^{\ell}_{\mathscr{A}_i}$ we have completely defined $\overline{\boldsymbol{\mathcal{U}}}_{h,i}$ within the block $\mathscr{A}_i$. Finally, $\bar{\boldsymbol{u}}_{h,i}$ is evaluated by restricting $\overline{\boldsymbol{\mathcal{U}}}_{h,i}$ just to sub-element $\kappa_i$. Namely:

$$\bar{\boldsymbol{u}}_{h,i} = \overline{\boldsymbol{\mathcal{U}}}_{h,i}\big|_{\kappa_i}, \qquad i = 0, \dots, N_{\text{art}} - 1. \tag{4.39}$$

A detailed description of the reconstruction approach is shown in Figure 4.8.

## 4.4 LOCAL MULTIRESOLUTION OF NEW RECONSTRUCTION

### 4.4.1 *One-dimensional multiwavelet decomposition*

The reconstruction methods presented in Section 4.3 allow us to assemble a new, more accurate approximation $\bar{u}_{h|K}$ to the exact solution than the original approximation $u_{h|K}$. This new approximation becomes the starting point of the local multiresolution method, as previously shown in Figure 4.4B. By means of the local MRA we are able to perform an independent two-level multiscale decomposition of $\bar{u}_{h|K}$ for every element $K \in \Omega_h$.

To proceed with the local MRA we remind the reader the procedure to connect the DGM and multiwavelets, as expressed by Eq. (4.4) and Eq. (4.12) in the one- and two-dimensional context, respectively. Although the 1-D context has been illustrated in detail in Figure 4.1, this previous development is associated with the global multiresolution approach proposed by Hovhannisyan et al. (2014) and Gerhard and Müller (2016), as the entire domain of the solution undergoes one unique multiscale decomposition. This approach can be visualized in Figure 4.4A. To adapt the development to our new element-wise MRA we must consider every $K \in \Omega_h$ as harboring one independent multiscale decomposition of $\bar{u}_{h|K}$. Consequently, for the 1-D local MRA we have the element-wise coupling expressed as

$$\bar{s}^{\ell}_{(\mathscr{M},j)} = 2^{-\mathscr{M}/2}\, \overline{U}^{\ell}_{(\mathscr{M},j)}, \qquad \ell = 1, ..., r; \quad j = 0, ..., 2^{\mathscr{M}-1}, \tag{4.40}$$

where $\overline{U}^{\ell}_{(\mathscr{M},j)}$ are the coefficients of $\bar{u}_{h|K}$ as calculated by one of the three reconstruction methods discussed in Section 4.3, and $\mathscr{M}$ represents the highest level of resolution within element $K$. Additionally, we consider that $r = N_p$, with $N_p = p + 1$. By nature of the two-level multiscale decomposition of $\bar{u}_{h|K}$, $\mathscr{M} = 1$ and we can further simplify Eq. (4.40) to

$$\bar{s}^{\ell}_{(1,j)} = \tfrac{1}{\sqrt{2}} \overline{U}^{\ell}_{(1,j)}, \qquad j = 0, 1; \tag{4.41}$$

where the indices $i = j = 0, 1$ coincide with the numbering of the artificial sub-elements $\kappa_i$ defined in Eq. (4.17). Therefore, we can establish a relation between the *multiwavelet nomenclature* of Eq. (4.41) and the *reconstruction terminology* of Eq. (4.17) and Eq. (4.18). Namely:

$$\bar{s}^{\ell}_{\kappa_i} = \tfrac{1}{\sqrt{2}} \overline{U}^{\ell}_{\kappa_i}, \qquad i = 0, \dots, N_{\text{art}} - 1; \tag{4.42}$$

with $N_{\text{art}} = 2$ in the current 1-D setting. We have linked the coefficients of the new enriched approximation, $\overline{U}^{\ell}_{\kappa_i}$, to the single-scale coefficients, $\bar{s}^{\ell}_{\kappa_i}$. The remaining lower-level single-scale and multiwavelet coefficients can be obtained by applying the QMF coefficients (Geronimo et al., 2017) (see Eq. (4.11)). They are rewritten as follows

$$\bar{s}^{\ell}_{K} = \sum_{k=1}^{r} \sum_{i=0}^{N_{\text{art}}-1} H^{(i)}_{\ell k} \bar{s}^{k}_{\kappa_i}, \qquad \ell = 1, ..., r; \tag{4.43a}$$

$$\overline{d}^{\ell}_{K} = \sum_{k=1}^{r} \sum_{i=0}^{N_{\text{art}}-1} G^{(i)}_{\ell k} \bar{s}^{k}_{\kappa_i}. \tag{4.43b}$$

We observe that the multiscale representation naturally connects the coefficients of the artificial sub-elements $\kappa_i$ to the coefficients of element $K$. Finally, the multiscale representation of $\bar{u}_{h|K}$ can now be expressed by Eq. (4.5) as a combination of single-scale functions and multiwavelets:

$$\bar{u}_{h|K} = \overline{\mathcal{S}}_K + \overline{\mathcal{D}}_K = \sum_{\ell=1}^{r} \left( \bar{s}^{\ell}_{K} \phi^{\ell} + \overline{d}^{\ell}_{K} \psi^{\ell} \right), \qquad K \in \Omega_h, \tag{4.44}$$

with $r = N_p$. We are particularly interested in how the multiscale information is carried by the multiwavelet contribution, $\overline{\mathcal{D}}_K$. This contribution carries the individual features of the new approximation $\bar{u}_{h|K}$ and, by extension, it becomes an instrument to measure the behavior of the original DG solution $u_{h|K}$. In this manner, in regions where the solution is regular $\overline{\mathcal{D}}_K$ would report minor or negligible values, whereas regions that harbour discontinuities would translate into $\overline{\mathcal{D}}_K$ reaching significant values. Certainly, the works of Shelton (2008) and Hovhannisyan et al. (2014) have capitalized on the multiwavelet contribution along a hierarchy of multiple levels to perform grid adaptation.

### 4.4.2 *Two-dimensional multiwavelet decomposition*

In the 2-D setting, Eq. (4.42) becomes

$$\bar{\boldsymbol{s}}^{\ell}_{\kappa_i} = \tfrac{1}{2} \overline{\boldsymbol{U}}^{\ell}_{\kappa_i}, \qquad \ell = 1, ..., r^2; \quad i = 0, \dots, N_{\text{art}} - 1; \tag{4.45}$$

where $r = N_p = (p+1)$ and $N_{\text{art}} = 4$. As a reminder, the artificial sub-elements $\kappa_i$ originate from element $K$ (see Figure 4.8), and they have been previously defined in Eq. (4.33). The QMF coefficients (Geronimo et al., 2017) described in Eq. (4.43) can be applied to calculate the single-scale coefficients and multiwavelet coefficients along the $x$-,$y$- and $xy$-directions (Vuik and Ryan, 2014). They read:

$$\bar{\boldsymbol{s}}^{\ell}_{K} = \sum_{i_x, i_y=0}^{1} \sum_{k_x, k_y=1}^{r} \left[ H^{(i_x)}_{\ell_x, k_x} H^{(i_y)}_{\ell_y, k_y} \bar{\boldsymbol{s}}^{k}_{\kappa_i} \right], \quad k = r(k_x - 1) + k_y, \tag{4.46a}$$

$$\overline{\boldsymbol{d}}^{\ell,\alpha}_{K} = \sum_{i_x, i_y=0}^{1} \sum_{k_x, k_y=1}^{r} \left[ G^{(i_x)}_{\ell_x, k_x} H^{(i_y)}_{\ell_y, k_y} \bar{\boldsymbol{s}}^{k}_{\kappa_i} \right], \quad \ell = r(\ell_x - 1) + \ell_y, \tag{4.46b}$$

$$\overline{\boldsymbol{d}}_K^{\ell,\beta} = \sum_{i_x,i_y=0}^{1} \sum_{k_x,k_y=1}^{r} \left[ H^{(i_x)}_{\ell_x,k_x} G^{(i_y)}_{\ell_y,k_y} \bar{\boldsymbol{s}}^k_{\kappa_i} \right], \quad i = 2i_x + i_y, \tag{4.46c}$$

$$\overline{\boldsymbol{d}}_K^{\ell,\gamma} = \sum_{i_x,i_y=0}^{1} \sum_{k_x,k_y=1}^{r} \left[ G^{(i_x)}_{\ell_x,k_x} G^{(i_y)}_{\ell_y,k_y} \bar{\boldsymbol{s}}^k_{\kappa_i} \right]. \tag{4.46d}$$

The link between the coefficients of element $K$ and the coefficients of subelements $\kappa_i$ has now been established. Lastly, the multiscale representation of $\bar{\boldsymbol{u}}_{h|K}$ resembles Eq. (4.44) and can be expressed as:

$$\begin{aligned} \bar{\boldsymbol{u}}_{h|K} &= \overline{\boldsymbol{\mathcal{S}}}_K + \overline{\boldsymbol{\mathcal{D}}}^{\alpha}_K + \overline{\boldsymbol{\mathcal{D}}}^{\beta}_K + \overline{\boldsymbol{\mathcal{D}}}^{\gamma}_K \\ &= \sum_{\ell=1}^{r^2} \left( \bar{\boldsymbol{s}}^{\ell}_K \boldsymbol{\Phi}^{\ell} + \overline{\boldsymbol{d}}^{\ell,\alpha}_K \boldsymbol{\Psi}^{\ell,\alpha} + \overline{\boldsymbol{d}}^{\ell,\beta}_K \boldsymbol{\Psi}^{\ell,\beta} + \overline{\boldsymbol{d}}^{\ell,\gamma}_K \boldsymbol{\Psi}^{\ell,\gamma} \right). \end{aligned} \tag{4.47}$$

## 4.5 CONCLUDING COMMENTARY

In this chapter we have presented a local multiresolution analysis as a new methodology to connect the multiwavelet expansion to the DG formulation. Unlike the global multiresolution analysis developed by Hovhannisyan et al. (2014), in which the MRA decomposition involves the full computational domain, we have designed a method that locally restricts the MRA decomposition to the element.

In order to perform the new methodology, the local DG solution has been subjected to different reconstruction procedures. They have ranged from considering the contribution of the immediate neighbors to the evaluation of the solution jumps at the element interfaces. A complete analysis of their performance will be presented in Chapter 6.

By applying the multiwavelet expansion to the new reconstruction we were able to extract the individual features of the reconstructed solution and, by association, it has provided us with an instrument to monitor the behavior of the original DG solution, as we will demonstrate in Chapter 5.

# Chapter 5

# HP-ADAPTATION BASED ON LOCAL MULTIRESOLUTION

The goal of this chapter is to build an *hp*-adaptation algorithm based on the local multiresolution analysis of the DG solution developed in Chapter 4. In a first step, we present an exhaustive literature review of the different challenges in the road to adaptation and then how we address them in our algorithm.

Section 5.1 offers a complete study of the most relevant literature on error estimation techniques (Section 5.1.1) and resolution adaptation. The latter comprises Sections 5.1.2 and 5.1.3, which deal with the different approaches to adaptation and the *hp*-adaptive strategies, respectively.

Section 5.2 describes the *hp*-adaptive scheme employed in this work. The different components/steps of the algorithm are presented in the subsequent sections. In this manner, Section 5.2.1 illustrates the error estimator, while Sections 5.2.2 to 5.2.3 explains in detail the construction of the regularity indicator. Section 5.2.4 outlines the element marking and *hp*-decision criteria. Additionally, the mesh enrichment methodology is reported in Section 5.2.5. Lastly, an overview of the *hp*-algorithm is summarized in Section 5.2.6.

Section 5.3 discusses the parallel implementation followed in this work when performing both uniform and adaptive simulations. Finally, the main developments of this chapter are reviewed in Section 5.4.

## 5.1 ON ERROR ESTIMATION AND RESOLUTION ADAPTATION

In Chapter 2 we presented the process of discretizing of the compressible Navier-Stokes equations by means of the discontinuous Galerkin method (DGM). This set of non-linear partial differential equations is characterized by a wide range of temporal and spatial scales that can make its numerical resolution a difficult endeavor. Particularly, the range of spatial scales require appropriate spatial resolution to attain good numerical accuracy.

At this point one may ask: *what is the accuracy of the numerical solution?* Answer to that question is essential in the design of reliable *adaptive schemes* (Ainsworth and Oden, 1997). To this end, we must firstly devise some means to judge the distribution of error in a numerical solution. Generally, this error will be assessed by an *error estimator*, also known as *refinement indicator*. The combination of the error estimator plus an adaptive approach will allow

us to systematically reduce error and minimize computational cost by either changing the mesh, the order of the polynomial approximation, or both simultaneously. In this latter case that mesh and polynomial order are revised at the same time (*hp*-adaptation), we require a companion to the error estimator to select one of the two. The error estimator only tells you which elements should be refined, but it does not indicate which change (mesh or approximation order) is the optimal choice. A method for making that judgement is commonly called an *hp-adaptive strategy* (Mitchell and McClain, 2014).

### 5.1.1 *Error estimation techniques*

There are numerous methodologies available to obtain estimates of the accuracy of the computed numerical solution. Generally, these methods can be classified as *a priori* methods and *a posteriori* methods.

*A priori* methods allow us to obtain a coarse estimation of the error without computing the numerical solution. They are often insufficient since they only provide reliable information in the asymptotic range (Roy, 2010) and require strict regularity conditions of the solution (Verfürth, 1994). Examples of *a priori* error estimates in the DGM framework can be found in Johnson and Pitkäranta (1986) and Romkes et al. (2003).

*A posteriori* methods, on the other hand, provide an error estimate based on the computed numerical solution. That is, the computed solution itself is used to assess the accuracy relative to the exact solution (Ainsworth and Oden, 1997; Roy, 2010). The construction of *a posteriori* error estimates goes back to the solution of ordinary differential equations and the use of predictor-corrector schemes to produce error estimates for time-step control (Oden et al., 1989). The pioneering work of Babuvška and Rheinboldt (1978a) popularized *a posteriori* methods in the finite-element community, where they have seen prolific developments (e.g., the monograph of Ainsworth and Oden (1997)). Regarding the DGM, *a posteriori* methods have been developed for elliptic (Rivière and Wheeler, 2003; Houston et al., 2007), hyperbolic (Adjerid et al., 2002; Adjerid and Massey, 2002), and convection–diffusion problems (Ern and Proft, 2005; Baccouch, 2014). Additionally, several *a posteriori* DG error estimates have been constructed for the Euler equations (Hartmann and Houston, 2002) and the Navier-Stokes equations (Barth, 2007; Fidkowski and Luo, 2011). *a posteriori* methodologies can be also categorized according to their refinement indicator. Generally the classification criteria somewhat vary depending on the literature (cf. Oden et al. (1989), Gerhard (2017), Naddei (2019), and Rueda-Ramírez (2019) for different designations), but we can broadly draw three main paradigms:

(a) *Feature-based indicators* stem from the study of certain physical features of the flow, which must be fully resolved to adequately represent the flow field. They are also called *sensor-based indicators* (Gerhard, 2017), as they are normally sensitive to changes in a broad array of flow quantities (e.g., density, pressure, vorticity), or in derived field quantities such as gradients and Hessian matrices. Examples range from vortex

detection (Kasmai et al., 2011), to shock wave detection (Kanamori and Suzuki, 2011), monitoring of boundary layer separation and reattachment (Kenwright et al., 1999), and detection of multiple flow phenomena simultaneously (Kallinderis et al., 2017). These indicators are economical and easy to implement, but do usually not give any control over the error and require an experienced user to perform satisfactorily.

(b) *Adjoint-based indicators* or *goal-oriented indicators* are normally used to estimate the error of specific target quantities, such as aerodynamic force coefficients (e.g., the drag or lift coefficients), by solving an adjoint problem (Kast, 2017). The adjoint then indicates how initial numerical errors from the discretization translate into errors in the final target value (Kompenhans et al., 2016b). Moreover, the adjoint also registers *where* in the domain this error originates from, providing a spatial distribution of the total target error. Therefore, they provide an accurate prediction of the production and propagation of numerical errors (Woopen et al., 2014). These indicators were originally developed in the context of finite-element methods (Becker and Rannacher, 1996, 2001) and later extended to DGMs (Hartmann and Houston, 2002), where their use has experienced a steady growth in both laminar (Hartmann and Houston, 2006) and turbulent flows (Hartmann et al., 2011). These indicators require high memory storage and a high computational cost to solve the adjoint problem.

(c) *Local error-based indicators* attempt to measure the local numerical error for every element of the domain. They emerge as a midpoint between the feature-based and adjoint-based indicators, as they provide a reasonably accurate prediction of the numerical error while remaining computationally affordable. There exists a vast literature dedicated to those indicators. We will build upon the nomenclature proposed by Naddei et al. (2018) and divide them into three main groups:

  (i) *DE-based indicators* measure the discretization error, which is the difference between the exact solution, $u$, and the approximate solution, $u_h$. Examples of these indicators include the use of a higher-order solution through local reconstruction patches (Dolejší and Solin, 2016) or based on the superconvergence phenomenon (Biswas et al., 1994), the extrapolation of the available Legendre expansion coefficients (Mavriplis, 1989, 1994), the quantification of interface jumps between elements (Krivodonova and Flaherty, 2003), and the evaluation of the higher-order modes of the numerical solution (Persson and Peraire, 2006; Kuru et al., 2016; Naddei et al., 2018).

  (ii) *TE-based indicators* estimate the truncation error, which measures the missing expansion terms between the infinite sum of the exact solution, $u$, and the truncated version of the same sum, $\Pi_h u$ (Mavriplis, 1989). The term $\Pi_h u$ refers to the projection of $u$ onto $\mathcal{V}_h^p$, Eq. (2.14). We remark that $\Pi_h u$ is the best polynomial approximation to $u$ and thus, not necessarily equal to $u_h$. Estimates of the

truncation error in the literature include an interpolation method based on the polynomial order (Gao and Wang, 2011) and the use of interpolation in the context of multiple grids (Shih and Williams, 2009). A popular approach, which also relies on the use of a hierarchy of grids, is the *τ-estimation method* (Brandt and Livne, 2011). Since its extension to DGMs (Rubio et al., 2015), it has experienced a prolific development (Kompenhans et al., 2016a; Rueda-Ramírez et al., 2019a,b).

(iii) *RE-based indicators* use the residual error in the approximate solution $u_h$ to estimate the local error, where the residual error is a function measuring how much is left over when $u_h$ is fed to the governing PDE for the individual DG element (Jasak and Gosman, 2003). They have been originally developed within the finite-element community under the name *element-residual method* (Ainsworth and Oden, 1992), and successfully extended later to DGMs (Bey and Oden, 1996; Hartmann and Houston, 2002; Dolejší et al., 2015).

Even though we have presented the above three groups separately, there exists a relation among the discretization, truncation, and residual errors (Rueda-Ramírez, 2019). This relation is established by the *discrete error transport equation* (Roy, 2010), in which the residual and truncation error are featured as source terms (Naddei, 2019), thus controlling the behavior of the discretization error across the domain. By monitoring the error transport equation, we observe how the discretization error can be either locally generated or transported from elsewhere in the domain (Hay and Visonneau, 2006). For further information, we refer the reader to the studies of Hay and Visonneau (2007) and Yan and Ollivier-Gooch (2018), where the error transport equation is applied to turbulent and unsteady flows, respectively.

In addition to the *a priori* and *a posteriori* classification presented above, it is also worth mentioning the so-called *perturbation methods*, as defined by Gerhard et al. (2021). The idea behind this methodology is to improve the efficiency of a given reference scheme on a uniform reference grid by operating only on a smaller adapted subgrid, while maintaining the accuracy of the discretization on the full uniform grid (Gerhard, 2017). The concept of *multiresolution-based adaptation* (Calle et al., 2005; Domingues et al., 2009; Müller, 2009; Hovhannisyan et al., 2014), which was introduced in Chapter 4, is a class of perturbation methods. This approach is designed around grid adaptation and does not rely on error estimation. Instead it uses an indicator based on thresholding of local details to drive adaptation.

In the current study, we focus our attention on a merge between local error-based indicators and perturbation methods. Particularly, we will present a novel indicator, the *multiwavelet error estimator*, which combines the concepts of DE-based indicators and multiresolution-based adaptation. To complete the analysis, two local error-based indicators from the literature will also be described: the *small-scale energy density* (Kuru et al., 2016; Naddei et al., 2018)

and the *spectral decay* indicators (Persson and Peraire, 2006; Naddei et al., 2018). These indicators will be introduced in Section 5.2.1.

We will make use of the next section to present the different adaptation approaches commonly followed to adjust the spatial resolution in the framework of DGMs.

### 5.1.2 *Approaches to resolution adaptation*

Having estimated the error in the numerical solution, we need to decide how to adjust the spatial resolution of the elements involved in order to obtain a better discretization for the problem at hand (i.e., using the least number of degrees of freedom for a given target accuracy). We can consider three different approaches to adapt the spatial resolution (Löhner, 1995):

1. *Mesh repositioning (r-adaptation)*. The idea is to optimally deform the computational grid and relocate the grid nodes so that the nodal density is increased in the areas of interest (see e.g., Zahr and Persson (2018) and Ben Ameur et al. (2022)). This approach maintains the mesh topology, thus preserving an even computational load when used in parallel computations (Marcon et al., 2020). However, any increase in resolution might bring about a decrease in mesh quality (e.g. excessive element distortion), as we are constrained by the initial number of nodes and grid connectivity.
2. *Remeshing (m-adaptation)*. In this approach the computational grid is entirely rebuilt in order to generate a more suitable discretization (see e.g., Mavriplis (1990) and Alauzet et al. (2006)). Remeshing has the advantage of not being constrained by the existence of the original mesh, in that a completely new mesh is independently generated. However, this approach introduces extra computational costs due to the construction of a new mesh and the need to project the solution onto the new mesh (Remacle et al., 2005; Alauzet and Loseille, 2016). Moreover, the latter step may also introduce additional errors associated with the projection operation.
3. *Mesh enrichment (h/p-adaptation)*. The key here is to locally add (refinement) or locally remove (coarsening) degrees of freedom to/from a computational grid in order to return a more efficient discretization of the domain. This approach allows us either to split/agglomerate elements into new ones ($h$-adaptation) (Kamkar et al., 2011; Mozaffari et al., 2022), or to increase/reduce the local order of the approximation ($p$-adaptation) (Ekelschot et al., 2017; Tugnoli et al., 2017). Additionally, both $h$- and $p$- can be performed isotropically (along all space directions; see e.g., Gerhard et al. (2015b) and Naddei et al. (2018)), or anisotropically (along a particular direction; see e.g., Wackers et al. (2012) and Rueda-Ramírez et al. (2019a)). One of the drawbacks of mesh enrichment lies in the non-conforming nature of the resulting

discretization, being composed of non-conforming elements or non-conforming polynomial approximations, which needs to be considered in the implementation (Hesthaven and Warburton, 2008). Further to this, the application of *h*-adaptation is prone to develop complex data structures, while *p*-adaptation is somewhat limited by the topology of the starting grid. Despite these challenges, the possibility of choosing between either *h*- or *p*- results in a versatile and efficient approach, as we will discuss next.

Discontinuous Galerkin methods are especially well-suited to *h/p*-adaptation, as they allow us to locally adjust mesh size ($h$) and approximation order ($p$). In this manner, by varying $h$ while keeping $p$ fixed, the numerical error is expected to decay algebraically. This choice is most suitable near discontinuous phenomena, such as shocks or singularities. Alternatively, in the case of a sufficiently smooth solution, maintaining $h$ constant and changing $p$ usually leads to the error converging exponentially (Karniadakis and Sherwin, 2005). Moreover, DGMs are able to handle the resulting non-conforming meshes with hanging nodes and/or different polynomial orders efficiently, as elements only communicate through fluxes computed using the information of the immediate neighbours (Rivière, 2008).

Identifying the benefits of both types of convergence, Szabo (1986) proposed a new method in the framework of FEMs that combined *h*- and *p*-adaptation simultaneously. Later, the work of Babuvška and Guo (1992) developed some important theoretical results that paved the way toward generating an optimal distribution of $h$ and $p$. Since then there has been a blooming in the development of *hp*-adaptive strategies driving high-order methods, including FEMs (Ainsworth and Senior, 1998; Demkowicz et al., 2002) and DGMs (Bey and Oden, 1996; Chalmers et al., 2019). In the next section we will present some of the most common strategies that have been historically employed to determine the *hp*-distribution, and how that context has shaped our contribution toward a novel *hp*-decision criteria.

### 5.1.3 *hp-adaptive strategies*

Up to this point we have characterized the estimation of the error by using a refinement indicator (Section 5.1.1), and described different options to resolution adaptation (Section 5.1.2). We have concluded that, of the different approaches, *h/p*-adaptation is especially well suited to DGMs. The combination of $h$ and $p$ holds particular relevance. Unlike the pure *h*-version or *p*-version of adaptation, we can judiciously modify both $h$ and $p$ according to the local regularity of the analytical solution (Rachowicz et al., 1989; Houston and Süli, 2005; Wihler, 2011). In this manner, *p*-adaptation would be used in regions with smooth solution behavior to deliver high accuracy, and *h*-adaptation would be employed in areas of low regularity to avoid unbounded oscillations that may result in a loss of stability (Wang and Mavriplis, 2009). However, since the solution is usually unknown analytically, the local regularity of the solution cannot be exactly computed. In order to estimate the

local smoothness of the analytical solution a *regularity* or *smoothness indicator* is usually employed instead. This indicator is paired with an *hp*-decision criterion to constitute a particular *hp*-adaptive strategy. Various *hp*-adaptive strategies have been developed in the literature (for a review, see e.g., Houston and Süli (2005), Eibner and Melenk (2007), Mitchell and McClain (2014), and Ringue (2019)). By building upon the existing classification proposed by Houston and Süli (2005), we have the following categories:

(A) *Use of a priori knowledge*. This strategy uses any *a priori* information about the geometrical or physical singularities occurring throughout the domain. An element is *h*-adapted if it contains possible irregularities, and *p*-adapted otherwise. This simple strategy has been employed in Valenciano and Owens (2000) and Ainsworth and Senior (1999).

(B) *Use of p-estimates*. This strategy estimates the convergence rate in $p$ by building approximations of different order. There exist various versions of this strategy. The *smaller p-estimates* variant (Süli et al., 2000) is built on $p-2$ and $p-1$ approximations, whereas the *larger p-estimates* alternative (Ainsworth and Senior, 1998) is based upon $p+1$, $p+2$, and $p+3$ spaces. Finally, the so-called *type-parameter* (Babuvška and Gui, 1986) approach can be also classified as a variant of *p*-estimates, as it relies on error estimates from $p$ and $p-1$ spaces.

(C) *Use of h- and p-estimates*. The idea behind this strategy is to apply either *h*- and *p*-adaptation, estimate the error (using one of the techniques explained in Section 5.1.1), and then choose which of the two leads to the largest decrease of the error with respect to the number of degrees of freedom. Multiple variants of this strategy can be found in the literature. The commonly known *mesh optimization* strategy (Rachowicz et al., 1989; Demkowicz et al., 2002) solves the problem on a globally *hp*-refined mesh. Related, but simpler, approaches were developed in Solin et al. (2003) and Schmidt and Siebert (2000). Another studies examine the use of *h*- and *p*-coarsening (Dolejší et al., 2016), or the use of a higher-order reconstruction (Dolejší and Solin, 2016). Lastly, the so-called *Texas 3-step* strategy (Bey and Oden, 1996), departs from the previous studies by using a more empirical approach. In this case, the *h*- and *p*-refinement are performed in a series of consecutive steps bounded by user-defined error tolerances.

(D) *Use of smoothness assumption*. This strategy relies on the prediction of what the error should be if the local solution is smooth and the optimal convergence rate (exponential convergence) has been achieved. It compares the current estimated error against a prediction on the previous mesh. If the hypothesis of smoothness is reasonable, *p*-enrichment is performed; otherwise *h*-refinement will be executed. This strategy was originally devised by Melenk and Wohlmuth (2001) and later applied to various studies, such as Heuveline and Rannacher (2003) and Eibner and Melenk (2007).

(E) *Use of local Sobolev regularity*. This strategy is based on the estimation of the local Sobolev regularity index associated with the analytical so-

lution. There exist several ways to perform the approximation. The earliest method was proposed by Ainsworth and Senior (1998) and relies on evaluating the Sobolev regularity index from a local refinement indicator based on different polynomial degrees. In a later approach, Houston et al. (2003) and Houston and Süli (2005) approximated the index according to the decay rate of the Legendre series expansion. More recently, Wihler (2011) and Fankhauser et al. (2014) made use of continuous Sobolev embeddings to perform the estimation.

(F) *Use of decay of Legendre expansion coefficients*. This strategy was born from the influential works of Mavriplis (1989, 1994) in adaptive spectral methods. There, the high-order numerical solution is first expanded to orthogonal polynomials. A second step involves extrapolation of the expansion coefficients to insure an accurate representation of the spectrum of the solution. Then the main idea is to verify whether the resulting spectrum decays sufficiently fast. If that is the case, an exponential convergence in $p$ can be assumed and $p$-enrichment is advised. In the presence of discontinuities, the decay rate is hindered and becomes slower, in which case $h$-refinement is performed. Since then, this strategy has been widely applied in spectral methods (Feng and Mavriplis, 2002), FEMs (Eibner and Melenk, 2007), and DGMs (Wang and Mavriplis, 2009; Leicht and Hartmann, 2011; Chalmers et al., 2019; Basile et al., 2022).

On a side note, it is worth mentioning some recently developed alternatives to the aforementioned *hp*-adaptation strategies. Instead of relying on smoothness evaluation, these alternative strategies are based on *optimal refinement decisions* (Balan et al., 2016) and normally paired with goal-oriented indicators (Section 5.1.1). The idea is to assume the existence of optimal distributions of degrees of freedom on the computational domain and construct an optimization-based framework for *hp*-adaptation accordingly. Examples range from the use of a selection process based on a merit function to locally minimize the error and the number of degrees of freedom (Ceze and Fidkowski, 2012), to the targeting of a globally optimal metric and polynomial degree fields which minimize the global error on an output quantity of interest (Ringue and Nadarajah, 2018).

If we return to the previous classification, we have drawn inspiration from the *hp*-strategy developed by Mavriplis (1989, 1994) to introduce a new smoothness indicator. We call it the *multiwavelet regularity indicator*. It builds upon the concepts behind the multiwavelet error estimator previously highlighted in Section 5.2.1, and it has been designed to be working as its companion, although it can also be used independently. Similarly to the smoothness indicator that Mavriplis developed as part of her *hp*-strategy, our indicator also measures the rate of decay of a given spectrum, this being the spectrum of the multiwavelet coefficients. Both indicators require an extra post-processing step to improve the estimation. Mavriplis's approach performs extrapolation to estimate the missing coefficients. On the other hand, our method is based on the work of Dolejší and Solin (2016) to build a more accurate solution by

considering the contributions from the neighbors (see Chapter 4). This new enriched solution is well-suited to the multiwavelet expansion, which in turn provides an estimation of the full signal spectrum. Our proposed strategy is clearly explained in the next sections.

## 5.2 NOVEL HP-ADAPTIVE SCHEME

In Section 5.1 we have presented the multiple challenges that any adaptive scheme in the framework of DGMs may face and how they have been historically investigated in the literature. We have also briefly hinted the ways in which the present work contributes to the topic.

In this section we will provide a thorough account of the design of our *hp*-adaptive algorithm. We first introduce the notation of *hp*-mesh, $\Omega_{h,p}$, which is simply the assignation of a local polynomial degree $p_K$ to each $K \in \Omega_h$. In other words:

$$\Omega_{h,p} = \{\Omega_h, p\}, \quad \text{with } p = \{p_K, K \in \Omega_h\}. \tag{5.1}$$

With this notation, the approximation space $\mathcal{V}_h^p$ that contains the corresponding DG solution $\boldsymbol{u}_{h,p} \in \mathcal{V}_h^p$ is an updated version of Eq. (2.14). Namely:

$$\mathcal{V}_h^p = \{\Phi_h \in L^2(\Omega_h) : \Phi_{h|K} \in \mathcal{P}^{p_K}(\Xi_K^{-1}(K)), \forall K \in \Omega_{h,p}\}, \tag{5.2}$$

where $\mathcal{P}^{p_K}(\Xi_K^{-1}(K))$ denotes the space of all polynomials of degree at most $p_K$ defined on K.

The objective is to determine a distinct sequence of *hp*-meshes, $\Omega_{h,p}^{(i)}$ with $i = 1, 2, \ldots$, such that the associated sequence of DG solutions $\boldsymbol{u}_{h,p}^{(i)}$ converges at a high, desirably exponential, rate to the exact solution $\boldsymbol{u}$. Mesh refinement of $\Omega_h$ will be solely guided by the multiwavelet error estimator, which will be described in detail in Section 5.2.1. Simultaneous adaptation of $\Omega_h$ as well as the degree distribution $p$ of the *hp*-mesh $\Omega_{h,p}$ necessitates the combination of the error estimator and the multiwavelet regularity indicator, which provides supplementary smoothness information to decide whether to perform mesh or degree adaptation. We give a prelude on how to link this information to a multiwavelet expansion in Section 5.2.2. The multiwavelet regularity indicator and the subsequent *hp*-decision criteria will be presented in Section 5.2.3 and Section 5.2.4, respectively. Section 5.2.5 describes how the spatial adaptation is implemented. Finally, an overview of the complete *hp*-algorithm is featured in Section 5.2.6.

### 5.2.1 *The multiwavelet error estimator*

In Chapter 4 we have described several post-enrichment methods applied to the original DG solution $u_{h|K}$. These reconstruction methods have allowed us to assemble a new approximation $\bar{u}_{h|K}$. Subsequent to this step, we have

performed a local MRA decomposition of $\bar{u}_{h|K}$ by means of a multiwavelet expansion.

In this section we resume from the local MRA representation given by Eq. (4.44). The next step is to evaluate its multiwavelet contribution, $\overline{\mathscr{D}}_K$, to achieve an estimation of the discretization error on element $K$. As highlighted in Section 5.1.1, the resulting local indicator constitutes a *hybrid* approach between DE-based indicators and multiresolution-based adaptation.

The main idea is to calculate the $L^2$-norm of $\overline{\mathscr{D}}_K$, which can be read as an evaluation of the *energy* associated with the individual fluctuations of $\bar{u}_{h|K}$. Consequently, in the 1-D context the underlying structure of the local estimator can be expressed as:

$$\eta_K = \|\overline{\mathscr{D}}_K\|_{L^2(K)} = \Big\| \sum_{\ell=1}^{r} \overline{d}_K^{\ell}\, \psi^{\ell} \Big\|_{L^2(K)} = \Big[ \sum_{\ell=1}^{r} \big(\overline{d}_K^{\ell}\big)^2 \Big]^{1/2}, \quad K \in \Omega_{h,p}, \tag{5.3}$$

with multiplicity $r = p+1$. Moreover, we have used $\langle \psi^{\ell}, \psi^{\ell'} \rangle_K = \delta_{\ell,\ell'}$ from the orthonormality relations in Eq. (3.31) to simplify the final expression. We propose three alternatives to the multiwavelet estimator derived from Eq. (5.3). The difference between them lies in the reconstruction method employed to reach $\bar{u}_h$ and their terminology reflects this fact (see sections 4.3.1 to 4.3.3). Consequently, we rewrite Eq. (5.3) to account for the post-enrichment procedure. In other words:

$$\eta_K \text{ becomes either } \begin{cases} \eta_K^{\kappa\text{-MW}}, & \text{if Eqs. (4.19) to (4.24)} \\ \eta_K^{K\text{-MW}}, & \text{if Eqs. (4.25) to (4.28)} \\ \eta_K^{\Gamma\text{-MW}}, & \text{if Eqs. (4.29) to (4.32)} \end{cases}, \tag{5.4}$$

which are labelled as the $\kappa$-, $K$, and $\Gamma$-multiwavelet estimator; respectively.

*Two-dimensional estimator* Similarly to the 1-D setting, we will evaluate the multiwavelet contribution resulting from applying a local MRA to the new approximation $\bar{\boldsymbol{u}}_{h|K}$ in order to assess the discretization error on element $K$. However, in the 2-D context only one error estimator will be developed. This estimator will be based on the $\kappa$-reconstruction procedure presented in Section 4.3.4. We will further justify this choice in Chapter 6.

Hence, the $\kappa$-multiwavelet estimator is defined by evaluating the $x$-,$y$- and $xy$- components of the multiwavelet contribution given by Eq. (4.47) in the $L^2$-norm. Namely:

$$\begin{aligned} \eta_K^{\kappa\text{-MW}} &= \|\overline{\boldsymbol{\mathscr{D}}}_K^{\alpha} + \overline{\boldsymbol{\mathscr{D}}}_K^{\beta} + \overline{\boldsymbol{\mathscr{D}}}_K^{\gamma}\|_{L^2(K)} \\ &= \Big\| \sum_{\ell=1}^{r^2} \Big( \overline{\boldsymbol{d}}_K^{\ell,\alpha}\, \boldsymbol{\Psi}^{\ell,\alpha} + \overline{\boldsymbol{d}}_K^{\ell,\beta}\, \boldsymbol{\Psi}^{\ell,\beta} + \overline{\boldsymbol{d}}_K^{\ell,\gamma}\, \boldsymbol{\Psi}^{\ell,\gamma} \Big) \Big\|_{L^2(K)}, \quad K \in \Omega_{h,p}\,. \end{aligned} \tag{5.5}$$

In general, if we extend the orthonormality relations in Eq. (3.31) to the current 2-D setting and consider the extra directions given by the superscripts $\alpha$,

$\beta$, and $\gamma$ we have the following new orthonormality relations between components:

$$\left\langle \boldsymbol{\Psi}^{\ell,\alpha}, \boldsymbol{\Psi}^{k,\alpha} \right\rangle_K = \delta_{\ell,k}, \quad \left\langle \boldsymbol{\Psi}^{\ell,\alpha}, \boldsymbol{\Psi}^{k,\beta} \right\rangle_K = 0, \quad \left\langle \boldsymbol{\Psi}^{\ell,\alpha}, \boldsymbol{\Psi}^{k,\gamma} \right\rangle_K = 0, \tag{5.6a}$$

$$\left\langle \boldsymbol{\Psi}^{\ell,\beta}, \boldsymbol{\Psi}^{k,\alpha} \right\rangle_K = 0, \quad \left\langle \boldsymbol{\Psi}^{\ell,\beta}, \boldsymbol{\Psi}^{k,\beta} \right\rangle_K = \delta_{\ell,k}, \quad \left\langle \boldsymbol{\Psi}^{\ell,\beta}, \boldsymbol{\Psi}^{k,\gamma} \right\rangle_K = 0, \tag{5.6b}$$

$$\left\langle \boldsymbol{\Psi}^{\ell,\gamma}, \boldsymbol{\Psi}^{k,\alpha} \right\rangle_K = 0, \quad \left\langle \boldsymbol{\Psi}^{\ell,\gamma}, \boldsymbol{\Psi}^{k,\beta} \right\rangle_K = 0, \quad \left\langle \boldsymbol{\Psi}^{\ell,\gamma}, \boldsymbol{\Psi}^{k,\gamma} \right\rangle_K = \delta_{\ell,k}. \tag{5.6c}$$

where $\ell, k = 1, ..., r$. Consequently, Eq. (5.5) can be simplified to

$$\eta_K^{\kappa\text{-MW}} = \left[ \sum_{\ell=1}^{r^2} \left(\overline{\boldsymbol{d}}_K^{\ell,\alpha}\right)^2 + \sum_{\ell=1}^{r^2} \left(\overline{\boldsymbol{d}}_K^{\ell,\beta}\right)^2 + \sum_{\ell=1}^{r^2} \left(\overline{\boldsymbol{d}}_K^{\ell,\gamma}\right)^2 \right]^{1/2}, \qquad K \in \Omega_{h,p}. \tag{5.7}$$

*Error estimators from the literature* We also include two estimators extensively tested in Naddei et al. (2018, 2019) and Taube et al. (2010) so that we can compare them against our MW-based estimators.

We consider the *small-scale energy density* (SSED) estimator (Kuru et al., 2016; Naddei et al., 2018) and the *spectral decay* (SD) estimator (Taube et al., 2010). The SSED estimator measures the energy associated with the highest-order modes. It is expressed as:

$$\eta_K^{\text{SSED}} = \frac{\left\| \sum_{\ell=1}^{N_p} \boldsymbol{U}_K^{\ell} \phi^{\ell} - \sum_{\ell=1}^{N_{p-1}} \boldsymbol{U}_K^{\ell} \phi^{\ell} \right\|_{L^2(K)}}{|K|^{1/2}}, \qquad K \in \Omega_{h,p}, \tag{5.8}$$

where the normalization is made using the volume of the element, $|K|$. The SD is similar to the SSED estimator, but instead normalised by the total energy within the element. That is:

$$\eta_K^{\text{SD}} = \frac{\left\| \sum_{\ell=1}^{N_p} \boldsymbol{U}_K^{\ell} \phi^{\ell} - \sum_{\ell=1}^{N_{p-1}} \boldsymbol{U}_K^{\ell} \phi^{\ell} \right\|_{L^2(K)}}{\left\| \sum_{\ell=1}^{N_p} \boldsymbol{U}_K^{\ell} \phi^{\ell} \right\|_{L^2(K)}}, \qquad K \in \Omega_{h,p}. \tag{5.9}$$

### 5.2.2 *On multiwavelets and smoothness estimation*

If we recall from Chapter 3, the multiwavelet coefficients resulting from applying the multiscale decomposition to a function $f$ are defined as

$$d_{(m,j)}^{\ell} = \left\langle f, \psi_{(m,j)}^{\ell} \right\rangle_{K_{(m,j)}}, \qquad m = 0, ..., \mathscr{M} - 1, \quad j = 0, ..., 2^m - 1, \tag{5.10}$$

where the index $m$ denotes the resolution level and the value $\mathscr{M}$ conveys the finest resolution level. Additionally, we also characterized Alpert's multiwavelets (Alpert, 1993; Alpert et al., 2002) as having $M$ vanishing moments. Namely,

$$M = \ell + r - 1, \qquad \ell = 1, ..., r, \tag{5.11}$$

with multiplicity $r = p + 1$. Consequently, by choosing $f = P$ with $P \in \mathscr{P}^{M-1}(K_{(m,j)})$, we have (see Eq. (3.32)):

$$d^{\ell}_{(m,j)} = \left\langle P, \psi^{\ell}_{(m,j)} \right\rangle_{K_{(m,j)}} = 0, \tag{5.12}$$

To put it in another way, Alpert's multiwavelets are orthogonal to polynomials of degree $M - 1$ and their associated multi-scaling functions $\phi^{\ell}_{(m,j)}$ would be able to reproduce these same polynomials exactly. For example, the related multi-scaling function of Alpert's multiwavelet with multiplicity $r = 1$ (Haar wavelet, Figure 3.3B) has $M = 1$ and only reproduces constant functions. If we increase the multiplicity to $r = 2$, we have two multiwavelets (Fig. 3.5B) with $M = 2$ and $M = 3$. Their associated multi-scaling functions are able to reproduce up to linear and quadratic functions, respectively.

If we continue increasing the multiplicity, a pattern emerges. The more vanishing moments, the better the multi-scaling functions model smooth functions and the smaller the multiwavelet coefficients will be for every successive resolution level $m$. In other words, the information of the function will be concentrated in a small number of coefficients (Hubbard, 1998).

Certainly, this idea is linked to the so-called *cancellation property* (Dahmen, 2001; Vuik, 2020), which describes the behavior of the multiwavelet coefficients as we increase the resolution level $m$ and the number of vanishing moments $M$. For a sufficiently smooth function $f_{|K_{m,j}} \in C^M(K_{m,j})$, we have

$$d^{\ell}_{m,j} \leq 2^{(-m+1)(M+1/2)} \frac{1}{M!} \left\| f^{(M)} \right\|_{L^{\infty}(K_{(m,j)})}. \tag{5.13}$$

The cancellation property sets an upper bound to the rate of decay but it does not tell us which is its value. Moreover, $f$ may not always be given analytically (e.g., DG solution), thus making it difficult to evaluate Eq. (5.13).

Even though Eq. (5.13) provides limited information about the rate of decay of the multiwavelet coefficients, it does offer some insight on how, for a fixed level $m = \mathscr{M}$, the higher the number of vanishing moments $M$, the faster the decay becomes. Then it may seem intuitive to arrange the details $d^{\ell}_{m,j}$ from lower to higher $M$ and analyze their behavior.

In a first approach, we will start by selecting two analytical functions, $f(x)$ and $g(x)$. The signal $f$ represents a non-polynomial smooth function, whereas $g$ defines a strong discontinuity. The functions are shown in Figure 5.1A and Figure 5.1B, respectively. Then, for each function, we perform a two-level multiscale decomposition with $\mathscr{M} = 1$, as described by Eq. (3.26). We have selected the functions so that $f, g \notin \mathscr{P}^M(K)$. Therefore, for either $f$ or $g$, Eq. (5.10) now guarantees

$$d^{\ell} = \left\langle \cdot\,, \psi^{\ell} \right\rangle_K \neq 0 \qquad \ell = 1, ..., r, \tag{5.14}$$

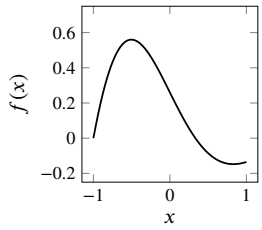


*(a)* $f = \mathrm{e}^{-x-1}\sin\left(\frac{3}{4}\pi(x+1)\right)$

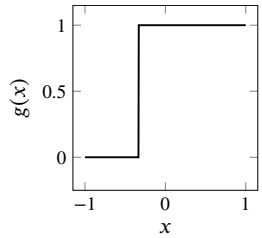


*(b)* $g = \begin{cases} 1, & x \geq -\frac{1}{3} \\ 0, & \text{elsewhere} \end{cases}$

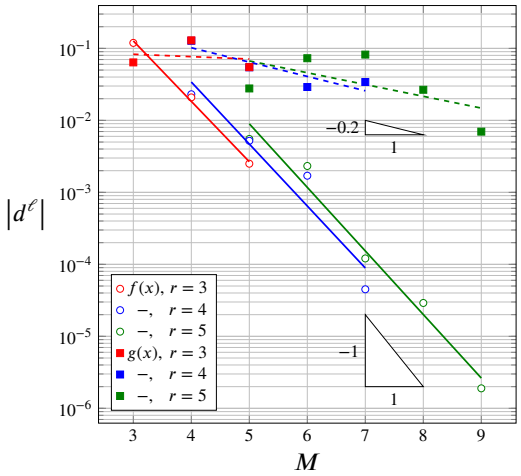


*(c)* MW coefficients versus the number of vanishing moments under different multiplicities on a log-linear scale. Linear regression shows the rate of decay $\varsigma$ for every family of coefficients with multiplicity $r$. Solid lines refer to $f$, dashed lines to $g$.

*Figure* 5.1: 1-D multiwavelet-based spectrum of a smooth function $f(x)$ and discontinuous function $g(x)$. Only the coefficients $d^\ell = d^\ell_{0,0}$ are considered.

where for simplicity $d^\ell = d^\ell_{0,0}$, $\psi^\ell = \psi^\ell_{0,0}$, and $K = K_{(0,0)}$. Figure 5.1c displays the resulting coefficients for different multiplicities $r$ on a log-linear scale. The number of vanishing moments associated with every coefficient, as described by Eq. (5.11), are arranged along the $x$-axis. We observe how the decline of the coefficients is similar to an exponential decay of the form:

$$\left|d^\ell\right| \sim c10^{-\varsigma M} \tag{5.15}$$

which corresponds to a straight line in a log-linear plot, as shown in Figure 5.1c. Similarly to the work of Mavriplis (1989), we employ linear regression to fit the $\log\left|d^\ell\right|$ to the straight line $h(M) = -\varsigma M + \log c$. Table 5.1 collects the values of the *decay parameter* $\varsigma$ for both $f$ and $g$ and different multiplicities $r$. It also measures the quality of the fit with the Pearson coefficient, denoted by $\mathscr{R}$. We notice that the discontinuity in $g$ translates to large coefficients with slow decay ($\varsigma < 0.2$). Conversely, the smoother signal $f$ reports smaller coefficients with a rapid decay ($\varsigma > 0.8$). Except for low values of $r$, the decay parameter does not seem to be greatly affected by changes in multiplicity. Finally, the quality of the fit deteriorates when facing discontinuities, which seems to suggest that the rate of decline ceases to be of exponential nature.

*Table* 5.1: Regression parameters of the 1-D multiwavelet-based spectrum from Figure 5.1.

| | | $\varsigma$ | $c$ | Pearson, $\mathscr{R}$ |
|---|---|---|---|---|
| $f(x)$, | $r = 3$ | 0.839 | 42. | −0.998 |
| −, | $r = 4$ | 0.861 | 95. | −0.962 |
| −, | $r = 5$ | 0.883 | 233. | −0.988 |
| $g(x)$, | $r = 3$ | 0.033 | 0.1 | −0.166 |
| −, | $r = 4$ | 0.199 | 0.6 | −0.892 |
| −, | $r = 5$ | 0.164 | 0.4 | −0.601 |

*Two-dimensional case* In two-dimensions the analysis becomes more elaborated. The vanishing moments are mixed due to the tensor product and we end up with horizontal, $\alpha$; vertical, $\beta$; and diagonal, $\gamma$, multiwavelet coefficients. Therefore, by considering Eq. (4.14) and Eq. (3.39) with $\mathscr{M} = 1$, we

*Table 5.2:* Distribution of lowest mode $a_{ij}$ resulting from applying Eq. (5.16) to Eq. (5.17). Multiplicities $r = 2$ and $r = 3$ are tested along the upper and lower row, respectively. Depending on the lowest mode and the location $\alpha, \beta, \gamma$, we reach a different quantity of the equivalent number of vanishing moments, $M_{eq}$ (circled), associated with each coefficient $\boldsymbol{d}^{\ell}$. Coefficients that share $M_{eq}$ are clustered together (dotted line).

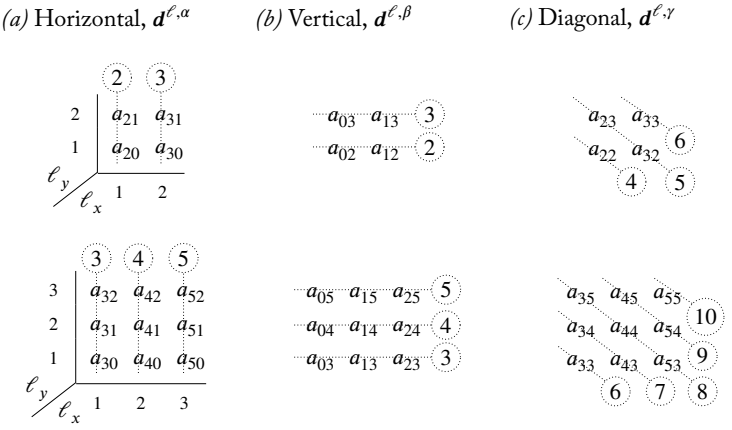


have

$$\boldsymbol{d}^{\ell,\alpha} = \left\langle F, \boldsymbol{\Psi}^{\ell,\alpha} \right\rangle_K, \qquad \text{with } \boldsymbol{\Psi}^{\ell,\alpha} = \psi^{\ell_x}\, \phi^{\ell_y}, \tag{5.16a}$$

$$\boldsymbol{d}^{\ell,\beta} = \left\langle F, \boldsymbol{\Psi}^{\ell,\beta} \right\rangle_K, \qquad \text{with } \boldsymbol{\Psi}^{\ell,\beta} = \phi^{\ell_x}\, \psi^{\ell_y}, \tag{5.16b}$$

$$\boldsymbol{d}^{\ell,\gamma} = \left\langle F, \boldsymbol{\Psi}^{\ell,\gamma} \right\rangle_K, \qquad \text{with } \boldsymbol{\Psi}^{\ell,\gamma} = \psi^{\ell_x}\, \psi^{\ell_y}, \tag{5.16c}$$

where $\ell = r(\ell_x - 1) + \ell_y$ with $\ell_x, \ell_y = 1, \dots, r$. Additionally, to improve readability we have simplified the nomenclature to $F = F(x, y)$, $\boldsymbol{d}^{\ell} = \boldsymbol{d}^{\ell}_{0,0}$, $\boldsymbol{\Psi}^{\ell} = \boldsymbol{\Psi}^{\ell}_{0,0}$, and $K = K_{(0,0)}$. The idea is to find out the *equivalent* vanishing moments $M_{eq}$ associated with the horizontal, vertical and diagonal details by comparing the evolution of these details for a generic polynomial function $F = P$ with $P \in \mathscr{P}^{r+1}(K)$. Namely,

$$F(x, y) = \sum_{i,j=0}^{r+1} a_{ij} x^i y^j \,. \tag{5.17}$$

The results for multiplicities $r = 2$ and $r = 3$ are reported in Table 5.2. The extension to higher multiplicities is straightforward. By observing the lowest non-vanishing mode $a_{ij}$, we conclude that the horizontal and vertical coefficients follow the same Eq. (5.11) defined in 1-D. Certainly, their tensor product in Eq. (5.16) only involves a single multiwavelet, either along the $x$- or $y$-direction, with the remaining direction not adding any extra vanishing moments. On the other hand, the diagonal coefficient features a tensor product of two multiwavelets. This means that their vanishing moments are happening along the $x$- and $y$-direction simultaneously. Therefore, we define the *number of equivalent vanishing moments* as

$$M_{eq}(\ell) = \begin{cases} \ell_x + r - 1 & \text{if } \boldsymbol{d}^{\ell,\alpha} \\ \ell_y + r - 1 & \text{if } \boldsymbol{d}^{\ell,\beta} \\ 2(r-1) + \ell_x + \ell_y & \text{if } \boldsymbol{d}^{\ell,\gamma} \end{cases} \tag{5.18}$$

Once $M_{eq}$ has been defined, we proceed to order the coefficients $\boldsymbol{d}^{\ell}$ from lower to higher $M_{eq}$ and monitor their behavior. The motivation here is to express the coefficients into a single decaying spectrum, in a similar manner

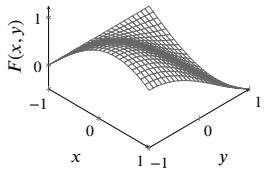


*(a)* $F = \sin\left(\frac{3}{8}\pi a\right)\cos\left(\frac{3}{8}\pi b\right)$, with $a = x + 1$ and $b = y + 1$.

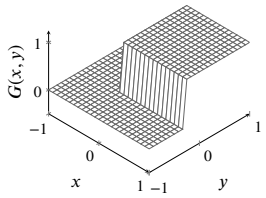


*(b)* $G = \begin{cases} 1, & x, y \geq -\frac{1}{3} \\ 0, & \text{elsewhere} \end{cases}$

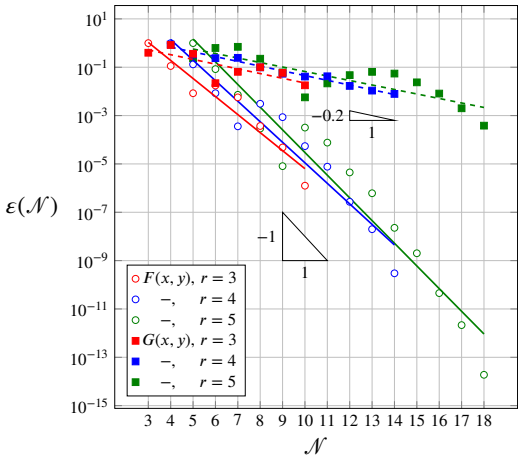


*(c)* Energy spectrum $\varepsilon(\mathcal{N})$ versus the number of equivalent vanishing moments $\mathcal{N}$ on a log-linear scale. Color separates the different multiplicities $r$. Solid and dashed lines denotes the fit to the spectrum of $f$ and $g$, respectively.

*Figure* 5.2: 2-D multiwavelet-based spectrum of a smooth function $F(x, y)$ and discontinuous function $G(x, y)$. Only the coefficients $\boldsymbol{d}^{\ell} = \boldsymbol{d}^{\ell}_{0,0}$ are considered.

to the one-dimensional case. To that end, we define the following energy spectrum

$$\varepsilon(\mathcal{N}) = \left\| \boldsymbol{d}^{\ell,\alpha} + \boldsymbol{d}^{\ell',\beta} + \boldsymbol{d}^{\ell'',\gamma} \right\|_{L^2}, \quad \forall \ell, \ell', \ell'' \mid \boldsymbol{M}_{eq}(\,\cdot\,) = \mathcal{N}\,, \tag{5.19}$$

where $\mathcal{N} = r, \ldots, 3r - 1$ limits the possible values of $\boldsymbol{M}_{eq}$. We test Eq. (5.19) by evaluating two different functions, denoted by $F(x, y)$ and $G(x, y)$. They are illustrated in Figure 5.2A and Figure 5.2B, respectively. The behavior of the spectrum under different multiplicities $r$ is shown in Figure 5.2C. Additionally, the log-linear plot features a regression line for every $r$-family to measure the rate of decay of $\varepsilon(\mathcal{N})$. The regression parameters are collected in Table 5.4. Analogously to the 1-D case, we observe a fast exponential decay and high quality of the fit when the signal is regular ($\varsigma > 0.7$, $\mathscr{R} > 0.9$), and a slower decline when facing discontinuities ($\varsigma \approx 0.2$). These behaviors remain more consistent with varying multiplicities compared to the 1-D case. This can be explained by the higher amount of data points, which helps to phase out outliers.

*Table* 5.4: Regression parameters of the 2-D multiwavelet-based spectrum from Figure 5.2. We fit $\log \varepsilon(\mathcal{N})$ to the straight line $h(\mathcal{N}) = -\varsigma\mathcal{N} + \log c$.

| | $\varsigma$ | $c$ | Pearson, $\mathscr{R}$ |
|---|---|---|---|
| $F(x)$, $r = 3$ | 0.746 | 185. | −0.965 |
| –, $r = 4$ | 0.850 | 3478. | −0.968 |
| –, $r = 5$ | 0.938 | 71663. | −0.970 |
| $G(x)$, $r = 3$ | 0.195 | 2. | −0.785 |
| –, $r = 4$ | 0.196 | 4. | −0.989 |
| –, $r = 5$ | 0.186 | 5. | −0.836 |

### 5.2.3 *The multiwavelet regularity indicator*

Up to this point we have proved how a clever arrangement of the multiwavelet coefficients allows us to estimate the regularity of a signal by measuring its rate of decay. However, the analysis has been only performed on analytical functions. In the next paragraphs we will described the extension to the DG framework. In particular, we will put under the microscope the new enriched solution $\bar{u}_{h|K}$ outlined in Chapter 4 and come up with a novel estimate of the local smoothness based on a multiwavelet expansion.

Firstly, we will focus our attention on the 1-D setting. With this in mind, we recall the reader the local multiresolution procedure applied to $\bar{u}_{h|K}$, as de-

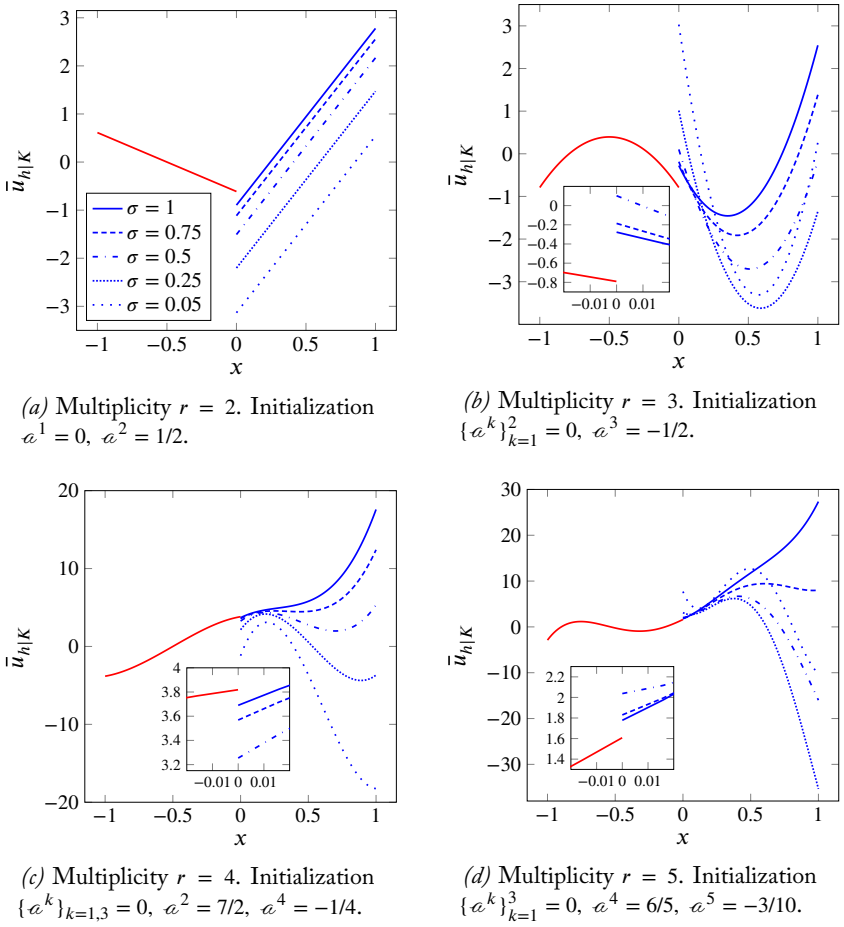


*(a)* Multiplicity $r = 2$. Initialization $a^1 = 0,\ a^2 = 1/2$.

*(b)* Multiplicity $r = 3$. Initialization $\{a^k\}_{k=1}^2 = 0,\ a^3 = -1/2$.

*(c)* Multiplicity $r = 4$. Initialization $\{a^k\}_{k=1,3} = 0,\ a^2 = 7/2,\ a^4 = -1/4$.

*(d)* Multiplicity $r = 5$. Initialization $\{a^k\}_{k=1}^3 = 0,\ a^4 = 6/5,\ a^5 = -3/10$.

*Figure 5.3:* Influence of the decay parameter $\varsigma_K$ on the enriched solution $\bar{u}_{h|K}$ for varying multiplicities $r$. By delimiting $\bar{u}_{h,0}$ we solve Eq. (5.23) and enable $\bar{u}_{h,1}$ to readjust according to the value of $\varsigma_K$. By increasing $\varsigma_K$ we gradually enlarge the interface jump between $\bar{u}_{h,0}$ and $\bar{u}_{h,1}$.

scribed by Eq. (4.42) and Eq. (4.43), from which the multiwavelet coefficients within an element $K$ can be written as follows

$$\bar{d}_K^\ell = \frac{1}{\sqrt{2}} \sum_{k=1}^{r} \sum_{i=0}^{N_{\text{art}}-1} G_{\ell k}^{(i)} \bar{U}_{\kappa_i}^k, \qquad \ell = 1, ..., r, \quad N_{\text{art}} = 2, \tag{5.20}$$

where $G_{\ell k}^{(i)}$ are the highpass QMF coefficient matrices (Geronimo et al., 2017) given by Eq. (4.8), $\bar{U}_{\kappa_i}^k$ are the coefficients of $\bar{u}_{h,i}$, and $\kappa_i$ refer to the finer echelon of the two-level multiwavelet expansion within $K$.

Drawing insight from the behavior of the spectrum $|d^\ell|$ associated with analytical functions (see Figure 5.1c), we expect to register a strong link between the regularity of $\bar{u}_{h|K}$ and the rate of decay of its multiwavelet spectrum, given by Eq. (5.20). To evaluate this hypothesis, we examine several values of the decay parameter $\varsigma_K$ associated with the multiwavelet expansion of $\bar{u}_{h|K}$ and monitor the subsequent changes in $\bar{d}_K^\ell$. Naturally, any modification in the details will reshape the original $\bar{u}_{h|K}$ and its regularity. We start by describing its left, $\bar{u}_{h,0}$, and right side, $\bar{u}_{h,1}$, with the generic coefficients

$$a^k = \bar{U}_{\kappa_0}^k, \quad b^k = \bar{U}_{\kappa_1}^k, \tag{5.21}$$

which transform Eq. (5.20) into

$$\overline{d}_K^{\ell} = \tfrac{1}{\sqrt{2}} \sum_{k=1}^{r} \left( G_{\ell k}^{(0)} \mathscr{a}^k + G_{\ell k}^{(1)} \mathscr{b}^k \right). \tag{5.22}$$

By assuming that the spectrum $|\overline{d}_K^{\ell}|$ decays exponentially, we can replace it in Eq. (5.15). Therefore, we have:

$$10^{-\varsigma_K \left(\ell + r - 1\right)} = \tfrac{1}{\sqrt{2}} \left| \sum_{k=1}^{r} \left( G_{\ell k}^{(0)} \mathscr{a}^k + G_{\ell k}^{(1)} \mathscr{b}^k \right) \right|, \qquad \ell = 1, \dots, r, \tag{5.23}$$

where we have injected expression (5.11) into the exponent. Additionally, without loss of generality we set that $c = 1$. Finally, to move from *similarity* in the original equation to *equality* we have assumed sufficiently high quality of fit. By choosing a multiplicity $r$ and setting a value for the parameter $\varsigma_K$, Eq. (5.23) becomes an undetermined linear system with $r$ equations and $2r$ unknowns (coefficients $\mathscr{a}^{\ell}$ and $\mathscr{b}^{\ell}$). To be able to solve the system we initialize $\mathscr{a}^{\ell}$, which causes $\bar{u}_{h,0}$ to be fixed and makes $\bar{u}_{h,1}$ dependent on the input value of $\varsigma_K$.

Figure 5.3 illustrates the resolution of Eq. (5.23) for different multiplicities and values of $\varsigma_K$. For the lowest multiplicity value $r = 2$, Figure 5.3A, shows a progressive increase in the interface jump between $\bar{u}_{h,0}$ and $\bar{u}_{h,1}$ when the rate of decay is reduced ($\varsigma_K \to 0$). Qualitatively speaking, the wider this gap grows, the larger the discontinuity and the less smooth $\bar{u}_{h|K}$ becomes. This result is in agreement with the low values of $\varsigma_K$ recorded for analytical functions when facing discontinuities. The same behavior can be observed for higher multiplicities (Figures 5.3B to 5.3D).

*Two-dimensional case* In the 2-D context we can describe a generic enriched solution $\bar{\boldsymbol{u}}_{h|K}$ by its four contributions $\{\bar{\boldsymbol{u}}_{h,i}\}_{i=0}^{3}$ with coefficients

$$\mathscr{a}^k = \overline{\boldsymbol{U}}_{\kappa_0}^k, \quad \mathscr{b}^k = \overline{\boldsymbol{U}}_{\kappa_1}^k, \tag{5.24a}$$

$$\mathscr{c}^k = \overline{\boldsymbol{U}}_{\kappa_2}^k, \quad \mathscr{d}^k = \overline{\boldsymbol{U}}_{\kappa_3}^k. \tag{5.24b}$$

By replacing Eq. (5.24) into Eq. (4.45) and Eq. (4.46), we have

$$\begin{aligned} \overline{\boldsymbol{d}}_K^{\ell,\alpha} = \tfrac{1}{2} \sum_{k_x,k_y=1}^{r} \Big[ & G_{\ell_x,k_x}^{(0)} H_{\ell_y,k_y}^{(0)} \mathscr{a}^k + G_{\ell_x,k_x}^{(0)} H_{\ell_y,k_y}^{(1)} \mathscr{b}^k \\ & + G_{\ell_x,k_x}^{(1)} H_{\ell_y,k_y}^{(0)} \mathscr{c}^k + G_{\ell_x,k_x}^{(1)} H_{\ell_y,k_y}^{(1)} \mathscr{d}^k \Big], \end{aligned} \tag{5.25a}$$

$$\begin{aligned} \overline{\boldsymbol{d}}_K^{\ell,\beta} = \tfrac{1}{2} \sum_{k_x,k_y=1}^{r} \Big[ & H_{\ell_x,k_x}^{(0)} G_{\ell_y,k_y}^{(0)} \mathscr{a}^k + H_{\ell_x,k_x}^{(0)} G_{\ell_y,k_y}^{(1)} \mathscr{b}^k \\ & + H_{\ell_x,k_x}^{(1)} G_{\ell_y,k_y}^{(0)} \mathscr{c}^k + H_{\ell_x,k_x}^{(1)} G_{\ell_y,k_y}^{(1)} \mathscr{d}^k \Big], \end{aligned} \tag{5.25b}$$

$$\overline{\boldsymbol{d}}_K^{\ell,\gamma} = \tfrac{1}{2} \sum_{k_x,k_y=1}^{r} \Big[ G_{\ell_x,k_x}^{(0)} G_{\ell_y,k_y}^{(0)} \mathscr{a}^k + G_{\ell_x,k_x}^{(0)} G_{\ell_y,k_y}^{(1)} \mathscr{b}^k$$

$$+ G^{(1)}_{\ell_x,k_x} G^{(0)}_{\ell_y,k_y} c^k + G^{(1)}_{\ell_x,k_x} G^{(1)}_{\ell_y,k_y} d^k \Big]. \tag{5.25c}$$

where $k = r(k_x - 1) + k_y$ and $\ell = r(\ell_x - 1) + \ell_y$, with $\ell_x, \ell_y = 1, \dots, r$. Instead of following the single decaying spectrum from Eq. (5.19), we will exceptionally analyze the horizontal, $|\bar{\boldsymbol{d}}^{\ell,\alpha}_K|$; vertical, $|\bar{\boldsymbol{d}}^{\ell,\beta}_K|$; and diagonal spectrum, $|\bar{\boldsymbol{d}}^{\ell,\gamma}_K|$, separately so that we can provide additional equations to properly solve the ensuing linear system. Therefore, we expect an exponential rate of decay of the form:

$$|\bar{\boldsymbol{d}}^{\ell}_K| \sim c 10^{-\varsigma_K M_{eq}}. \tag{5.26}$$

By considering the expression of the number of equivalent vanishing moments $M_{eq}$, given by Eq. (5.18), and assuming $c = 1$ and a high quality of fit (see Table 5.4), Eq. (5.26) becomes

$$|\bar{\boldsymbol{d}}^{\ell,\alpha}_K| = 10^{-\varsigma_K (\ell_x + r - 1)}, \tag{5.27a}$$

$$|\bar{\boldsymbol{d}}^{\ell,\beta}_K| = 10^{-\varsigma_K (\ell_y + r - 1)}, \tag{5.27b}$$

$$|\bar{\boldsymbol{d}}^{\ell,\gamma}_K| = 10^{-\varsigma_K (2(r-1) + \ell_x + \ell_y)}. \tag{5.27c}$$

In the same manner as in the 1-D case, by quantifying the multiplicity $r$ and the decay parameter $\varsigma_K$, the set of equations Eq. (5.27a) to Eq. (5.27c) turn into an undetermined system with $3r^2$ equations and $4r^2$ unknowns (coefficients $a^k, b^k, c^k$, and $d^k$). Initialization of $a^k$ enables us to solve the system by fixing the contribution $\bar{\boldsymbol{u}}_{h,0}$ and making the remaining enriched solution unknowns $\{\bar{\boldsymbol{u}}_{h,i}\}_{i=1}^{3}$, dependent on the decay parameter $\varsigma_K$. In the next paragraphs we evaluate multiple values of $\varsigma_K$ under different multiplicities $r$ and examine how they influence the final shape of $\bar{u}_{h|K}$.

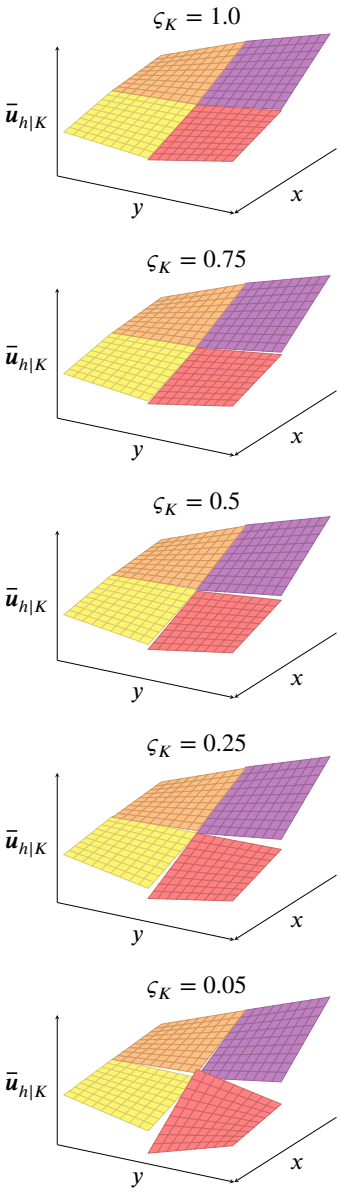


*Figure 5.4:* Effect of the decay parameter $\varsigma_K$ on the enriched solution $\bar{\boldsymbol{u}}_{h|K}$ with multiplicity $r = 2$. We have initialized the system resulting from Eq. (5.26) and Eq. (5.27) by $a^1 = 0$, $a^2 = 4$, $a^3 = -4$, and $a^4 = -7/4$. Consequently, $\bar{\boldsymbol{u}}_{h,0}$ is fixed and the remaining contributions ● ● ● change according to the parameter $\varsigma_K$.

Figure 5.4 outlines the solution to the system for $r = 2$. Similarly to the behavior observed in 1-D, rapid decay rates ($\varsigma_K \approx 1$) report smaller interface jumps between contributions $\bar{\boldsymbol{u}}_{h,i}$, which in turn imply a more regular final $\bar{\boldsymbol{u}}_{h|K}$. When the rate of decay is progressively slowed down ($\varsigma_K \to 0$), the gap between interfaces widens and substantial discontinuities start to emerge, causing $\bar{\boldsymbol{u}}_{h|K}$ to lose regularity. Figure 5.5 illustrates the analysis for $r = 3$, which reports comparable results.

From the study of analytical functions in Section 5.2.2 to the previous discussion on the DG solution, we have proved the existence of a consistent connection between signal regularity and the decline of the spectrum of the multiwavelet coefficients. If we focus our attention exclusively on the DG framework, this result seems to suggest that the decay parameter $\varsigma_K$ represents a reliable estimate of the local regularity of $\bar{\boldsymbol{u}}_{h|K}$ and, by extension, of the original solution $\boldsymbol{u}_{h|K}$.

In light of this result, we can assign the decay parameter $\varsigma_K$ to the role of local regularity indicator. Consequently, by putting together each multiwavelet component $\bar{\boldsymbol{d}}^{\ell,\alpha}_K$, $\bar{\boldsymbol{d}}^{\ell,\beta}_K$, and $\bar{\boldsymbol{d}}^{\ell,\gamma}_K$ into a single decaying spectrum similarly to

Eq. (5.19), and performing a least-squares fit, we finally have:

$$\log \left\| \bar{\boldsymbol{d}}_K^{\ell,\alpha} + \bar{\boldsymbol{d}}_K^{\ell',\beta} + \bar{\boldsymbol{d}}_K^{\ell'',\gamma} \right\|_{L^2} \sim \log c - \varsigma_K M_{eq}\,, \tag{5.28}$$

where $\ell, \ell', \ell'' = 1, \dots, r$ are such that $M_{eq}(\cdot) = \mathcal{N}$, with $\mathcal{N} = r, \dots, 3r-1$. The number of equivalent vanishing moments $M_{eq}$ is given by Eq. (5.18).

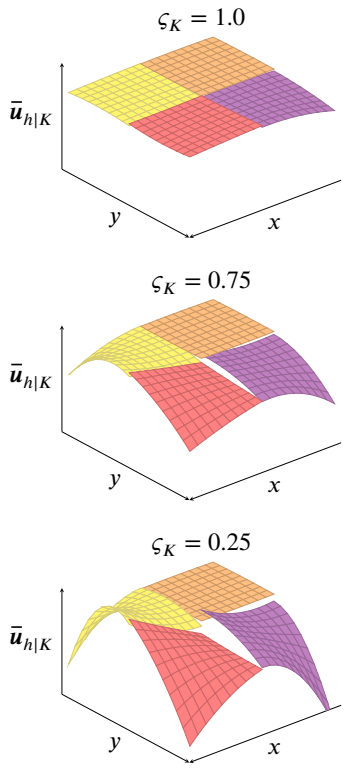


*Figure 5.5:* Influence of decay parameter $\varsigma_K$ on the enriched solution $\bar{\boldsymbol{u}}_{h|K}$ for $r = 3$ and initialization $\{\alpha^k\}_{k=1}^{6} = 0$, $\{\alpha^k\}_{k=7}^{8} = 3/4$, and $\alpha^9 = 0$.

### 5.2.4 *Element marking and hp-decision criteria*

*Element marking criterion* Once we have determined the local error estimates $\eta_K$ for every $K \in \Omega_{h,p}$ (see Section 5.2.1), we now will use this information to select (*mark*) which elements require higher spatial resolution. Note that the error estimates could be used to identify elements which require lower spatial resolution as well. However, neither element agglomeration nor local polynomial reduction will be considered in this study.

There are numerous marking criteria developed in the literature. Based on the analysis presented in Naddei (2019) we have opted for the two following procedures:

(a) *Local threshold criterion*. It is the most intuitive and widely used criterion (see e.g. Oden et al. (1989) or Rueda-Ramírez et al. (2019a)). The idea is to flag an element $K$ if the local value of the error indicator $\eta_K$ is above a user-defined tolerance, $\eta_{\text{tol}}$. Therefore, we define the set of marked elements, $\Omega_{\text{mark}}$, as follows:

$$\Omega_{\text{mark}} = \{K \in \Omega_{h,p} \,|\, \eta_K > \eta_{\text{tol}}\}. \tag{5.29}$$

(b) *Maximum marking criterion*. Initially proposed by Babuvška and Rheinboldt (1978b), it has seen widespread adoption (see e.g. Dörfler and Heuveline (2007)). In this case, $K$ is flagged if $\eta_K$ is above a specified percentage of its maximum. Namely:

$$\Omega_{\text{mark}} = \left\{ K \in \Omega_{h,p} \,|\, \eta_K > \theta \max_{K \in \Omega_{h,p}} \eta_K \right\}, \tag{5.30}$$

where the user-defined parameter $\theta \in [0, 1]$ is called *marking fraction*. The lower this parameter, the higher the number of total marked elements.

*hp-decision criterion* The two marking criteria presented in the previous paragraphs inform us on which elements should be spatially adapted. However, they do not tell us whether to adapt the size, or the polynomial order of the flagged elements to obtain an optimal solution. We base this judgement on the rate of decay of the multiwavelet spectrum. From the observations collected in sections 5.2.2 to 5.2.3, rapid decline of the spectrum suggests high regularity in the solution, which means that $p$-adaptation is indicated.

Otherwise, $h$-adaptation is required. Application of this $hp$-decision criterion leads to the following two element subsets:

$$\Omega_{\text{mark},h} = \left\{K \in \Omega_{\text{mark}} \,|\, \hat{\varsigma}_K < \varsigma_{\text{tol}}\right\}, \tag{5.31a}$$

$$\Omega_{\text{mark},p} = \left\{K \in \Omega_{\text{mark}} \,|\, \hat{\varsigma}_K \geq \varsigma_{\text{tol}}\right\}, \tag{5.31b}$$

where $\Omega_{\text{mark},h}$ and $\Omega_{\text{mark},p}$ represent the subset of the elements flagged for $h$- and $p$-adaptation, respectively; and $\hat{\varsigma}_K$ is the normalized version of the multiwavelet regularity indicator defined as

$$\hat{\varsigma}_K = \frac{1}{\varsigma_{\max} - \varsigma_{\min}} \varsigma_K - \frac{\varsigma_{\min}}{\varsigma_{\max} - \varsigma_{\min}}, \tag{5.32}$$

with $\varsigma_K$ given by Eq. (5.28), and the values $\varsigma_{\min}$ and $\varsigma_{\max}$ provided by

$$\varsigma_{\min} = \min_{K \in \Omega_{h,p}} \varsigma_K, \quad \varsigma_{\max} = \max_{K \in \Omega_{h,p}} \varsigma_K. \tag{5.33}$$

The normalization outlined in Eq. (5.32) ensures that $\hat{\varsigma}_K \in [0, 1]$ for all $K \in \Omega_{h,p}$, independently of the problem under study. Additionally, the user-defined parameter $\varsigma_{\text{tol}} \in [0, 1]$ revealed in Eq. (5.31) allows us to establish an $hp$-threshold to control the advantage of one adaptation type over the other. In other words, we can increase the overall proportion of $\Omega_{\text{mark},h}$ or $\Omega_{\text{mark},p}$ with respect to the larger set $\Omega_{\text{mark}}$ by increasing or reducing $\varsigma_{\text{tol}}$, respectively. Namely:

$$\Omega_{\text{mark}} = \begin{cases} \Omega_{\text{mark},h} & \text{if } \varsigma_{\text{tol}} = 1 \\ \Omega_{\text{mark},h} \cup \Omega_{\text{mark},p} & \text{if } 0 < \varsigma_{\text{tol}} < 1 \\ \Omega_{\text{mark},p} & \text{if } \varsigma_{\text{tol}} = 0 \end{cases} \tag{5.34}$$

Finally we also have

$$\Omega_{\text{mark},h} \cap \Omega_{\text{mark},p} = \varnothing, \tag{5.35}$$

which means that any element $K \in \Omega_{\text{mark}}$ cannot be designated for both $h$- and $p$-adaptation simultaneously.

*Supplementary marking* Right after the marking and $hp$-decision criteria have been applied and we have obtained $\Omega_{\text{mark},h}$ and $\Omega_{\text{mark},p}$, additional restrictions might be enforced. In regard to $h$-adaptation, we limit the separation in refinement levels between neighbouring elements to at most one by marking additional elements if necessary, which we denote by the subset $\Omega_{2:1}$. This condition is frequently called the *two-to-one* rule (Demkowicz et al., 1989) and safeguards that neighbouring elements are not of exceedingly different size. Therefore:

$$\Omega_{2:1} \subset \Omega_{\text{mark},h}. \tag{5.36}$$

Equivalently, regarding $p$-adaptation we limit the change of the local polynomial degree between two neighboring elements to be no larger than one. As a

result of this limitation, additional elements might be flagged for polynomial increase to fulfill this condition. If we symbolize them by the subset $\Omega_{\Delta p=1}$ we have:

$$\Omega_{\Delta p=1} \subset \Omega_{\text{mark},p}\,. \tag{5.37}$$

### 5.2.5 *hp-mesh enrichment methodology*

After selecting one of the marking criteria proposed in Section 5.2.4 together with the *hp*-decision criterion described in the same section, we proceed to the construction of the new *hp*-mesh resulting from the application of the aforementioned guidelines. The *hp*-mesh $\Omega_{h,p}$ is made up by the pair of sets $\Omega_h$ and $p$ (see Eq. (5.1)), each of which require separate handling.

To adapt the mesh $\Omega_h$ we follow the so-called *local mesh refinement* methodology (Bank and Sherman, 1999), which restrict the adaptation to individual marked elements. This is in contrast to *semi-local* approaches such as AMR (Berger and Oliger, 1984), in which elements of one or more regions of the mesh are refined as a group.

In particular, the element-refinement methodology pursued in this study is based on the work by Kuru et al. (2016) and Naddei (2019), where they have implemented an (isotropic) local mesh refinement approach on non-conforming curvilinear hexahedral and quadrilateral meshes. Their idea is to divide each of the marked elements into $2^d$ new elements, where $d$ is the dimension of the problem.

In our case, we consider simpler non-conforming Cartesian meshes in 2-D. Consequently, elements become rectangles that, if marked for refinement, may produce four new geometrically similar rectangles. To visualize this concept let $\Omega_h^{(0)}$ be the given initial mesh and $\Omega_h^{(1)}$ be the resulting mesh after one refinement step. We denote any $K^{(0)} \in \Omega_{\text{mark},h}^{(0)}$ a *parent* element. Its associated *child* elements are denoted by the set $\{K_j^{(1)}\}_{j=0}^{3} \in \Omega_h^{(1)}$. Then, thanks to the refinement operator $\mathcal{Q} : \{K^{(0)}\} \to \{K_0^{(1)}, ..., K_3^{(1)}\}$ we can explicitly define the link between parent and children in physical space. The operator $\mathcal{Q}$ can be further expressed in the reference space as follows:

$$\mathcal{Q} = \Xi_K \hat{\mathcal{Q}}\, \Xi_K^{-1} \tag{5.38}$$

where $\hat{\mathcal{Q}} : \{\hat{K}\} \to \{\hat{K}_0, ..., \hat{K}_3\}$ denotes the operator that divides the reference element into four identical children, and $\Xi_K$ is the bijective transformation from reference to physical space. Because we work with rectangles, the transformation is simply a scaling of the reference space by the constant Jacobian of the transformation. Figure 5.6 describes the procedure in detail.

The second contribution of the *hp*-mesh $\Omega_{h,p}$ is given by the degree distribution $p$, which is just the allocation of a local polynomial degree $p_K$ to each $K \in \Omega_h$. To adapt the vector $p$ we adjust the local polynomial degree $p_K$ individually. Particularly, our approach is based on the isotropic $p$-adaptive

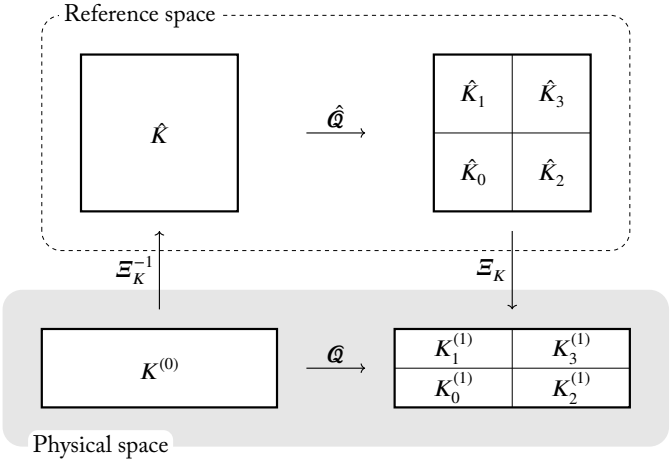


*Figure* 5.6: Isotropic $h$-refinement in the context of reference and physical element.

methodology described by Naddei et al. (2018). In the study the authors increase the local order of the approximation by one when the element is flagged for $p$-enrichment. If we consider $\mathcal{p}^{(0)}$ as the initial $p$-vector, the $p$-distribution after adaptation is given by

$$\mathcal{p}^{(1)} = \left\{ p_K, K^{(0)} \notin \Omega^{(0)}_{\text{mark},p} \right\} \cup \left\{ p_K + 1, K^{(0)} \in \Omega^{(0)}_{\text{mark},p} \right\} \tag{5.39}$$

### 5.2.6 *The hp-adaptive algorithm*

A flow chart describing our $hp$-adaptive algorithm for steady problems is shown in Figure 5.7. The first step of the algorithm consists in providing an initial $hp$-mesh $\Omega^{(0)}_{h,\mathcal{p}}$ and solving for the corresponding DG approximate solution $\boldsymbol{u}^{(0)}_{h,\mathcal{p}}$. Namely, the non-linear system of ordinary differential equations given by Eq. (2.26) is first linearized by Newton's method and then the resulting linear system is solved by the GMRES iterative method combined with an incomplete LU preconditioning. In case that an explicit scheme to evolve the solution in time is used instead, we use the SSP Runge-Kutta method presented in Section 2.2.7. The time evolution is stopped once the time residual is dropped below $1 \times 10^{-10}$ (implicit) or $1 \times 10^{-12}$ (explicit). It is worth mentioning that the lowest discretizations errors reported in the numerical results (see next Chapters 6 and 7) are in the range $1 \times 10^{-7}$ to $1 \times 10^{-8}$. Therefore, we make sure that the time residual does not dominate the discretization error.

Once the numerical solution $\boldsymbol{u}^{(0)}_{h,\mathcal{p}}$ is converged, its element-wise contribution $\boldsymbol{u}^{(0)}_{h,\mathcal{p}|K}$ is subjected to a series of post-processing operations. Firstly, we build a more accurate approximate solution $\bar{\boldsymbol{u}}^{(0)}_{h,\mathcal{p}|K}$ by employing any of the reconstruction methods described in Section 4.3. Secondly, we perform a local multiscale decomposition of $\bar{\boldsymbol{u}}^{(0)}_{h,\mathcal{p}|K}$ to extract its multiwavelet contribution $\overline{\mathscr{D}}^{(0)}_K$, as explained in Section 4.4. Lastly, we construct the error estimator $\eta^{(0)}_K$ and regularity indicator $\varsigma^{(0)}_K$ based on the spectrum $\overline{\mathscr{D}}^{(0)}_K$ of the multiwavelet coefficients, as presented in sections 5.2.1 and 5.2.3, respectively. On the one hand, $\eta^{(0)}_K$ offers an insight into the quality of the solution and thus it

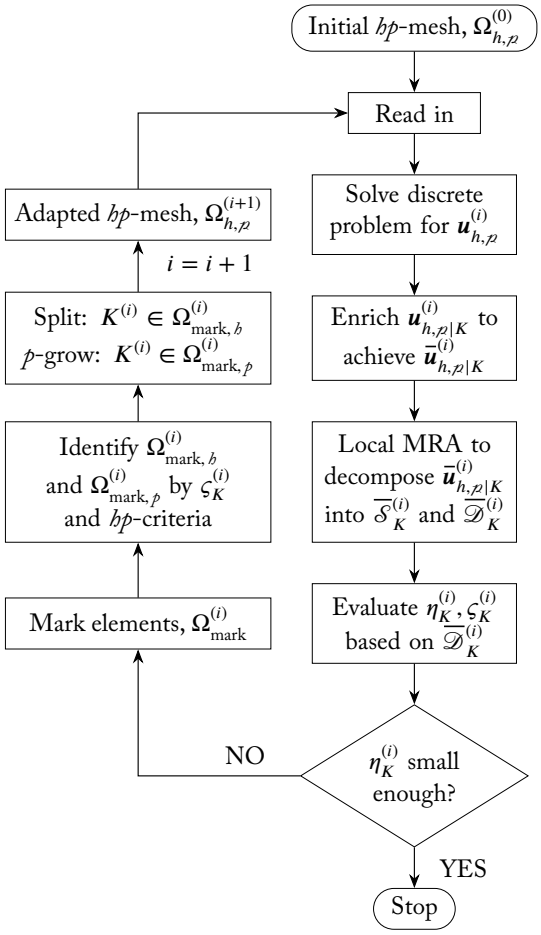


*Figure 5.7:* Flow chart of the proposed $hp$-adaptive algorithm.

determines if the spatial resolution must be upgraded. If that is the case, we proceed to flag the elements that demand higher resolution, $\Omega^{(0)}_{\text{mark}}$, according to the marking strategies identified in Section 5.2.4. On the other hand, $\varsigma^{(0)}_K$ and the $hp$-decision criterion work together to estimate the smoothness of the solution and assign either $h$- or $p$-adaptation to the elements in $\Omega^{(0)}_{\text{mark}}$ accordingly. We then proceed to adapt the elements belonging to $\Omega^{(0)}_{\text{mark},h}$ and $\Omega^{(0)}_{\text{mark},p}$ by following the methodology presented in Section 5.2.5 to arrive to the adapted $hp$-mesh $\Omega^{(1)}_{h,p}$. The discrete problem for the new mesh is solved again and the entire procedure is repeated until certain error criteria are fulfilled.

Generally, two extra steps are applied right after obtaining $\Omega^{(1)}_{h,p}$. The first step is the so-called *reinitialization* operation. It means that the $L^2$-projection of the previous solution $\boldsymbol{u}^{(0)}_{h,p}$ is used as the initial condition on the newly generated $\Omega^{(1)}_{h,p}$. The second step is *load balancing* in the context of parallel computations. This operation leads to a uniform distribution of the computational load by efficiently partitioning $\Omega^{(1)}_{h,p}$ taking into account the new number of degrees of freedom and the element-wise distribution of polynomial degrees.

## 5.3 PARALLEL IMPLEMENTATION

It is widely accepted that the compact stencil and discontinuous behavior of the DG spatial operators make the implementation of DGMs over multi-processor distributed-memory architectures to scale remarkably well, as the number of processors increases (see e.g., Biswas et al. (1994)).

In the present work, parallelization is implemented by using *message passing interface* (MPI). In particular, the computational domain is divided into a number of partitions and each partition is allocated to an available MPI process. This operation is generally labelled as *mesh partitioning*. Since the flux evaluations in the DGM involve only the current element and its immediate neighbors, mesh partitioning guarantees that the greater part of the flux computations within an individual MPI process demand no inter-process communication. To enable communication between two distinct MPI processes a buffer of values is constructed along their shared boundary and the relevant information is delivered by carrying out a single MPI message exchange. The main goal of mesh partitioning is to distribute the workload among the available processors (*load balancing*), while minimizing the communication between MPI processors. In doing so, the operation of the multi-processor environment is optimized.

Load balancing becomes an important question for *hp*-meshes due to the number of degrees of freedom (and hence the computational load) varying from element to element. In this case, well-balanced mesh partitioning must include some element-wise measure of the computational load.

In the context of *h/p*-adaptations, Naddei (2019) has performed a detailed comparison of different methodologies to estimate the computational load and their effect on improving the resulting domain decomposition. Naddei evaluates the mesh partitioning quality by measuring the MPI imbalance under various circumstances. If the effect of the local polynomial degree is ignored, high MPI imbalances are obtained. Conversely, factoring in computational load estimates based on operation counts per element (proportional to the local $p$) seem to reduce the imbalance but the results are not consistent. The most balanced results are achieved when the estimates are based on direct measurements of computational times.

For that reason, to drive the mesh partitioning in the present work we have chosen the later approach. Most importantly, Naddei (2019) claims that it does not require to be performed every time a new simulation is launched. Once the calibration has been completed for a given set of discretization, physical model, and hardware, these parameters can be recycled for any future simulation sharing similar characteristics.

## 5.4 CONCLUDING COMMENTARY

In this chapter we have developed an *hp*-adaptive scheme built on the local multiresolution analysis of the DG solution. We have made significant devel-

opments in computing the estimation of the error, in choosing the adaptive approach, and in deciding on the appropriate *hp*-adaptive strategy.

The estimation of the error has been assigned to the multiwavelet error estimator, which combines the concepts of discretization-based indicators and multiresolution-based adaptation by evaluating the $L^2$-norm of the local multiwavelet contribution.

In order to adjust the spatial resolution, we have selected local mesh enrichment by *hp*-adaptation as the adaptive approach, which is especially well-suited to discontinuous Galerkin methods. In particular, we have chosen isotropic mesh and polynomial order refinement.

Lastly, we have built a suitable *hp*-adaptive strategy by pairing the multiwavelet regularity indicator, which measures the rate of decay of the spectrum of the multiwavelet coefficients, with an *hp*-decision criterion based on the findings of a consistent connection between solution smoothness and the decline of the multiwavelet spectrum.

# Part III

# NUMERICAL RESULTS

# Chapter 6

# H-ADAPTIVE SIMULATIONS

In this chapter, the multiwavelet error estimators developed in Section 5.2.1 are assessed and compared against relevant estimators from the literature. Our objective is to evaluate their overall performance in the context of *h*-adaptive simulations. For each error estimator we analyze the convergence history of the adaptive algorithm, the memory savings achieved, and the regions of the mesh selected for adaptation. It is well known that, local *h*-refinement produces optimal adaptation of the spatial resolution in the vicinity of irregular features, such as physical and geometrical singularities. Therefore, we focus our attention into two configurations that would potentially benefit from *h*-adaptation: the one-dimensional viscous Burgers equation in the presence of a shock, and the two-dimensional laminar flow over a backward-facing step. This step acts as a geometrical singularity which has a strong influence on the downstream flow.

It is worth mentioning that in this chapter we are exclusively focused on *h*-adaptation. Therefore, the regularity indicator, which has been presented in Section 5.2.3 as a companion of the error estimator, is not used here. We thus configure the *hp*-criterion from Section 5.2.4 to solely allow for mesh refinement.

This chapter is organized as follows. We begin the chapter by studying the 1-D viscous Burgers equation in Section 6.1. We describe the computational details employed in the simulations in Section 6.1.1. The effect of the different estimators on the *h*-adaptive results are analyzed by means of the discretization error and the effectivity index, which are the subjects of Sections 6.1.3 and 6.1.5, respectively. The 1-D configuration is followed by Section 6.2, in which we present the 2-D laminar flow over a backward-facing step. The problem configuration is described in Section 6.2.1. In Section 6.2.2 we compare our reference solution with results from the literature to establish a solid baseline for *h*-refinement. Adaptation is introduced in Section 6.2.3, followed by the review of the *h*-adapted meshes in Section 6.2.4, and the analysis of the error in Section 6.2.5. We also discuss the memory and cpu-time gains by activating adaptation in Section 6.2.6 and 6.2.7, respectively. Additionally, Section 6.2.8 presents the evolution of separation/reattachment lengths. Finally, we close the chapter by examining the performance of the family of multiwavelet estimators in Section 6.2.9. and by outlining the main conclusions of the chapter in Section 6.3.

## 6.1 viscous burgers equation

### 6.1.1 *Computational parameters*

Based on the the one-dimensional viscous Burgers equation, which has been described in detail in Section 2.1.2, we perform a series of steady simulations on the computational domain $\Omega_h = [-1, 1]$. We cover two configurations with different initial conditions (ICs) and boundary conditions (BCs).

(a) Firstly, a stationary front (IC-*shock*) which simulates the presence of a sharp gradient in the middle of the domain. For this configuration we have

$$u(x, 0) = -\tanh(x/2\nu) \qquad \text{with } \nu = 0.02 \text{ and } u(\mp 1, t) = \pm 1\,. \tag{6.1}$$

These conditions are analogous to the solution of the Riemann problem for large enough $t > 0$.

(b) The second configuration is determined by a sinusoidal function and it is representative of a smooth solution (IC-*smooth*). Thus we define

$$u(x, 0) = \sin(2\pi x) \qquad \text{with } u(\mp 1, t) = 0\,. \tag{6.2}$$

A source term is added to ensure the convergence to a forced steady solution. In addition, the corresponding steady solution is smooth without sharp gradients. Namely:

$$S(x) = (2\pi)\sin(2\pi x)\cos(2\pi x) + \nu(2\pi)^2 \sin(2\pi x). \tag{6.3}$$

To evolve the solution in time from either of the initial conditions up to the steady-state, the explicit scheme presented in Section 2.2.7 is employed. We then apply recursively the *hp*-adaptive algorithm explained in Section 5.2.6 and Figure 5.7 until we achieve the desired adapted solution. As we have mentioned in the beginning of the chapter, by calibrating the *hp*-criterion to uniquely allow for mesh refinement the algorithm becomes an *h*-adaptive procedure.

The aforementioned algorithm determines if refinement is required based on the value provided by an error estimator in conjunction with the *local threshold* marking strategy described by Eq. (5.29) in Section 5.2.4. We consider the three variations of the multiwavelet error estimator developed in Section 5.2.1 and presented in Eq. (5.4). We remind the reader of the terminology of these estimators:

1. $\kappa$-*multiwavelet* estimator, denoted by $\eta_K^{\kappa\text{-MW}}$.
2. $K$-*multiwavelet* estimator, symbolized by $\eta_K^{K\text{-MW}}$.
3. $\Gamma$-*multiwavelet* estimator, given by $\eta_K^{\Gamma\text{-MW}}$.

and the additional two estimators from the literature:

4. *Small-scale energy density* estimator, $\eta_K^{\text{SSED}}$ (Kuru et al., 2016).

5. *Spectral decay* estimator, $\eta_K^{\mathrm{SD}}$ (Taube et al., 2010).

### 6.1.2 *Definition of errors*

We now define several quantities that will be used to better understand the numerical results that will be presented in the following sections. Let $u$ be the exact solution to the viscous Burgers equation and $u_h \in \mathscr{V}_h^p$ its approximate DG solution. We define the discretization error as follows:

$$\|e_h\|_{L^2(\Omega)} = \|u - u_h\|_{L^2(\Omega)}. \tag{6.4}$$

Additionally, we measure the difference between the approximate DG solution $u_h$ and the reconstruction $\bar{u}_h \in \mathscr{V}_h^p$ built in Chapter 4 by:

$$\|\mathscr{E}_h\|_{L^2(\Omega)} = \|\bar{u}_h - u_h\|_{L^2(\Omega)} \quad \text{with} \quad \bar{u}_h = \sum_K \bar{u}_{h|K}, \quad \forall K \in \Omega_h, \tag{6.5}$$

which follows the nomenclature in Dolejší and Solin (2016). The authors set Eq. (6.5) as their estimation of the discretization error. We call this measure the *Dolejší estimation*. In our case, the value of $\bar{u}_{h|K}$ is given by the reconstruction methods described in Sections 4.3.1 to 4.3.3. Therefore, we have three versions of the Dolejší estimation, corresponding to the three post-enrichment methods studied. They are denoted by $\mathscr{E}_h^\kappa$, $\mathscr{E}_h^K$, and $\mathscr{E}_h^\Gamma$. The Dolejší estimation becomes another entry to the comparison between the multiwavelet-based estimators and the SSED and SD estimators.

It is also interesting to measure the quality of the error estimation. To this end, we define the *effectivity index* as the ratio between the error given by the indicator and the discretization error. It reads

$$\imath^{\mathrm{eff}} = \frac{\eta}{e_h}, \tag{6.6}$$

where $\eta = \left(\sum_{K\in\Omega_h} \eta_K^2\right)^{1/2}$. An index close to unity means that the estimator accurately mimics the evolution of the discretization error. For each computation of the $h$-adaptive algorithm, we evaluate the error estimator over the full domain, $\eta$; the discretization error, $e_h$; and the Dolejší estimation, $\mathscr{E}_h$, as well as the effectivity index for the selected cases.

### 6.1.3 *Error analysis of the h-adaptive results*

An analysis of the effect of the estimators in the adaptation of the viscous Burgers equation under IC-*shock* is plotted in Figure 6.1 for different degrees $p$ of the numerical solution. Figures 6.1A to 6.1C show the variation of the discretization error $e_h$ in the conservative variable $u$ versus the number of degrees of freedom (#DOFs) when uniform $h$-refinement is performed as well as for the locally $h$-adapted solution under the different error estimators. The #DOFs is calculated by evaluating the number of degrees of freedom in each element $(p+1)^d$ (with $d$ the dimension of the problem) multiplied by the

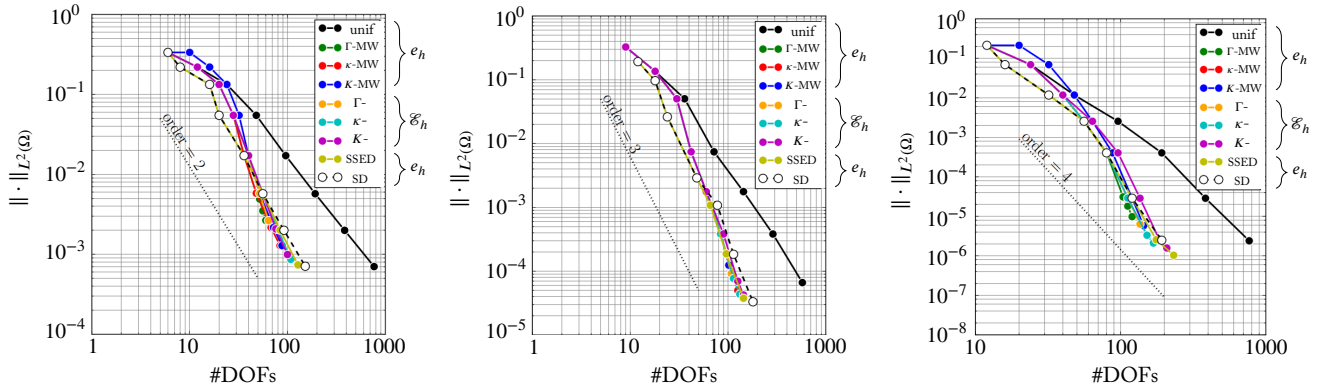


*(a)* $p = 1$ *(b)* $p = 2$. *(c)* $p = 3$.

*Figure* 6.1*:* Viscous Burgers equation. Discretization error in $L^2$-norm under uniform and $h$-adaptive refinement for selected orders of the numerical solution. Adaptation is guided by various estimators. The multiwavelet family of estimators, Eq. (5.3), is denoted by ● ● ●, the estimators from the literature, Eqs. (5.8) and (5.9), are symbolized by ● ○, and the Dolejší estimation, Eq. (6.5), is showcased by ● ● ●. For all estimators, the adaptive process is performed up to the 7th adaptation step.

total number of elements in the computational domain. For every analyzed degree, the error associated with the uniform $h$-refinement follows the theoretical slope determined by the order of the method, as illustrated by the dashed lines.

As regards the adaptive procedure, all the estimators lead to a large decrease in the #DOFs for a given level of accuracy. The SSED and SD estimators show a marginally faster reduction of the #DOFs during the initial refinement steps. However, the multiwavelet-based estimators display a slightly better performance in the last refinement steps, especially at lower degrees of the approximation. They achieve savings in #DOFs of about 85 % in $p = 1$, see Figure 6.1A, whereas the SSED and SD estimators show a reduction of around 81 % for the same degree. The savings are scaled down to 77 % for the MW-based estimators and 75 % for the SSED and SD estimators when the degree is increased to $p = 3$, as can be seen in Figure 6.1C. This shows that the higher the degree, the closer is the behavior of the MW-based estimators to the SSED and SD estimators. Indeed, the difference in the savings of #DOFs goes from 4 % to 2 % when jumping from $p = 1$ to $p = 3$. Overall, the evolution of the MW-based estimators closely resembles the behavior of the estimators from the literature while showing slightly larger savings at lower degrees. This low-order outcome is expected, as the SSED and SD estimators are known to underperform at low orders of the approximation (Naddei, 2019). These results yield a validation of our proposed estimators.

Finally, in the same figures we observe that the different Dolejší estimations behave similarly to their homologous MW-based error estimators. This further validates the idea of using reconstruction techniques as an important tool in mesh adaptation. At this point, the question of why using a multiwavelet expansion which is computationally more expensive than a direct comparison between the original DG solution and a post-enriched solution may arise. The answer resides in the fact that the multiwavelet expansion yields more detailed

information about the solution and its local regularity. This is especially true in higher dimensions, where the details are directly given component-wisely. We will address these concerns in Chapter 7, where this extra information is used to drive *hp*-adaptivity. Moreover, studies of the effectivity index (not presented in this work) show a behavior closer to unity when employing the multiwavelet decomposition. Hence, these reasons motivate the use of a multiwavelet expansion to compute the error estimators.

### 6.1.4 *Analysis of the h-adapted meshes*

We now focus our attention on the final *h*-adapted mesh resulting from the activation of the three different local multiwavelet-based estimators proposed in this research. We have just seen that the SSED estimator shows a slightly better agreement with our estimators compared to the SD. Thus from now on we will only use the SSED estimator for comparison purposes.

The distributions of the refinement levels along the computational domain for each estimator are plotted in Figures 6.2A, 6.2B, and 6.2C for $p = 1$, $p = 2$, and $p = 3$, respectively. It can be observed that, predictably, the area surrounding the discontinuity is subjected to a higher level of refinement. This is true for all estimators. When we increase the degree of the solution, the number of refinement levels decreases. This behavior is expected because we are increasing the spatial resolution by modifying the local polynomial degree and thus fewer elements are required to achieve a prescribed level of accuracy. The dashed line represents the required refinement level of an uniform mesh to reach the user defined tolerance $\eta_{\text{tol}} = 1 \times 10^{-6}$.

The activation of the $K$-multiwavelet and $\kappa$-multiwavelet estimators leads to an almost identical pattern of refinement centered around the discontinuity, regardless of the degree. The $\Gamma$-multiwavelet estimator seems to perform marginally better by generating a narrower refined region surrounding the discontinuity. In the case of the SSED estimator, the wider refined region translates into a higher amount of #DOFs compared the MW-based estimators. Again, this is due to the better performance of the multiwavelet family in the last refinement steps. Certainly, they never surpass the dashed line. This behavior is ideal because this means that their highest refinement level remains below the level of the uniform mesh imposed by the tolerance $\eta_{\text{tol}}$. For the SSED estimator the behavior is different, it exceeds the threshold leading to an over-refined mesh. Particularly severe is the behavior for $p = 1$, surpassing six levels above $\eta_{\text{tol}}$. The over-refinement is mitigated by using $p = 3$, in which the difference is reduced to one level. This behavior is closely related to the effectivity index, as will be discussed in the next paragraph.

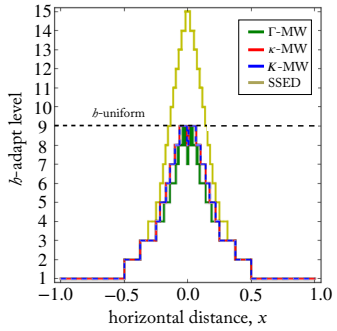


*(a)* $p = 1$

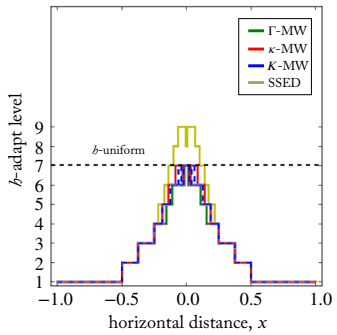


*(b)* $p = 2$.

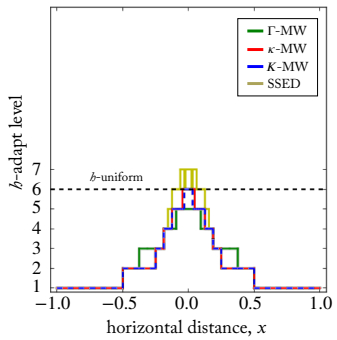


*(c)* $p = 3$.

*Figure 6.2:* Viscous Burgers equation. Different levels of refinement achieved by every error estimator at the last iteration step for selected solution orders. The dashed line corresponds to an uniform mesh with discretization error $\|e_{h|K}\| < \eta_{\text{tol}}$ for all $K \in \Omega_h$ where $\eta_{\text{tol}} = 1 \times 10^{-6}$. The adaptive process is then performed for each estimator until we achieve $\eta_K < \eta_{\text{tol}}$ in every element of the domain.

### 6.1.5 *Effectivity index of the h-adaptive results*

*Solution with shock* The evolution of the discretization error for the $p = 3$ adapted and uniform grid solutions for the initial condition IC-*shock* is illustrated in Figure 6.3. In this figure the error on the adapted mesh is compared

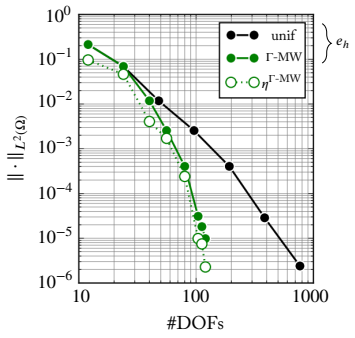


*(a)* Γ-multiwavelet estimator.

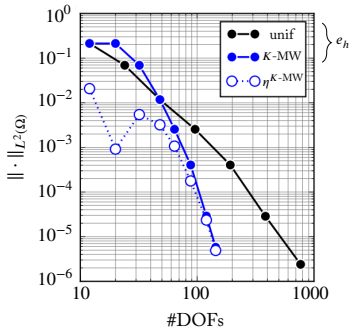


*(b)* $\kappa$-multiwavelet estimator.

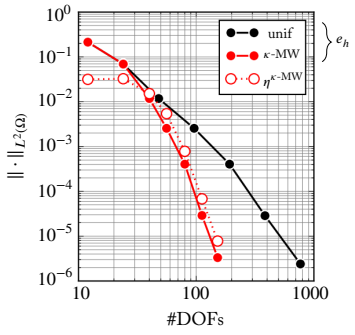


*(c)* $\kappa$-multiwavelet estimator.

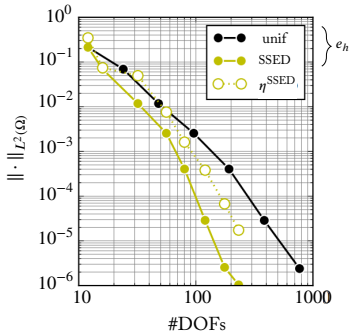


*(d)* SSED estimator.

*Figure 6.3:* Viscous Burgers equation for IC-*shock* and $p = 3$. Error estimator performance under $h$-adaptation. We compare the discretization error (solid line) versus the estimation reported by the indicator (dashed line).

to the value given by the estimator. If these values show a similar evolution along the refinement process, then the effectivity index associated with the estimator, $\iota^{\text{eff}}$ (see Eq. (6.6)), is close to unity. That is $\eta \simeq e_h$. It is understood that values of the effectivity index close to unity are desirable for *a posteriori* indicators (see e.g. error estimation for elliptic problems in Babuvška and Rheinboldt (1980)). However, when dealing with hyperbolic or parabolic problems such as the viscous Burgers equation, you may come up with possibly less precise estimates and obtain effectivity indices higher than unity (see e.g. Johnson (1990)).

Figure 6.3A presents the estimated error computed by the Γ-multiwavelet indicator versus the #DOFs corresponding to each iteration of the adaptation process. The estimator reports an effectivity index between $0.4 < \iota^{\text{eff}} < 0.7$ during the first iterations. Then progressively drops to $\iota^{\text{eff}} = 0.3$ in the last steps of refinement. The same behavior is observed in Figure 6.3B for the $K$-multiwavelet indicator. However, the first refinement steps report a poor effectivity index for this estimator, which may explain the error overshoot on the adapted mesh. After the first iterations, the effectivity index gradually improves until achieving values close to unity in the last refinement steps. Moving to the $\kappa$-multiwavelet indicator, Figure 6.3C, we observe a more uniform behavior. Except during the first steps of refinement, the effectivity index remains mostly constant at $\iota^{\text{eff}} = 2$. The estimation mimics the behavior of the discretization error, while remaining slightly higher. Lastly, the SSED indicator displayed in Figure 6.3D reports an erratic behavior, with a precise estimate during the first refinement steps and effectivity ratios progressively deteriorating to $\iota^{\text{eff}} > 10$. This behavior may justify the over-refinement observed in Figure 6.2.

*Smooth solution* Before drawing any conclusion, it is worth studying the behavior of the estimators for a more regular solution. A further analysis of the effectivity index for the initial conditions IC-*smooth* and $p = 3$ is performed in Figure 6.4. This example shows virtually no difference between the use of the uniform and the adapted mesh. This is a consequence of the regularity of the solution. In this situation, performing adaptation is not justified because the final adapted grid is nearly indistinguishable from the uniform mesh. However, a few interesting conclusions can be extracted from this analysis.

Firstly, the Γ-multiwavelet indicator, displayed in Figure 6.4A, behaves inadequately when the solution is smooth. In this case, the effectivity index steadily drops to $\iota^{\text{eff}} < 0.1$ in the last steps of refinement. It seems that the influence of the jump of the conservative quantity at the interface between elements is not well captured by the reconstruction. Thus the disparity between estimation and discretization error. Secondly, the $K$-multiwavelet indicator, illustrated in Figure 6.4B, follows the discretization error particularly well, with $\iota^{\text{eff}} = 1$ during the last steps of refinement. However, a slight overshoot of the estimator appears in the first stage of the refinement. This has been likely caused by under-refining during the early steps. If we pay attention to the previous

results reported in Figure 6.3B, we can resolve that the $K$-multiwavelet indicator is prone to this sort of behavior. The same overshoot can be observed for the SSED indicator, Figure 6.4D, though happening at later refinement stage. This estimator continues to report high values of the effectivity index, $\imath^{\text{eff}} > 10$, similarly to what we observed when IC-*shock* was studied. Finally, the $\kappa$-multiwavelet indicator, Figure 6.4C, maintains its characteristic regular behavior with a nearly constant $\imath^{\text{eff}} = 2$ and a satisfactory tracking performance.

From the analysis of Figures 6.3 and 6.4 we thus conclude that the multiwavelet-based indicators constitute a consistent approach for tracking the discretization error of the DG approximation. They perform substantially better than the SSED indicator provided by the literature, which shows an excessively high value of the effectivity index. In particular, the $\kappa$-multiwavelet indicator features a regular behavior while maintaining an acceptable effectivity index so that it can be reliably used to control the adaptation process. Based on this analysis, the $\kappa$-multiwavelet indicator has been selected to drive the $h$-adaptive algorithm in the following study of the two-dimensional backward-facing step flow.

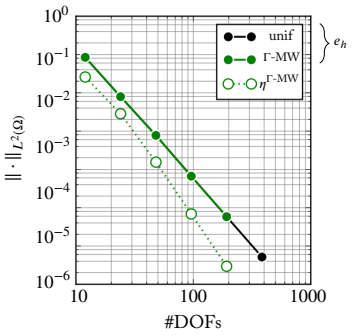


*(a)* Γ-multiwavelet estimator.

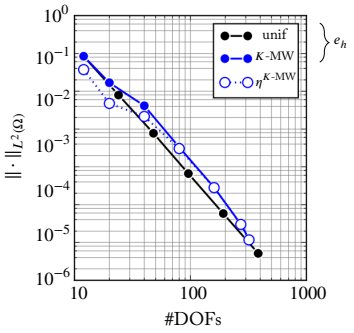


*(b)* $K$-multiwavelet estimator.

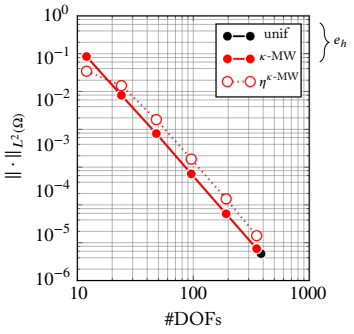


*(c)* $\kappa$-multiwavelet estimator.

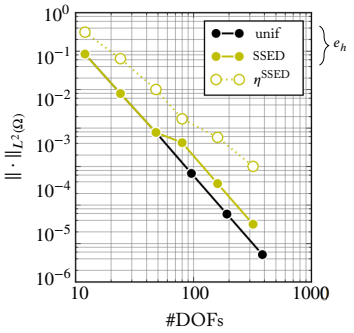


*(d)* SSED estimator.

*Figure* 6.4*:* Viscous Burgers equation for IC-*smooth* and $p = 3$. We measure the discretization error (solid line) against the estimation reported by the indicator (dashed line) to evaluate the performance of the said indicator.

## 6.2 LAMINAR BACKWARD-FACING STEP

In this section a series of numerical simulations of a two-dimensional steady laminar flow over a backward-facing step is performed to assess the validity of the multiwavelet error estimator (see Section 5.2.1) in the context of mesh adaptation.

### 6.2.1 *Computational parameters I: h-uniform simulations*

The geometry of the computational domain is shown in Figure 6.5A. Following the work of Barton (1997), an extra inlet channel has been considered to reduce the influence of the step in the upstream flow region. Similarly, Erturk (2008) has concluded that its length must be at least five times the height of the step to be effective. Thus we have sized our inlet channel accordingly. With regard to the outlet or exit boundary, it must be located at a distance sufficiently far away from the step so that the flow becomes fully developed. Similar studies by Keskar and Lyn (1999) and Gartling (1990) have found that placing the exit boundary at 60 step heights downstream from the step is sufficient to recover a fully developed flow. Therefore, we have sized our expanded channel in accordance. The height of the inlet channel is equal to the dimension of the step, and the channel height in the expanded region (downstream of the step), $H$, is twice the height of the step, $h$. Therefore, the expansion ratio of the backward-facing step results in $H/h = 2$. The Reynolds number of the problem is $Re = 800$ and defined as $Re = \frac{UH}{\nu}$, where $U$ is the inlet mean velocity, i.e. two thirds of the maximum inlet velocity. Lastly, to insure the incompressibility of the problem the Mach number is set to $Ma = 0.1$.

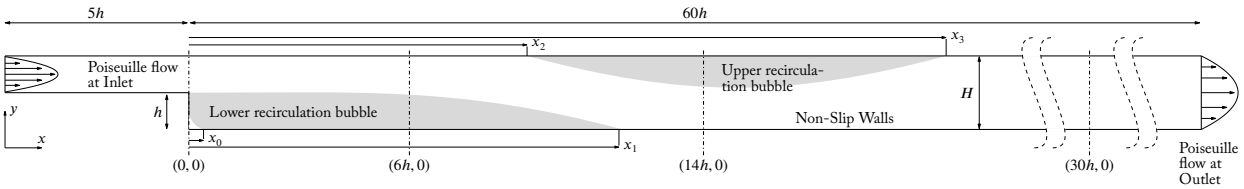


*(a)* Computational domain and boundary conditions.

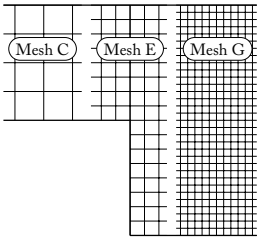


*(b)* Illustration of uniform grids employed.

| Mesh | #Elts | #DOFs | | | #Elts–$y$ | #DOFs–$y$ | | |
|---|---|---|---|---|---|---|---|---|
| | | $p=1$ | $p=2$ | $p=3$ | | $p=1$ | $p=2$ | $p=3$ |
| **A** | 536 | | | 8576 | 4 | | | 16 |
| **B** | 1206 | | 10 854 | | 6 | | 18 | |
| **C** | 2144 | 8576 | | 34 304 | 8 | 16 | | 32 |
| D | 4554 | | 40 986 | | 12 | | 36 | |
| E | 8096 | 32 384 | | 129 536 | 16 | 32 | | 64 |
| F | 18 000 | | 162 000 | | 24 | | 72 | |
| G | 32 000 | 128 000 | | 512 000 | 32 | 64 | | 128 |
| H | 72 000 | | 648 000 | | 48 | | 144 | |
| I | 128 000 | 512 000 | | 2 048 000 | 64 | 128 | | 256 |
| J | 288 000 | | 2 592 000 | | 96 | | 288 | |
| **K** | 512 000 | 2 048 000 | 4 608 000 | | 128 | 256 | 384 | |

*(c)* Number of elements (#Elts) and degrees of freedom (#DOFs) for every uniform grid in the study, both in total and along the $y$-direction (#Elts–$y$ and #DOFs–$y$) of the expanded channel. Color grouping refers to an approximate equivalence in the #DOFs between different orders in the computations.

*Figure 6.5:* Laminar backward-facing step. Description of the computational domain, boundary conditions, and grids employed.

Regarding the boundary conditions, we impose at the inlet boundary a fully developed plane Poiseuille flow so that the velocity profile at the entrance of the domain is parabolic. At the exit boundary, a non-reflecting boundary condition is imposed such that the velocity profile of the numerical solution at the exit boundary matches the analytical parabolic profile of a Poiseuille flow. Finally, wall boundary conditions are imposed on the upper and bottom walls of the channel, as well as on the surface of the step. The details regarding the considered configuration are reported in Figure 6.5A.

To mesh the domain we have considered 11 different Cartesian uniform grids, depending on the order of the numerical solution at hand. Table 6.5C describes the configurations in detail. The grids are named A to K, and ordered by increasing resolution. A sample of the meshes C, E and G is displayed in Figure 6.5B. The grids A, B and C (gray shaded cells) correspond to the three initial computational grids from which the adapted grids will be built. They represent the coarsest starting meshes for $p = 1$, $p = 2$, and $p = 3$, respectively. The grid K with $p = 2$ (boxed cell) corresponds to the reference solution of the present study. Figure 6.6 showcases the behavior of the latter solution downstream of the step. The presence of the geometrical singularity generates two main recirculation regions along the upper and bottom wall, and an additional recirculation bubble at the corner beneath the step.

Those grids that retain an equivalent number of degrees of freedom (#DOFs) for different orders in the computations are labelled with the same color nomenclature. That means that their numerical solution should be comparable between computations based on different polynomial orders. Table 6.5C

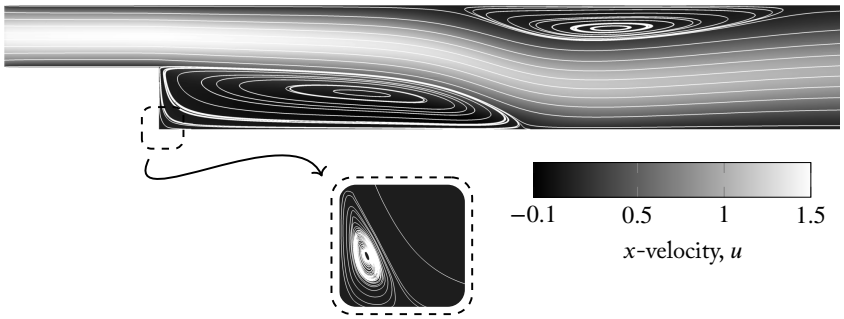


*Figure 6.6:* Laminar backward-facing step. Illustration of the streamlines and recirculation bubbles downstream of the step.

also reports how this equivalence in #DOFs is maintained along the $y$-direction of the expanded channel. The uniform grids obviously display the same #DOFs per unit distance in both $x$- and $y$-direction. Finally, for the coarser meshes (grids A to E), the region immediately after the inlet has been locally refined so that we are able to properly capture the parabolic inflow from the initial steps of the adaptation process and therefore impose an appropriate inlet profile.

Regarding the aforementioned coarser meshes, the study by Yee et al. (1997) shows that when a low resolution grid is employed in the backward-facing step flow at $Re = 800$, a spurious oscillating numerical solution is obtained and the steady-state cannot be reached. The work of Erturk (2008), in which an interval of $Re = [100, 3000]$ is investigated by solving the flow using a second order finite-difference method, employs a very fine mesh so that convergence to the steady-state can be achieved. For the low resolution meshes employed in this work, and the polynomial orders considered in the DGM, the convergence problems reported by Yee et al. (1997) were not encountered, even for solutions with low polynomial degrees such as $p = 1$.

### 6.2.2 *Validation of reference solution*

To evaluate the quality of our numerical solution, we have selected three streamwise locations along the expanded channel, as reported in Figure 6.5A. They cover the lower and upper recirculation bubbles ($x = 6h$ and $x = 14h$), and an overview of the developed flow far away downstream ($x = 30h$). The idea is to extract the profiles of the relevant physical quantities along the vertical direction of the main channel. We will consider the profiles of the horizontal and vertical components of the velocity, given by $u$ and $v$. The profile vorticity, defined as $\omega = \partial v/\partial x - \partial u/\partial y$, is also included in the analysis. These profiles are examined and compared to the results from the study of Erturk (2008) at the same streamwise locations. In that study, the author uses a grid of 101 uniform elements along the vertical direction of the expanded channel and their scheme is second order accurate. Thus we count 202 DOFs along the $y$-direction. In comparison, we have described our reference solution as a third order numerical solution with 384 DOFs along the same direction (see Table 6.5C).

The results comparing the solution obtained by Erturk (2008) versus our reference solution are shown in Figure 6.7. We observe that our computed profiles

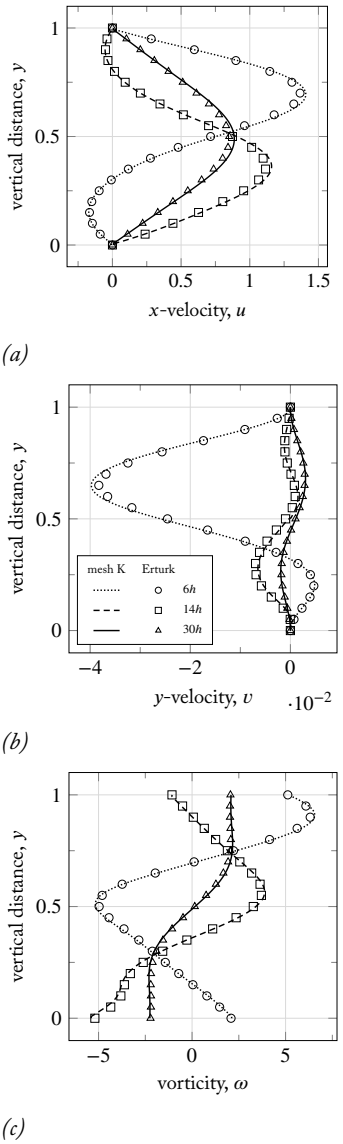


*Figure 6.7:* Laminar backward-facing step. Profiles for different physical quantities at three different streamwise locations along the expanded channel. The profiles have been extracted from our reference numerical solution (mesh K with $p = 2$) and compared with the literature at the same locations.

agree well with those of the literature for every physical quantity analyzed. There are small discrepancies in the maximum values of the $x$- and $y$- velocities. We believe this is due to the fact that in our simulations the maximum $x$-velocity of the parabolic profile is slightly higher right at the fall of the step than at the upstream inlet. However, Erturk shows that for $Re = 800$, these two profiles must be nearly identical. We think that by using a compressible solver (to solve for an incompressible flow) makes it much harder to adjust the inflow/ouflow boundary conditions to attenuate the small increase in the horizontal velocity at the step. We consider that this slight deviation does not substantially affect the outcome of the $h$-adaptation analysis, which is the main focus of our study.

### 6.2.3 *Computational parameters II: h-adaptive simulations*

After validating the numerical results on uniform grids, we now investigate how to reduce the grid size locally, and thus the computational load, for a given level of accuracy. The idea is to start from a coarse mesh, such as the mesh A, B or C reported in Table 6.5c, and to detect the regions in which the approximate DG solution is underresolved and a finer local mesh resolution might be required. To that end, the algorithm described in Section 5.2.6 is applied repeatedly until the desired adapted solution is reached. We remind the reader that by adjusting the $hp$-criterion to exclusively allow for mesh refinement, the algorithm becomes an $h$-adaptive procedure. To select those elements that require $h$-refinement we use an error estimator (Section 5.2.1) in conjunction with an appropriate marking strategy (Section 5.2.4).

Next, we will enumerate the error estimators employed for this configuration, and later we will stress the importance of a suitable marking strategy associated with the estimation. We focus our computations on the $\kappa$-multiwavelet indicator as defined by Eq. (5.7). We recall that this choice of the error estimator was justified by the encouraging results reported from the computations of the 1-D viscous Burgers equation in Section 6.1, where it proved to have the best overall behavior. The $\kappa$-multiwavelet indicator may be evaluated for every conservative variable $\boldsymbol{u} = (\rho, \rho\boldsymbol{v}, \rho E)$ or any other derived quantity. For the study of the backward-facing step we have selected the horizontal and vertical components of the momentum density vector ($\rho\boldsymbol{v}$), the pressure ($p$), and the vorticity ($\omega$). They constitute relevant quantities representative of the behavior of the overall solution. Therefore we come up with three different variations of the multiwavelet-based indicator that will be used in the computations, namely:

1. $\kappa$-multiwavelet *on density momentum* indicator (MW-$\rho\boldsymbol{v}$), $\eta_K^{\text{MW-}\rho\boldsymbol{v}}$.
2. $\kappa$-multiwavelet *on pressure* indicator (MW-$p$), given by $\eta_K^{\text{MW-}p}$.
3. $\kappa$-multiwavelet *on vorticity* indicator (MW-$\omega$), symbolized by $\eta_K^{\text{MW-}\omega}$.

It is worth mentioning that from now on we will drop the "$\kappa$-" terminology when symbolizing the new estimators to simplify the nomenclature. However, we remind the reader that when denoting MW-based indicators in this

section, we exclusively refer to the $\kappa$-multiwavelet indicator applied to selected conservative and derived quantities.

Similarly to the one-dimensional configuration in Section 6.1, the estimators proposed above will be compared to the following two estimators from the literature:

4. *Small-scale energy density* estimator, $\eta_K^{\mathrm{SSED}}$ (Kuru et al., 2016).
5. *Spectral decay* estimator, $\eta_K^{\mathrm{SD}}$ (Taube et al., 2010).

Regarding the marking strategy, we had initially used the local threshold strategy defined by Eq. (5.29), analogously to Section 6.1. However, this strategy proved to be inadequate when comparing estimators of different nature in the context of the more complex backward-facing step. The reason is that we are dealing with differences of several orders of magnitude between the estimators, especially when comparing the SSED and SD indicators to the multiwavelet-based indicators. Therefore it was not possible to find a user-defined tolerance that fitted them all satisfactorily and kept the comparison meaningful. In a more general framework, it might be more convenient to opt for the maximum marking strategy as defined by Eq. (5.30), in which the refining threshold is defined as a percentage of the highest value of the estimator. This allows us to set a given fraction of elements to be marked regardless of the absolute value of the estimator.

### 6.2.4 *Interpretation of the h-adapted meshes*

Figure 6.8 shows the final adapted grids driven by the multiwavelet-based indicators (MW-$\rho\boldsymbol{v}$, MW-$p$, and MW-$\omega$) and the two indicators from the literature (SD and SSED). The leftmost column corresponds to the simulation $p = 1$ and its associated initial uniform grid is Mesh C. The column in the middle corresponds to $p = 2$ and the starting grid is Mesh B. Finally, the rightmost column corresponds to the simulation starting from Mesh A and a polynomial degree equal to $p = 3$.

The adapted grids associated with the lowest degree $p = 1$ exhibit the highest number of refined elements. Clearly, the SSED indicator in Figure 6.8E produces the finest grid. This is due to the fact that it tends to over-refine along the entire channel. However, it only manages to partially capture the geometrical jump. This tendency to over-refining is explained by the low-order approximation used in this simulation. It does not have enough modes to capture the high-frequency content of the solution and thus the indicator, which measures the energy of the highest modes, does not properly work (Naddei et al., 2018).

On the other hand, the SD indicator used in Figure 6.8D is refining aggressively at the walls and along the recirculation bubbles (locations $x = 6h$ and $x = 14h$). This behavior is not surprising and is a consequence of the normalization by the total energy of the flow, which approaches zero near walls,

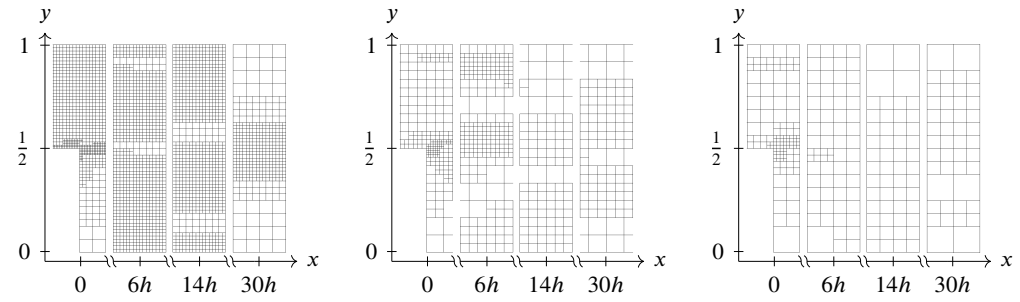


*(a)* MW-$\rho\boldsymbol{v}$

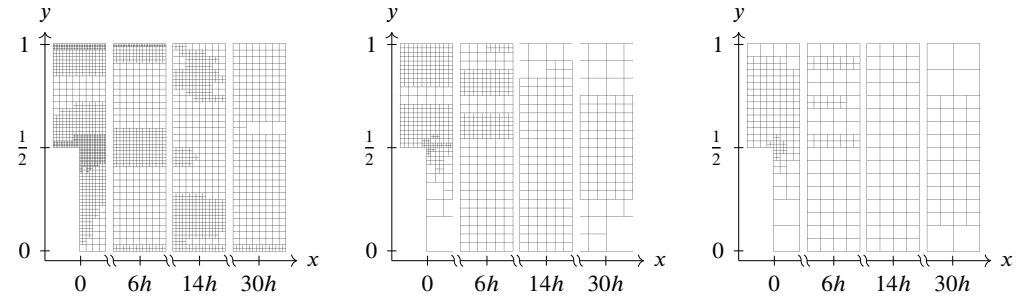


*(b)* MW-$p$

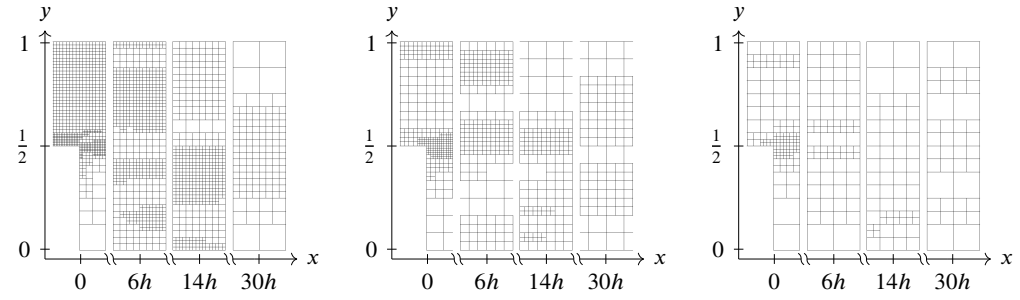


*(c)* MW-$\omega$

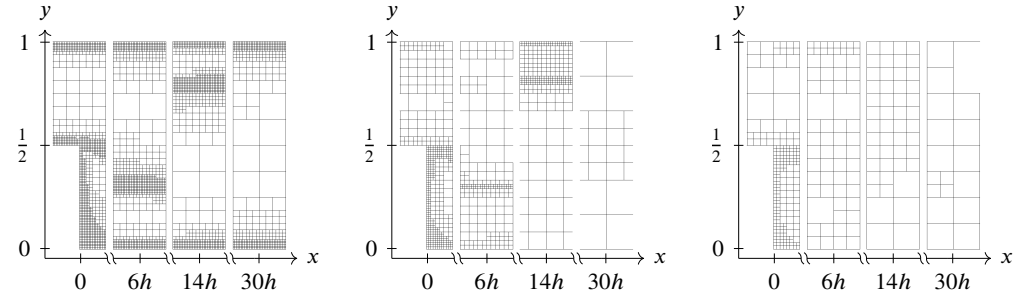


*(d)* SD

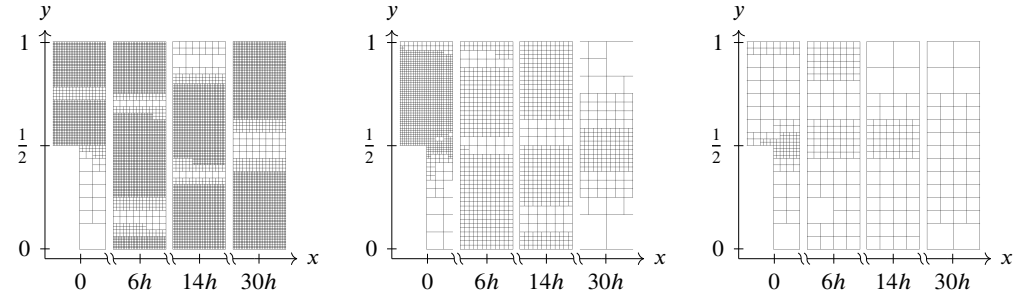


*(e)* SSED

*Figure* 6.8*:* Laminar backward-facing-step. Final *h*-refined grids at four selected regions along the expanded channel. Figures are organized by error estimator and computational degree, from $p = 1$ (left column), $p = 2$ (middle column), and $p = 3$ (right column).

making the values of the estimator meaningless in these wall regions. Additionally, the SD indicator detects regions that simultaneously report low values of high-frequency content and of the total energy, such as recirculation regions (Naddei, 2019).

By contrast, the refinement produced by the multiwavelet-based estimators is more consistent with the physics, with similar patterns of $h$-refinement for all indicators. Indeed, the MW-$\rho\boldsymbol{v}$ and MW-$\omega$ indicators, reported in Figures 6.8A and 6.8C, respectively, follow the dynamics of the flow and refine the stream accordingly, with the latter showing a slightly lower number of adapted elements overall. The region around the geometrical jump together with the separated shear layer yields the highest level of refinement. The top and bottom recirculation regions caused by the separation of the flow at the step corner are also adapted to a lesser extent, which can be explained by the regularity of the solution in that region. The MW-$p$ indicator given in Figure 6.8B displays a higher tendency to refine the region around the step and the separated shear layer. Moreover, it emphasizes adaptation where the flow changes direction to fill the expanded channel (between $x = 6h$ and $x = 14h$), as the pressure changes abruptly in this region.

We now draw our attention to the final adapted grid associated with $p = 3$. We observe that a much lower level of $h$-refinement is displayed by the adapted grid. This is expected as the grid cell now holds a larger amount of information (corresponding to more DOFs). Yet, regions with geometrical singularities will stand out. Surely, the MW-$\rho\boldsymbol{v}$ and MW-$\omega$ indicators shown in Figure 6.8A and Figure 6.8C, respectively, focus the adaptation efforts on the separated shear layer and in the vicinity of the step. Indeed, a strong velocity gradient appears due to the presence of the geometrical jump. In contrast, the lower and upper recirculation regions along the expanded channel undergo little refinement. Similar conclusions can be obtained for the MW-$p$ indicator in Figure 6.8B. The main difference lies in the further refinement along the inlet channel. The higher count of DOFs allows the SSED indicator in Figure 6.8E to amend the deficiencies reported for the low-order approximation, obtaining a similar pattern of $h$-refinement as compared to the multiwavelet-based indicators. Though still gaining a larger number of elements in general. Figure (6.8D) shows that the SD indicator also benefits from a larger number of DOFs per element. It does fully correct the behavior on the walls but still continues to over-refine in the lower recirculation region.

Lastly, regarding the final adapted grid obtained for the quadratic approximation $p = 2$, the outcome for all estimators appears to be in between those obtained for $p = 1$ and $p = 3$. Indeed, Figures 6.8A to 6.8C show how the multiwavelet-based estimators moderately follow the changing stream right after the channel expansion. This behavior is less pronounced for the MW-$p$ indicator in Figure 6.8B, which tends to refine more elements in the inlet region. As for the adaptive $p = 1$ simulation, the multiwavelet estimators lead to the highest level of refinement in the shear layer and in the region in the proximity of the corner, while the more regular recirculation regions display a considerable lower refinement level, closer to the grids obtained for $p = 3$.

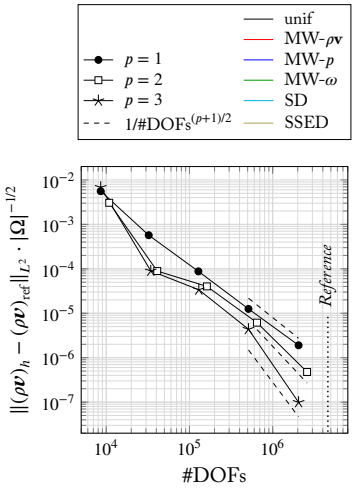


*(a)* Uniformly refined grids.

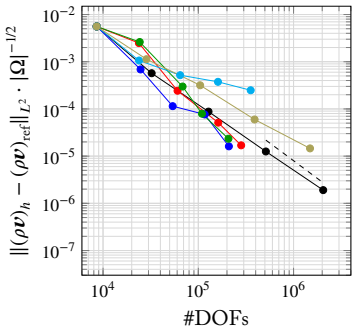


*(b)* *h*-refined grids, $p = 1$.

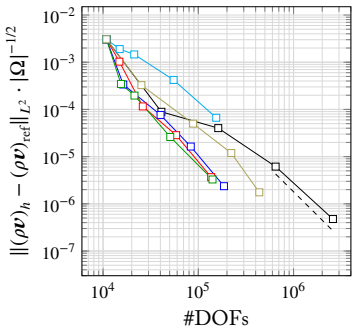


*(c)* *h*-refined grids, $p = 2$.

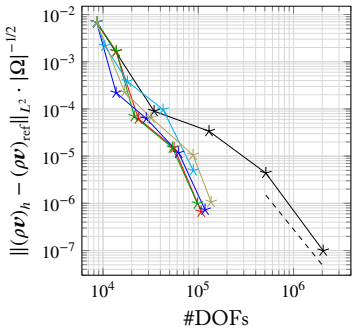


*(d)* *h*-refined grids, $p = 3$.

*Figure 6.9:* Laminar backward-facing-step. $L^2$-norm of the momentum density error under uniform and adaptive *h*-refinement for varying values of *p*.

With respect to the SSED and SD indicators, the increase in the number of DOFs somewhat lessens the deficiencies observed in $p = 1$. Figure 6.8E shows a more targeted adaptation with the SSED indicator, though still heavily refining along the inlet and immediately after. The SD indicator in Figure 6.8D significantly reduces refinement closer to walls while excessively adapting the recirculation regions akin to $p = 1$.

### 6.2.5 *Error analysis of the h-adaptive results*

In order to measure the accuracy of the *h*-refined solutions resulting from the different error estimators, we will analyze the convergence history of the error in the $L^2$-norm of the momentum density versus the number of DOFs. Later we will study the locations of flow detachment/reattachment along the expanded channel versus the #DOFs. The reference solution employed to obtain these error quantities is based on the uniform mesh K described in Table 6.5C and $p = 2$.

Figure 6.9 shows the convergence history of the error in the $L^2$-norm of the momentum density under uniform and adaptive *h*-refinement for different orders of the DGM. The evolution of the error on the uniform grids is recorded in Figure 6.9A. We start the adaptation from relatively coarse grids and we want to make sure that we eventually achieve the asymptotic region. Indeed, the plotted data confirm that the asymptotic convergence rate is reached for sufficiently fine grids. The delayed convergence behavior observed in the higher-order solutions can be explained due to the influence of the singularity at the step.

Figures 6.9B to 6.9D describe the behavior of the error in the *h*-adaptive solutions driven by the five error estimators. We make the observation that the maximum local refinement level is limited to reaching the same element size as its uniform counterpart. Four uniformly refined simulations are reported, including the starting grid. Therefore, four refinement steps are performed for each indicator. As we previously explained while describing the adapted grids in Figure 6.8, the SD and SSED indicators perform poorly for low-orders of the solution. This is due to their dependency on the higher-order modes of the numerical approximation, which are not well captured for low-orders. By contrast, the multiwavelet-based estimators do not show this dependence and their behavior is more consistent for every order of the adapted solution.

This is evident in Figure 6.9B for $p = 1$, where the error lines of the SD and SSED indicators lie above the uniformly refined line, meaning that no benefit is gained by activating adaptation with these estimators. In the case of the SD indicator, the extremely slow decay of the error is explained by its tendency to incorrectly refine on walls and recirculations regions, which are not the main source of error in the backward-facing step configuration. The SSED indicator actually manages to reach the same level of accuracy than the multiwavelet-based indicators but at the expense of a much larger amount of degrees of freedom, a clear sign of over-refinement. On the other hand, the family of multiwavelet-based estimators leads to a moderate reduction (30 %

to 48 %) in the total number of DOFs as compared to uniform refinement, with the MW-$p$ indicator reporting the highest savings.

When the polynomial degree is increased to $p = 2$, as illustrated in Figure 6.9C, the multiwavelet-based indicators lead to a reduction of one order of magnitude in the error with respect to $p = 1$ while keeping an equivalent total number of degrees of freedom. When they are measured against uniform refinement with the same total error we obtain a decrease of the total number of DOFs of approximately 80 %. By contrast, the SSED indicator achieves a similar level of accuracy yet reporting a significantly lower performance of about 66 %. Its tendency to over-refine is improved but not fully corrected. In a similar manner, the SD indicator seems to slightly improve its behavior compared to $p = 1$ but it still retains a slower convergence rate than the uniformly refined simulations and it continues to lag behind the other estimators.

Finally the highest order of the $h$-adapted solution with $p = 3$ is reported in Figure 6.9D. Every error estimator leads to a substantial reduction of the required number of degrees of freedom to attain a given level of accuracy. Again, the error is further decreased compared to lower degrees for a similar number of DOFs. The multiwavelet-based indicators achieve the best performance, with savings of approximately 90 % compared to uniform refinement. The differences are small, but the MW-$\rho\boldsymbol{v}$ indicator reports a small lead. The family of multiwavelet-based indicators become more accurate when we increase the number of DOFs because more information can be efficiently stored by the multiwavelet coefficients. In the same way, a higher-order solution also benefits the SSED and SD indicators. The former achieves a reduction in the total number of DOFs of about 84 %, while the latter shows a slightly slower convergence rate only reaching in accuracy the third uniformly refined simulation with savings of around 82 %.

### 6.2.6 *Memory savings*

Table 6.1 offers a summary of the savings in the number of degrees of freedom when the $h$-adaptive algorithm is activated. The multiwavelet-based indicators display a more consistent and reliable behavior with savings increasing from 30 % for $p = 1$ to over 80 % for $p = 2$ to almost 90 % for the highest order. By contrast, the SSED and SD indicators underperform the multiwavelet family of indicators for the lower-order simulations, and only manage to achieve savings of about 80 % for $p = 3$. Finally, similar percentages

| Error estimator | #DOFs change (%) | | | Memory change (%) | | |
|---|---|---|---|---|---|---|
| | $p = 1$ | $p = 2$ | $p = 3$ | $p = 1$ | $p = 2$ | $p = 3$ |
| MW-$\rho\mathbf{v}$ | 30 | 83 | 90 | 33 | 82 | 89 |
| MW-$p$ | 48 | 84 | 88 | 52 | 81 | 87 |
| MW-$\omega$ | 31 | 83 | 89 | 35 | 82 | 89 |
| SD | −491 | −120 | 82 | −481 | −114 | 79 |
| SSED | −198 | 66 | 84 | −220 | 64 | 82 |

*Table* 6.1*:* Laminar backward-facing-step. #DOFs and memory comparison with varying values of $p$ for final $h$-adapted grids. Percentages are measured with respect to uniform grids that report similar solution accuracy. Positive percentages represent savings, while negative values mean higher #DOFs/memory consumption.

*Table* 6.2*:* Laminar backward-facing-step. Memory change with varying values of $p$ for final $h$-adapted grids. Percentages are evaluated with respect to an equivalent uniform grid with fixed $p = 1$. Positive percentages speak for higher memory consumption, while negative values describe a lower memory utilization.

| Error estimator | $h$-refined (%) | | | Uniform refinement (%) | | |
|---|---|---|---|---|---|---|
| | $p = 1$ | $p = 2$ | $p = 3$ | $p = 1$ | $p = 2$ | $p = 3$ |
| MW-$\rho\mathbf{v}$ | −33 | −56 | −53 | — | 145 | 320 |
| MW-$p$ | −52 | −44 | −52 | — | 204 | 280 |
| MW-$\omega$ | −35 | −40 | −42 | — | 238 | 371 |
| SSED | 220 | 23 | −43 | — | 244 | 221 |

in memory savings show how the number of DOFs and memory are closely linked. Certainly, the differences between these two quantities are not higher than 10 %, even when the order is increased. This happens despite the fact that implicit time integration with higher-order DG methods imposes larger memory requirements (Renac et al., 2015).

Memory behavior is further studied in Table 6.2. Only those error estimators which reach a similar level of accuracy are analyzed. We have set the memory consumption of the uniformly refined simulation with $p = 1$ as reference to measure the effect of increasing the order in memory growth. We observe a constant decrease in memory of approximately 30 % to 50 % for the multiwavelet family of estimators, almost independent of the order. Conversely, the uniformly refined simulations report an increase of about three to four times in memory requirements following the increment in order to achieve the same prescribed level of accuracy than its $h$-adapted counterpart. We remark that the irregular results of the SSED indicator are due to its poorly performance for low-order simulations.

### 6.2.7 *Computational times*

Figure 6.10 outlines the behavior of the error versus the computational cost for the different $h$-adaptive simulations. Interestingly, the rate of convergence in CPU-time for the $h$-adaptive simulations with $p = 1$ is slower in the last iterations than the uniformly refined simulations, as illustrated by Figure 6.10A. We expect this result for the SD and SSED indicators, as they report significantly higher number of degrees of freedom than the uniform simulations for a similar accuracy (see Table 6.1). However, the multiwavelet estimators do show moderate number of DOFs reductions which do not translate into computational savings. This may occur because for a similar number of DOFs adapted meshes with hanging nodes may take longer to reach convergence than uniform ones.

On the other hand, higher order simulations report clear computational gains when adaptation is activated. This is the case of Figure 6.10B with $p = 2$, where most of the estimators except the SD outperform uniform refinement. This trend continues for $p = 3$, with Figure 6.10C reporting substantial cost improvements for every indicator. Remarkably, the multiwavelet indicators provide the best performance among all the proposed error estimators.

Table 6.3 collects the CPU-time and speedup values of the $h$-adaptive simulations applied to the final adapted grids. These quantities are relative to

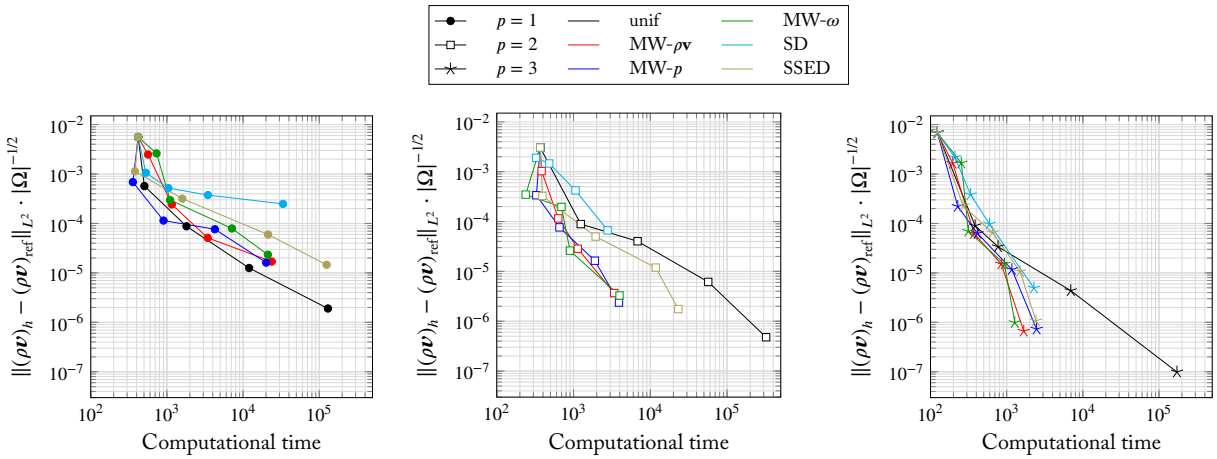


*(a)* $p = 1$. *(b)* $p = 2$. *(c)* $p = 3$.

*Figure* 6.10*:* Laminar backward-facing-step. $L^2$-norm of the error in momentum density vs the computational time under uniform and adaptive $h$-refinement for various values of $p$.

the final uniformly refined mesh. As reported in Figure 6.10, we observe a strong variation depending on the order of the adapted solution and the error estimator employed. In this manner, adaptation with $p = 1$ underperforms compared to uniform refinement, whereas higher orders achieve significant speedups for selected estimators. The SD indicator offers the lowest performance, with no gain in $p = 2$ and a speedup of three times in $p = 3$. Conversely, the multiwavelet indicators are the most efficient, delivering more than 20 times faster solutions in $p = 2$ and between 12 and 19 times in $p = 3$. Lastly, the SSED indicator lands in between, by providing a speedup of five times in $p = 2$ and of nine in $p = 3$. Sensor estimation, element marking and refining times have not been included in the previous analysis. However, they never constitute more than 5 % of the total computational time.

| Indicator | CPU-time (%) | Speedup |
|---|---|---|
| Uniform | 100.00 | 1.00 |
| MW-$\rho\boldsymbol{v}$ | 264.26 | 0.38 |
| MW-$p$ | 223.30 | 0.45 |
| MW-$\omega$ | 352.23 | 0.28 |
| SD | 3713.44 | 0.03 |
| SSED | 1250.00 | 0.08 |

*(a)* $p = 1$.

| Indicator | CPU-time (%) | Speedup |
|---|---|---|
| Uniform | 100.00 | 1.00 |
| MW-$\rho\boldsymbol{v}$ | 4.22 | 23.68 |
| MW-$p$ | 3.91 | 25.59 |
| MW-$\omega$ | 4.41 | 22.65 |
| SD | 100.00 | 1.00 |
| SSED | 21.06 | 4.75 |

*(b)* $p = 2$.

| Indicator | CPU-time (%) | Speedup |
|---|---|---|
| Uniform | 100.00 | 1.00 |
| MW-$\rho\boldsymbol{v}$ | 5.23 | 19.10 |
| MW-$p$ | 8.24 | 12.14 |
| MW-$\omega$ | 5.56 | 18.00 |
| SD | 32.90 | 3.05 |
| SSED | 11.03 | 9.07 |

*(c)* $p = 3$.

*Table* 6.3*:* Laminar backward-facing-step. Simulation time speedups between uniform and adapted grids for the final adaptation step in Figure 6.10. The results are presented for the different values of $p$.

### 6.2.8 *Measure of separation/reattachment lengths under h-adaptation*

We complete the study of the adapted solutions by analyzing the normalized lengths of flow separation/reattachment. Unlike the previous analysis of the error, these quantities can be found in literature and thus it will allow us to compare and validate our results.

Table 6.4 collects some of the most relevant studies and how their values compare to the reference solution used in the present work. Their domains are slightly different with the main divergence being the length of the expanded channel and the absence/presence of the inlet channel. As reported by Barton (1997), the presence of an inlet results in the reduction of the lower reattachment length, denoted by $x_1$, the upper separation length, $x_2$, and to a lesser extent, the upper reattachment length, $x_3$, with respect to the use of no entrance at all. Only the study of Erturk (2008) provides results on the separation length at the step, $x_0$. Our reference solution agrees very well with the values $x_0$ and $x_1$ provided by Erturk. The lengths $x_2$ and $x_3$, defining the upper recirculation region, show a small deviation from the study. However,

*Table* 6.4: Laminar backward-facing step. Normalized separation and reattachment locations found in the literature and how they compare to the reference solution of the present study.

| | $x_0$ | $x_1$ | $x_2$ | $x_3$ | Domain |
|---|---|---|---|---|---|
| Gartling (1990) | — | 12.20 | 9.70 | 20.96 | $60h$, *no entrance* |
| Barton (1997) | — | 12.03 | 9.64 | 20.96 | $32h$, *no entrance* |
| | — | 11.51 | 9.14 | 20.66 | $32h$ + *inlet channel* ($10h$) |
| Cruchaga (1998) | — | 12.00 | 9.60 | 20.20 | $60h$, *no entrance* |
| | — | 12.00 | 9.40 | 19.40 | $60h$ + *inlet channel* ($h$) |
| Erturk (2008) | 0.15 | 11.83 | 9.47 | 20.55 | $300h$ + *inlet channel* ($20h$) |
| Present study | 0.15 | 11.81 | 9.31 | 20.83 | $60h$ + *inlet channel* ($5h$) |

the former is still within the values provided by Cruchaga (1998) and Barton (1997), and the latter, being the furthest from the step, is the least influenced by the absence/presence of the inlet channel and thus it is reasonable that it may be found to be in between the estimates given by Barton.

Figures 6.11 and 6.12 show the convergence history of the normalized separation/reattachment lengths for every error estimator and different orders of the numerical solution. The evolution of the separation length at the step, denoted by $x_0$, shines a new light on indicator behavior not reported in the previous analysis of Figure 6.9. Certainly, the SD indicator shows the fastest convergence and highest accuracy of the error estimators examined. Moreover, it is the only indicator that reaches the target reference length when $p > 1$ while achieving a large reduction on the number of degrees of freedom (above 90 %) compared to uniform refinement. This unexpected result can be explained by two confluent factors. These are, the weak influence on this region of the stream itself and the strong tendency of the SD indicator to refine in the low-energy regions. The first factor ameliorates the poor performance of the indicator overall, and the second factor allows for over-refinement in the recirculation regions, which is beneficial to accurately secure the separation/reattachment locations. By contrast, the rest of the indicators do not focus as much on regions of low energy and thus struggle to reach the target length.

The convergence history of the remaining locations $x_1$, $x_2$, and $x_3$ shows patterns already observed during the previous analysis of the error in Figure 6.9. For the lowest degree $p = 1$, the SD indicator reports the largest divergence on achieving the reference target length. This happens despite its tendency to heavily refine in recirculation regions and on walls, which should help converge to the target length. This contradicting result can be attributed to an insufficient resolution along the upstream flow which, in turn, has a negative impact on accurately capturing the locations further from the step. Therefore, adequate resolution adaptation along the upstream flow is key. On the other hand, the SSED indicator displays a mixed record on reaching the reference target length, together with a slower convergence rate compared to uniform refinement. Finally, the multiwavelet-based indicators show analogous rates of convergence between them when analyzing $x_1$, $x_2$, and $x_3$ for $p = 1$ simulations. Apart from $x_3$, for which only the MW-$\rho\boldsymbol{v}$ indicator achieves the target, every multiwavelet-based estimator reaches the reference value with savings in the range of 45 % to 60 %.

When the order is increased to $p = 2$, every indicator substantially improves

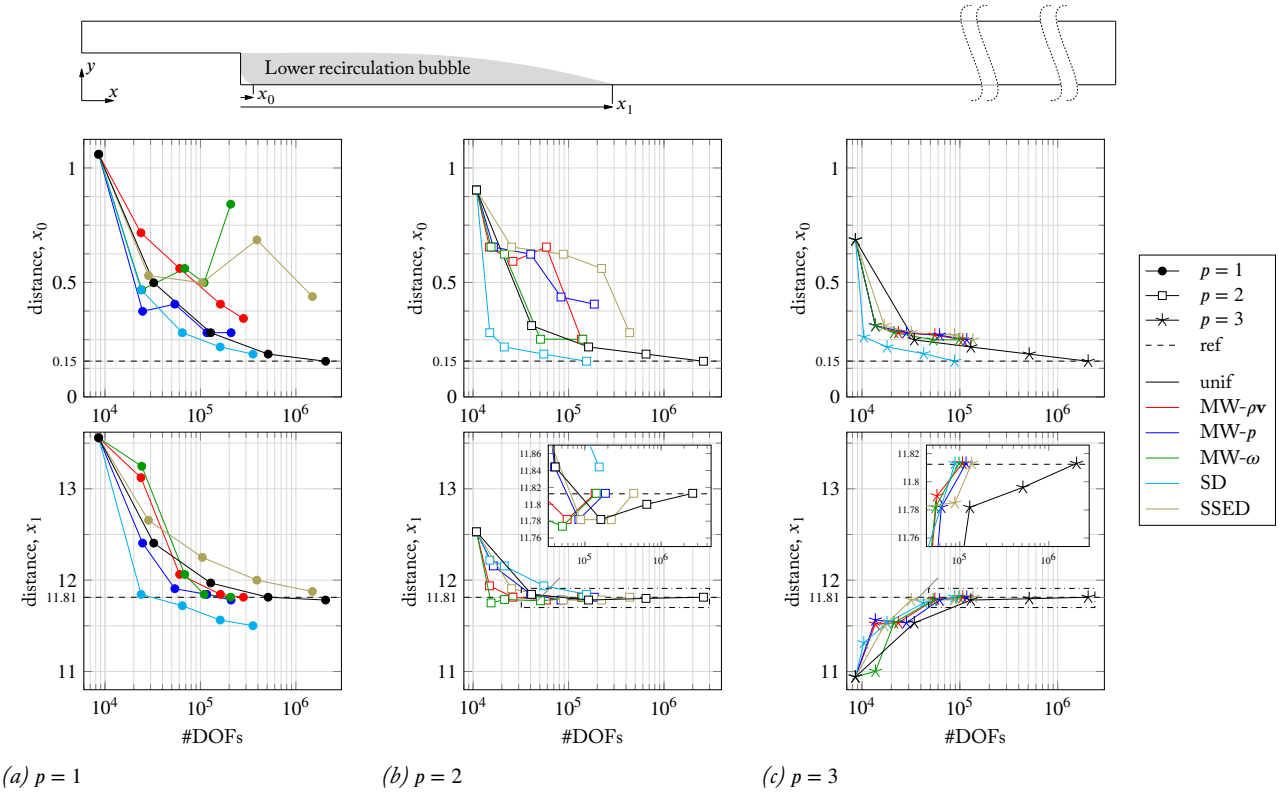


*(a)* $p = 1$ *(b)* $p = 2$ *(c)* $p = 3$

*Figure* 6.11*:* Laminar backward-facing step. Normalized locations of flow detachment/reattachment of the lower recirculation bubble under uniform and adaptive $h$-refinement with varying values of $p$.

their convergence rate. The SSED indicator attains a reduction of about 83 % in the number of DOFs and the multiwavelet-based indicators obtain a further decrease to be within the interval of 93 % to 95 %. The SD indicator remains as the only error estimator which does not achieve the target length.

Finally, for the highest order $p = 3$ all refinement indicators reach the prescribed reference length while achieving a significant reduction in the number of DOFs. They all perform similarly with savings in the range of 93 % to 96 %. The only exception is the upper reattachment length, $x_3$, for which the MW-$\omega$ and the SSED indicators do not converge to the target. It is also worth mentioning that in this case the SD indicator performs better than in the previous Figure 6.9, due to the nature of the separation/reattachemt location quantity, which benefits from indicators that lean toward refinement on the recirculation regions.

### 6.2.9 *Input influence on multiwavelet estimator performance*

To finalize this chapter, we examine the different estimators within the multiwavelet family (i.e. the MW estimators based on different flow quantities). So far, when comparing them to the SSED and SD indicators we have treated them mainly as a group. Now we analyze their performance with respect to each other. To this end, we evaluate the error in the $L^2$-norm of the different physical quantities that characterise each of the multiwavelet indicators

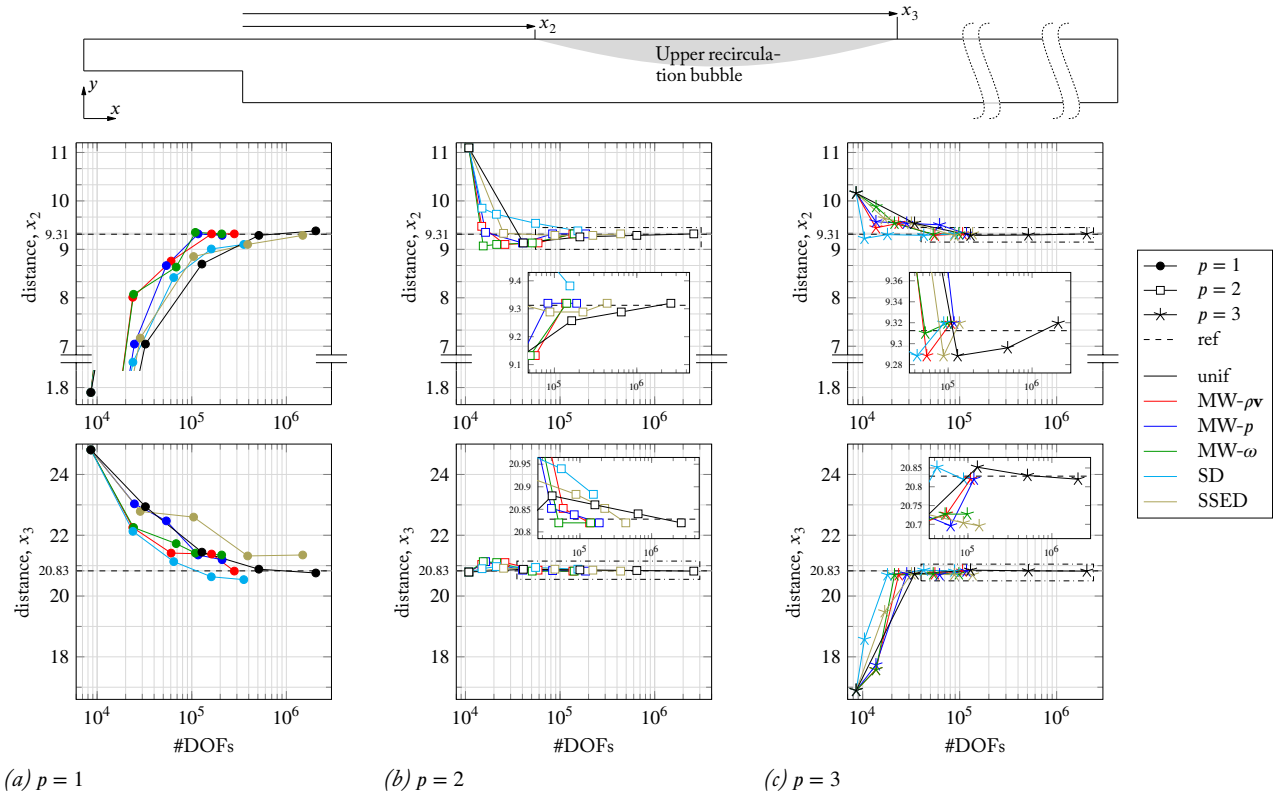


*(a)* $p = 1$ *(b)* $p = 2$ *(c)* $p = 3$

*Figure* 6.12*:* Laminar backward-facing step. Normalized locations of flow detachment/reattachment of the upper recirculation bubble under uniform and adaptive $h$-refinement with varying values of $p$.

along vertical profiles at the selected locations $x = 0, 6h, 14h, 30h$ shown in Figure 6.5A.

We remind the reader that the indicators involve density momentum, pressure and vorticity, and thus the error is based on these as well. As reported in Figure 6.9, the final adapted grids associated with each indicator of the multiwavelet family have reached an similar global level of accuracy. This result ensures that we can have a fair comparison when evaluating the effect of the different flow quantities on the behavior of the estimator.

Figure 6.13 shows the comparison between the multiwavelet-based indicators. Figures 6.13A to 6.13C represent every profile location along the $x$-axis and its associated error along the $y$-axis. For each figure there are three line styles covering $p = 1$ to $p = 3$. Color preference is given to those indicators that typify the same physical quantity than the current error. For example, Figure 6.13A illustrates the error in momentum density, and thus the red line represents the $h$-adapted mesh associated with the momentum density indicator, MW-$\rho\boldsymbol{v}$. The remaining black lines represent the $h$-adapted mesh driven by the pressure indicator, MW-$p$, and vorticity indicator, MW-$\omega$, in no preferential order. In general, we observe that $p = 1$ reports a more even distribution of error along the channel. When we increase the approximation order the error is concentrated in the region around the step while decreasing at the other locations, a clear sign that the downstream convection of the error is ameliorated. Interestingly, the best results in these locations $x > 0$ with $p > 1$

| Error estimator | $p=1$ | $p=2$ | $p=3$ |
|---|---|---|---|
| | $\|(\rho\mathbf{v})_h - (\rho\mathbf{v})_{\text{ref}}\|_{L^2}$ | | |
| MW-$\rho\mathbf{v}$ | $1.52\times10^{-3}$ | $2.97\times10^{-4}$ | $3.51\times10^{-5}$ |
| MW-$p$ | $1.61\times10^{-3}$ | $2.59\times10^{-4}$ | $4.56\times10^{-5}$ |
| MW-$\omega$ | $2.24\times10^{-3}$ | $1.68\times10^{-4}$ | $5.19\times10^{-5}$ |
| | $\|p_h - p_{\text{ref}}\|_{L^2}$ | | |
| MW-$\rho\mathbf{v}$ | $7.36\times10^{-4}$ | $1.93\times10^{-4}$ | $1.26\times10^{-4}$ |
| MW-$p$ | $7.71\times10^{-4}$ | $2.80\times10^{-4}$ | $1.26\times10^{-4}$ |
| MW-$\omega$ | $2.07\times10^{-3}$ | $1.47\times10^{-4}$ | $1.27\times10^{-4}$ |
| | $\|\omega_h - \omega_{\text{ref}}\|_{L^2}$ | | |
| MW-$\rho\mathbf{v}$ | $1.31\times10^{-1}$ | $8.30\times10^{-2}$ | $5.33\times10^{-2}$ |
| MW-$p$ | $2.13\times10^{-1}$ | $5.73\times10^{-2}$ | $5.08\times10^{-2}$ |
| MW-$\omega$ | $1.65\times10^{-1}$ | $3.35\times10^{-2}$ | $5.43\times10^{-2}$ |

*Table 6.5:* Laminar backward-facing step. $L^2$-norm of the total error resulting from the combination of the profiles analyzed in Figure 6.13. Best result given by cell in grey.

are generally obtained by the indicator that shares physical variable with the error, e.g. error in pressure is better captured by the MW-$p$ indicator. This is somehow expected, as an indicator based on a particular physical variable would usually monitor better its associated error.

Table 6.5 measures the error of these profiles combined. We observe that for low-order and evenly distribution of the error, the MW-$\rho\mathbf{v}$ indicator offers the best performance overall, reporting the most accurate results in momentum density, pressure, and vorticity. When the order is increased, the step region gains more influence and the indicator that reports lower error there will perform best. In our case it is the MW-$\omega$ indicator for $p=2$ and the MW-$\rho\mathbf{v}$ and MW-$p$ indicators for $p=3$. Therefore, we believe that near a singularity there is no clear indicator that outperform the others. All of them perform similarly, with slight variations depending on the order of the simulation.

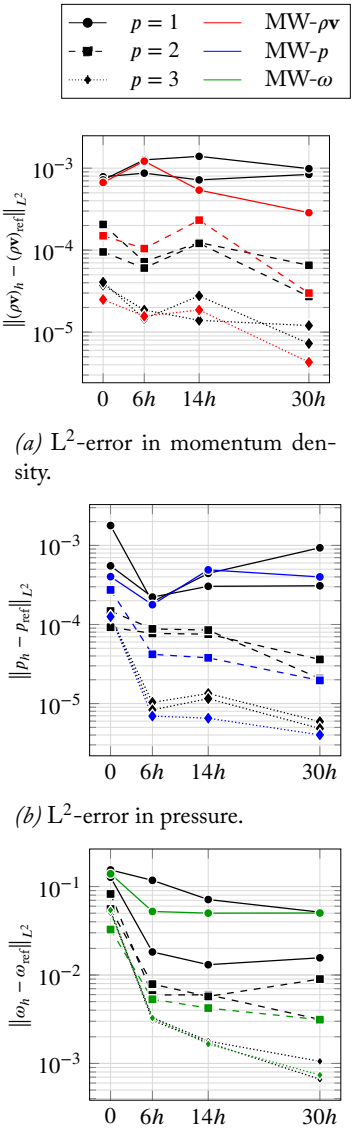


*(a)* $L^2$-error in momentum density.

*(b)* $L^2$-error in pressure.

*(c)* $L^2$-error in vorticity.

*Figure 6.13:* Laminar backward-facing step. Performance comparison with varying $p$ among multiwavelet-based error estimators at selected profiles along the expanded channel.

## 6.3 CONCLUDING COMMENTARY

In this chapter we have analyzed multiple variations of the error estimator based on the local multiresolution analysis of the DG solution to guide $h$-adaptive simulations. Specifically, we have studied flow configurations defined by the presence of physical and geometrical discontinuities, which would considerably profit from pure mesh adaptation.

Adaptive simulations of the one-dimensional viscous Burgers equation driven by the multiwavelet methodology have shown compelling results. The multiwavelet error estimator has been tested under multiple reconstruction paradigms and they all have reported significant reductions in the number of degrees of freedom when adaptation is activated. A comparison of their performance against the modal error estimators SSED (Kuru et al., 2016) and SD (Taube et al., 2010) has shown that our proposed estimators report effectivity indices closer to unity, which means that they are able to better monitor the evolution of the discretization error of the numerical solution. Particularly, the $\kappa$-multiwavelet estimator has reported the best performance within the multiwavelet family.

Encouraged by the promising results of the one-dimensional simulations, we have extended the $\kappa$-multiwavelet estimator to higher dimensions. In this regard, we have studied a steady laminar backward-facing step flow at $Re = 800$ and $Ma = 0.1$. This more demanding configuration certainly has demonstrated the viability of the estimator to achieve a substantial computational gain with respect to uniformly refined grids. Particularly, we have applied the estimator to different physical quantities and recorded their resulting $h$-adaptive simulations separately. For a prescribed level of accuracy, depending on the order of the simulation, the different variations of the multiwavelet estimator have achieved a peak reduction in the numbers of degrees of freedom of 48 %, 84 %, 90 % for DG $p = 1$, $p = 2$, and $p = 3$ simulations, respectively. The convergence study of the separation/reattachment lengths has led to similar savings and has further justified the use of $h$-adaptation to reduce the computational load.

With regards to physical quantities put under the umbrella of the multiwavelet expansion, we have discovered that, when the underlying solution is smooth and for a prescribed level of accuracy, building the $\kappa$-multiwavelet estimator on a given physical quantity (e.g. momentum density) has led to refined grids that better predict the given physical quantity. However, in the presence of a singularity, we have found that the causality seemed to be weakened and the choice of the physical quantity as input for the estimator did not have a significant effect on the final solution.

A thorough comparison of the family of $\kappa$-multiwavelet estimators against the literature estimators SSED and SD has found the largest differences in behavior for the low-order simulations. These differences have been highlighted in the analysis of the $h$-adapted grids. In low-orders, the SSED estimator has reported the largest refined grid, whereas the SD estimator has refined aggressively at the walls and along the recirculation regions. By contrast, the multiwavelet-based estimators have displayed a more consistent adaptation, focusing the adaptation efforts on the separated shear layer and on the vicinity of the singularity. With the exception of the SD, all estimators have reported similar patterns of $h$-refinement as the order was increased. In this case, the multiwavelet-based estimators have become more accurate when increasing the number of DOFs per element thanks to the higher quantity of details captured during the multiwavelet decomposition. In a similar manner, the SSED and SD estimators have also benefited from a larger number of DOFs, which allowed for a better representation of the higher modes. But in spite of that, they have not achieved the performance levels of the multiwavelet-based estimators.

With respect to the computational times for the different $h$-adaptive simulations, we have observed underperforming results for the lowest order $p = 1$ in all the estimators. We have attributed this behavior to the fact that adapted grids with hanging nodes may have taken longer to reach convergence than uniform meshes with a similar number of DOFs. In contrast, higher order $h$-adaptive simulations have reported conclusive computational gains. In this manner, the SD estimator has delivered the lowest performance with a peak

speedup of three times in $p = 3$. The SSED estimator has reported a better performance, with a maximum speedup of nine times for the same degree. Finally, the multiwavelet-based estimators have offered the best performance, with a maximum speedup of 20 times in $p = 2$ and delivering between 12 and 19 times faster solutions in $p = 3$.

# Chapter 7

# HP-ADAPTIVE SIMULATIONS

The study performed in Chapter 6 has paved the way to validate the multiwavelet indicator as a capable error estimator for *h*-adaptive simulations. In particular, the $\kappa$-multiwavelet indicator applied on the density momentum reported the best performance. This estimator is thus selected for the research presented in this chapter.

Building on these results, we now shift our attention to the analysis of *hp*-adaptive simulations. In contrast to the pure *h*-version of the adaptive simulations studied in the previous chapter and driven exclusively by error estimators, we can come up with a more suitable distribution of *h* and *p* based on the multiwavelet *hp*-strategy developed in Chapter 5. This strategy brings to the table the multiwavelet regularity indicator and the *hp*-decision criterion developed in Sections 5.2.3 and 5.2.4, respectively.

The objective of the present chapter is to evaluate the performance of our multiwavelet *hp*-strategy in guiding *hp*-adaptation in relevant steady simulations by using the algorithm showcased in Section 5.2.6. We judge the performance of our strategy by conducting two studies. Firstly, we carry out a parametric analysis of the *hp*-threshold to determine the optimal *hp*-distribution. In a second step, the *hp*-adaptive results derived from this distribution are compared to equivalent purely *h/p*-adaptive results to determine which is the best approach. Both global and local quantities are assessed in this manner. In each step we analyze the convergence history of different quantities and the regions of the *hp*-mesh subjected for adaptation. As one would expect, *p*-adaptation would be employed in regions characterized by regular solution behavior to provide high accuracy, and *h*-adaptation would be most appropriate in the proximity of discontinuous phenomena, such as shocks or singularities.

The described methodology is applied to two configurations, which form the main structure of the chapter: the 2-D laminar flow over a backward-facing step (Section 7.1) already studied in Chapter 6, and the 2-D laminar flow past a square cylinder (Section 7.2). In the first configuration we present a brief extension to *hp* of the results obtained in Chapter 6. The new *hp*-meshes are analyzed in Section 7.1.1, while the analysis of the *hp*-results is presented globally in Section 7.1.2 and locally in Section 7.1.3. We introduce the computational details of the second configuration in Section 7.2.1, followed by an analysis of the error across uniformly refined meshes in Section 7.2.2. Section 7.2.3 outlines the *h/p*-results for different global quantities. The *hp*-results of these same quantities are described in Sections 7.2.4 to 7.2.6. We

perform a comparison of the *h/p*- and *hp*-results in both global and local quantities in Sections 7.2.7 and Sections 7.2.8, in that order. Finally, the main conclusions of the chapter are summarized in Section 7.3.

## 7.1 LAMINAR BACKWARD-FACING STEP

In this section we extend the *h*-adaptive approach of the laminar backward-facing step conducted in Section 6.2 of Chapter 6 to both local polynomial and mesh adaptation guided by the multiwavelet regularity indicator developed in Section 5.2.3 of Chapter 5.

Consequently, we employ once more the computational domain showcased in Figure 6.5A with $Re = 800$ and $Ma = 0.1$, and boundary conditions described in Section 6.2.1. Similarly to the *h*-refinement study, we use the numerical results obtained with grid K and $p = 2$ from Table 6.5C as the reference solution. We remind the reader that this solution has been previously validated in Section 6.2.2.

We use the grid C from Table 6.5C as initial computational grid $\Omega_h^{(0)}$ combined with the constant *p*-distribution $\not{p} = 1$. From this pair a sequence of *hp*-meshes $\Omega_{h,\not{p}}^{(i)}$ is generated. We bound the local polynomial degree to the interval $p_K \in [p_{\min}, p_{\max}]$ with $p_{\min} = 1$ and $p_{\max} = 5$ being the minimum and maximum polynomial degrees permitted, respectively. We perform a sequence of simulations driven by a combination of the multiwavelet-based estimator and regularity indicator under the umbrella of the *hp*-algorithm. These computations are organised in three groups as follows:

(i) The first group collects uniform and adaptive mesh refinement of $\Omega_{h,\not{p}}$ under constant $\not{p}$. We simply refer to them as h-*simulations*.
(ii) The second group consists of uniform and adaptive polynomial adaptation of $\Omega_{h,\not{p}}$ with $\not{p} \in [1,5]$ and constant mesh $\Omega_h^{(0)}$. We denote them as p-*simulations*.
(iii) The last group comprises *hp*-adaptation of $\Omega_{h,\not{p}}$, with both $\not{p}$ and $\Omega_h$ subjected to change. We refer to them as hp-*simulations*. The *hp*-threshold $\varsigma_{\text{tol}}$ employed in these computations is given by the interval $(0.25 < \varsigma_{\text{tol}} < 0.35)$.

### 7.1.1 *Comparison of the h-, p-, and hp-adapted meshes*

Figure 7.1 outlines the final *h*-, *p*-, and *hp*-adapted meshes. They correspond to the three groups of computations (i) to (iii) previously described. On the one hand, Figure 7.1B showcases the final *h*-adapted mesh under constant polynomial degree, as obtained in the previous Chapter 6. On the other hand, Figure 7.1C illustrates the the final *p*-adapted mesh under constant mesh topology. Finally, Figures 7.1D to 7.1G show the different iterations of the actual *hp*-mesh up to reaching the the final step.

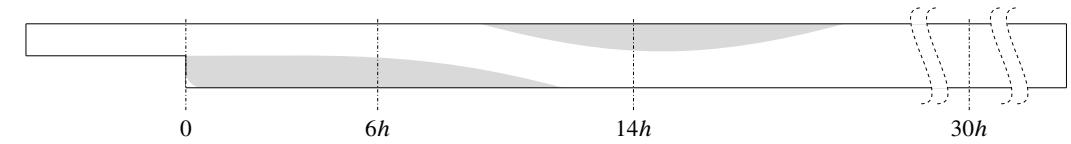


*(a)* Computational domain.

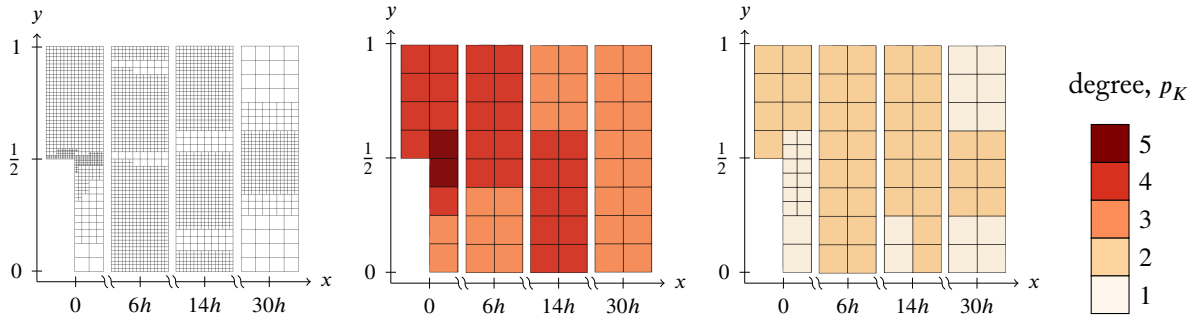


*(b)* Final *h*-refined mesh. *(c)* Final *p*-enriched mesh. *(d)* 1st *hp*-adapted mesh.

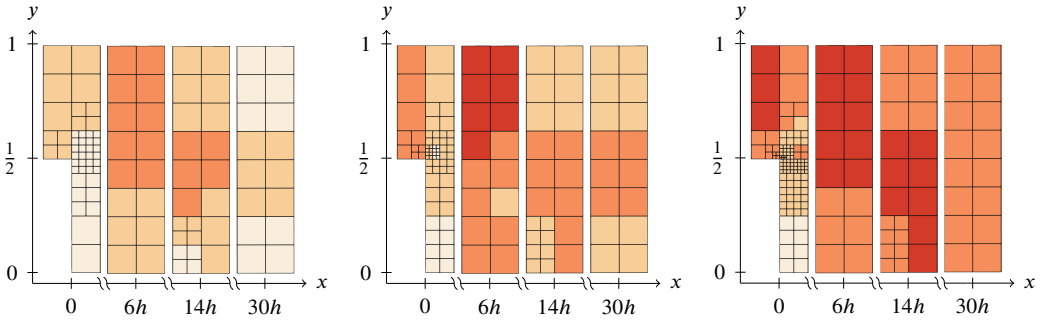


*(e)* 2nd *hp*-adapted mesh. *(f)* 3rd *hp*-adapted mesh. *(g)* 4th (final) *hp*-adapted mesh.

*Figure 7.1:* Backward-facing step. Adapted *hp*-meshes resulting from multiple adaptation approaches at four regions along the expanded channel. The starting mesh and *p*-distribution are given by grid C from Table 6.5c and $p = 1$, respectively.

The refined mesh in Figure 7.1b has already been discussed in Chapter 6. We concluded that the adaptation successfully captured the geometrical jump and the separated shear layer by applying the highest level of refinement. Likewise, the top and bottom recirculation regions displayed lower levels of refinement due to the regularity of the solution in these regions.

The *p*-adapted mesh in Figure 7.1c can be understood as a map of the local polynomial degree. By looking at this map we observe that the initial $p = 1$ sits quite below the given level of accuracy, thus the minimal degree in the final mesh is increased to $p = 3$. The highest value of the local polynomial occurs in the proximity of the corner and, to a lesser extent, along the shear layer. The inlet channel and the regions where the flow changes direction to adjust to the channel expansion are also subjected to moderate local degrees. The lowest values are reported in the recirculation regions. Overall, the distribution map behaves similarly to the *h*-refinement pattern discussed earlier.

In the single *h*- or *p*-adapted meshes described so far we can not clearly distinguish the nature of the error that drives adaptation. For example, the strong velocity gradient caused by the step justifies adaptation in that region. However, the previous analyzes are not conclusive as to whether *h* or *p* is the ideal

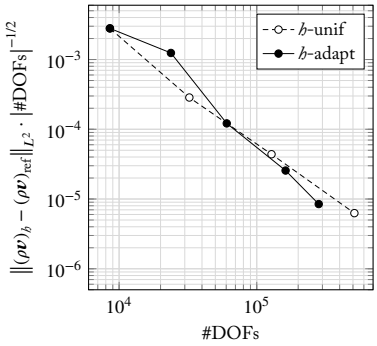


*(a)* $h$-uniform vs adaptive.

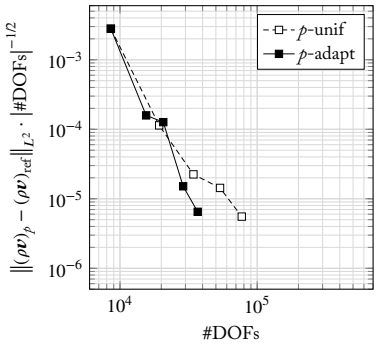


*(b)* $p$-uniform vs adaptive.

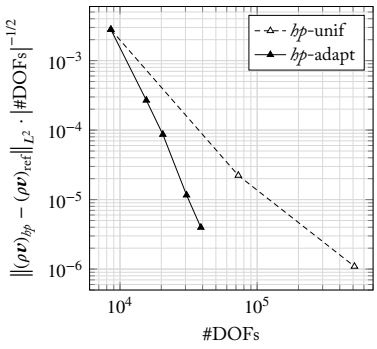


*(c)* $hp$-uniform vs adaptive.

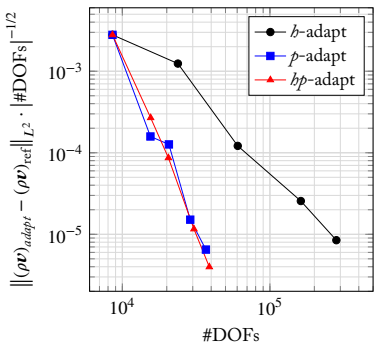


*(d)* Comparison $h$-, $p$-, and $hp$-adaptive

*Figure 7.2:* Backward-facing step. $L^2$-norm of the error in momentum density under various adaptation approaches.

choice. To address this issue, Figures 7.1D to 7.1G display the combination of $h$-refinement and $p$-enrichment for different iterations of the adaptive procedure. We observe how the area surrounding the geometric singularity is subjected to mesh refinement. This is a result of the regularity indicator detecting this region as non-regular. To a lesser extent, the zone in the vicinity $x = 14h$ is also marked as non-regular. This is due to the flow stream lightly reaching the lower wall while adjusting to the expanded channel. Interestingly, as the density of the mesh increases, these zones become progressively more regular and the algorithm ends up switching to $p$-enrichment. Conversely, the inlet channel, recirculation bubbles, and the main stream of the flow are all flagged as smooth regions, and therefore put through $p$-enrichment.

### 7.1.2 *Global analysis of the h-, p-, and hp-adaptive results*

In order to measure the performance of the $hp$-simulations with respect to the single $h$- and $p$-computations, Figure 7.2 showcases the convergence history of the error in the $L^2$-norm of the momentum density versus the number of degrees of freedom. In Chapter 6, we demonstrated that the asymptotic region is reached for sufficiently fine grids, as is also the case here.

Figure 7.2A illustrates the convergence history associated with the $h$-simulations, both uniform and adaptive. These results are those presented in Chapter 6 and used for comparison purposes. We remind the reader that we found a moderate reduction of around 40 % in the total number of DOFs as compared to uniform refinement for a given level of accuracy.

The convergence history of the uniform and adaptive $p$-simulations is shown in Figure 7.2B. The convergence rate is considerably faster than the reported for $h$-simulations, especially during the first and the last iterations of the adaptive procedure. This suggests that the singular effect of the step on the overall smoothness of the flow may be less severe than anticipated. Observe also that between the errors reported by uniform and adaptive $p$-simulations nearly overlap for the first iteration of the algorithm. This is due to the even distribution of the error over the course of the first iteration. In this case, the increase of the polynomial degree must be extended to the entire computational domain, as reported in Section 7.1.1. In the last steps of the adaptation and for a similar level of accuracy, we achieve a reduction in the number of DOFs of approximately 50 % with respect to $p$-uniform.

Moving on to $hp$-simulations, Figure 7.2C pictures their convergence history. In this case, we report only three iterations for the uniform results, as the computations become quickly very expensive. The savings between uniform and adaptive $hp$-simulations are the largest of all the adaptation approaches, with a decrease of the total number of DOFs of roughly 92 %.

Finally, we collect the results from the $h$-, $p$-, and $hp$-adaptive simulations in Figure 7.2D. The $p$- and $hp$-adaptive computations behave comparably and report significantly better performance with respect to the $h$-adaptive computations, with savings of approximately 80 % compared to the latter. Despite


*(a)* Computational domain.

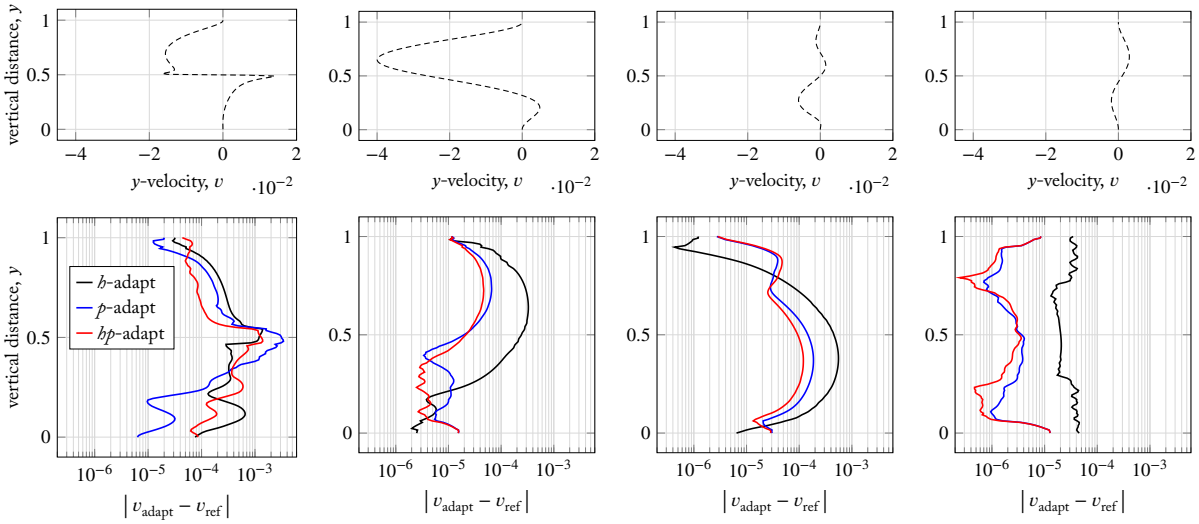


*(b)* Local $y$-velocity evaluation at the step.

*(c)* Local $y$-velocity evaluation at $6h$.

*(d)* Local $y$-velocity evaluation at $14h$.

*(e)* Local $y$-velocity evaluation at $30h$.

*Figure 7.3:* Backward-facing step. Comparison of the $h$-, $p$- and $hp$-simulations at the final adaptation step. We study various $y$-velocity profiles downstream of the step and measure the error with respect to the reference solution.

behaving similarly, a close examination of $p$ and $hp$ reveal substantial differences. Firstly, the $hp$-adaptive results display a more consistent convergence rate, which means that the $hp$-approach is more efficient in addressing the error distribution. And secondly, the $hp$-approach provides a slightly higher level of accuracy for a similar number of DOFs.

### 7.1.3 *Local flow field analysis of the h-, p-, and hp-adaptive results*

The present section outlines a detailed comparison of multiple $y$-velocity profiles along the expanded channel downstream of the step. The idea is to examine the effects of each of the adaptation approaches addressed in Section 7.1.2 at a local level. Specifically, we pay particular attention to the local behavior of the $p$- and $hp$-adaptive computations, which have displayed close resemblance when studied globally.

Figure 7.3 depicts the difference between computed adaptive $y$-velocity and reference $y$-velocity at the final adaptation step. We notice how the overall error associated each adaptive simulation, recorded by the horizontal axis, is at least one order of magnitude smaller at the locations downstream of the step. In Figure 7.3B the step acts as a geometrical singularity thus it is reasonable for the largest values of the error to be concentrated in that region. Interestingly, the regions where the flow changes direction to adjust to the channel expansion ($y > \frac{1}{2}$ in Figure 7.3C and $y < \frac{1}{2}$ in Figure 7.3D) report moderate

concentrations of the error. This is coherent with the modest refining in the same area performed in Section 7.1.1. As expected, the lowest values of the error are reported in the recirculation regions and at the developed parabolic flow of Figure 7.3E.

With respect to each adaptive simulation individually, the *h*-approach underperforms the *p*- and *hp*-simulations at the locations downstream of the step. If we define the average error of a given profile as $\Delta v_{\text{avg}} = \frac{1}{\Delta y} \int \Delta v \, \mathrm{d}y$ and particularize it for the profile of the *h*-approach, we report almost four times higher average errors in Figure 7.3C, two times in Figure 7.3D, and nine times in Figure 7.3E when compared to either the *p*- or *hp*-approach. These regions are characterized by a smoother flow and thus benefit from the increase in solution order provided by either the *p*- or *hp*-approach. Regarding these two, they seem to behave similarly from Figures 7.3C to 7.3E, with *hp*-adaptation slightly outperforming *p*-enrichment. The most significant results can be found in the region near the step, as showcased by Figure 7.3B. Here, the *p*-simulation features the highest error peak caused by the oscillations introduced by the higher-order solution around the singularity. By contrast, the *h*-simulation maintains a low polynomial order and reports a better performance, reducing around 26 % the average error with respect to the *p*-approach. The *hp*-approach further improves the percentage to 38 %. It achieves a high-order solution where the flow is smooth yet it averts the oscillations of the *p*-enrichment next to singularities by employing *h*-enrichment and low orders.

## 7.2 LAMINAR SQUARE CYLINDER

Throughout this section a sequence of numerical simulations of a two-dimensional steady laminar flow past a square cylinder is performed to evaluate the performance of the pair formed by the multiwavelet error estimator and the multiwavelet regularity indicator in the context of *hp*-adaptation.

### 7.2.1 *Computational parameters*

The study of the flow past bluff bodies has been historically an active field of research within the CFD community. The majority of the studies are centered on the circular cylinder (see e.g., Strykowski and Sreenivasan (1990), Williamson (1996), and Gautier et al. (2013)), with the square counterpart receiving substantially less attention (see e.g., Franke et al. (1990)). The flow around a square cylinder behaves comparably to the flow around a circular cylinder; the major deviation being that the location of the separation is anchored at the sharp corners of the cylinder.

It is well understood that the square cylinder configuration can can lead to different flow regimes depending on the value of the Reynolds number (Breuer et al., 2000), based on the edge length $D$ and constant inflow velocity $u_0$. At $Re < 1$ the flow is dominated by viscous forces and no separation occurs. For

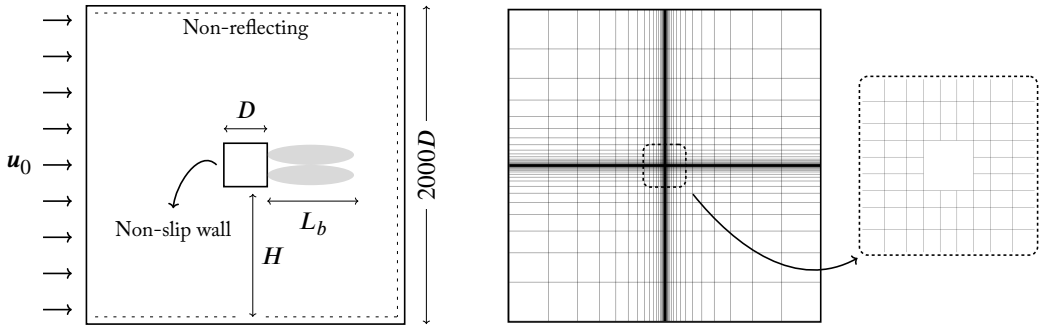


*(a)* Computational domain and BC. *(b)* Initial mesh.

*Figure 7.4:* Square cylinder. Description of the computational domain, boundary conditions, and initial grid employed.

higher $Re$, the flow detaches first at the trailing corners of the cylinder and two symmetric recirculation regions develop in the rear of the body (see Figure 7.5A). The scale of these regions grow proportionally with $Re$. When a critical Reynolds number $Re_{\text{crit}}$ is surpassed, the characteristic von Karman vortex street can be observed along the wake.

There exists no clear consensus in the literature on a fixed value of $Re_{\text{crit}}$. In this work, the choice of $Re$ has been based on the conservative estimation of $Re_{\text{crit}} = 54$ provided by Kelkar and Patankar (1992). In particular, by choosing $Re = 40$ we guarantee that the flow around the square cylinder is steady.

The body is placed in the center of a squared computational domain (see Figure 7.4A). In order to reduce the influence of the inflow and outflow boundary conditions, we follow the recommendations from Posdziech and Grundmann (2007) and Naddei (2019) and set the distance $H$ from the center to the outer boundary $H = 1000D$. The inflow boundary condition is made of a constant flow $u_0$ from left to right of the computational domain. We impose non-slip boundary conditions at the walls of the body and non-reflecting boundary conditions on the outer boundary.

Figure 7.4B illustrates the initial mesh $\Omega_h^{(0)}$. We use a Cartesian non-uniform structured mesh with 2592 elements. Starting from the outer boundary, the elements progressively decrease in size such that they are highly clustered in the vicinity of the cylinder (geometrical series).

### 7.2.2 *Reference solution and mesh convergence*

To achieve a sufficiently fine mesh from which to compute an adequate reference solution, we perform multiple mesh refinement iterations $\Omega_h^{(i)}$ of the initial grid $\Omega_h^{(0)}$. The first grids are generated by uniform global refinement. In order to limit the computational cost, we restrict the uniform refinement to the vicinity of the body, creating successive rectangular patches with ever increasing spatial resolution. Figure 7.5B depicts this process by analyzing the global $L^2$-norm of the error in the momentum density of the $p = 2$ solution obtained for each of the globally refined meshes. As can be seen in this graph, the last refined meshes achieve the asymptotic convergence rate. We obtain

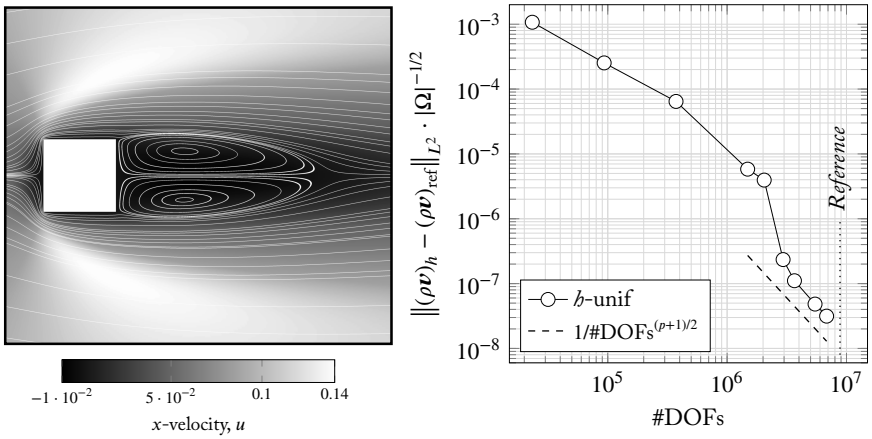


*(a)* Streamlines and recirculation bubbles in the rear of the body.

*(b)* Mesh convergence analysis. We start from the initial mesh outlined in Figure 7.4B and $p = 2$

*Figure 7.5:* Square cylinder. Overview of the configuration's relevant phenomena and roadmap to reference solution by analyzing successive uniformly refined meshes.

a final reference mesh composed of 980 853 elements, which engenders a reference solution involving 8 827 677 DOFs.

Table 7.1 presents some relevant integral flow parameters such as recirculation length and dimensionless force coefficients (drag). They are collected from some of the most relevant literature and put side by side to our reference solution. They are organised from lower to higher *blockage ratio*, which is defined as the ratio between the cylinder side length and the domain extension, $B = D/H$. This ratio helps to understand the influence of the boundary on the solution. The study of Posdziech and Grundmann (2007) concluded that if the blockage ratio is decreased to $B \leq 0.001$, the solution can be considered as being grid independent. Indeed, the deviation of the drag value between our asymptotic solution and Basile et al. (2021) is below 0.02 % for $B = 0.001$. An equally low deviation of 0.2 % is observed in the recirculation length. With increasing blockage ratios the disparity is accentuated, which means that the solution is more influenced by errors introduced by blockage. From Meliga et al. (2014) to Franke et al. (1990), the deviation in the drag coefficient increases from 2 % to 20 %, respectively.

### 7.2.3 *Overview of the h- and p-adaptive results*

We employ the initial computational grid $\Omega_h^{(0)}$ described in Section 7.2.1 with the constant $p$-distribution $\not{p} = 2$ to perform a series of $h/p$-pure adaptive computations. From the initial $\Omega_{h,\not{p}}^{(0)}$ we build a series of $hp$-meshes for which

*Table 7.1:* Integral flow quantities found in the literature and how they compare to the reference solution from the present study.

| | $C_D$ | $C_{D\,\text{press}}$ | $C_{D\,\text{visc}}$ | $L_b/D$ | $B$ |
|---|---|---|---|---|---|
| Franke et al. (1990) | 1.98 | 1.69 | 0.029 | — | 0.166 |
| Dhiman et al. (2006) | 1.7670 | — | — | 2.8220 | 0.1 |
| Sen et al. (2011) | 1.6680 | — | — | 2.8552 | 0.02 |
| Meliga et al. (2014) | 1.67 | — | — | 2.83 | 0.02 |
| Basile et al. (2021) | 1.643049 | 1.417378 | 0.225671 | 2.8318 | 0.001 |
| Present study | 1.642730 | 1.414128 | 0.228602 | 2.83596 | 0.001 |

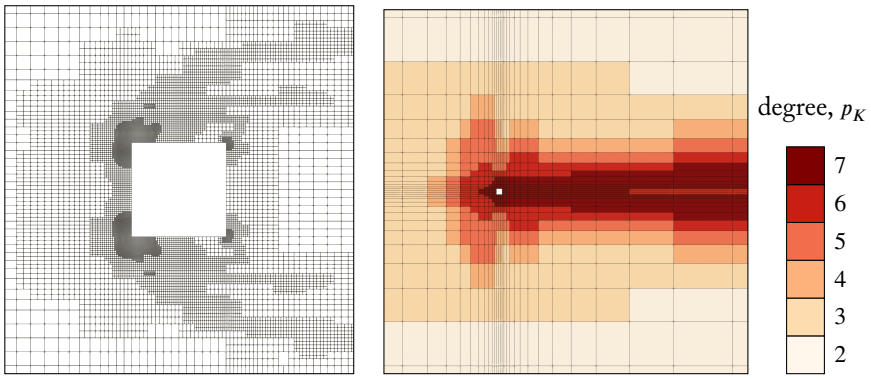


*(a)* $h$-refinement. *(b)* $p$-enrichment.

*Figure 7.6:* Square cylinder. Zooming in the vicinity of the $hp$-mesh for pure $h$- or $p$-approaches. The initial mesh and $p$-distribution are given by Figure 7.4B and $p = 2$, respectively.

$\mathcal{P}^{(i)}$ or $\Omega_h^{(i)}$ remains fixed, depending on whether we perform strictly $h$- or $p$-simulations. In the latter, we limit the local polynomial degree to the interval $p_K \in [2, 9]$.

*h/p-adapted meshes* Figure 7.6 outlines the $h$- and $p$-adapted meshes resulting from the adaptive procedure. If we pay attention first to the $h$-refined mesh in Figure 7.6A, we observe that the vicinity of the cylinder is subjected to various levels of refinement, becoming more pronounced in the region approaching the solid body. In particular, we highlight the intense local refinement at the leading corners of the cylinder and, to a lesser extent, at the trailing edge, where the separation of the laminar boundary layers occurs. This is expected, as these sharp corners generate a sudden velocity gradient in the flow. We can also clearly notice the refinement pattern along the shear layers extending downstream. In the near-wake, the two symmetrical recirculation regions display considerably lower refinement levels, which can be justified by the smoothness of the solution in that region. Finally, the far-wake area stretching to the exit boundary (not shown here) reveals unusually high levels of refinement. This behavior was also reported by Naddei et al. (2018). The authors suggested high-aspect ratio and poor mesh quality as the cause. We also believe that, despite the large distance between the cylinder and the exit, the wake may be not fully dissipated. This fact contradicts the imposed boundary conditions, causing a spurious behavior at the outflow.

Figure 7.6B illustrates the map of the local polynomial degree. Most of the observations drawn from the $h$-refined mesh are applicable to $p$-adaptation. The areas subjected to $p$-enrichment are centered around the square cylinder and along the wake in the rear of the body. The highest values of the $p$-distribution are reported in the vicinity of the square and follow the shear layer downstream. Finally, we observe a larger spread of the $p$-distribution than the equivalent mesh refinement. This is due to $p$-enrichment being constrained by the topology of the initial mesh, which is not modified. The limitation enforced in the jump of the polynomial degree between two neighboring elements causes multiple extra elements to be marked for $p$-enrichment. This prompts successive iterations of the $p$-distribution to occupy a larger area, as the number of elements in the grid is not increased.

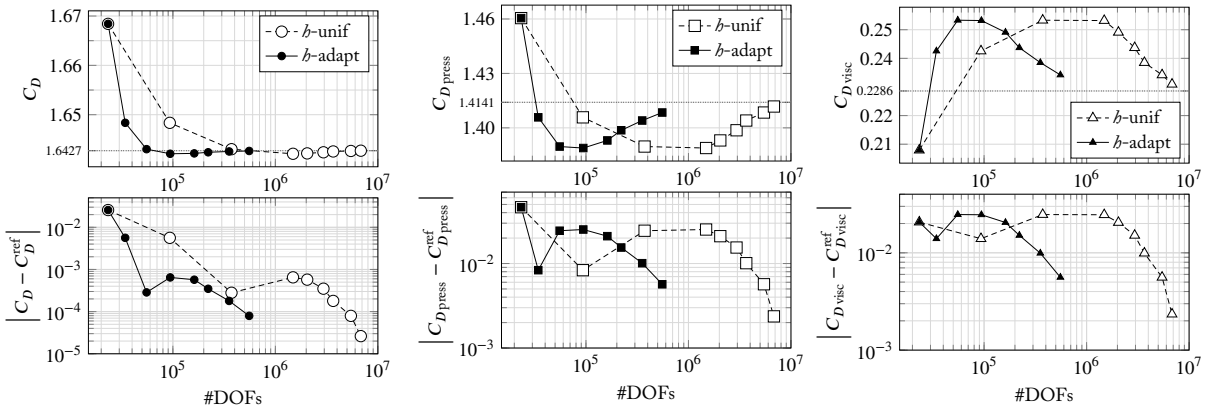


*(a)* Drag coefficient, $C_D$.

*(b)* Pressure factor on drag, $C_{D\,\text{press}}$.

*(c)* Viscous factor on drag, $C_{D\,\text{visc}}$.

*Figure 7.7:* Square cylinder. Convergence history of drag coefficients ($C_D$, $C_{D\,\text{press}}$, $C_{D\,\text{visc}}$) in $h$-adaptive vs $h$-uniform simulations.

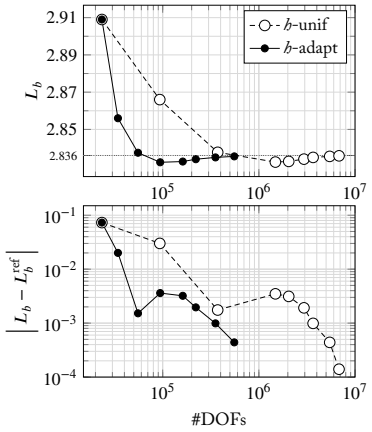


*Figure 7.8:* Square cylinder. Convergence history of recirculation length $L_b$ in $h$-adaptive vs $h$-uniform simulations.

*Integral flow quantities* The $h$- and $p$-computations are analyzed by comparing the integral flow parameters such as recirculation lengths and drag coefficients. We also study the the contributions of the viscous and pressure forces to the total drag.

Figure 7.7 shows the convergence history of the drag coefficient and its components using uniform and adaptive $h$-refinement with respect to the reference solution discussed in Section 7.2.2 for which the benchmark quantities are given in Table 7.1. We can observe that for a target value of the error in the drag coefficient of $\Delta C_D = 1 \times 10^{-4}$, we achieve a reduction of 90 % in the number of DOFs with respect to the uniform refinement, as illustrated by Figure 7.7A. We report a fast rate of decay during the first adaptive iterations. Then the procedure reports a slow down around the third iteration. We believe this is caused by the presence of the geometrical singularities at the corners of the cylinder. The converge rate is recovered after a short plateau and continues to decrease, albeit at a lower pace. The behavior of the uniform solution is equivalent, yet using a much larger number of DOFs. A similar pattern of convergence history is reported in Figures 7.7B and 7.7C for the two components of the drag. We notice an overestimation of the viscous component of the drag and an underestimation of the pressure component. While the drag achieves the target value of $\Delta C_D = 1 \times 10^{-4}$, its two components reach a higher error of $\Delta C_{D\,\text{press}} = \Delta C_{D\,\text{visc}} = 6 \times 10^{-3}$. This behavior comes from the cancellation of the errors due to the combination of the pressure and viscous coefficients.

Figure 7.8 summarizes the computed values for the recirculation length using uniform and adaptive $h$-refinement with respect to the benchmark value from the reference solution. Similarly to the drag coefficient, we reach a level of error on the recirculation length lower than that corresponding to the uniformly refined meshes.

Figure 7.9 illustrates the convergence history of the drag coefficient and its components using uniform and adaptive $p$-enrichment with regards to the reference drag. For a target value of the error in the drag coefficient of $\Delta C_D =$

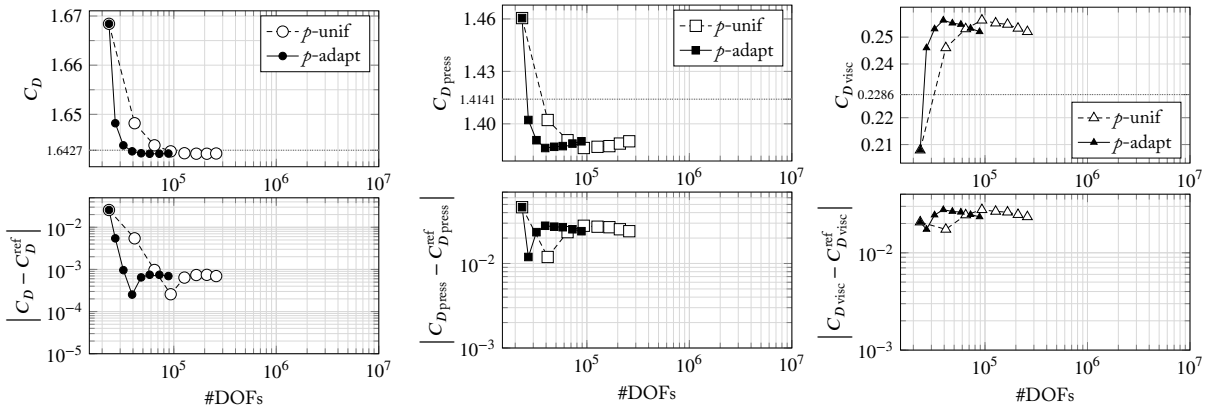


*(a)* Drag coefficient, $C_D$. *(b)* Pressure factor on drag, $C_{D\,\text{press}}$. *(c)* Viscous factor on drag, $C_{D\,\text{visc}}$.

*Figure 7.9:* Square cylinder. Convergence history of drag coefficients ($C_D$, $C_{D\,\text{press}}$, $C_{D\,\text{visc}}$) in $p$-adaptive vs $p$-uniform simulations.

$7 \times 10^{-4}$, the reduction in the number of DOFs in connection with the uniform refinement is of about 64 %, as showcased in Figure 7.9A. After a very fast decline in the convergence, the drag coefficient seems to become almost constant for the remaining adaptive iterations. This seem to suggest that $p$-enrichment alone is not able to overcome the effect of the singularity in the solution. A similar pattern is observed for the pressure and viscous component of the drag, Figures 7.9B and 7.9C, respectively. Interestingly, the convergence pace is much slower in those cases. Again, the separate components cancel each other, producing a much lower total value of the drag.

Figure 7.10 displays the computed quantities for the recirculation length using uniform and adaptive $p$-enrichment together with the reference value (horizontal dashed line). Equivalently to the drag analysis, the gains are modest with respect to uniform $p$-enrichment. We report a fast decay followed by a stabilization of the measured length.

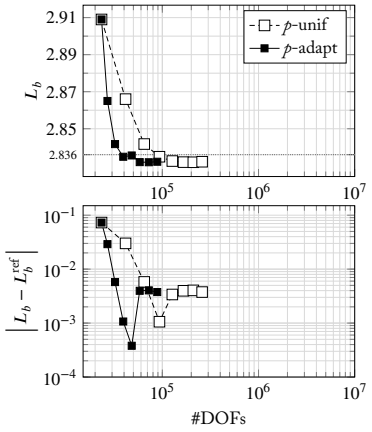


*Figure 7.10:* Square cylinder. Convergence history of recirculation length $L_b$ in $p$-adaptive vs $p$-uniform simulations.

### 7.2.4 *Parametric hp-adaptive results I: review of hp-meshes*

Similarly to the Section 7.2.3, we start from the initial computational grid $\Omega_h^{(0)}$ and the initial $p$-distribution $\mathcal{p} = 2$ and perform a series of $hp$-adaptive simulations. From the initial $\Omega_{h,\mathcal{p}}^{(0)}$ we generate a sequence of $hp$-meshes $\Omega_{h,\mathcal{p}}^{(i)}$. Unlike Section 7.2.3, the successive $p$-distributions $\mathcal{p}^{(i)}$ and refined meshes $\Omega_h^{(i)}$ would be adapted simultaneously. The choice between modifying one or the other is guided by the multiwavelet regularity indicator under different ranges of the $hp$-threshold parameter $\varsigma_{\text{tol}}$. Again, the local polynomial degree is constrained to $p_K \in [2, 9]$.

Figure 7.11 displays the resulting $hp$-meshes for different iterations of the adaptive procedure under $0.4 \leq \varsigma_{\text{tol}} < 0.5$. This configuration of the regularity indicator gives a strong preference to $h$-refinement over $p$-enrichment. At the first iteration mesh refinement is performed around the body and along the rear wake up to the exit, as illustrated in Figure 7.11A. The pattern of $h$-refinement near the body remains for the next iterations, including the trailing edges and

the two symmetrical vortexes. On the other hand, $p$-enrichment is activated at later iterations in the region immediately upstream of the body and along the downstream wake. A zoomed detail of the square cylinder allows us to see that the highest levels of refinement are achieved at the frontal and rear corners, as showcased by Figure 7.11F. The highest $p$-value of this configuration is $p = 6$, which can be found along the near-wake.

Figure 7.12 illustrates the $hp$-meshes under $0.3 \leq \varsigma_{\text{tol}} < 0.4$. This setting represents a more moderate preference toward mesh refinement. We still report adaptation of the mesh in the vicinity of the body, but it is progressively replaced by the adaptation of the local polynomial in subsequent iterations, especially along the wake extending towards the boundary. The corners, immediate shear-layer, and recirculation bubbles still require $h$-refinement. By looking at the magnified square cylinder in Figure 7.12F, we reveal the highest density of the grid around the upstream corners, whereas the narrow near-wake and a small region at the front of the cylinder report a polynomial degree of $p = 6$, the highest value of the $p$-distribution in this configuration.

Figure 7.13 showcases a shift towards $p$-adaptation, with a $hp$-threshold parameter within the interval $0.2 \leq \varsigma_{\text{tol}} < 0.3$. In this case only the areas close to the front and rear of the body are selected for mesh refinement. Early on, $p$-enrichment spreads to the upstream and downstream of the cylinder, forming a clear $p$-distribution tail extending to the exit. The zoomed window in Figure 7.13F offers a view on the highly $h$-refined frontal corners, while the frontward area and the wide region starting at the near-wake collects the maximum polynomial degree of $p = 7$.

Figure 7.14 is using $0.1 \leq \varsigma_{\text{tol}} < 0.2$ and describes an acute trend towards $p$-adaptation, whereas the zones that report mesh refinement are minimal. In fact, early iterations of the adaptive procedure are fully governed by $p$-enrichment, with the exception of the small regions around the forward corners of the cylinder. Later iterations only accentuate this trend. Indeed, a remarkable focus on refining the mesh is shown in Figure 7.14F, where a zoom of the cylinder is depicted. Every other element selected for adaptation is subjected to an increase in the polynomial degree. The maximum polynomial degree in this configuration is $p = 7$.

### 7.2.5 *Parametric hp-adaptive results II: drag coefficient*

In this section we provide a detailed comparison of the possible ramifications of the multiwavelet regularity indicator regarding its $hp$-sensitivity. The idea is to compare different $hp$ outcomes based on a parametric analysis of the $hp$-threshold $\varsigma_{\text{tol}}$. To measure the effect of the parameter $\varsigma_{\text{tol}}$ into the $hp$-adaptive process we analyze the behavior of the drag coefficient.

Figure 7.15 portrays the convergence history of the drag coefficient and its components using $hp$-adaptation versus uniform $h$-refinement with respect

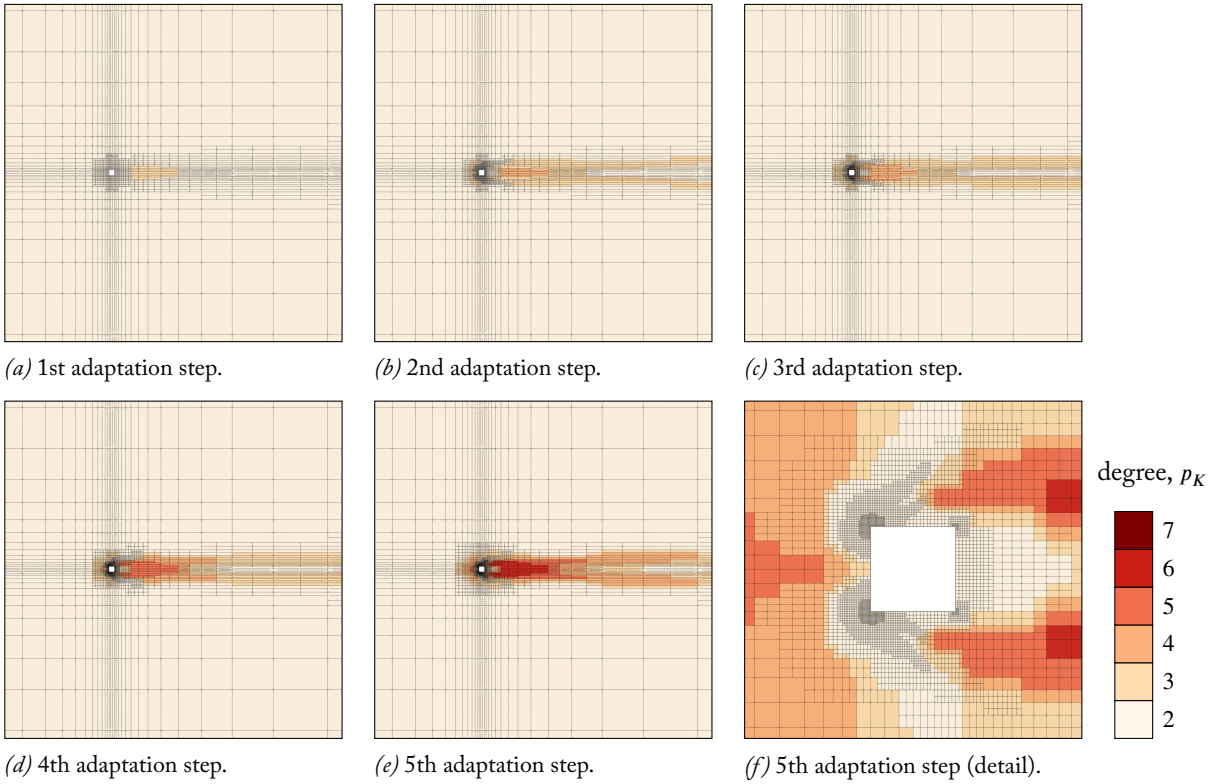


*(a)* 1st adaptation step. *(b)* 2nd adaptation step. *(c)* 3rd adaptation step.

*(d)* 4th adaptation step. *(e)* 5th adaptation step. *(f)* 5th adaptation step (detail).

*Figure 7.11:* Square cylinder. Successive iterations of the *hp*-meshes under *hp*-adaptation with a strong leaning towards *h*-refinement. That is, we use the *h*++ tolerance $(0.4 \leq \varsigma_{\text{tol}} < 0.5)$.

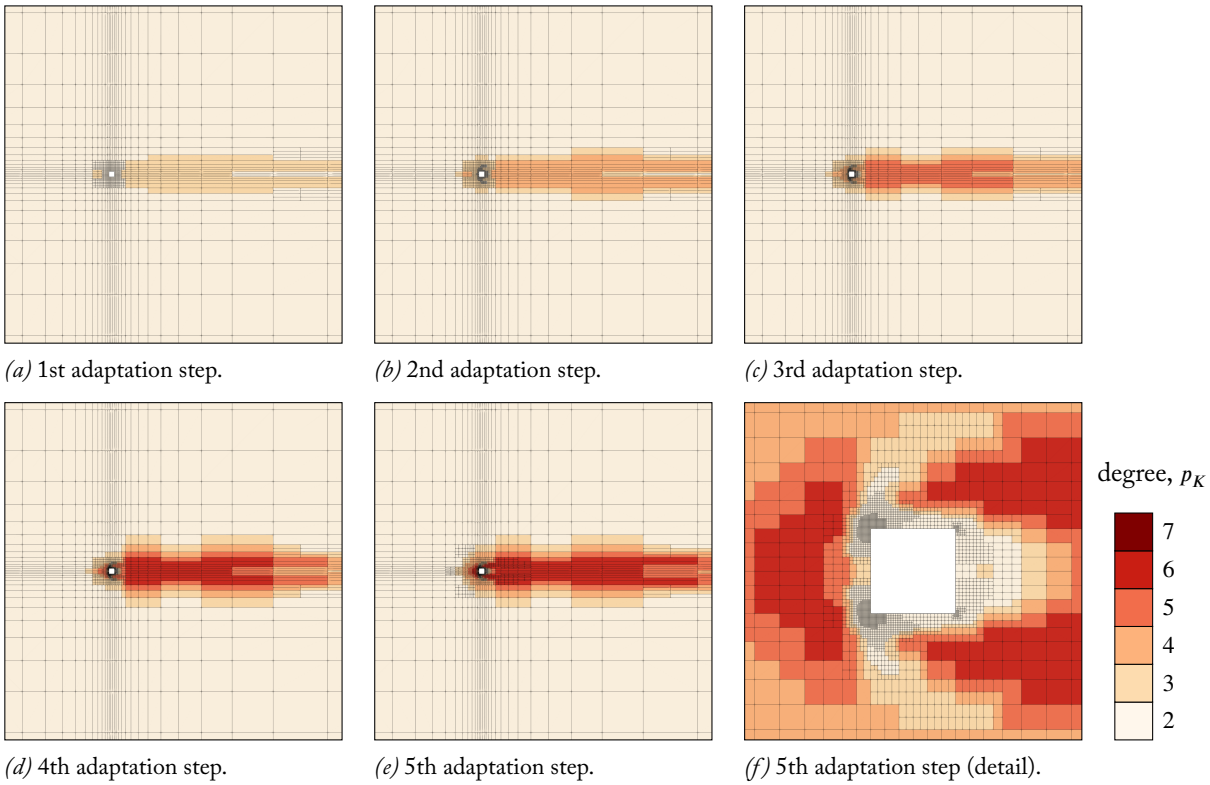


*(a)* 1st adaptation step. *(b)* 2nd adaptation step. *(c)* 3rd adaptation step.

*(d)* 4th adaptation step. *(e)* 5th adaptation step. *(f)* 5th adaptation step (detail).

*Figure 7.12:* Square cylinder. Successive iterations of the *hp*-meshes under *hp*-adaptation with a moderate tendency towards *h*-refinement. Which is to say, we follow the *h*+ tolerance $(0.3 \leq \varsigma_{\text{tol}} < 0.4)$.

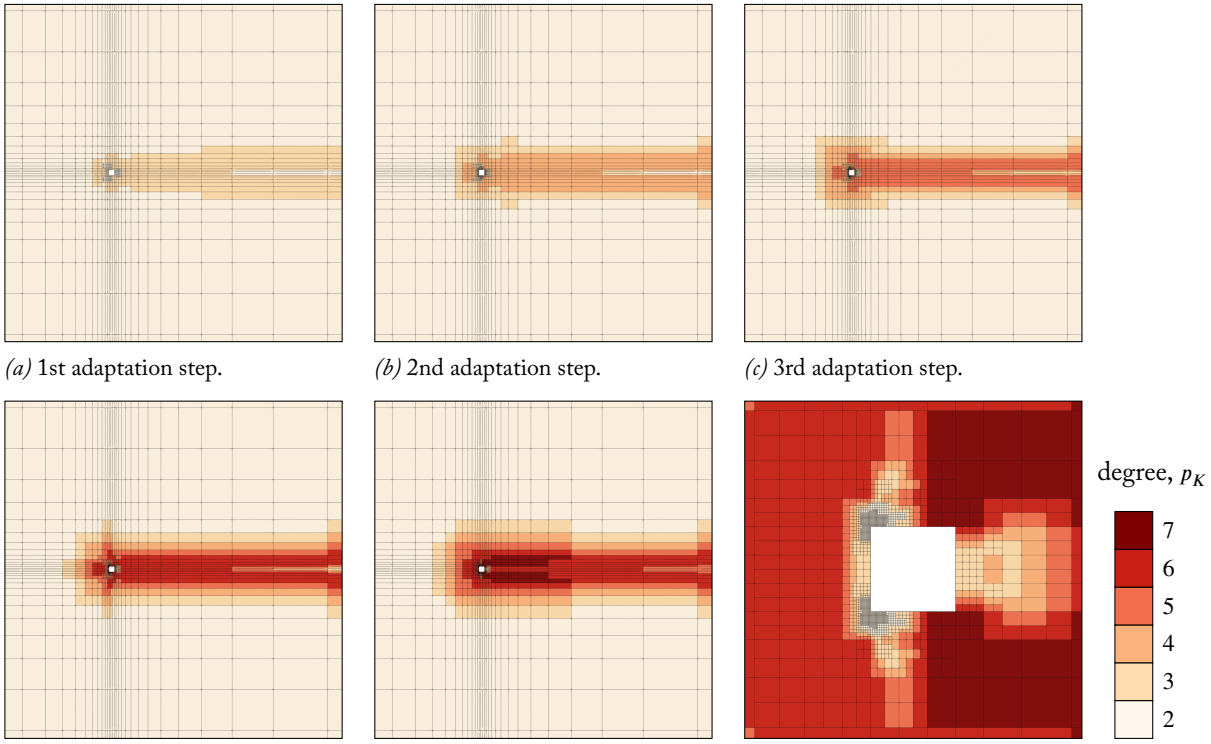


*(a)* 1st adaptation step. *(b)* 2nd adaptation step. *(c)* 3rd adaptation step.

*(d)* 4th adaptation step. *(e)* 5th adaptation step. *(f)* 5th adaptation step (detail).

*Figure 7.13:* Square cylinder. Successive iterations of the *hp*-meshes under *hp*-adaptation with a moderate affinity towards *p*-refinement. Which implies that we implement the *p*+ tolerance $(0.2 \leq \varsigma_{\text{tol}} < 0.3)$.

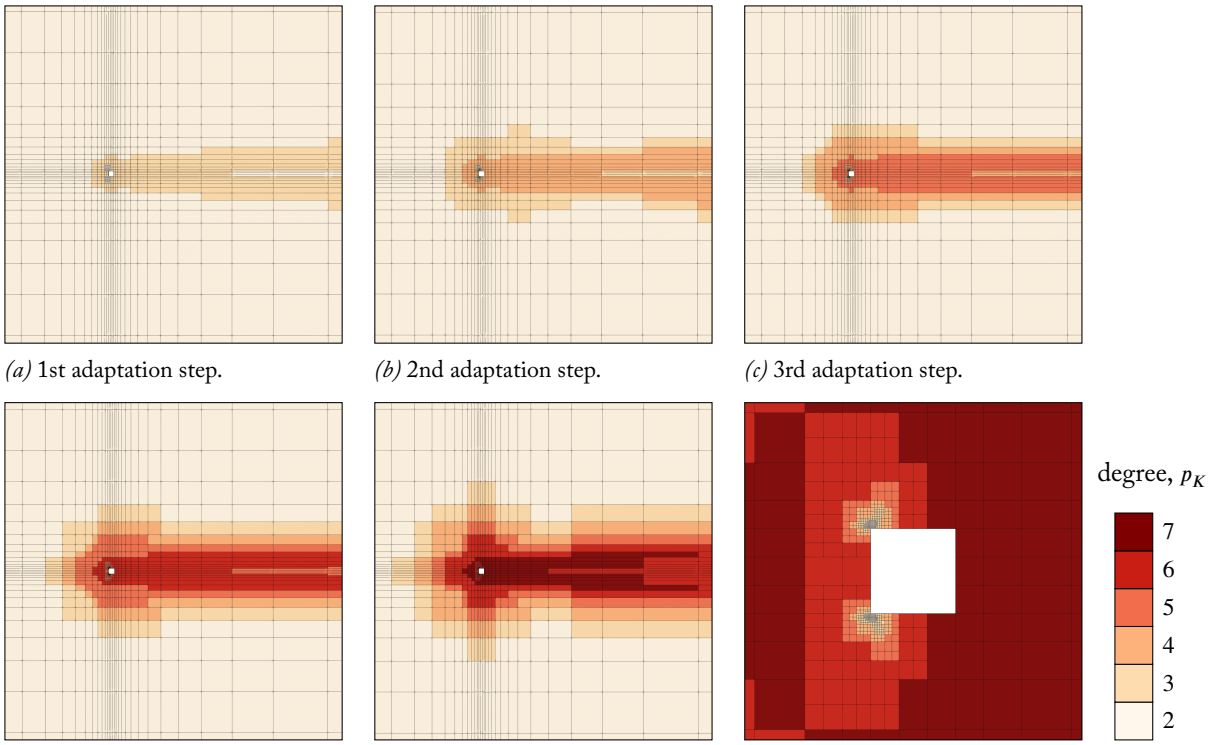


*(a)* 1st adaptation step. *(b)* 2nd adaptation step. *(c)* 3rd adaptation step.

*(d)* 4th adaptation step. *(e)* 5th adaptation step. *(f)* 5th adaptation step (detail).

*Figure 7.14:* Square cylinder. Successive iterations of the *hp*-meshes under *hp*-adaptation with a strong predisposition towards *p*-refinement. Meaning that we apply the *p*++ tolerance $(0.1 \leq \varsigma_{\text{tol}} < 0.2)$.

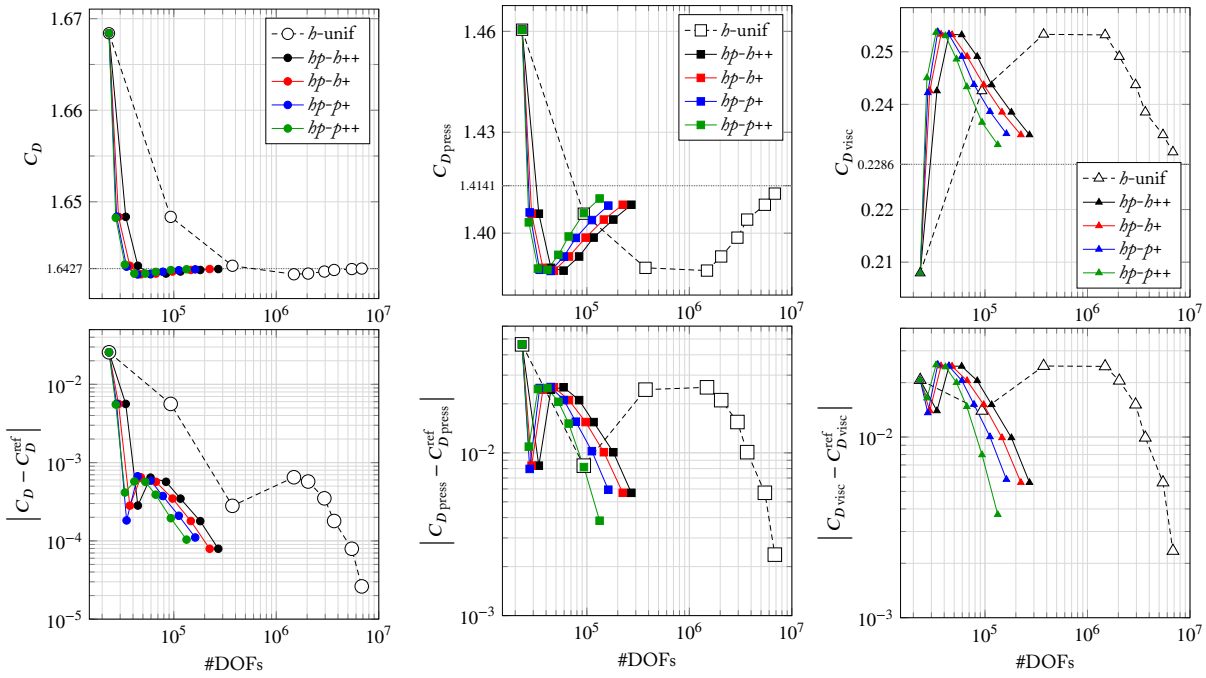


*(a)* Drag coefficient, $C_D$. *(b)* Pressure factor on drag, $C_{D\,\mathrm{press}}$. *(c)* Viscous factor on drag, $C_{D\,\mathrm{visc}}$.

*Figure 7.15:* Square cylinder. Convergence history of drag coefficients ($C_D$, $C_{D\,\mathrm{press}}$, $C_{D\,\mathrm{visc}}$) in *hp*-adaptive vs *h*-uniform simulations.

to the value given by the reference solution. The different values of the *hp*-threshold $\varsigma_{\mathrm{tol}}$ are represented by the different colored graphs. The nomenclature is the following:

(i) *h*++ tolerance, defined by the span $0.4 \leq \varsigma_{\mathrm{tol}} < 0.5$.
(ii) *h*+ tolerance, denoted by $0.3 \leq \varsigma_{\mathrm{tol}} < 0.4$
(iii) *p*+ tolerance, identified by $0.2 \leq \varsigma_{\mathrm{tol}} < 0.3$
(iv) *p*++ tolerance, represented by $0.1 \leq \varsigma_{\mathrm{tol}} < 0.2$

Given a target error of $\Delta C_D = 1 \times 10^{-4}$ in the drag coefficient, the number of DOFs with respect to the uniform refinement is significantly reduced. This is true for all of the prescribed tolerances, as illustrated by Figure 7.15A. We report savings ranging from 95 % for *h*++ to 98 % for *p*++. In a similar manner, they display a rapid downward progression, then a deceleration, and finally they feature a restored decay, yet at a slower pace. The pressure and viscous contributions to the drag, Figures 7.15B and 7.15C, display a similar behavior. However, we observe again a compensation of errors (due to the components of the drag remaining similarly underestimated and/or overpredicted) being transferred to the total drag, causing the latter to reach lower values of the error compared to its components.

The dissimilarities among the prescribed tolerances are worth investigating. The results from $C_{D\,\mathrm{press}}$ and $C_{D\,\mathrm{visc}}$ seem to suggest for this configuration a slight benefit of choosing tolerances leaning towards *p*-enrichment, with the tolerance *p*++, which seems to be the most efficient, achieving higher accuracy for the same number of adaptation steps. However, for the total drag the outcome is less clear, with the tolerances leaning towards *h*-refinement

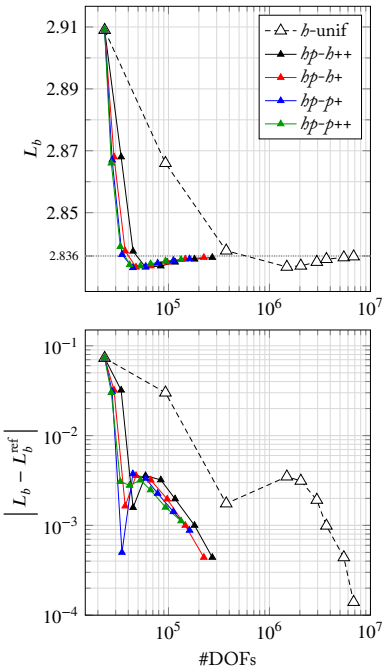


*Figure 7.16:* Square cylinder. Convergence history of recirculation length $L_b$ in *hp*-adaptive vs *h*-uniform simulations.

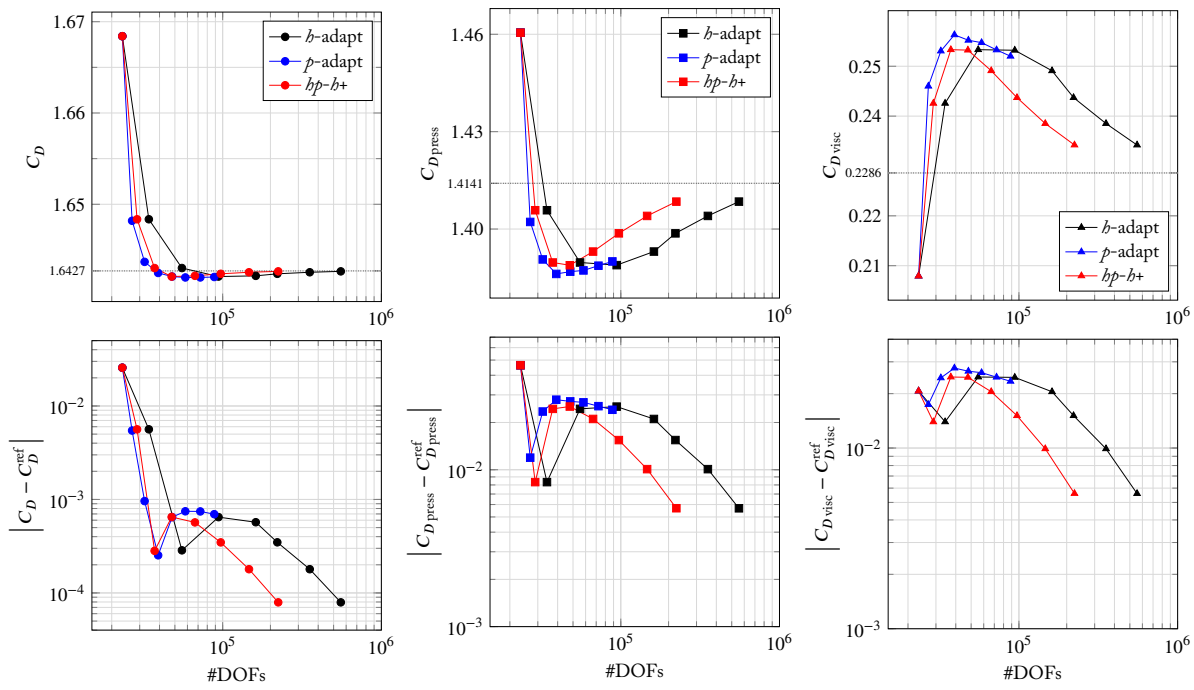


*(a)* Drag coefficient, $C_D$. *(b)* Pressure factor on drag, $C_{D\,\text{press}}$. *(c)* Viscous factor on drag, $C_{D\,\text{visc}}$.

*Figure 7.17:* Square cylinder. Comparison of the convergence history among *h*-, *p*- and *hp*-adaptive simulations for the drag coefficient $C_D$ and its contributions $C_{D\,\text{press}}$ and $C_{D\,\text{visc}}$.

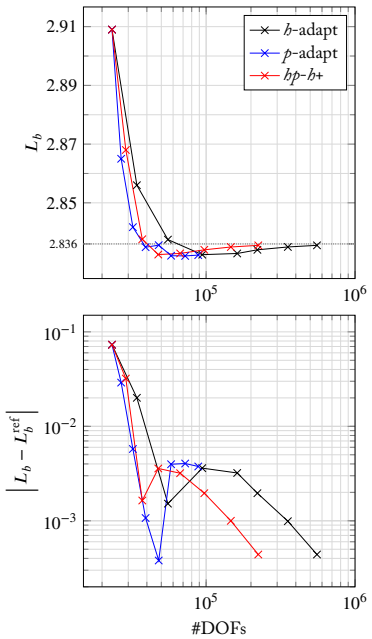


*Figure 7.18:* Square cylinder. Comparison of the convergence history among *h*-, *p*- and *hp*-adaptive simulations for the recirculation length $L_b$.

reporting narrowly higher accuracy. In particular, the moderate tolerance *h*+ outperforms all others. As discussed before, these differences between total drag and its components are likely caused by a compensation of errors. In the next section we further investigate the behavior of the *hp*-adaptive algorithm by looking into the recirculation bubble length.

### 7.2.6 *Parametric hp-adaptive results III: recirculation region*

Figure 7.16 shows the computed values of the recirculation length using *hp*-adaptation and uniform *h*-refinement and compares them to those obtained from the reference solution. As for the $C_D$, we observe similar convergence histories for all the prescribed tolerances. However, the tolerances weighted towards *p*-enrichment require a larger number of adaptation steps to arrive at the same accuracy reported by either *h*+ or *h*++. Specifically, the moderate tolerance *h*+ seems to be the most efficient.

### 7.2.7 *Global analysis for h-, p-, and hp-adaptive results*

In this section we collect the best results from the different adaptive strategies for the integral flow quantities obtained from *hp*-adaptation (Sections 7.2.5 and 7.2.6) and compare their performance against their pure *h* and *p* counterparts obtained in Section 7.2.3.

The adaptive results for the drag coefficient and its pressure and viscous contributions are outlined in Figure 7.17. During the analysis of the total drag,

Figure 7.17A, we observe that $p$-adaptation yields a fast error convergence during the first iterations but quickly reaches a plateau at $\Delta C_D = 7 \times 10^{-4}$, well above the value of $\Delta C_D = 8 \times 10^{-5}$ reached by either $h$ or $hp$. This is expected given the coarse initial grid and the presence of the strong geometrical singularity at the corners of the cylinder. We suspect that not being able to adjust the topology of the initial mesh clearly becomes a limitation. Conversely, $h$-adaptation produces a slower convergence rate. This decay ends on a similar plateau but, unlike $p$-enrichment, it does not fully stagnates and it restores the error convergence to a moderate pace by upholding fine grid sizes and low order approximations around the corners of the cylinder. Clearly, $hp$-adaptation provides the optimal approach. On the one hand it provides the rapid error convergence characteristic of $p$-enrichment during the first steps of the adaptive procedure. On the other hand, it does inherit from $h$-refinement the possibility to overcome the effect of the geometrical singularity by locally adapting the mesh and thus producing a proper error convergence. These factors allow $hp$-adaptation to reach the target level of accuracy $\Delta C_D = 8 \times 10^{-5}$ while achieving a reduction of 62 % in the total #DOFs with respect to $h$-adaptation. These behaviors are similarly reported for $C_{D\,\text{press}}$ and $C_{D\,\text{visc}}$ in Figures 7.17B and 7.17C, respectively; even when we take into account the error compensation between these quantities.

Finally, Figure 7.18 showcases the adaptive results for the recirculation length. Analogously to the drag analysis, the use of pure $p$-adaptation achieves early fast error convergence but ends up stagnating the progression, while the pure $h$-simulation improves the error convergence at the expense of using a larger #DOFs. The $hp$-adaptive approach appears thus as the ideal choice by attaining rapid convergence while substantially reducing the #DOFs.

### 7.2.8 *Local flow field analysis for h-, p-, and hp-adaptive results*

The current section presents a detailed comparison of relevant velocity and pressure profiles at several locations in the flow field. In particular, we are interested in analyzing the effects of each of the adaptation approaches discussed so far ($h$, $p$, and $hp$) at a local level.

*Profiles in the streamwise direction* First, we focus on the horizontal profiles following the direction of the flow, as illustrated in the top row of Figure 7.19. The first of these profiles spans from the frontal corner to the rear corner, and extends along the trailing edge. Figure 7.19A collects the values of the difference between the computed and the reference pressure for every adaptive iteration. If we define the average error of a given profile as $\Delta p_{\text{avg}} = \frac{1}{\Delta x} \int \Delta p \, \mathrm{d}x$, the error profiles obtained for the $p$-enrichment strategy display a reduction of the average error between successive iterations of 24 %, with the initial steps reporting a maximum of 45 % and the later stages providing a negative reduction of −6 %. The final profile seems to be crowded with little fluctuations generated by the high-order approximations being unable to capture the singularities. This may explain the slow error convergence and stagnation of the

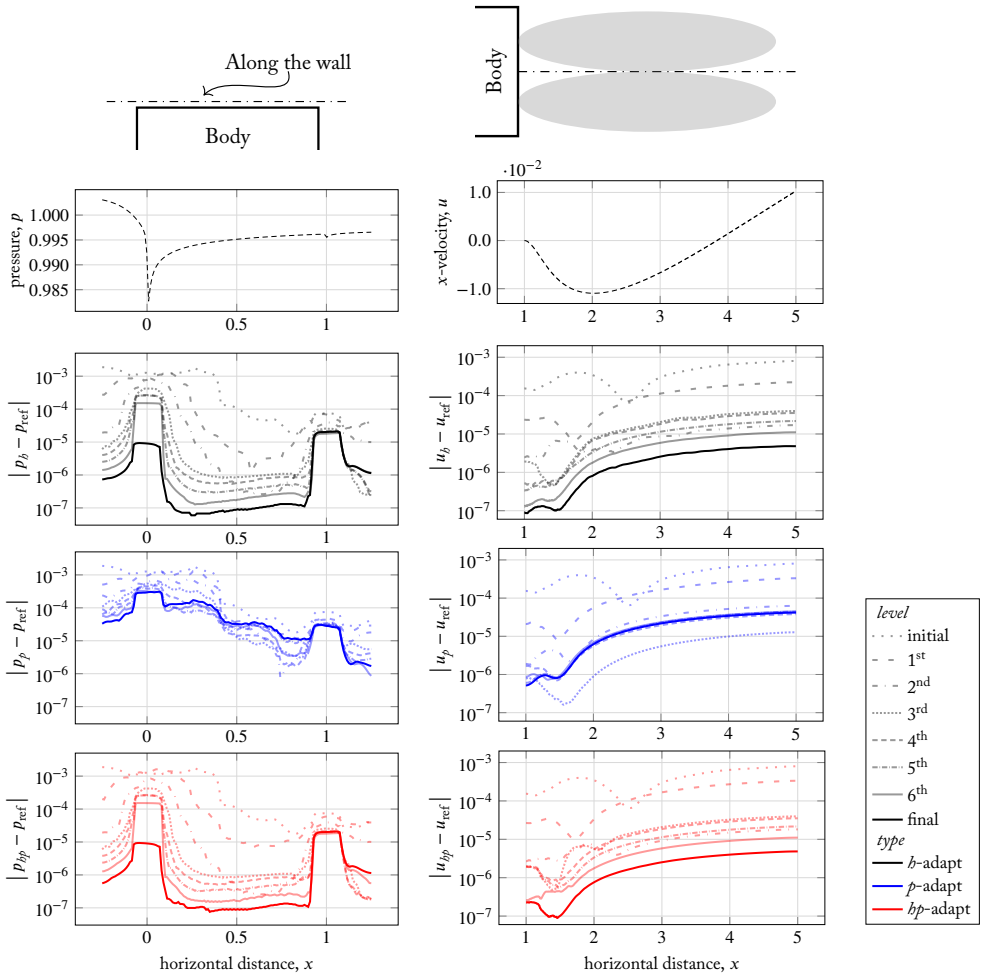


*(a)* Local pressure analysis on top wall, along frontal and rear corners.

*(b)* Local horizontal velocity analysis along the near-wake region, $0 \leq x \leq 5D$.

*Figure 7.19:* Square cylinder. Comparison of the *h*-, *p*- and *hp*-simulations at every adaptation step. We study various physical variables at selected profiles in the vicinity of the body and evaluate the error in relation to the reference solution.

global quantities observed in Sections 7.2.5 and 7.2.6. By contrast, *h*- and *hp*-adaptation feature a mean decrease of the error between successive adaptation steps of 47 %. Interestingly, from the fourth iteration of the adaptive algorithm the two sharp corners become the main source of the error. The average error decline is however slowed down to a minimum of 6 %. By concentrating the mesh refinement on the singularities we progressively recover the percentage to the maximum of 81 % at the final adaptation step. The differences between the final *h* and *hp* profiles are minimal. Revealingly, these profiles achieve a reduction of the average error with respect to the final *p* profile of approximately 95 %.

Figure 7.19B outlines a second horizontal profile along the symmetry axis of the vortexes and follows the near-wake region behind the body. Here, we study the difference between computed adaptive and reference horizontal velocity for every iteration of the adaptive procedure. The evolution of the *p*-enrichment reports a rapid decline of its the error profile during the initial steps followed by a sudden stagnation. By contrast, the *h*- and *hp*-results dis-

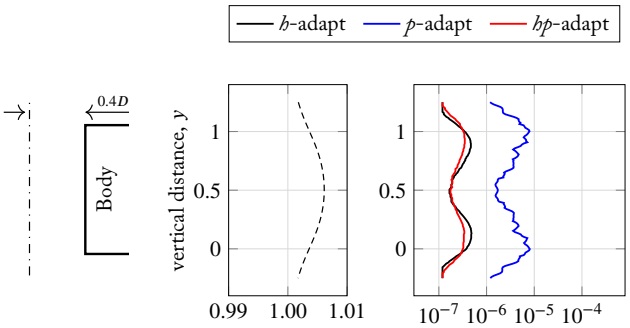


*(a)* Local pressure evaluation at $0.4D$ away from the upstream wall.

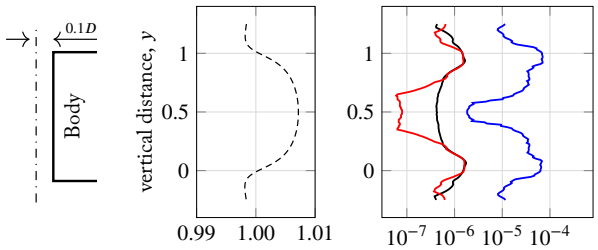


*(b)* Local pressure evaluation at $0.1D$ away from the upstream wall.

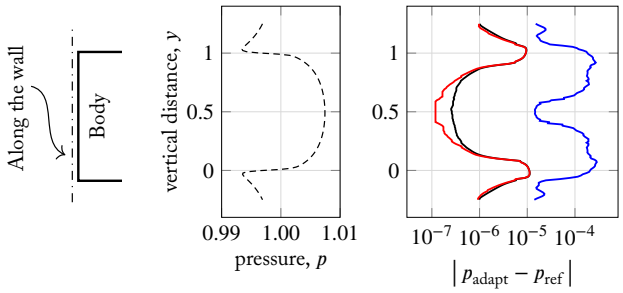


*(c)* Local pressure evaluation on the upstream wall.

*Figure 7.20:* Square cylinder. Comparison of the *h*-, *p*- and *hp*-simulations at the final adaptation step. We analyze multiple pressure profiles upstream of the body and measure the error with respect to the reference solution.

play a more monotonic decline of the average error of approximately 30 %, with the average error measured as $\Delta u_{\text{avg}} = \frac{1}{\Delta x} \int \Delta u \, \mathrm{d}x$. This seems to suggest that not capturing properly the singularities in the vicinity of the body affects the downstream flow. Again, there exists minimal variations between the final *h* and *hp* profiles. Similarly to the pressure analysis in Figure 7.19A, they accomplish a decrease of the average error with respect to the final *p* profile of about 88 %.

*Profiles in the cross-stream direction* Finally, we assess the pressure profiles perpendicular to the direction of the flow. Figure 7.20 illustrates the balance between computed adaptive pressure and reference pressure at the final adaptation step. We analyze three different locations upstream of the cylinder, which are ordered from farthest to closest to the body in Figures 7.20A to 7.20C. We can observe how the overall error of each adaptive approach, given by the horizontal axis, becomes larger as we approach the body. This is expected, as the singularities are the main source of the error in this configuration. Regarding each of the adaptive approaches individually and defining the average error as $\Delta p_{\text{avg}} = \frac{1}{\Delta y} \int \Delta p \, \mathrm{d}y$, we notice how *hp*-adaptation is again the

most efficient of the group. With this in mind, it reports extensive savings in the average error between 93 % and 97 % when its profile is compared to the profile of the *p*-approach, and between 6 % and 22 % when compared to the *h*-approach. In this analysis the *p*-approach reports fluctuations in the error and wider error areas around the singularities due to the ill-fitting behavior of the high-order approximations at those points. The *hp*-approach manages to be higher-order where the solution is regular yet avoiding the oscillations reported by *p*-enrichment.

## 7.3 CONCLUDING COMMENTARY

In this chapter we have evaluated the performance of our multiwavelet *hp*-adaptive scheme applied to two steady configurations at $Ma = 0.1$ and different Reynolds numbers: the 2-D laminar flow over a backward-facing step at $Re = 800$ and the 2-D laminar flow past a square cylinder at $Re = 40$. These two configurations are characterized by the presence of singularities that severely impact the behavior of the flow overall. Therefore, they are especially relevant configurations to be subjected to an adaptive scheme.

With regards to the backward-facing step, we have compared the global convergence history of *h*-, *p*-, and *hp*-adaptive simulations with respect to simulations based on uniformly refined grids, polynomials, or both; respectively. Every adaptive approach has outperformed its uniform counterpart, with reductions in the numbers of degrees of freedom of between 40 % and 92 %. Among the adaptive approaches, both the *p*- and *hp*- approaches have reported similar behavior and they have been substantially more efficient than the pure *h*-approach, achieving savings of about 80 % when they were set side by side to the latter. We have further studied the local behavior of the solution and found that either the *p*- or *hp*- approach has again outperformed the *h*-approach in regions of high regularity of the solution, such as the the expanded channel downstream of the step. However, in regions close to the step (singularity), the *p*-approach introduced spurious oscillations which have worsened the quality of the approximation. By contrast, here the previously insufficient *h*-approach has outmatched the *p*-enrichment with a lower average error of about 26 %. But the best local performance has been reported by the *hp*-approach, further improving the savings to 38 %.

On the square cylinder configuration we have conducted a more exhaustive study of the *hp*-simulations by performing two different exercises. In the first place, we have investigated the optimal *hp*-distribution by executing a parametric evaluation of plausible tolerances for the *hp*-threshold. We have appointed four ranges of tolerances. On the one hand, the first two tolerances display an intense affinity towards mesh refinement (*h*++) or polynomial enrichment (*p*++), whereas the remaining two tolerances show a more moderate preference to each approach, being named *h*+ and *p*+, respectively. We have studied the convergence history of both the drag coefficient and the recirculation length to assess their performance. In this regard, we have observed savings in the number of DOFs of between 95 % and 98 % with respect to

uniform mesh refinement. In particular, the moderate predisposition *h*+ has shown the best performance, achieving a higher accuracy for the same number of adaptation steps.

In the second place, the *hp*-adaptive results due to the tolerance *h*+ have been compared to equivalent *h*- and *p*-adaptive computations to determine which was the best adaptive approach. Both a series of global and local quantities have been analyzed in this context. In the global setting, pure *h*-adaptation has achieved a reduction of 90 % in the number of DOFs with respect to the uniform mesh refinement, while *p*-adaptation has reported more modest savings of 64 % compared to uniform polynomial refinement. However, the *p*-approach did not reach the target level of accuracy and showed signs of stagnation. By contrast, the *hp*-approach under tolerance *h*+ did achieve the target level of accuracy while attaining a extensive reduction of 96 % in the number of DOFs with respect to uniform mesh refinement. If *hp*-*h*+ is compared directly to pure *h*-adaptation, we have reported savings of 62 %.

In the local setting we have evaluated multiple pressure and velocity profiles around the cylinder and along the near wake, respectively. We have found minimal variations between the profiles associated with the *h*-approach and *hp*-approach under tolerance *h*+. On the other hand, the profiles related to *p*-enrichment were deteriorated by oscillations introduced by high-order approximations near the corners of the body (singularities). Due to this reason, either the *h* or *hp*-*h*+ profiles have routinely outperformed the *p*-profiles, with savings in the average error of about 90 % with respect to the latter.

# Chapter 8

# CONCLUSIONS AND FUTURE WORK

## 8.1 CONCLUSIONS

The main objective of this work was to develop computationally efficient *hp*-adaptive discontinuous Galerkin methods to numerically solve the Navier-Stokes equations under various steady-flow configurations.

In order to achieve this goal, we have brought together the *flexibility* of *a posteriori* driven adaptation and the *accuracy* of multiresolution-based adaptation. This pairing has allowed us to overcome the limitations of traditional multiresolution-based adaptation methods and to advance an alternative multiwavelet-based methodology in the context of *a posteriori* local error estimation and mesh adaptation. Most interestingly, we have superseded the restriction of traditional MRA-based approaches to mesh adaptation by providing the new multiwavelet-based methodology with both grid size (*h*-) and polynomial degree (*p*-) adaptation capabilities.

In the first part of this research, we have investigated how multiwavelets could become active agents on driving adaptive discontinuous Galerkin schemes. We have concluded that, in order for the multiwavelets to be able to extract meaningful information locally, the high-order solution must be put through a post-processing treatment to enrich its polynomial constituents. With that in mind, we have successfully developed and tested multiple reconstruction paradigms involving the current element and its immediate neighbors. This new reconstructed solution can then be broken apart into a hierarchy of low-resolution data and subsequently finer details. Based on this methodology, we have demonstrated how to make use of the multiwavelet properties while being local to the element, thereby maintaining the compacity of the DG method.

We have first employed the local multiwavelet-based methodology to measure the discretization error of the numerical solution in the context of *h*-adaptive simulations. In order to investigate the capabilities and limitations of the method, we have selected flow configurations characterized by physical and geometrical singularities, which would significantly benefit from mesh refinement. Adaptive computations of the one-dimensional viscous Burgers equation have proved the efficiency of the multiwavelet-based methodology against relevant estimators provided in the literature (in particular the SD (Taube et al., 2010) and SSED (Kuru et al., 2016) estimators). From these

results, we have heralded the $\kappa$-multiwavelet estimator, based on the reconstruction paradigm with the most element-neighbor interactions, as the best performing from the multiwavelet family.

Supported by the encouraging results, we have applied the estimator to the two-dimensional steady $h$-adaptive computations of the laminar backward-facing step flow at $Re = 800$ and $Ma = 0.1$. This more challenging configuration has demonstrated that, for a prescribed level of accuracy in the density momentum variable, the $\kappa$-multiwavelet estimator applied to various physical quantities achieves a reduction between 48 % and 90 % of the number of degrees of freedom compared to uniformly refined simulations, with the larger percentages obtained by higher-order computations. The convergence study of the separation/reattachment lengths has led to similar savings. Overall, we have identified the $\kappa$-multiwavelet estimator applied on the density momentum displaying a performance slightly above all others.

We have observed how the size of the mesh and the order of the approximation have also become key drivers of the magnitude of the simulation times. Computational times need to be interpreted with caution because they are hard to measure consistently and are subjected to many variables not always fully understood. However, the data presented have demonstrated that, by activating a multiwavelet-guided adaptation in simulations of higher order, we have achieved substantial speedup times. Particularly, in the best case scenario, the family of the $\kappa$-multiwavelet estimators have enabled more than 20 times faster solutions when compared to the uniformly refined solution.

We have noticed that the $\kappa$-multiwavelet estimator did not suffer from a series of deficiencies reported by the SSED and SD estimators when operating in low-order adaptive simulations and displays a more consistent behavior across different orders. Most notably, we have observed that the $\kappa$-multiwavelet estimator becomes more accurate when the local order is increased thanks to the higher quantity of details captured during the multiwavelet decomposition. Admittedly, this behavior is not unique to the multiwavelet-based estimator, as the SSED and SD estimators are also known to benefit from the increase in $p$. However, they still did not surpass the overall performance of the $\kappa$-multiwavelet estimator.

The second line of investigation addressed the analysis and development of a new $hp$-adaptive strategy. The idea was to provide enhanced sub-optimal accuracy through mesh refinement in non-smooth regions, and simultaneously increase local polynomial order in smooth areas to reach exponential-like accuracy. We have performed a thorough study of the behavior of the multiwavelet coefficients on various analytical functions and on the post-reconstructed DG solution and we have established the existence of a consistent association between function regularity and the rate of decay of the spectrum of the multiwavelet coefficients. From here we have constructed a multiwavelet regularity indicator based on this spectrum to drive $hp$-adaptive simulations of the 2-D laminar backward-facing step and the steady laminar flow past a square cylinder at $Re = 40$ and $Ma = 0.1$.

For the backward-facing step configuration we have performed a sequence of *h*-, *p*-, and *hp*-adaptive computations. The convergence behavior of each of the adaptive approaches was compared with its equivalent uniform adaptation. Every adaptive approach has outperformed its uniform counterpart, with reductions in the numbers of degrees of freedom of between 40 % and 92 %. When it comes to the individual adaptive approaches, both the *p*- and *hp*-adaptive computations behaved equivalently and reported significantly better performance in regards to the pure *h*-adaptive computations, with savings of approximately 80 % compared to the latter. A further analysis of the local behavior of the solution has found that the pure *p*-approach introduced spurious fluctuations in the regions close to the step, due to the presence of strong gradients. This phenomena has caused the *p*-approach to fall behind in *hp*-approach in the local analysis. In this regard, we have quantified a lower average error of about 38 % when the latter is compared to the former approach. From the implications of the global and local results we have determined *hp*-adaptation as the most efficient adaptive approach.

We have then performed a more detailed analysis of the *hp*-computations for the laminar square cylinder configuration. In a first step, we have investigated the optimal *hp*-distribution by designing a parametric study of reasonable tolerances for the *hp*-threshold. By adjusting the tolerance we could have controlled the sensitivity towards polynomial enrichment or mesh refinement. In this manner, we have selected four intervals of tolerances. From an intense affinity towards mesh refinement (*h*++) or polynomial enrichment (*p*++) to a more moderate leaning to each approach, symbolized by *h*+ or *p*+, respectively. To evaluate their performance for this configuration, we have analyzed the convergence history of both the drag coefficient and the recirculation length. Within this context, we have recorded a reduction in the number of degrees of freedom of between 95 % and 98 % with respect to uniform mesh refinement. In particular, the moderate tolerance *h*+ has reported the best performance, attaining a higher accuracy for the same number of adaptation steps.

We have also compared the *hp*-adaptive results ascribed to the tolerance *h*+ to equivalent *h*- and *p*-adaptive simulations to identify the best adaptive approach. In this regard, the pure *p*-simulations were heavily influenced by the strong gradients in the vicinity of the sharp-edged body. This fact caused the error convergence to decay fast in the early stages of the algorithm and to progressively reach stagnation far from the target level of accuracy. Conversely, the pure *h*-simulations displayed a slower error convergence but their progression steadily reached the target value. Definitely, the *hp*-adaptation strategy under *h*+ provided an optimal approach. It inherited the early rapid convergence of the *p*-approach while adjusting to the strong gradients by locally adapting the mesh and thus retaining a proper error convergence. These factors have allowed the *hp*-*h*+ to reach the target level of accuracy while attaining a substantial reduction of 62 % in the total number of degrees of freedom with respect to the pure *h*-approach.

The analysis of the local flow quantities by evaluating successive pressure profiles upstream of the cylinder revealed the presence of oscillations when *p*-

enrichment is activated. Similarly to the analysis of the backward-facing step, this was caused by the ill-fitting behavior of the high-order solution in the vicinity of the sharp corners. Conversely, the *hp*-approach under tolerance *h*+ successfully managed to become higher-order where the solution was smooth yet avoiding the fluctuations reported by the pure *p*-enrichment. Due to this reason, the *hp*-*h*+ profiles have substantially outperformed the *p*-profiles, with savings in the average error of about 90 % with respect to the latter. In summary, the *hp*-approach under *h*+ has proved best equipped to localize the regions requiring increased resolution, thus minimizing the use of the available computational resources.

## 8.2 PERSPECTIVES

Multiple lines of research regarding the novel *hp*-adaptive scheme and the local multiwavelet-based methodology have remained unexplored. In this section, general guidelines for future research are outlined and briefly discussed.

*Support of more general grids* The current adaptive scheme has been developed in the context of non-structured stretched Cartesian grids, where the construction of the multiwavelets is performed only once for a reference cell and then mapped to the local elements by an affine mapping. By contrast, in non-Cartesian grids no affine mapping is available and multiwavelets must be calculated element-wise, which substantially increases the cost of the computations. A possible solution would be the use of the *wavelet-free* approach, developed by Gerhard, 2017. This approach avoids the use of the *highpass* QMF coefficients associated with the multiwavelets (Geronimo et al., 2017). Instead, the detail coefficients are calculated by exclusively using the *low-pass* QMF coefficients, which are associated with the multi-scaling functions. This alternative methodology would make the application of the MRA on non-Cartesian grids (such as grids with curved elements) significantly more efficient to compute.

*Extension to three dimensions* An extension to three dimensions would be straightforward. The Alpert algorithm to generate multiwavelets (Alpert, 1993) is readily extended to 3-D by tensor products. In this case, the multiwavelet space would be made up of seven contributions (three along the $x, y, z$-axes and four along their respective diagonals). Similarly to 2-D case, the local multiwavelet error estimator, defined in Eq. (5.7), would be directly evaluated, by just adding the new contributions. By contrast, the local multiwavelet regularity indicator, given by Eq. (5.28), would require a more thorough study of the multiwavelet spectrum for the new contributions. Nevertheless, we could expect that spectrum will behave similarly to the results from Table 5.18.

*Extension to anisotropic hp-adaptation* The analysis of the multiwavelet contribution along the $x$-, $y$- and $xy$- directions opens the door to the development of an anisotropic adaptation algorithm in both $h$ and $p$. In that context, the local multiwavelet error estimator could be easily reevaluated by measuring the contribution for the $x$- and $y$-direction separately. Similarly, the local multiwavelet regularity indicator would be built up as a summation of the different directional contributions (see Table 5.18), thus the analysis of the component-wise regularity would be straightforward. In addition, regarding $p$-anisotropy, further changes in the solver would be required to accommodate different polynomial degrees within the element.

*Integration of hp-coarsening capabilities into the adaptive algorithm* In this case, the local multiwavelet error estimator would need to identify a neighborhood of elements that share a similar magnitude of the error below an imposed threshold. Once detected, this group of elements could be either agglomerated ($h$-coarsening), or have their polynomial degree lowered ($p$-decreasing), depending on the average value of the local multiwavelet regularity indicator. The latter would be straightforward to put into practice, whereas the former would require a tree-like structure to keep track of the changes in the grid and would be more challenging to implement.

*Application to unsteady flows* The present adaptive scheme could be generalised for static $hp$-adaptation of unsteady periodic flows, similarly to the procedure described in Naddei et al. (2018). In this manner, we would activate the $hp$-adaptive algorithm once the periodic state of the flow is achieved. Then, the local multiwavelet error estimator and regularity indicator could be computed as the maximum of the instantaneous values over a defined time interval. The frequency of these instantaneous values may be adjusted to avoid their computation at every discrete time step.

*Application to RANS simulations* The current implementation could be extended to high-Reynolds turbulent flows. In a first approach, we would extend the solution adaptation capability to fully developed, statistically steady flows that are well described by the RANS methodology. In particular, the local multiwavelet analysis of the eddy viscosity from the Spalart-Allmaras model (Allmaras et al., 2012) would hold special relevance. In this way, the estimation of its error and regularity would guide the $hp$-adaptation. The implementation would require a post-processed (enriched) version of the eddy viscosity so that the multiwavelet expansion could be applied.

## 8.3 LIST OF PUBLICATIONS

*Publications*

- J. García Bautista, M. de la Llave Plata, V. Couaillier, M. Visonneau, and K. Schneider, 'h-Adaptation for High-Order Discontinuous Galerkin Schemes Built on Local Multiwavelet Analysis', (*submitted to Computers & Fluids. Revised and awaiting acceptance*, 2021).

- J. García Bautista, M. de la Llave Plata, V. Couaillier, M. Visonneau, and K. Schneider, 'A Local Multiwavelet hp-Adaptive Strategy in the Context of Discontinuous Galerkin Methods', (*under preparation to be submitted to the J. Comput. Phys.*, 2022).

*International conferences with proceedings*

- J. García Bautista, M. de la Llave Plata, V. Couaillier, M. Visonneau, and K. Schneider, 'Local Multiwavelet-Based Adaptation within a Discontinuous Galerkin Framework', *AIAA Scitech 2021 Forum* (moved to virtual event, 2021).

*International conferences*

- J. García Bautista, M. de la Llave Plata, V. Couaillier, M. Visonneau, and K. Schneider, 'Adaptive Discontinuous Galerkin Approach Based on Local Multiwavelets Analysis', *14th WCCM & ECCOMAS Congress 2020* (moved to virtual event, 2021).

*Secondments*

- During the course of the thesis I had the opportunity to spend one month from 17 June to 19 July 2019 at the *Department of Aeronautics* of the *Imperial College London*. In that period, I conceptualized and developed part of the multiwavelet formulation presented in this thesis.

# BIBLIOGRAPHY

Here are the references in alphabetical order.


Adjerid, S., K. D. Devine, J. E. Flaherty, and L. Krivodonova (2002). 'A posteriori error estimation for discontinuous Galerkin solutions of hyperbolic problems'. *Computer Methods in Applied Mechanics and Engineering* 191.11, pp. 1097–1112. DOI: 10.1016/S0045-7825(01)00318-8 (cited on pages 43, 54).

Adjerid, S. and T. C. Massey (2002). 'A posteriori discontinuous finite element error estimation for two-dimensional hyperbolic problems'. *Computer Methods in Applied Mechanics and Engineering* 191.51, pp. 5877–5897. DOI: 10.1016/S0045-7825(02)00502-9 (cited on page 54).

Ainsworth, M. and J. T. Oden (1992). 'A procedure for a posteriori error estimation for h-p finite element methods'. *Computer Methods in Applied Mechanics and Engineering* 101.1, pp. 73–96. DOI: 10.1016/0045-7825(92)90016-D (cited on page 56).

– (1997). 'A posteriori error estimation in finite element analysis'. *Computer Methods in Applied Mechanics and Engineering* 142.1, pp. 1–88. DOI: https://doi.org/10.1016/S0045-7825(96)01107-3 (cited on pages 2, 53, 54).

Ainsworth, M. and B. Senior (1998). 'An adaptive refinement strategy for hp-finite element computations'. *Applied Numerical Mathematics* 26.1, pp. 165–178. DOI: 10.1016/S0168-9274(97)00083-4 (cited on pages 58–60).

– (1999). 'hp-Finite Element Procedures on Non-Uniform Geometric Meshes: Adaptivity and Constrained Approximation'. In: *Grid Generation and Adaptive Algorithms*. Ed. by M. W. Bern, J. E. Flaherty, and M. Luskin. New York, NY: Springer New York, pp. 1–27. DOI: 10.1007/978-1-4612-1556-1_1 (cited on page 59).

Alauzet, F., X. Li, E. S. Seol, and M. S. Shephard (2006). 'Parallel Anisotropic 3D Mesh Adaptation by Mesh Modification'. *Eng. with Comput.* 21.3, pp. 247–258. DOI: 10.1007/s00366-005-0009-3 (cited on page 57).

Alauzet, F. and A. Loseille (2016). 'A decade of progress on anisotropic mesh adaptation for computational fluid dynamics'. *Computer-Aided Design* 72. 23rd International Meshing Roundtable Special Issue: Advances in Mesh Generation, pp. 13–39. DOI: 10.1016/j.cad.2015.09.005 (cited on page 57).

Alhawwary, M. and Z. J. Wang (2018). *On the Accuracy and Stability of Various DG Formulations for Diffusion*. arXiv: Numerical Analysis (cited on pages 17, 19).

Allmaras, S., F. Johnson, and P. Spalart (2012). 'Modifications and clarifications for the implementation of the Spalart-Allmaras turbulence model'. *Seventh International Conference on Computational Fluid Dynamics (ICCFD7)* (cited on page 131).

Alpert, B. K. (1993). 'A Class of Bases in $L^2$ for the Sparse Representation of Integral Operators'. *SIAM Journal on Mathematical Analysis* 24.1, pp. 246–262. DOI: 10.1137/0524016 (cited on pages 29, 31, 63, 130).

Alpert, B. K., G. Beylkin, D. Gines, and L. Vozovoi (2002). 'Adaptive Solution of Partial Differential Equations in Multiwavelet Bases'. *Journal of Computational Physics* 182.1, pp. 149–190. DOI: 10.1006/jcph.2002.7160 (cited on pages 15, 29, 31, 63).

Archibald, R., G. Fann, and W. Shelton (2011). 'Adaptive discontinuous Galerkin methods in multiwavelets bases'. *Applied Numerical Mathematics* 61.7, pp. 879–890. DOI: 10.1016/j.apnum.2011.02.005 (cited on page 3).

Arnold, D. N., F. Brezzi, B. Cockburn, and L. D. Marini (2002). 'Unified Analysis of Discontinuous Galerkin Methods for Elliptic Problems'. *SIAM Journal on Numerical Analysis* 39.5, pp. 1749–1779. DOI: 10.1137/S0036142901384162 (cited on pages 13, 19).

Babuvška, I. (1973). 'The Finite Element Method with Lagrangian Multipliers.' *Numerische Mathematik* 20, pp. 179–192 (cited on page 1).

Babuvška, I. and W. Gui (1986). 'The h, p and h-p Versions of the Finite Element Method in 1 Dimension. Part III. The Adaptive h-p Version.' *Numerische Mathematik* 49, pp. 659–684 (cited on page 59).

Babuvška, I. and B. Q. Guo (1992). 'The h, p and h-p version of the finite element method; basis theory and applications'. *Advances in Engineering Software* 15.3, pp. 159–174. DOI: 10.1016/0965-9978(92)90097-Y (cited on page 58).

Babuvška, I. and W. C. Rheinboldt (1978a). 'A-posteriori error estimates for the finite element method'. *International Journal for Numerical Methods in Engineering* 12.10, pp. 1597–1615. DOI: 10.1002/nme.1620121010 (cited on page 54).

– (1978b). 'Error Estimates for Adaptive Finite Element Computations'. *SIAM Journal on Numerical Analysis* 15, pp. 736–754. DOI: 10.1137/0715049 (cited on page 71).

– (1980). 'Reliable error estimation and mesh adaptation for the finite element method'. In: pp. 67–108 (cited on page 86).

Baccouch, M. (2014). 'Asymptotically exact a posteriori LDG error estimates for one-dimensional transient convection–diffusion problems'. *Applied Mathematics and Computation* 226, pp. 455–483. DOI: 10.1016/j.amc.2013.10.026 (cited on page 54).

Balan, A., M. Woopen, and G. May (2016). 'Adjoint-based hp-adaptivity on anisotropic meshes for high-order compressible flow simulations'. *Computers & Fluids* 139, pp. 47–67. DOI: 10.1016/j.compfluid.2016.03.029 (cited on page 60).

Bank, R. and A. Sherman (1999). *Some Refinement Algorithms And Data Structures for Regular Local Mesh Refinement*. Applications of Mathematics and Computing to the Physical Sciences (cited on page 73).

Barth, T. J. (2007). 'Space-Time Error Representation and Estimation in Navier-Stokes Calculations'. In: *Complex Effects in Large Eddy Simulations*. Ed. by S. C. Kassinos, C. A. Langer, G. Iaccarino, and P. Moin. Berlin, Heidelberg: Springer Berlin Heidelberg, pp. 29–48. DOI: 10.1007/978-3-540-34234-2_3 (cited on page 54).

Barton, I. E. (1997). 'The Entrance Effect of Laminar Flow over a Backward-Facing Step Geometry'. *International Journal for Numerical Methods in Fluids* 25.6, pp. 633–644. DOI: 10.1002/(SICI)1097-0363(19970930)25:6<633::AID-FLD551>3.0.CO;2-H (cited on pages 87, 97, 98).

Basile, F., J.-B. Chapelier, M. de la Llave Plata, R. Laraufie, and P. Frey (2021). 'A high-order h-adaptive discontinuous Galerkin method for unstructured grids based on a posteriori error estimation.' In: *AIAA Scitech 2021 Forum*. DOI: 10.2514/6.2021-1696 (cited on page 112).

– (2022). 'Unstructured h- and hp-adaptive strategies for discontinuous Galerkin methods based on a posteriori error estimation for compressible flows'. *Computers & Fluids* 233. DOI: 10.1016/j.compfluid.2021.105245 (cited on page 60).

Bassi, F., A. Crivellini, S. Rebay, and M. Savini (2005). 'Discontinuous Galerkin solution of the Reynolds-averaged Navier–Stokes and k–$\omega$ turbulence model equations'. *Computers & Fluids* 34, pp. 507–540 (cited on pages 18, 20).

Bassi, F. and S. Rebay (1997). 'A High-Order Accurate Discontinuous Finite Element Method for the Numerical Solution of the Compressible Navier–Stokes Equations'. *Journal of Computational Physics* 131.2, pp. 267–279. DOI: 10.1006/jcph.1996.5572 (cited on pages 13, 17, 18).

– (2000). 'A High Order Discontinuous Galerkin Method for Compressible Turbulent Flows'. Ed. by B. Cockburn, G. E. Karniadakis, and C.-W. Shu, pp. 77–88 (cited on page 17).

Baumann, C. E. and J. T. Oden (1999). 'A discontinuous hp finite element method for convection—diffusion problems'. *Computer Methods in Applied Mechanics and Engineering* 175.3, pp. 311–341. DOI: https://doi.org/10.1016/S0045-7825(98)00359-4 (cited on page 13).

Becker, R. and R. Rannacher (1996). 'A Feed-Back Approach to Error Control in Finite Element Methods: Basic Analysis and Examples'. *East-West J. Numer. Math* 4, pp. 237–264 (cited on page 55).

– (2001). 'An optimal control approach to a posteriori error estimation in finite element methods'. *Acta Numerica* 10, pp. 1–102. DOI: 10.1017/S0962492901000010 (cited on page 55).

Ben Ameur, F., J. Balis, R. Vandenhoeck, A. Lani, and S. Poedts (2022). 'r-adaptive algorithms for supersonic flows with high-order Flux Reconstruction methods'. *Computer Physics Communications* 276. DOI: 10.1016/j.cpc.2022.108373 (cited on page 57).

Berger, M. J. and J. Oliger (1984). 'Adaptive mesh refinement for hyperbolic partial differential equations'. *Journal of Computational Physics* 53.3, pp. 484–512. DOI: 10.1016/0021-9991(84)90073-1 (cited on page 73).

Bey, K. S. and J. T. Oden (1996). '*hp*-Version discontinuous Galerkin methods for hyperbolic conservation laws'. *Computer Methods in Applied Mechanics and Engineering* 133.3, pp. 259–286. DOI: 10.1016/0045-7825(95)00944-2 (cited on pages 43, 56, 58, 59).

Biswas, R., K. D. Devine, and J. E. Flaherty (1994). 'Parallel, adaptive finite element methods for conservation laws'. *Applied Numerical Mathematics* 14.1, pp. 255–283. DOI: 10.1016/0168-9274(94)90029-9 (cited on pages 55, 76).

Blackman, R. B. and J. W. Tukey (1958). 'The measurement of power spectra from the point of view of communications engineering — Part I'. *The Bell System Technical Journal* 37.1, pp. 185–282. DOI: 10.1002/j.1538-7305.1958.tb03874.x (cited on page 24).

Boyd, J. P. (2001). *Chebyshev and Fourier Spectral Methods*. Second. Dover Publications (cited on pages 1, 15).

Bramkamp, F., Ph. Lamby, and S. Müller (2004). 'An adaptive multiscale finite volume solver for unsteady and steady state flow computations'. *Journal of Computational Physics* 197.2, pp. 460–490. DOI: 10.1016/j.jcp.2003.12.005 (cited on page 4).

Brandt, A. and O. E Livne (2011). *Multigrid Techniques: 1984 Guide with Applications to Fluid Dynamics, Revised Edition*. SIAM (cited on page 56).

Brandt, Achi (1977). 'Multi-Level Adaptive Solutions to Boundary-Value Problems'. *Mathematics of Computation* 31.138, pp. 333–390. DOI: 10.1090/S0025-5718-1977-0431719-X (cited on page 4).

Breuer, M., J. Bernsdorf, T. Zeiser, and F. Durst (2000). 'Accurate computations of the laminar flow past a square cylinder based on two different methods: lattice-Boltzmann and finite-volume'. *International Journal of Heat and Fluid Flow* 21.2, pp. 186–196. DOI: 10.1016/s0142-727x(99)00081-8 (cited on page 110).

Burgers, J. M. (1995). *Mathematical Examples Illustrating Relations Occurring in the Theory of Turbulent Fluid Motion*. Springer Netherlands, pp. 281–334 (cited on page 13).

Calle, J., P. Devloo, and S. Gomes (2005). 'Wavelets and adaptive grids for the discontinuous Galerkin method'. *Numerical Algorithms* 39, pp. 143–154. DOI: 10.1007/s11075-004-3626-9 (cited on page 56).

Carpenter, M. H. and C. A. Kennedy (1994). *Fourth-Order 2N-storage Runge-Kutta Schemes*. NASA reports TM, 109112 (cited on page 20).

Ceze, M. and K. Fidkowski (2012). 'Anisotropic hp-Adaptation Framework for Functional Prediction'. *AIAA Journal*. DOI: 10.2514/1.J051845 (cited on page 60).

Chalmers, N., G. Agbaglah, M. Chrust, and C. Mavriplis (2019). 'A parallel hp-adaptive high order discontinuous Galerkin method for the incompressible Navier-Stokes equations'. *Journal of Computational Physics: X* 2. DOI: 10.1016/j.jcpx.2019.100023 (cited on pages 58, 60).

Chapelier, J.-B., M. de la Llave Plata, and F. Renac (2012). *Inviscid and Viscous Simulations of the Taylor-Green Vortex Flow Using a Modal Discontinuous Galerkin Approach*. 42nd AIAA Fluid Dynamics Conference and Exhibit (cited on pages 5, 13).

Chapelier, J.-B., M. de la Llave Plata, F. Renac, and E. Lamballais (2014). 'Evaluation of a High-Order Discontinuous Galerkin Method for the DNS of Turbulent Flows'. *Computers & Fluids* 95, pp. 210–226. DOI: 10.1016/j.compfluid.2014.02.015 (cited on page 5).

Cockburn, B. (1998). 'An Introduction to the Discontinuous Galerkin Method for Convection-Dominated Problems'. *Springer Berlin Heidelberg* 1, pp. 150–268. DOI: 10.1007/BFb0096353 (cited on page 17).

Cockburn, B. and C.-W. Shu (1998). 'The Local Discontinuous Galerkin Method for Time-Dependent Convection-Diffusion Systems'. *SIAM Journal on Numerical Analysis* 35.6, pp. 2440–2463 (cited on page 13).

– (2001). 'Runge–Kutta Discontinuous Galerkin Methods for Convection-Dominated Problems'. 16.3, pp. 173–261. DOI: 10.1023/A:1012873910884 (cited on page 13).

Cruchaga, M. A. (1998). 'A study of the backward-facing step problem using a generalized streamline formulation'. *Communications in Numerical Methods in Engineering* 14.8, pp. 697–708. DOI: 10.1002/(SICI)1099-0887(199808)14:8<697::AID-CNM155>3.0.CO;2-0 (cited on page 98).

Dahmen, W. (2001). 'Wavelet methods for PDEs — some recent developments'. *Journal of Computational and Applied Mathematics* 128.1, pp. 133–185. DOI: 10.1016/S0377-0427(00)00511-2 (cited on page 64).

Daubechies, I. (1992). *Ten Lectures on Wavelets*. Society for Industrial and Applied Mathematics (cited on pages 24, 26, 28, 29, 32).

De la Llave Plata, M., V. Couaillier, and M.-C. le Pape (2018). 'On the use of a high-order discontinuous Galerkin method for DNS and LES of wall-bounded turbulence'. *Computers & Fluids* 176, pp. 320–337. DOI: 10.1016/j.compfluid.2017.05.013 (cited on page 5).

Deiterding, R., M. O. Domingues, S. M. Gomes, O. Roussel, and K. Schneider (2009). 'Adaptive Multiresolution or Adaptive Mesh Refinement? A Case Study for 2D Euler Equations'. *ESAIM: Proc.* 29, pp. 28–42. DOI: 10.1051/proc/2009053 (cited on page 3).

Deiterding, R., M. O. Domingues, S. M. Gomes, and K. Schneider (2016). 'Comparison of Adaptive Multiresolution and Adaptive Mesh Refinement Applied to Simulations of the Compressible Euler Equations'. *SIAM Journal on Scientific Computing* 38.5, pp. 173–193. DOI: 10.1137/15M1026043 (cited on page 3).

Demkowicz, L., J. T. Oden, W. Rachowicz, and O. Hardy (1989). 'Toward a universal h-p adaptive finite element strategy, part 1. Constrained approximation and data structure'. *Computer Methods in Applied Mechanics and Engineering* 77.1, pp. 79–112. DOI: 10.1016/0045-7825(89)90129-1 (cited on page 72).

Demkowicz, L., W. Rachowicz, and P. Devloo (2002). 'A Fully Automatic hp-Adaptivity'. *Journal of Scientific Computing* 17. DOI: 10.1023/A:1015192312705 (cited on pages 58, 59).

Dhiman, A. K., R. P. Chhabra, A. Sharma, and V. Eswaran (2006). 'Effects of Reynolds and Prandtl Numbers on Heat Transfer Across a Square Cylinder in the Steady Flow Regime'. *Numerical Heat Transfer, Part A: Applications* 49.7, pp. 717–731. DOI: 10.1080/10407780500283325 (cited on page 112).

Dolejší, V., A. Ern, and M. Vohralík (2016). '$hp$-Adaptation Driven by Polynomial-Degree-Robust A Posteriori Error Estimates for Elliptic Problems'. *SIAM Journal on Scientific Computing* 38.5, A3220–A3246. DOI: 10.1137/15M1026687 (cited on page 59).

Dolejší, V., F. Roskovec, and M. Vlasák (2015). 'Residual based error estimates for the space–time discontinuous Galerkin method applied to the compressible flows'. *Computers & Fluids* 117, pp. 304–324. DOI: 10.1016/j.compfluid.2015.05.027 (cited on page 56).

Dolejší, V. and P. Solin (2016). '*hp*-Discontinuous Galerkin Method Based on Local Higher Order Reconstruction'. *Applied Mathematics and Computation* 279, pp. 219–235. DOI: 10.1016/j.amc.2016.01.024 (cited on pages 44, 46, 55, 59, 60, 83).

Domingues, M. O., S. M. Gomes, O. Roussel, and K. Schneider (2009). 'Space-Time Adaptive Multiresolution Methods for Hyperbolic Conservation Laws: Applications to Compressible Euler Equations'. *Applied Numerical Mathematics* 59.9, pp. 2303–2321. DOI: 10.1016/j.apnum.2008.12.018 (cited on pages 3, 56).

Donéa, J. and A. Huerta (2003). *Finite element methods for flow problems*. Wiley (cited on page 1).

Donovan, G. C., J. S. Geronimo, D. P. Hardin, and P. R. Massopust (1996). 'Construction of Orthogonal Wavelets Using Fractal Interpolation Functions'. *SIAM Journal on Mathematical Analysis* 27.4, pp. 1158–1192. DOI: 10.1137/S0036141093256526 (cited on page 29).

Dörfler, W. and V. Heuveline (2007). 'Convergence of an adaptive *hp* finite element strategy in one space dimension'. *Applied Numerical Mathematics* 57.10, pp. 1108–1124. DOI: 10.1016/j.apnum.2006.10.003 (cited on page 71).

Eibner, T. and J. M. Melenk (2007). 'An adaptive strategy for hp-FEM based on testing for analyticity'. *Computational Mechanics* 39, pp. 575–595. DOI: 10.1007/s00466-006-0107-0 (cited on pages 59, 60).

Ekelschot, D., D. Moxey, S. J. Sherwin, and J. Peiró (2017). 'A p-adaptation method for compressible flow problems using a goal-based error indicator'. *Computers & Structures* 181, pp. 55–69. DOI: 10.1016/j.compstruc.2016.03.004 (cited on page 57).

Ern, A. and J. Proft (2005). 'A posteriori discontinuous Galerkin error estimates for transient convection–diffusion equations'. *Applied Mathematics Letters* 18.7, pp. 833–841. DOI: 10.1016/j.aml.2004.05.019 (cited on page 54).

Erturk, E. (2008). 'Numerical Solutions of 2-D Steady Incompressible Flow Over a Backward-Facing Step, Part I: High Reynolds Number Solutions'. *Computers & Fluids* 37.6, pp. 633–655. DOI: 10.1016/j.compfluid.2007.09.003 (cited on pages 87, 89, 97, 98).

Eymard, R., T. Gallouët, and R. Herbin (2000). 'Finite volume methods'. In: vol. 7. Handbook of Numerical Analysis. Elsevier, pp. 713–1018. DOI: https://doi.org/10.1016/S1570-8659(00)07005-8 (cited on page 1).

Fankhauser, T., T. P. Wihler, and M. Wirz (2014). 'The hp-adaptive FEM based on continuous Sobolev embeddings: Isotropic refinements'. *Computers & Mathematics with Applications* 67.4, pp. 854–868. DOI: 10.1016/j.camwa.2013.05.024 (cited on page 60).

Farge, M. (1992). 'Wavelet Transforms and their Applications to Turbulence'. *Annual Review of Fluid Mechanics* 24, pp. 395–457. DOI: 10.1146/annurev.fl.24.010192.002143 (cited on page 25).

Feng, H. and C. Mavriplis (2002). 'Adaptive Spectral Element Simulations of Thin Premixed Flame Sheet Deformations'. *J. Sci. Comput.* 17, pp. 385–395. DOI: 10.1023/A:1015137722700 (cited on page 60).

Ferziger, J., M. Perić, and R. Street (2020). *Computational Methods for Fluid Dynamics*. 4th ed. Springer International Publishing (cited on page 1).

Fidkowski, K. J. and Y. Luo (2011). 'Output-based space–time mesh adaptation for the compressible Navier–Stokes equations'. *Journal of Computational Physics* 230.14, pp. 5753–5773. DOI: 10.1016/j.jcp.2011.03.059 (cited on page 54).

Franke, R., W. Rodi, and B. Schönung (1990). 'Numerical calculation of laminar vortex-shedding flow past cylinders'. *Journal of Wind Engineering and Industrial Aerodynamics* 35, pp. 237–257. DOI: 10.1016/0167-6105(90)90219-3 (cited on pages 110, 112).

Gabor, D. (1946). 'Theory of communication'. *J. Inst. Electr. Engineering* 93, pp. 429–457 (cited on page 24).

Gao, H. and Z. J. Wang (2011). 'A residual-based procedure for hp-adaptation on 2-d hybrid meshes'. *49th AIAA Aerospace Sciences Meeting including the New Horizons Forum and Aerospace Exposition* (cited on page 56).

Gartling, D. K. (1990). 'A test problem for outflow boundary conditions—flow over a backward-facing step'. *International Journal for Numerical Methods in Fluids* 11.7, pp. 953–967. DOI: 10.1002/fld.1650110704 (cited on pages 87, 98).

Gautier, R., D. Biau, and E. Lamballais (2013). 'A reference solution of the flow over a circular cylinder at Re=40'. *Computers & Fluids* 75, pp. 103–111. DOI: 10.1016/j.compfluid.2012.12.017 (cited on page 110).

Gerhard, N. (2017). 'An adaptive multiresolution discontinuous Galerkin scheme for conservation laws'. PhD thesis. RWTH Aachen University (cited on pages 3, 4, 43, 54, 56, 130).

Gerhard, N., D. Caviedes-Voullième, S. Müller, and G. Kesserwani (2015a). 'Multiwavelet-Based Grid Adaptation with Discontinuous Galerkin Schemes for Shallow Water Equations'. *Journal of Computational Physics* 301, pp. 265–288. DOI: 10.1016/j.jcp.2015.08.030 (cited on pages 3, 42).

Gerhard, N., F. Iacono, G. May, S. Müller, and R. Schäfer (2015b). 'A High-Order Discontinuous Galerkin Discretization with Multiwavelet-Based Grid Adaptation for Compressible Flows'. *Journal of Scientific Computing* 62.1, pp. 25–52. DOI: 10.1007/s10915-014-9846-9 (cited on pages 3, 37, 38, 42, 57).

Gerhard, N. and S. Müller (2016). 'Adaptive Multiresolution Discontinuous Galerkin Schemes for Conservation Laws: multi-dimensional case'. *Computational and Applied Mathematics* 35, pp. 321–349. DOI: 10.1007/s40314-014-0134-y (cited on pages 3, 42–44, 49).

Gerhard, N., S. Müller, and A. Sikstel (2021). 'A Wavelet-Free Approach for Multiresolution-Based Grid Adaptation for Conservation Laws'. *Communications on Applied Mathematics and Computation* 4, pp. 108–142 (cited on page 56).

Geronimo, J. S., P. Iliev, and W. V. Assche (2017). 'Alpert Multiwavelets and Legendre-Angelesco Multiple Orthogonal Polynomials'. *SIAM Journal on Mathematical Analysis* 49, pp. 626–645. DOI: 10.1137/16M1064465 (cited on pages 39, 41, 50, 68, 130).

Giraldo, F. X. and M. Restelli (2008). 'A study of spectral element and discontinuous Galerkin methods for the Navier–Stokes equations in nonhydrostatic mesoscale atmospheric modeling: Equation sets and test cases'. *Journal of Computational Physics* 227.8, pp. 3849–3877. DOI: 10.1016/j.jcp.2007.12.009 (cited on page 2).

Godlewski, E. and P. A. Raviart (1996). *Numerical Approximation of Hyperbolic Systems of Conservation Laws*. Springer New York (cited on page 1).

Gottschlich-Müller, B. and S. Müller (1999). 'Adaptive Finite Volume Schemes for Conservation Laws Based on Local Multiresolution Techniques'. In: *Hyperbolic Problems: Theory, Numerics, Applications*. Ed. by Michael Fey and Rolf Jeltsch. Birkhäuser Basel, pp. 385–394. DOI: 10.1007/978-3-0348-8720-5_42 (cited on page 3).

Haar, A. (1910). 'Zur Theorie der orthogonalen Funktionensysteme'. *Mathematische Annalen* 69, pp. 331–371 (cited on page 28).

Harten, A. (1996). 'Multiresolution Representation of Data: A General Framework'. *SIAM Journal on Numerical Analysis* 33.3, pp. 1205–1256. DOI: 10.1137/0733060 (cited on pages 3, 26).

Hartmann, R., J. Held, and T. Leicht (2011). 'Adjoint-based error estimation and adaptive mesh refinement for the RANS and k–ω turbulence model equations'. *Journal of Computational Physics* 230.11, pp. 4268–4284. DOI: 10.1016/j.jcp.2010.10.026 (cited on page 55).

Hartmann, R. and P. Houston (2002). 'Adaptive Discontinuous Galerkin Finite Element Methods for the Compressible Euler Equations'. *Journal of Computational Physics* 183.2, pp. 508–532. DOI: 10.1006/jcph.2002.7206 (cited on pages 54–56).

– (2006). 'Symmetric Interior Penalty DG Methods for the Compressible Navier–Stokes Equations II: Goal–Oriented A Posteriori Error Estimation'. *International Journal of Numerical Analysis & Modeling* 3, pp. 141–162 (cited on page 55).
Hay, A. and M. Visonneau (2006). 'Error estimation using the error transport equation for finite-volume methods and arbitrary meshes'. *International Journal of Computational Fluid Dynamics* 20.7, pp. 463–479. DOI: 10.1080/10618560600835934 (cited on page 56).
– (2007). 'Adaptive finite-volume solution of complex turbulent flows'. *Computers & Fluids* 36.8, pp. 1347–1363. DOI: https://doi.org/10.1016/j.compfluid.2006.12.008 (cited on page 56).
Hesthaven, J. S. and T. Warburton (2008). *Nodal Discontinuous Galerkin Methods*. First. Springer-Verlag (cited on pages 1, 15, 58).
Heuveline, V. and R. Rannacher (2003). 'Duality-Based Adaptivity in the Hp-Finite Element Method'. *Journal of Numerical Mathematics* 11, pp. 95–113. DOI: 10.1163/156939503766614126 (cited on page 59).
Houston, P., D. Schoetzau, and T. Wihler (2007). 'Energy norm a posteriori error estimation of hp-adaptive discontinuous Galerkin methods for elliptic problems'. *Mathematical Models and Methods in Applied Sciences* 14, pp. 33–62. DOI: 10.1142/S0218202507001826 (cited on page 54).
Houston, P., B. Senior, and E. Süli (2003). 'Sobolev regularity estimation for hp-adaptive finite element methods'. In: *Numerical Mathematics and Advanced Applications*. Ed. by F. Brezzi, A. Buffa, S. Corsaro, and A. Murli. Milano: Springer Milan, pp. 631–656. DOI: 10.1007/978-88-470-2089-4_58 (cited on page 60).
Houston, P. and E. Süli (2005). 'A note on the design of hp-adaptive finite element methods for elliptic partial differential equations'. *Computer Methods in Applied Mechanics and Engineering* 194.2, pp. 229–243. DOI: 10.1016/j.cma.2004.04.009 (cited on pages 58–60).
Hovhannisyan, N., S. Müller, and R. Schäfer (2014). 'Adaptive Multiresolution Discontinuous Galerkin Schemes for Conservation Laws'. *Mathematics of Computation* 83.285, pp. 113–151. DOI: 10.1090/S0025-5718-2013-02732-9 (cited on pages 3, 31, 42–44, 49–51, 56).
Hubbard, B. B. (1998). *The World According to Wavelets: The Story of a Mathematical Technique in the Making*. Second. A K Peters/CRC Press (cited on pages 23–26, 28, 64).
Jasak, H. and A. D. Gosman (2003). 'Element residual error estimate for the finite volume method'. *Computers & Fluids* 32.2, pp. 223–248. DOI: 10.1016/S0045-7930(02)00004-X (cited on page 56).
Johnson, C. (1990). 'Adaptive finite element methods for diffusion and convection problems'. *Computer Methods in Applied Mechanics and Engineering* 82.1, pp. 301–322. DOI: 10.1016/0045-7825(90)90169-M (cited on page 86).
Johnson, C. and J. Pitkäranta (1986). 'An Analysis of the Discontinuous Galerkin Method for a Scalar Hyperbolic Equation'. *Mathematics of Computation* 46.173, pp. 1–26 (cited on page 54).
Kallinderis, Y., E. M. Lymperopoulou, and P. Antonellis (2017). 'Flow feature detection for grid adaptation and flow visualization'. *Journal of Computational Physics* 341, pp. 182–207. DOI: 10.1016/j.jcp.2017.04.001 (cited on page 55).
Kamkar, S. J., A. M. Wissink, V. Sankaran, and A. Jameson (2011). 'Feature-driven Cartesian adaptive mesh refinement for vortex-dominated flows'. *Journal of Computational Physics* 230.16, pp. 6271–6298. DOI: 10.1016/j.jcp.2011.04.024 (cited on page 57).
Kanamori, M. and K. Suzuki (2011). 'Shock wave detection in two-dimensional flow based on the theory of characteristics from CFD data'. *Journal of Computational Physics* 230.8, pp. 3085–3092. DOI: https://doi.org/10.1016/j.jcp.2011.01.007 (cited on page 55).
Karniadakis, G. and S. Sherwin (2005). *Spectral/hp Element Methods for Computational Fluid Dynamics*. Second. Oxford University Press (cited on pages 1, 14, 21, 58).

Kasmai, N., D. Thompson, E. Luke, M. Jankun-Kelly, and R. Machiraju (2011). 'Feature-based adaptive mesh refinement for wingtip vortices'. *International Journal for Numerical Methods in Fluids* 66.10, pp. 1274–1294. DOI: 10.1002/fld.2312 (cited on pages 2, 55).

Kast, S. M. (2017). *An Introduction to Adjoints and Output Error Estimation in Computational Fluid Dynamics*. DOI: 10.48550/ARXIV.1712.00693 (cited on pages 2, 55).

Keinert, F. (2003). *Wavelets and Multiwavelets*. First. Chapman and Hall/CRC (cited on pages 24, 29).

Kelkar, K. M. and S. V. Patankar (1992). 'Numerical prediction of vortex shedding behind a square cylinder'. *International Journal for Numerical Methods in Fluids* 14.3, pp. 327–341. DOI: 10.1002/fld.1650140306 (cited on page 111).

Kenwright, D.N., C. Henze, and C. Levit (1999). 'Feature extraction of separation and attachment lines'. *IEEE Transactions on Visualization and Computer Graphics* 5.2, pp. 135–144. DOI: 10.1109/2945.773805 (cited on page 55).

Keskar, J. and D. A. Lyn (1999). 'Computations of a Laminar Backward-Facing Step Flow at *Re*=800 with a Spectral Domain Decomposition Method'. *International Journal for Numerical Methods in Fluids* 29.4, pp. 411–427. DOI: 10.1002/(SICI)1097-0363(19990228)29:4<411::AID-FLD794>3.0.CO;2-6 (cited on page 87).

Kompenhans, M., G. Rubio, E. Ferrer, and E. Valero (2016a). 'Adaptation strategies for high order discontinuous Galerkin methods based on Tau-estimation'. *Journal of Computational Physics* 306, pp. 216–236. DOI: 10.1016/j.jcp.2015.11.032 (cited on page 56).

– (2016b). 'Comparisons of p-adaptation strategies based on truncation- and discretisation-errors for high order discontinuous Galerkin methods'. *Computers & Fluids* 139, pp. 36–46. DOI: 10.1016/j.compfluid.2016.03.026 (cited on page 55).

Krivodonova, L. and J. Flaherty (2003). 'Error Estimation for Discontinuous Galerkin Solutions of Two-Dimensional Hyperbolic Problems'. *Adv. Comput. Math.* 19, pp. 57–71. DOI: 10.1023/A:1022894504834 (cited on page 55).

Kuru, G., M. de la Llave Plata, V. Couaillier, R. Abgrall, and F. Coquel (2016). *An Adaptive Variational Multiscale Discontinuous Galerkin Method For Large Eddy Simulation*. 54th AIAA Aerospace Sciences Meeting (cited on pages 55, 56, 63, 73, 82, 91, 101, 127).

Leicht, T. and R. Hartmann (2011). 'Error estimation and hp-adaptive mesh refinement for discontinuous Galerkin methods'. In: *Adaptive High-Order Methods in Computational Fluid Dynamics*, pp. 67–94. DOI: 10.1142/9789814313193_0003 (cited on page 60).

LeVeque, R. J. (2002). *Finite Volume Methods for Hyperbolic Problems*. Cambridge University Press (cited on page 1).

Löhner, R. (1995). 'Mesh adaptation in fluid mechanics'. *Engineering Fracture Mechanics* 50.5, pp. 819–847. DOI: 10.1016/0013-7944(94)E0062-L (cited on page 57).

Lorteau, M., M. de la Llave Plata, and V. Couaillier (2018). 'Turbulent jet simulation using high-order DG methods for aeroacoustic analysis'. *International Journal of Heat and Fluid Flow* 70, pp. 380–390. DOI: 10.1016/j.ijheatfluidflow.2018.01.012 (cited on page 5).

Mallat, S. (2008). *A Wavelet Tour of Signal Processing*. 3rd ed. Academic Press, Inc. (cited on page 3).

Mallat, S. G. (1989). 'Multiresolution Approximations and Wavelet Orthonormal Bases of L2(R)'. *Transactions of the American Mathematical Society* 315.1, pp. 69–87 (cited on pages 26, 28, 32).

Marcon, J., G. Castiglioni, D. Moxey, S. J. Sherwin, and J. Peiró (2020). 'rp-adaptation for compressible flows'. *International Journal for Numerical Methods in Engineering* 121.23, pp. 5405–5425. DOI: 10.1002/nme.6529 (cited on page 57).

Mavriplis, C. (1989). 'Nonconforming discretizations and a posteriori error estimators for adaptive spectral element techniques'. PhD thesis. Massachusetts Institute of Technology (cited on pages 55, 60, 65).

– (1994). 'Adaptive mesh strategies for the spectral element method'. *Computer Methods in Applied Mechanics and Engineering* 116.1, pp. 77–86. DOI: 10.1016/S0045-7825(94)80010-3 (cited on pages 3, 43, 55, 60).
Mavriplis, D. J. (1990). 'Adaptive mesh generation for viscous flows using triangulation'. *Journal of Computational Physics* 90.2, pp. 271–291. DOI: https:10.1016/0021-9991(90)90167-Y (cited on pages 2, 57).
Melenk, J. M. and B. Wohlmuth (2001). 'On residual-based a posteriori error estimation in hp-FEM'. *Advances in Computational Mathematics* 15, pp. 311–331. DOI: 10.1023/A:1014268310921 (cited on page 59).
Meliga, P., E. Boujo, G. Pujals, and F. Gallaire (2014). 'Sensitivity of aerodynamic forces in laminar and turbulent flow past a square cylinder'. *Physics of Fluids* 26.10. DOI: 10.1063/1.4896941 (cited on page 112).
Mitchell, W. F. and M. A. McClain (2014). 'A Comparison of *hp*-Adaptive Strategies for Elliptic Partial Differential Equations'. *ACM Trans. Math. Softw.* 41.1. DOI: 10.1145/2629459 (cited on pages 43, 54, 59).
Mozaffari, S., E. Guilmineau, M. Visonneau, and J. Wackers (2022). 'Average-based mesh adaptation for hybrid RANS/LES simulation of complex flows'. *Computers & Fluids* 232. DOI: 10.1016/j.compfluid.2021.105202 (cited on page 57).
Müller, S. (2003). 'Adaptive Multiscale Schemes for Conservation Laws'. *Springer-Verlag Berlin Heidelberg* 27. DOI: 10.1007/978-3-642-18164-1 (cited on page 3).
– (2009). 'Multiresolution Schemes for Conservation Laws'. *Springer-Verlag Berlin Heidelberg* 1, pp. 379–408. DOI: 10.1007/978-3-642-03413-8_11 (cited on pages 3, 56).
Müller, S. and Y. Stiriba (2009). 'A multilevel finite volume method with multiscale-based grid adaptation for steady compressible flows'. *Journal of Computational and Applied Mathematics* 227.2, pp. 223–233. DOI: 10.1016/j.cam.2008.03.035 (cited on page 4).
Naddei, F. (2019). 'Simulation adaptative des grandes échelles d'écoulements turbulents fondée sur une méthode Galerkine discontinue'. PhD thesis. Université Paris Saclay (COmUE) (cited on pages 5, 54, 56, 71, 73, 76, 84, 93, 111).
Naddei, F., M. de la Llave Plata, and V. Couaillier (2018). *A comparison of refinement indicators for p-adaptive discontinuous Galerkin methods for the Euler and Navier-Stokes equations*. 2018 AIAA Aerospace Sciences Meeting (cited on pages 3, 5, 55–57, 63, 74, 91, 113, 131).
Naddei, F., M. de la Llave Plata, V. Couaillier, and F. Coquel (2019). 'A Comparison of Refinement Indicators for *p*-adaptive Simulations of Steady and Unsteady Flows Using Discontinuous Galerkin Methods'. *Journal of Computational Physics* 376, pp. 508–533. DOI: 10.1016/j.jcp.2018.09.045 (cited on pages 5, 63).
Oden, J. T., L. Demkowicz, W. Rachowicz, and T.A. Westermann (1989). 'Toward a universal h-p adaptive finite element strategy, part 2. A posteriori error estimation'. *Computer Methods in Applied Mechanics and Engineering* 77.1, pp. 113–180. DOI: 10.1016/0045-7825(89)90130-8 (cited on pages 54, 71).
Patera, A. T. (1984). 'A spectral element method for fluid dynamics: Laminar flow in a channel expansion'. *Journal of Computational Physics* 54.3, pp. 468–488. DOI: 10.1016/0021-9991(84)90128-1 (cited on page 1).
Persson, P.-O. and J. Peraire (2006). 'Sub-Cell Shock Capturing for Discontinuous Galerkin Methods'. *AIAA paper*. DOI: 10.2514/6.2006-112 (cited on pages 55, 57).
Pironneau, O. (1989). *Finite Element Methods for Fluids*. Masson J. Wiley & Sons (cited on page 1).
Plonka, G. and V. Strela (1998). 'From Wavelets to Multiwavelets', pp. 375–399. DOI: 10.5555/285607.285646 (cited on page 29).

Posdziech, O. and R. Grundmann (2007). 'A systematic approach to the numerical calculation of fundamental quantities of the two-dimensional flow over a circular cylinder'. *Journal of Fluids and Structures* 23.3, pp. 479–499. DOI: 10.1016/j.jfluidstructs.2006.09.004 (cited on pages 111, 112).

Rachowicz, W., J. T. Oden, and L. Demkowicz (1989). 'Toward a universal h-p adaptive finite element strategy part 3. design of h-p meshes'. *Computer Methods in Applied Mechanics and Engineering* 77.1, pp. 181–212. DOI: 10.1016/0045-7825(89)90131-X (cited on pages 58, 59).

Rai, P., F. Coquel, C. Marmignon, and F. Renac (2021). 'An entropy stable high-order discontinuous Galerkin spectral element method for the Baer-Nunziato two-phase flow model'. *Journal of Computational Physics* 431, p. 110135. DOI: 10.1016/j.jcp.2021.110135 (cited on page 5).

Reddy, J. N. and D. K. Gartling (2010). *The Finite Element Method in Heat Transfer and Fluid Dynamics*. 3rd. CRC Press (cited on page 1).

Reed, W. H. and T. R. Hill (1973). *Triangular mesh methods for the neutron transport equation*. Tech. rep. Los Alamos Scientific Lab., N. Mex.(USA) (cited on page 13).

Remacle, J.-F., X. Li, M. S. Shephard, and J. E. Flaherty (2005). 'Anisotropic adaptive simulation of transient flows using discontinuous Galerkin methods'. *International Journal for Numerical Methods in Engineering* 62.7, pp. 899–923. DOI: 10.1002/nme.1196 (cited on page 57).

Renac, F., M. de la Llave Plata, E. Martin, J.-B. Chapelier, and V. Couaillier (2015). 'Aghora: A High-Order DG Solver for Turbulent Flow Simulations'. *IDIHOM, Springer International Publishing* 1, pp. 315–335. DOI: 10.1007/978-3-319-12886-3_15 (cited on pages 5, 20, 96).

Ringue, N. (2019). ' An Optimization-based Approach to Mesh-Polynomial Adaptation of High-Order Discretizations'. PhD thesis. McGill University (cited on page 59).

Ringue, N. and S. Nadarajah (2018). 'An optimization-based framework for anisotropic hp-adaptation of high-order discretizations'. *Journal of Computational Physics* 375, pp. 589–618. DOI: 10.1016/j.jcp.2018.09.005 (cited on page 60).

Rivière, B. and M. F. Wheeler (2003). 'A Posteriori error estimates for a discontinuous galerkin method applied to elliptic problems'. *Computers & Mathematics with Applications* 46.1, pp. 141–163. DOI: https://doi.org/10.1016/S0898-1221(03)90086-1 (cited on page 54).

Rivière, B. M. (2008). *Discontinuous Galerkin methods for solving elliptic and parabolic equations - theory and implementation*. Frontiers in applied mathematics (cited on page 58).

Romkes, A., S. Prudhomme, and J. T. Oden (2003). 'A Priori error analyses of a stabilized discontinuous Galerkin method'. *Computers & Mathematics with Applications* 46.8, pp. 1289–1311. DOI: https://doi.org/10.1016/S0898-1221(03)90220-3 (cited on page 54).

Roussel, O., K. Schneider, A. Tsigulin, and H. Bockhorn (2003). 'A Conservative Fully Adaptive Multiresolution Algorithm for Parabolic PDEs'. *Journal of Computational Physics* 188.2, pp. 493–523. DOI: 10.1016/S0021-9991(03)00189-X (cited on page 3).

Roy, C. (2010). 'Review of Discretization Error Estimators in Scientific Computing'. *48th AIAA Aerospace Sciences Meeting Including the New Horizons Forum and Aerospace Exposition*. DOI: 10.2514/6.2010-126 (cited on pages 54, 56).

Rubio, G., F. Fraysse, D. Kopriva, and E. Valero (2015). 'Quasi-a priori truncation error estimation in the DGSEM'. *Journal of Scientific Computing* 64, pp. 425–455. DOI: 10.1007/s10915-014-9938-6 (cited on page 56).

Rueda-Ramírez, A. M. (2019). 'Efficient Space and Time Solution Techniques for High-Order Discontinuous Galerkin Discretizations of the 3D Compressible Navier-Stokes Equations'. PhD thesis. E.T.S. de Ingeniería Aeronáutica y del Espacio (UPM). DOI: 10.20868/UPM.thesis.57182 (cited on pages 54, 56).

Rueda-Ramírez, A. M., J. Manzanero, E. Ferrer, G. Rubio, and E. Valero (2019a). 'A $p$-multigrid strategy with anisotropic $p$-adaptation based on truncation errors for high-order discontinuous Galerkin

methods'. *Journal of Computational Physics* 378, pp. 209–233. DOI: 10.1016/j.jcp.2018.11.009 (cited on pages 2, 56, 57, 71).
– (2019b). 'A p-multigrid strategy with anisotropic p-adaptation based on truncation errors for high-order discontinuous Galerkin methods'. *Journal of Computational Physics* 378, pp. 209–233. DOI: 10.1016/j.jcp.2018.11.009 (cited on page 56).
Schlichting, H., K. Gersten, E. Krause, and H. Oertel (2017). *Boundary-Layer Theory*. 9th ed. Berlin: Springer (cited on page 12).
Schmidt, A. and K. G. Siebert (2000). 'A posteriori estimators for the h – p version of the finite element method in 1D'. *Applied Numerical Mathematics* 35.1, pp. 43–66. DOI: 10.1016/S0168-9274(99)00046-X (cited on page 59).
Schneider, K. and O. V. Vasilyev (2010). 'Wavelet Methods in Computational Fluid Dynamics'. *Annual Review of Fluid Mechanics* 42.1, pp. 473–503. DOI: 10.1146/annurev-fluid-121108-145637 (cited on page 3).
Sen, S., S. Mittal, and G. Biswas (2011). 'Flow past a square cylinder at low Reynolds numbers'. *International Journal for Numerical Methods in Fluids* 67.9, pp. 1160–1174. DOI: 10.1002/fld.2416 (cited on page 112).
Shelton, A. B. (2008). 'A multi-resolution discontinuous Galerkin method for unsteady compressible flows'. PhD thesis. Georgia Tech (cited on pages 3, 50).
Shih, T. and B. Williams (2009). 'Development and Evaluation of an a Posteriori Method for Estimating and Correcting Grid-Induced Errors in Solutions of the Navier-Stokes Equations'. *47th AIAA Aerospace Sciences Meeting including the New Horizons Forum and Aerospace Exposition*. DOI: 10.2514/6.2009-1499 (cited on page 56).
Smith, M. and T. Barnwell (1986). 'Exact reconstruction techniques for tree-structured subband coders'. *IEEE Transactions on Acoustics, Speech, and Signal Processing* 34.3, pp. 434–441. DOI: 10.1109/TASSP.1986.1164832 (cited on page 39).
Solin, P., K. Segeth, and I. Dolezel (2003). *Higher-Order Finite Element Methods*. First. Chapman and Hall/CRC (cited on page 59).
Strela, V. (1996). 'Multiwavelets–theory and applications'. PhD thesis. Massachusetts Institute of Technology (cited on pages 3, 29, 30).
Strykowski, P. J. and K. R. Sreenivasan (1990). 'On the formation and suppression of vortex 'shedding' at low Reynolds numbers'. *Journal of Fluid Mechanics* 218, pp. 71–107. DOI: 10.1017/S0022112090000933 (cited on page 110).
Süli, E., P. Houston, and C. Schwab (2000). 'hp-finite element methods for hyperbolic problems'. *The Mathematics of Finite Elements and Applications X*, pp. 143–162 (cited on page 59).
Szabo, B. A. (1986). 'Implementation of a finite element software system with H and P extension capabilities'. *Finite Elements in Analysis and Design* 2.1, pp. 177–194. DOI: 10.1016/0168-874X(86)90016-8 (cited on page 58).
Taube, A., G. Gassner, and C.-D. Munz (2010). '*hp*-Adaptation in Space-Time within an Explicit Discontinuous Galerkin Framework'. *Springer Berlin Heidelberg*, pp. 427–439. DOI: 10.1007/978-3-642-03707-8_30 (cited on pages 63, 83, 91, 101, 127).
Toro, E. F. (2009). *Riemann Solvers and Numerical Methods for Fluid Dynamics*. Third. Springer-Verlag Berlin Heidelberg (cited on pages 1, 17).
Tugnoli, M., A. Abbà, L. Bonaventura, and M. Restelli (2017). 'A locally p-adaptive approach for Large Eddy Simulation of compressible flows in a DG framework'. *Journal of Computational Physics* 349, pp. 33–58. DOI: 10.1016/j.jcp.2017.08.007 (cited on page 57).

Valenciano, J. and R. G. Owens (2000). 'An h–p adaptive spectral element method for Stokes flow'. *Applied Numerical Mathematics* 33.1, pp. 365–371. DOI: 10.1016/S0168-9274(99)00103-8 (cited on page 59).

Van der Vegt, J. J. W. and H. van der Ven (2002). 'Space–Time Discontinuous Galerkin Finite Element Method with Dynamic Grid Motion for Inviscid Compressible Flows: I. General Formulation'. *Journal of Computational Physics* 182.2, pp. 546–585. DOI: https://doi.org/10.1006/jcph.2002.7185 (cited on page 13).

Verfürth, R. (1994). 'A posteriori error estimation and adaptive mesh-refinement techniques'. *Journal of Computational and Applied Mathematics* 50.1, pp. 67–83. DOI: https://doi.org/10.1016/0377-0427(94)90290-9 (cited on page 54).

Vuik, M. J. (2017). 'Multiwavelets and outlier detection for troubled-cell indication in discontinuous Galerkin methods'. PhD thesis. Delft University of Technology (cited on pages 3, 33, 39, 42).

– (2020). 'Multiwavelet Troubled-Cell Indication: A Comparison of Utilizing Theory Versus Outlier Detection'. In: *Spectral and High Order Methods for Partial Differential Equations ICOSAHOM 2018*. Ed. by S. J. Sherwin, D. Moxey, J. Peiró, P. E. Vincent, and C. Schwab. Springer International Publishing, pp. 537–548. DOI: 10.1007/978-3-030-39647-3_43 (cited on page 64).

Vuik, M. J. and J. K. Ryan (2014). 'Multiwavelet Troubled-Cell Indicator for Discontinuity Detection of Discontinuous Galerkin Schemes'. *Journal of Computational Physics* 270, pp. 138–160. DOI: 10.1016/j.jcp.2014.03.047 (cited on pages 3, 15, 33, 38, 42, 50).

– (2016). 'Automated Parameters for Troubled-Cell Indicators Using Outlier Detection'. *SIAM Journal on Scientific Computing* 38.1, pp. 84–104. DOI: 10.1137/15M1018393 (cited on pages 3, 15, 42).

Wackers, J., G. Deng, A. Leroyer, P. Queutey, and M. Visonneau (2012). 'Adaptive grid refinement for hydrodynamic flows'. *Computers & Fluids* 55, pp. 85–100. DOI: 10.1016/j.compfluid.2011.11.004 (cited on pages 2, 57).

Wang, L. and D. J. Mavriplis (2009). 'Adjoint-based h–p adaptive discontinuous Galerkin methods for the 2D compressible Euler equations'. *Journal of Computational Physics* 228.20, pp. 7643–7661. DOI: 10.1016/j.jcp.2009.07.012 (cited on pages 58, 60).

Wihler, T. P. (2011). 'An hp-adaptive strategy based on continuous Sobolev embeddings'. *Journal of Computational and Applied Mathematics* 235.8, pp. 2731–2739. DOI: 10.1016/j.cam.2010.11.023 (cited on pages 58, 60).

Williamson, C. H. K. (1996). 'Vortex Dynamics in the Cylinder Wake'. *Annual Review of Fluid Mechanics* 28.1, pp. 477–539. DOI: 10.1146/annurev.fl.28.010196.002401 (cited on page 110).

Woopen, M., G. May, and J. Schütz (2014). 'Adjoint-based error estimation and mesh adaptation for hybridized discontinuous Galerkin methods'. *International Journal for Numerical Methods in Fluids* 76.11, pp. 811–834. DOI: 10.1002/fld.3959 (cited on page 55).

Wurst, M., M. Keßler, and E. Krämer (2015). 'A high-order Discontinuous Galerkin Chimera method for laminar and turbulent flows'. *Computers & Fluids* 121, pp. 102–113 (cited on page 13).

Yan, G. and C. Ollivier-Gooch (2018). 'Applications of the Unsteady Error Transport Equation on Unstructured Meshes'. *AIAA Journal* 56, pp. 1–11. DOI: 10.2514/1.J057024 (cited on page 56).

Yee, H., J. Torczynski, S. Morton, M. Visbal, and P. Sweby (1997). *On Spurious Behavior of CFD Simulations*. 13th Computational Fluid Dynamics Conference (cited on page 89).

Yu, T., K. Kolarov, and W. Lynch (1999). 'Barysymmetric Multiwavelets on Triangle'. IRC Report 1997-006 (cited on page 4).

Zahr, M.J. and P.-O. Persson (2018). 'An optimization-based approach for high-order accurate discretization of conservation laws with discontinuous solutions'. *Journal of Computational Physics* 365, pp. 105–134. DOI: 10.1016/j.jcp.2018.03.029 (cited on page 57).

**Titre :** Adaptation *hp* par ondelettes pour les méthodes Galerkine discontinues

**Mot clés :** Mécanique des fluides, Navier-Stokes, méthodes numériques, méthodes adaptatives, ondelettes

**Résumé :** L'objectif principal de cette thèse est de développer une méthode *hp*-adaptative efficace en termes de coût et précision pour les schémas Galerkin discontinus appliqués aux équations de Navier-Stokes, en combinant flexibilité de l'adaptation a posteriori et précision de l'adaptation multi-résolution. Les performances de l'algorithme d'adaptation *hp* sont illustrées sur plusieurs cas d'écoulements stationnaires en une et deux dimensions.

La première direction de recherche emploie une nouvelle méthodologie basée sur les multi-ondelettes pour estimer l'erreur de discrétisation de la solution numérique dans le contexte de simulations avec adaptation *h*. Les résultats démontrent clairement la viabilité de cette méthode pour atteindre un gain de calcul significatif par rapport à un raffinement de maillage uniforme.

La deuxième voie de recherche aborde l'analyse et le développement d'une nouvelle stratégie d'adaptation *hp* basée sur la décroissance du spectre des multi-ondelettes comme critère adaptation *hp*. Cette stratégie permet de discriminer avec succès les régions caractérisées par une grande régularité de celles contenant des phénomènes discontinus. De manière remarquable, l'algorithme d'adaptation *hp* est capable d'atteindre une haute précision caractéristique des solutions numériques d'ordre élevé tout en évitant les oscillations indésirables en adoptant des approximations d'ordre réduit à proximité des singularités.

**Title:** Multiwavelet-based *hp*-adaptation for discontinuous Galerkin methods

**Keywords:** Fluid Mechanics, Navier-Stokes, Numerical methods, Adaptive methods, Wavelets

**Abstract:** The main objective of the present thesis is to devise, construct and validate computationally efficient *hp*-adaptive discontinuous Galerkin schemes of the Navier-Stokes equations by bringing together the flexibility of a posteriori error driven adaptation and the accuracy of multiresolution-based adaptation. The performance of the hp-algorithm is illustrated by several steady flows in one and two dimensions.

The first research direction employs a new multiwavelet-based methodology to estimate the discretization error of the numerical solution in the context of *h*-adaptive simulations. The results certainly demonstrate the viability of *h*-refinement to reach a significant computational gain with respect to uniformly refined grids.

The second line of investigation addresses the analysis and development of a new *hp*-adaptive strategy based on the decay of the multiwavelet spectrum to drive *hp*-adaptive simulations. The strategy successfully discriminates between regions characterized by high regularity and discontinuous phenomena and their vicinity. Remarkably, the developed *hp*-adaptation algorithm is able to achieve the high accuracy characteristic of high-order numerical solutions while avoiding unwanted oscillations by adopting low-order approximations in the proximity of singularities.